

METAL LOADED G-C₃N₄ FOR VISIBLE LIGHT-DRIVEN H₂ PRODUCTION

Federica Fina

**A Thesis Submitted for the Degree of PhD
at the
University of St Andrews**



2014

**Full metadata for this item is available in
St Andrews Research Repository
at:**

<http://research-repository.st-andrews.ac.uk/>

Please use this identifier to cite or link to this item:

<http://hdl.handle.net/10023/6322>

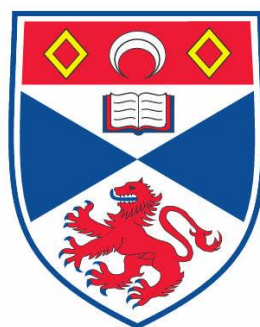
This item is protected by original copyright

**This item is licensed under a
Creative Commons Licence**

Metal loaded g-C₃N₄ for visible light-driven H₂ production

by

Federica Fina



A thesis submitted in partial fulfilment for the degree of PhD
at the
University of St Andrews

2014

I, Federica Fina hereby certify that this thesis, which is approximately 50,000 words in length, has been written by me, and that it is the record of work carried out by me and that it has not been submitted in any previous application for a higher degree.

I was admitted as a research student in January 2011 and as a candidate for the degree of Doctor of Philosophy in August 2014; the higher study for which this is a record was carried out in the University of St Andrews between 2011 and 2014.

Date Signature of candidate

I hereby certify that the candidate has fulfilled the conditions of the Resolution and Regulations appropriate for the degree of Doctor of Philosophy in the University of St Andrews and that the candidate is qualified to submit this thesis in application for that degree.

Date Signature of supervisor

In submitting this thesis to the University of St Andrews I understand that I am giving permission for it to be made available for use in accordance with the regulations of the University Library for the time being in force, subject to any copyright vested in the work not being affected thereby. I also understand that the title and the abstract will be published, and that a copy of the work may be made and supplied to any bona fide library or research worker, that my thesis will be electronically accessible for personal or research use unless exempt by award of an embargo as requested below, and that the library has the right to migrate my thesis into new electronic forms as required to ensure continued access to the thesis. I have requested the appropriate embargo below.

The following is an agreed request by candidate and supervisor regarding the publication of this thesis:

Embargo on all of electronic copy for a period of 2 years on the following ground:

Publication would preclude future publication.

Date Signature of candidate

Date Signature of supervisor

Acknowledgements

I would like to thank my supervisor Professor John T. S. Irvine for giving me the opportunity to do my PhD and for his guidance and advice.

I would like to thank Dr. Xiaoxiang Xu for helping me at the beginning of the project. My gratitude goes also to the JTSI group especially to Dr. Paul Connor for the discussions and the advice on the set-up, and to Dr. Dragos Neagu for the assistance on the XRD.

A special thank you goes to George Anthony from the mechanical workshop for making the reactor, for being there when things needed fixing and for his advice.

Thank you to Ross Blackley for being patient in teaching me to use the SEM and the TEM. I would also like to thank Sylvia Williamson for BET and TGA analysis, Derek Waddell for XRD measurements and Dr. Hervé Ménard (Sasol Ltd.) for XPS analysis.

Finally, I would like to express my gratitude to my family and in particular my parents who supported me for all this time.

"Yes, my friends, I believe that water will someday be employed as fuel, that hydrogen and oxygen, which constitute it, used singly or together, will furnish an inexhaustible source of heat and light....I believe, then, that when the deposits of coal are exhausted, we shall heat and warm ourselves with water.

Water will be the coal of the future."

The Mysterious Island, Jules Verne, 1874¹

Abstract

The need for green and renewable fuels has led to the investigation of ways to exploit renewable resources. Solar among all the renewables is the most powerful and its conversion into usable energy would help in solving the energy problem our society is facing. Photocatalytic water splitting for hydrogen production is an example of solar energy storage into chemical bonds. The hydrogen produced in this way can then be employed as carbon free fuel creating the “Hydrogen Cycle”.

This work investigates the structure and the activity of graphitic carbon nitride (g-C₃N₄), an organic semiconductor that proved a suitable photocatalyst for hydrogen production from water. Synthesised by thermal polycondensation of melamine it is a graphitic like material with a band gap of 2.7 eV which makes it a visible light-active catalyst. In a first instance the effect of the synthesis conditions on its structure and morphology are investigated to find the optimum parameters. The temperature of condensation is varied from 450 °C up to 650 °C and the length from 2.5 h to 15 h. The structural changes are monitored *via* x-ray diffraction (XRD) and elemental analysis while the effect on the morphology and the band gap of g-C₃N₄ are investigated by mean of scanning electron microscopy and UV-Vis absorption. Subsequently, a study of the crystal structure of the catalyst is carried out. Using structures proposed in the literature, x-ray diffraction and neutron scattering simulations are used to narrow down the number of possible 3D structures.

After structural characterisation, the activity of g-C₃N₄ for photocatalytic hydrogen evolution is evaluated. It is confirmed that loading 1 wt.% Pt on its surface significantly increases the hydrogen evolution rate. The attention then focuses on the loading

procedures, the reduction pre-treatments of the co-catalyst and the reasons of the different performances when different procedures are employed. The catalytic system is characterised by mean of x-ray photoelectron spectroscopy (XPS), transmission electron microscopy (TEM) and XRD. By investigating the composition and the morphology of the platinum nanoparticles under different conditions, the main factors responsible for the changes in activity of g-C₃N₄ for hydrogen evolution are identified. Additionally, the role of the co-catalyst and its interaction with g-C₃N₄ is also elucidated.

Finally, taking forward the knowledge acquired on the Pt-g-C₃N₄ system, the effect on the hydrogen evolution rate of alloying platinum with a second metal (Cu, Ag, Ni and Co) is studied. The nanoparticles are characterised by XRD and TEM. A screening of the loading procedures and bimetallic systems is performed to identify the most promising for photocatalytic hydrogen evolution with the aim of bringing them towards further investigation.

Contents

Contents	iii
Table of figures	vi
List of tables	x
Glossary	xii
Chapter 1 Introduction	1
1.1. Energy scenario	1
1.1.1. Current energy situation.....	1
1.1.2. Renewable alternatives	2
1.2. Hydrogen Economy.....	3
1.2.1. What is the Hydrogen Economy?	3
1.2.2. Why hydrogen?	4
1.2.3. Hydrogen production: today and tomorrow.....	5
1.3. Photocatalytic water splitting	6
1.3.1. General principles and mechanism	7
1.3.2. Improving the activity of the catalyst	10
1.3.3. Overall water splitting.....	13
1.3.4. Half reaction and sacrificial reagents.....	14
1.4. Graphitic carbon nitride.....	15
1.4.1. General description	15
1.4.2. State of the art: synthesis	17
1.4.3. State of the art: photocatalytic applications	18
1.5. Aim of the work.....	21

Chapter 2 Experimental.....	23
2.1. Synthesis.....	23
2.1.1. Graphitic Carbon Nitride synthesis.....	23
2.1.2. Platinum loading and reduction	24
2.1.3. Synthesis of supported bimetallic alloys.....	24
2.2. Characterisation methods	25
2.2.1. Powder x-ray diffraction	25
2.2.2. Neutron scattering	29
2.2.3. Solid State Nuclear Magnetic Resonance (SSNMR).....	33
2.2.4. Thermal Gravimetric Analysis.....	35
2.2.5. Brunauer-Emmet-Teller Analysis	36
2.2.6. Elemental Analysis	36
2.2.7. Solid UV-Vis spectroscopy.....	36
2.2.8. Transmission Electron Microscopy (TEM)	37
2.2.9. Scanning Electron Microscopy (SEM)	41
2.2.10. X-ray Photoelectron Spectroscopy (XPS).....	42
2.3. Hydrogen evolution.....	43
2.3.1. Reaction vessel.....	43
2.3.2. Reaction conditions.....	45
2.3.3. Gas sampling.....	46
2.3.4. Gas analysis.....	47
Chapter 3 The catalyst: Graphitic Carbon Nitride.....	49
3.1. Introduction	49
3.2. Influence of synthesis conditions on structure and morphology	51
3.2.1. Effect of condensation temperature on the structure	51
3.2.2. Effect of temperature on the morphology	60
3.2.3. Effect of condensation length on the structure and morphology	61
3.3. Further characterisation	64
3.3.1. Solid State NMR	64
3.4. Structure investigation I: XRD	66
3.4.1. Comparison with fully polymerised g-C ₃ N ₄	66
3.4.2. Comparison with partially polymerised g-C ₃ N ₄	68
3.4.3. Comparison with Melon.....	71

3.4.4. Symmetry considerations	79
3.4.5. Summary of results	80
3.5. Structure investigation II: Neutron Scattering.....	82
3.5.1. Single phases.....	88
3.5.2. Multiple phases	92
3.6. Summary and preliminary conclusions	93
Chapter 4 The co-catalyst: Platinum.....	96
4.1. Introduction	96
4.2. Preliminary activity investigation.....	98
4.3. Effect of the loading procedure	99
4.4. Interaction with light	108
4.5. Reduction pre-treatment	111
4.6. Effect of the sacrificial agent.....	122
4.7. Role of platinum in the process: plasmonic behaviour?.....	128
4.8. Assessing the catalytic characteristic of Pt-g-C ₃ N ₄	130
4.9. Conclusions	132
Chapter 5 The co-catalyst: Bimetallic Alloys.....	134
5.1. Introduction	134
5.2. Synthesis and performance.....	137
5.2.1. PtCu-g-C ₃ N ₄	139
5.2.2. PtAg-g-C ₃ N ₄	143
5.2.3. PtNi-g-C ₃ N ₄	147
5.2.4. PtCo-g-C ₃ N ₄	152
5.2.5. Further discussion	156
5.3. Conclusions and future works	158
Chapter 6 Conclusions and Future Work	160
6.1. Conclusions	160
6.2. Future work	164
Appendix A Crystallographic information	165
Bibliography.....	180

Table of figures

Figure 1.1 World energy consumption by fuel type. ²	2
Figure 1.2 The Hydrogen Economy.	4
Figure 1.3 The Hydrogen Cycle.	5
Figure 1.4 Schematic based on the Fujishima-Honda electrochemical cell.....	6
Figure 1.5 Water splitting as an uphill reaction.....	7
Figure 1.6 Energy of light.	8
Figure 1.7 Photocatalytic water splitting.....	9
Figure 1.8 Charges recombination.	10
Figure 1.9 Role of a co-catalyst as an electron trap.....	11
Figure 1.10 Doping options for band engineering.....	12
Figure 1.11 Z-scheme photocatalytic water splitting.	13
Figure 1.12 Sacrificial reagent systems.....	14
Figure 1.13 Possible g-C ₃ N ₄ structures.	15
Figure 1.14 g-C ₃ N ₄ XRD pattern and DFT calculations of band structure. ⁵⁴	16
Figure 1.15 Reaction pathway to g-C ₃ N ₄	18
Figure 2.1 Images of g-C ₃ N ₄ preparation.....	23
Figure 2.2 Bragg's law.	26
Figure 2.3 XRD pattern of a silicon standard.....	27
Figure 2.4 Schematic of a Neutron diffractometer.....	29
Figure 2.5 Physical meaning of Q.	30
Figure 2.6 Examples of g(r) and D(r) for melamine.....	32

Figure 2.7 Sample holder for a neutron scattering experiment.	33
Figure 2.8 Effect of a magnetic field on magnetic moments.....	34
Figure 2.9 Effect of a 90_x° pulse on the bulk magnetisation vector.	34
Figure 2.10 Schematic of TEM working principles.	38
Figure 2.11 Example of (HR)TEM images.	39
Figure 2.12 Distribution of Pt d_{111} from HRTEM measurements.	40
Figure 2.13 Schematic of the principle of SEM imaging.	41
Figure 2.14 Working principle of an x-ray photoelectron spectrometer.	42
Figure 2.15 Photocatalytic Set-up.	43
Figure 2.16 UV lamp wavelength distribution.	44
Figure 2.17 Temperature profile.....	45
Figure 2.18 Automatic System.	46
Figure 2.19 Example of Gas Chromatograph.	47
Figure 3.1 Structural representation of Melon and g- C_3N_4	50
Figure 3.2 TGA of melamine.	52
Figure 3.3 Effect of temperature on crystal structure.	53
Figure 3.4 XRD pattern of Melem and C_3N_4 -450.	54
Figure 3.5 C:N atomic ratio vs. number of units per polymeric fragment.	55
Figure 3.6 Comparison of C_3N_4 -450 and Melon.	56
Figure 3.7 Thermal Gravimetric Analysis of different g- C_3N_4	57
Figure 3.8 UV-Vis absorption spectra.	58
Figure 3.9 SEM images of g- C_3N_4 synthesised at different temperatures.....	61
Figure 3.10 Effect of condensation length on the XRD pattern of C_3N_4 -550 and -600. 62	
Figure 3.11 Effect of condensation length on the XRD pattern of C_3N_4 -500.	63
Figure 3.12 Solid state NMR spectra of different C_3N_4	65
Figure 3.13 XRD: comparison of C_3N_4 -500 with triazine and heptazine g- C_3N_4	67
Figure 3.14 Theoretical pattern generated for Döblinger structure. ¹²²	69
Figure 3.15 Triazine- and heptazine-based partially polymerised structures.	70
Figure 3.16 Theoretical patterns based on Melon structures. ^{123, 126}	72
Figure 3.17 I_{hkl}/I_{002} and 2θ vs. γ	74
Figure 3.18 Buckled structure for Melon.	75
Figure 3.19 Melon structures with shifted layers.	77
Figure 3.20 I_{210}/I_{002} and 2θ vs. α and β	78
Figure 3.21 Possible space groups.....	80

Figure 3.22 Total structure factor, $F(Q)$	83
Figure 3.23 Effect of H and D on the $D(r)$ of C_3N_4 -500.	84
Figure 3.24 Inter-atomic distances in heptazine units.	85
Figure 3.25 Differential pair correlation function for different C_3N_4	86
Figure 3.26 Calculated $D(r)$ for modified and Tyborski's Melon.	88
Figure 3.27 Effect of unit cell angle γ on $D(r)$	89
Figure 3.28 Effect of unit cell angles α and β on $D(r)$	90
Figure 3.29 Effect on the $D(r)$ of shifted layers.	91
Figure 3.30 Crystal structure of Melon.	91
Figure 4.1 N 1s and C 1s XP spectra of samples before test.	101
Figure 4.2 Pt 4f XP spectra before photocatalysis.	102
Figure 4.3 TEM and HRTEM images of Pt-g- C_3N_4 before photocatalytic test.	103
Figure 4.4 Pt 4f XP spectra after photocatalysis.	105
Figure 4.5 TEM and HRTEM of Pt-g- C_3N_4 after photocatalysis.	106
Figure 4.6 XRD patterns of sample after photocatalysis.	107
Figure 4.7 H_2 evolution rate vs. time.	108
Figure 4.8 H_2 evolution rate and T vs. time upon cooling.	109
Figure 4.9 Pt 4f spectra of Pt-g- C_3N_4 at different test lengths.	110
Figure 4.10 Pt^0 relative amount vs. time.	111
Figure 4.11 H_2 production steady state for reduced Pt-g- C_3N_4	112
Figure 4.12 H_2 evolution rate profile for reduced Pt-g- C_3N_4	113
Figure 4.13 TEM images of Pt-g- C_3N_4 reduced under 5 % H_2	114
Figure 4.14 XRD pattern of reduced Pt-g- C_3N_4	116
Figure 4.15 Platinum NPs morphology for Pt-g- C_3N_4 reduced with $NaBH_4$	117
Figure 4.16 XP spectra of Pt 4f region of Pt-g- C_3N_4 reduced with $NaBH_4$	118
Figure 4.17 UV-Vis spectra of impregnated and reduced Pt-g- C_3N_4	119
Figure 4.18 Platinum NPs morphology for Pt-g- C_3N_4 after double reduction.	120
Figure 4.19 H_2 evolution rate vs. pH.	123
Figure 4.20 Sacrificial agent influence on H_2 evolution rate profile.	124
Figure 4.21 XPS Pt 4f spectra of Pt-g- C_3N_4 : TEOA.	124
Figure 4.22 TEM images of Pt-g- C_3N_4 tested with TEOA.	126
Figure 4.23 XPS and H_2 evolution of Pt-g- C_3N_4 using $Na_2C_2O_4$ as ED.	127
Figure 4.24 Role of Pt^0 NPs in photocatalytic H_2 evolution.	128
Figure 4.25 Influence of single wavelength-light test on UV-Vis spectra.	129

Figure 4.26 Shelf life evaluation.	131
Figure 4.27 Reusability of the catalyst.	131
Figure 5.1 Metal-Semiconductor heterojunction.	135
Figure 5.2 Work function of some metals compared to VB and CB of g-C ₃ N ₄	136
Figure 5.3 TGA of PtMe-g-C ₃ N ₄	137
Figure 5.4 H ₂ evolution rates of PtCu-g-C ₃ N ₄	139
Figure 5.5 XRD of PtCu-g-C ₃ N ₄	140
Figure 5.6 (HR)TEM images of PtCu-g-C ₃ N ₄	143
Figure 5.7 H ₂ evolution rates of PtAg-g-C ₃ N ₄	144
Figure 5.8 XRD of PtAg-g-C ₃ N ₄	145
Figure 5.9 (HR)TEM images of PtAg-g-C ₃ N ₄	147
Figure 5.10 H ₂ evolution rates of PtNi-g-C ₃ N ₄	148
Figure 5.11 XRD of PtNi-g-C ₃ N ₄	149
Figure 5.12 (HR)TEM images of PtNi-g-C ₃ N ₄	151
Figure 5.13 H ₂ evolution rates of PtCo-g-C ₃ N ₄	152
Figure 5.14 XRD of PtCo-g-C ₃ N ₄	153
Figure 5.15 (HR)TEM images of PtCo-g-C ₃ N ₄	154
Figure 5.16 HRTEM of ring-like PtCo nanoparticle.	155
Figure 5.17 H ₂ evolution rate vs. NPs particle size and metal work function.	157
Figure A.1 D(r) plot of modified Melon.	176
Figure A.2 D(r) plot of Tyborski's Melon.	177
Figure A.3 D(r) plot of Melon $\gamma = 88^\circ$	177
Figure A.4 D(r) plot of Melon $\gamma = 89^\circ$	178
Figure A.5 D(r) plot of Melon $\alpha = 98^\circ$	178
Figure A.6 D(r) plot of Melon $\beta = 98^\circ$	179
Figure A.7 D(r) plot of Melon with shifted layers.	179

List of tables

Table 3.1 Miscellaneous information about g-C ₃ N ₄ synthesised at different temperatures.	59
Table 3.2 Surface area and particle size of different g-C ₃ N ₄	60
Table 3.3 Miscellaneous information about C ₃ N ₄ -500 synthesised for different time lengths.....	64
Table 3.4 Summary of the modelled structures.....	81
Table 3.5 Summary of peak areas from D(r) of single phase.....	92
Table 3.6 Summary of peak areas from D(r) of mixed phases.....	93
Table 4.1 H ₂ evolution rates for C ₃ N ₄ -500, -550, -600.	98
Table 4.2 Comparison of loading methods.....	100
Table 4.3 XPS Pt 4f summary for Pt-g-C ₃ N ₄ reduced in H ₂	113
Table 4.4 Comparison of reduced with not reduced Pt-g-C ₃ N ₄	121
Table 4.5 Summary of the effect of different sacrificial agents.	125
Table 5.1 List of synthetic procedures for PtMe alloys.....	138
Table 5.2 Summary of results obtained for the bimetallic alloys.....	156
Table A.1 Melem crystallographic information as from ref. ⁶⁹	165
Table A.2 Melon from Lotsch ¹²⁶	166
Table A.3 Teter & Hemley triazine-based g-C ₃ N ₄ crystallographic information. ¹¹⁶ ...	167
Table A.4 Heptazine-based g-C ₃ N ₄ crystallographic information.	167
Table A.5 Heptazine based g-C ₃ N ₄ as from Döblinger. ¹²²	168
Table A.6 Triazine-based partially polymerised graphitic carbon nitride (A-A).....	169

Table A.7 Triazine-based partially polymerised graphitic carbon nitride (A-B).	169
Table A.8 Heptazine-based partially polymerised graphitic carbon nitride (A-A).	170
Table A.9 Heptazine-based partially polymerised graphitic carbon nitride (A-B).	171
Table A.10 Melon with closer chains.....	172
Table A.11 Buckled modified Melon.....	174

Glossary

VB	= valence band
CB	= conduction band
E_g	= band gap
AQY	= apparent quantum yield
NHE	= normal hydrogen electrode
NPs	= nanoparticles
ED	= electron donor
EA	= electron acceptor
CIF	= crystallographic information file
CHN	= elemental analysis
XPS	= x-ray photoelectron spectroscopy
TEM	= transmission electron spectroscopy
TOF	= time of flight
OA	= oxalic acid
TEOA	= triethanolamine
ϕ	= work function
SC	= semiconductor

Chapter 1

Introduction

1.1. Energy scenario

1.1.1. Current energy situation

Today our society is facing two important issues which could affect our future: increasing energy demand accompanied by depletion of the commonly used energy sources (fossil fuels) and consequent increase in CO₂ emissions, cause of drastic and dangerous climate changes. According to the U.S. Energy Information Administration, the world energy consumption will increase by 56 % from 2010 to 2040. The International Energy Outlook 2013 (IEO2013) projects that even though nuclear and renewables will be the energy resources with the fastest growing consumption (2.5 %/year, Figure 1.1), fossil fuels will remain the main supply of energy until 2040 representing a significant 80 % of the total energy use.² It is also predicted that the actual fossil fuels reserves (oil, natural gas and coal) will last for centuries.³ However the estimated increasing utilisation rate could drastically accelerate their depletion. An additional consequence for this high carbon fuels consumption is the increase (46 %) in CO₂ emissions until 2040² that will bring negative climate changes. For all of these reasons there is a great need of finding solutions to these issues. Three possibilities are being considered: decarbonisation of fossil fuels, nuclear energy and renewables.⁴ *Decarbonisation of fossil fuels* consists in reducing the amount of CO₂ evolved during the utilisation of oil, natural gas and coal by carbon capture and sequestration (CCS). With this process the carbon dioxide produced by the power plant is collected and stored in geological reservoirs or oceans.⁴ This solution only looks at one

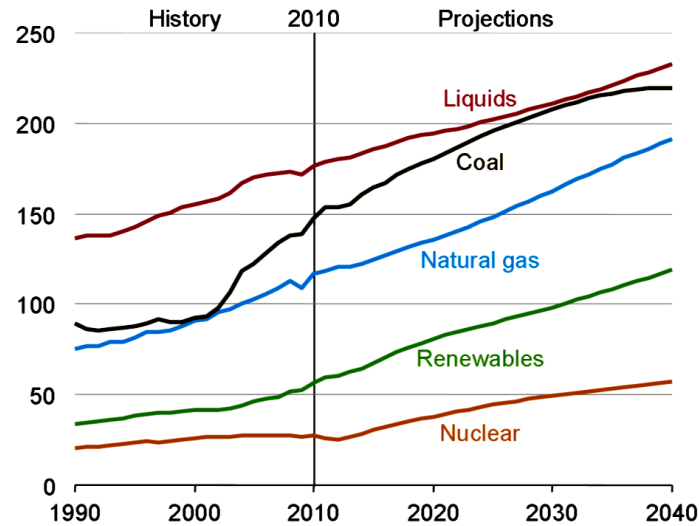


Figure 1.1 World energy consumption by fuel type.² (quadrillion Btu) Reproduced with permission from International Energy Outlook 2013.²

of the issues but the limited availability of the fuels remains. In addition, it adds all the problems linked to the effect of stored CO₂ to our ecosystem. The *nuclear* option is considered being carbon free, however it would only be a temporary alternative due to the limited availability of Uranium.⁴ Our best option for a long-term solution lies in *renewable energy sources* (wind, solar, tidal, biomass etc.). These are unlimited and carbon neutral providing a solution for both of the above issues.

1.1.2. Renewable alternatives

Renewable energy sources can be classified in different categories by considering their intermittent nature and their carbon content.⁴ The intermittent sources: wind, solar and tidal, are challenging to “harvest” while non-intermittent: hydro, geothermal, biomass and landfill waste are instead more constantly available. Looking at their carbon content (linked to possible CO₂ emission), carbon free are those resources that would not produce CO₂ upon use (solar, wind, tidal, etc.). Carbon neutral instead are those which produce CO₂ when employed, but during the production of the actual energy source the same amount of CO₂ is consumed, bringing the total carbon balance to zero. Typical examples are biomasses that, while growing, consume carbon dioxide.⁴ Today the main contribution to the total energy production is given by hydropower, followed by wind.^{5,6} Among all, however, solar is potentially the biggest source of renewable energy available. The energy content of sunlight that reaches our planet in one hour is more than what is

consumed in the whole world in one year.³ Even though renewables are an exciting alternative to our current energy situation, they present many challenges. Biomasses, for example, have to be cultivated and this would require a large surface area subtracted from agriculture.⁴ Other resources are intermittent, requiring their conversion into a form of energy that can be stored. For this reason, today, they are mainly converted into electricity. Photovoltaic (PV) is a typical example of a technology that converts solar energy into electricity. However the efficiency to production cost ratio of these methods, including PV, does not make them competitive enough to replace fossil fuels in the current energy economy.⁴ In addition electricity also has to be stored. Usually batteries are employed as storage systems together with other technologies: compressed air, hydrostatic, electrolysis of water to produce hydrogen.⁴ Unfortunately all of these methods have drawbacks; they are either too expensive or require large areas and reservoirs.

An interesting alternative for storing the energy of renewables is their conversion to chemical energy in the form of molecular bonds, for example by converting them directly to hydrogen. Hydrogen could then be stored and used as a green fuel. Great attention is being focused in developing processes for hydrogen production from renewables in an efficient and cost effective manner. The long term goal is to establish a “Hydrogen Economy”⁷ where hydrogen will be employed as the main fuel and CO₂ emissions will be drastically reduced.

1.2. Hydrogen Economy

1.2.1. What is the Hydrogen Economy?

The term “Hydrogen Economy” was introduced for the first time by John Bockris in 1970⁷ during a General Motors meeting. During a discussion at the meeting, it was concluded that hydrogen would replace fossil fuels in the transport sector.⁷ An extension of its application to other sectors (household and industry) was also considered.⁷ Bockris’ idea for the hydrogen economy was that of generating H₂ *via* electrolysis of water (both fresh and sea water) which would employ electricity produced with the exploitation of solar energy.⁷ In a brief summary, hydrogen would be produced in an entirely clean and renewable way. If more than forty years ago this concept was only the result of a conversation, it has nowadays a great importance. Due to increasing CO₂ emissions and consumption of fossil fuels, the Hydrogen Economy has now become a necessity. Various

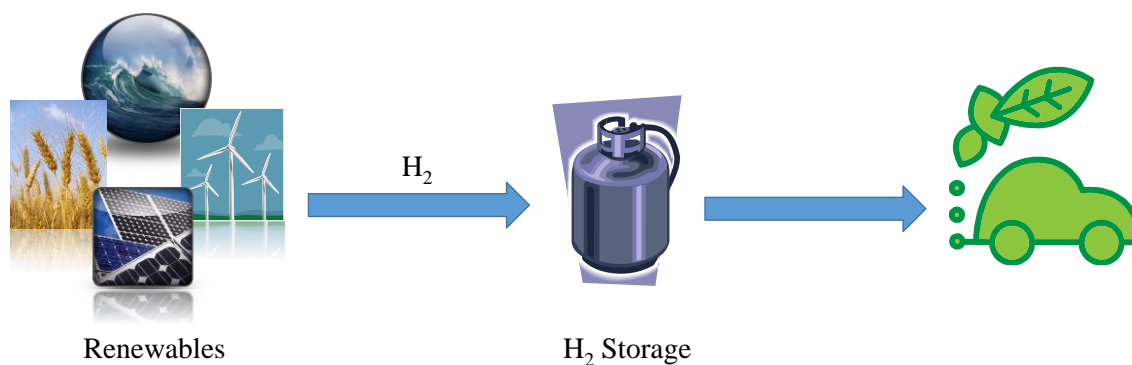


Figure 1.2 The Hydrogen Economy. Schematic representation of the “Hydrogen Economy” where renewables are used to produce hydrogen.

milestones have been established on our future energy path in order to introduce renewables and hydrogen in the world energy consumption. An example is the HyWay project that in 2008 published the European Hydrogen Energy Roadmap.⁸ This project illustrates a long-term scenario (2050) where hydrogen becomes more and more important in our energy economy and it lists some of the benefits that could come from this. In the most optimistic scenario of the Roadmap, by 2050, hydrogen fuel cell passenger vehicles could represent 75 % of the total passenger transport.^{7, 8} As a consequence the CO₂ emissions could be reduced by ~50 %.⁸

The hydrogen economy is in continuous evolution and adaptation, and it is not unique for all the countries. It is highly affected not only by technological and cost factors, but also geopolitical ones. It is therefore a dynamic concept. However, it still retains the basic principles of Bockris’ idea: hydrogen is produced by renewables and used as fuel (Figure 1.2).

1.2.2. Why hydrogen?

Hydrogen is considered the fuel of the future because, per unit of mass, it has the highest content of energy (33.3 kWh·kg⁻¹), if compared with the traditional fuels like: methane (12.8 kWh·kg⁻¹), gasoline (12.4 kWh·kg⁻¹) and diesel (11.8 kWh·kg⁻¹).⁹ However, by being the lightest it is not as competitive if the energy per unit of volume is considered. Therefore, a suitable storage option has to be found.

Another characteristic of hydrogen that makes it so suitable for a clean energy future is its carbon free nature. Obviously it does not contain any carbon atoms, therefore no CO₂ is produced when it is employed as fuel. The only by-product is water.⁹ It is important to

specify, however, that hydrogen is not an *energy source*, but it has to be considered as an *energy carrier*. This is because hydrogen cannot be found naturally in reservoirs, it has to be produced.

1.2.3. Hydrogen production: today and tomorrow.

The concept of the Hydrogen Economy can only work if hydrogen is produced entirely from clean energy sources. Today this is not yet the case. The main hydrogen production processes that find industrial application are not green methods, and from those CO₂ is produced. The reason for this is that currently H₂ is mainly obtained from fossil fuels specifically from steam reforming of natural gases.¹⁰ Obviously this generates high quantities of CO₂ to be released in the atmosphere. Only a small part of the total H₂ production is *via* electrolysis which employs electricity. However, even in this case fossil fuels are used to generate electricity in the first place.¹⁰ Hence, in any case greenhouse gases are evolved. A solution to the CO₂ emissions caused by hydrogen production is CO₂ capture and sequestration. The basic principle is that of storing the carbon dioxide produced in underground empty reservoir.⁷ This however does not appear to be a long-term and clean solution. An alternative that is proposed for a carbon-free production of hydrogen is nuclear power. This method as well has its drawbacks: it is not renewable and produces radioactive waste.^{4, 7}

The long-term solution for a renewable and carbon-free hydrogen production is the use of renewable energy sources. The electricity required for water electrolysis could be produce from wind, tidal, geothermal and solar energy.⁷ Among all the possible green technologies, the most direct and simple one is the production of hydrogen from water

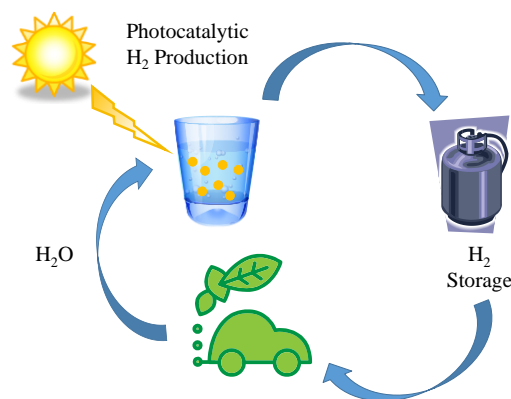


Figure 1.3 The Hydrogen Cycle. Schematic representation of the hydrogen cycle where H₂ is produced from water with sunlight to be used as fuels.

via photocatalysis (photocatalytic water splitting). In this case the energy required will be provided directly from sunlight and no intermediate electricity is required. In addition the only product of hydrogen utilisation is water which can be re-introduced in the “Hydrogen Cycle” (Figure 1.3).

1.3. Photocatalytic water splitting

Photocatalytic water splitting takes inspiration from a natural process that converts sunlight into fuel: photosynthesis, where plants absorb sunlight and convert its energy into chemical bonds which will then be used to power the plant itself. Photocatalytic water splitting, similarly to photosynthesis, aims to use solar energy to produce hydrogen from water, and use it as a green fuel. For this reason it is also referred to as *artificial photosynthesis*.¹¹

The first example reported in the literature of water splitting driven by light irradiation dates back to 1972 by Fujishima and Honda.¹² They reported the photoelectrochemical water splitting in which light provided the required energy to drive the process. Figure 1.4 illustrates a schematic of the set-up used for their experiment. They employed a TiO_2 electrode as oxygen evolution centre and a platinum electrode as hydrogen evolution centre.¹² The energy was provided by UV light irradiation of TiO_2 through a side window, producing electrons for the production of H_2 at the platinum electrode.¹² Following their pioneering work, a great effort has been put into developing new materials and an entirely photocatalytic process.

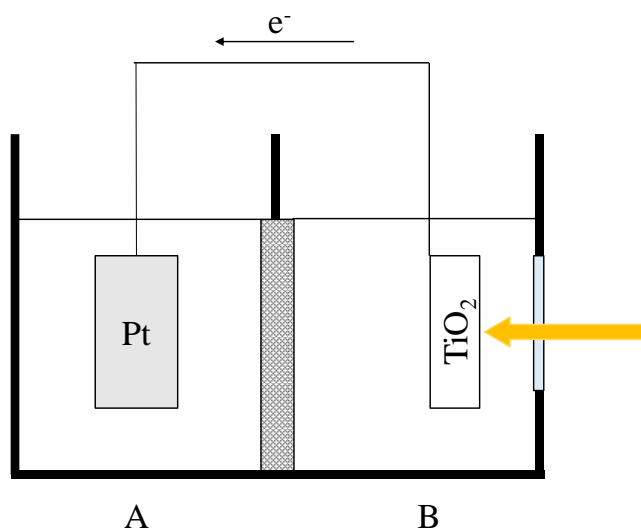


Figure 1.4 Schematic based on the Fujishima-Honda electrochemical cell. TiO_2 is the O_2 -evolution electrode and it is irradiated by light. This generates an electron flow that will reach the platinum counter electrode for the production of H_2 .¹²

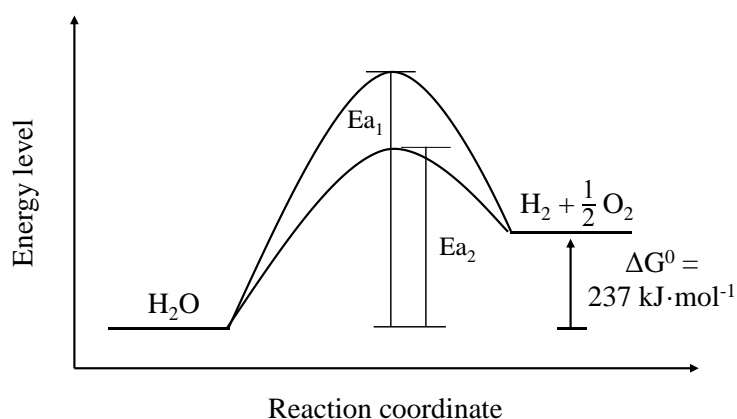
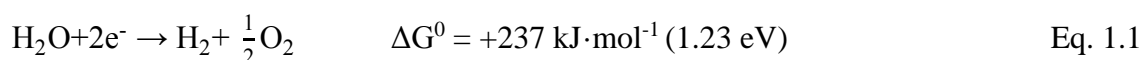


Figure 1.5 Water splitting as an uphill reaction. Energy diagram of the water splitting reaction. The products are at a more energetic state than the starting material. E_{a1} and E_{a2} represent the activation energies in the absence and presence of a catalyst, respectively.

1.3.1. General principles and mechanism

The concept of photocatalytic water splitting is fairly simple. Only a few elements are involved: water, a catalyst and light irradiation. However, its direct application is more challenging. The formation of H_2 and O_2 from water is an uphill reaction,^{13, 14} meaning that the products are at a higher energy than the starting materials. This explains why energy has to be provided to the system (Figure 1.5). This also implies that the reverse reaction (i.e. H_2 and O_2 to water) can easily occur.

The Gibbs free energy needed to produce H_2 and O_2 from water, Equation 1.1, is $+237 \text{ kJ}\cdot\text{mol}^{-1}$ (1.23 eV).¹³⁻¹⁵



In a photocatalytic process this energy can be provided through light irradiation. The value of 1.23 eV, the minimum energy required, puts a limit to the employable wavelengths. The maximum wavelength that could promote water splitting is 1000 nm, a wavelength which is in the infrared (IR) region (Figure 1.6).¹⁵

Photocatalytic water splitting is an example of heterogeneous catalysis¹⁶ where the reactions occur at the interface of a solid catalyst and a liquid media where the reactants are dissolved (in this specific case the reactant is the media itself: water). The catalysts involved in water splitting are semiconductors.^{14, 16} A semiconductor is characterised by a difference in energy between valence (VB, highest occupied energy level) and

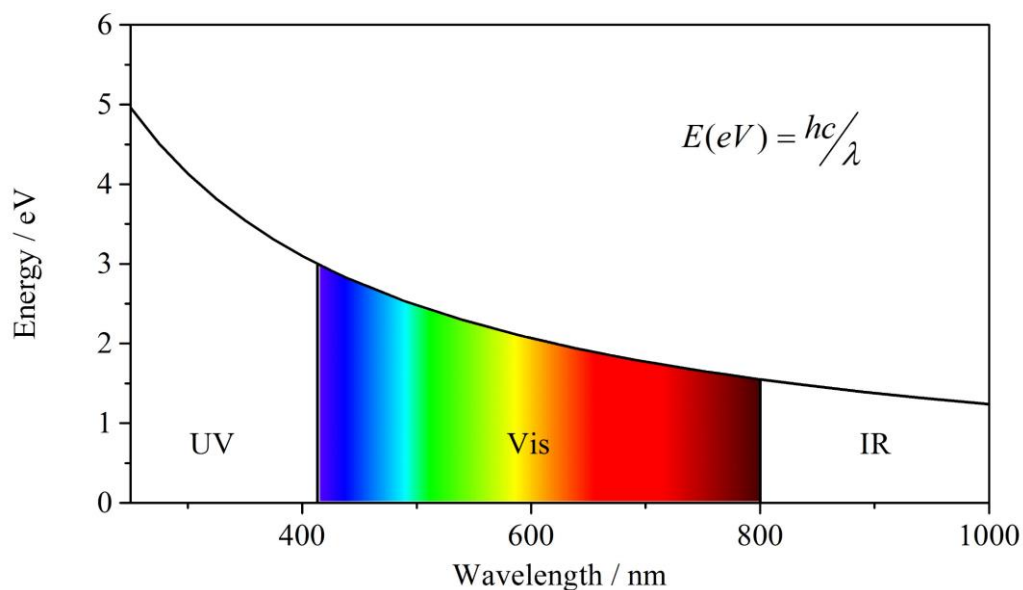


Figure 1.6 Energy of light. Distinction of ultra-violet, visible and infrared wavelengths (nm) and their energy content (eV).

conduction band (CB, lowest unoccupied energy level). This energy gap is defined as the Band Gap (E_g) of the material (Figure 1.7). A semiconductor has a Band Gap smaller than ~ 4 eV (germanium: 0.7 eV¹⁷; silicon: 1.11 eV¹⁸; ZnS: 3.6 eV¹⁸).¹⁹ This energy gap can therefore be exploited to generate electrons of suitable energy for water splitting.²

A schematic representation of photocatalytic water splitting is illustrated in Figure 1.7. When light irradiation of suitable energy ($E_\lambda \geq E_g$) strikes the semiconductor, the photons are absorbed and lead to the excitation and promotion of electrons from the valence to the conduction band of the semiconductor. The electrons (e^-) jump into the conduction band and leaves empty *holes* (h^+) in the valence band. Once formed, the charges in VB and CB migrate toward the surface of the catalyst where the electrons will reduce and the holes will oxidise water.^{13, 14, 16, 20}

There are few requirements a semiconductor has to fulfil to be considered a suitable catalyst for photocatalytic water splitting. As already mentioned, the minimum energy required to split water is 1.23 eV, therefore the band gap of the material has to have a value higher than 1.23 eV. Another important aspect is the position of the bands with respect to the redox potential of water. The reduction potential of H^+ to H_2 is 0 eV (vs. NHE at pH = 0) and the oxidation potential of H_2O to O_2 is 1.23 eV (vs. NHE at pH = 0).²¹ Therefore, to be able to oxidise water, the VB of the semiconductor will have to be more positive than the oxidation potential and the CB more negative than the reduction

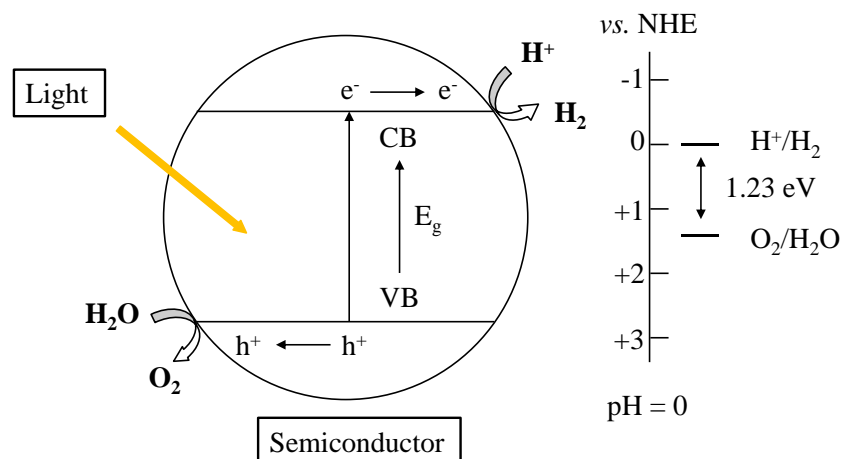


Figure 1.7 Photocatalytic water splitting. Schematic representation of the steps involved in photocatalytic water splitting. VB: valence band and CB: conduction band.

potential (Figure 1.7).^{13, 14, 16} However, the width of the band gap dictates the irradiation that can be employed for the process of water splitting. So far the majority of the catalysts developed are active under UV radiation.¹⁴ Since UV light represents only ca. 4 % of the solar spectrum and visible light ca. 46 %, ¹⁴ a semiconductor able to absorb visible light could increase the efficiency of the process. The wavelength limit between visible and ultraviolet light is 400 nm, which corresponds to an energy of 3.0 eV (Figure 1.6), therefore, the band gap of a visible-active catalyst for water splitting should be in the range: $1.23 \text{ eV} < E_g < 3.00 \text{ eV}$.¹⁴ Even if all the conditions are satisfied, *charge recombination* can prevent a catalyst to be active and efficient for water splitting. When the electrons and the holes migrate towards the surface they can recombine either in the bulk or at the surface of the catalyst (Figure 1.8).^{13, 14, 16} The presence of defects in the structure of the semiconductor can act as recombination centres.^{13, 16} This phenomenon decreases the number of charges available for the redox reactions, lowering the activity of the catalyst.¹³

In summary, the ideal characteristics of a suitable catalyst from a chemical and industrial point of view are:

- E_g wider than 1.23 eV;
- E_g narrower than 3.0 eV to guarantee maximum absorption of the solar irradiation;
- suitable band position to be able to produce H_2 and O_2 from water;
- ability, upon irradiation, to generate charges (e^- and h^+) and not dissipating the energy as heat;

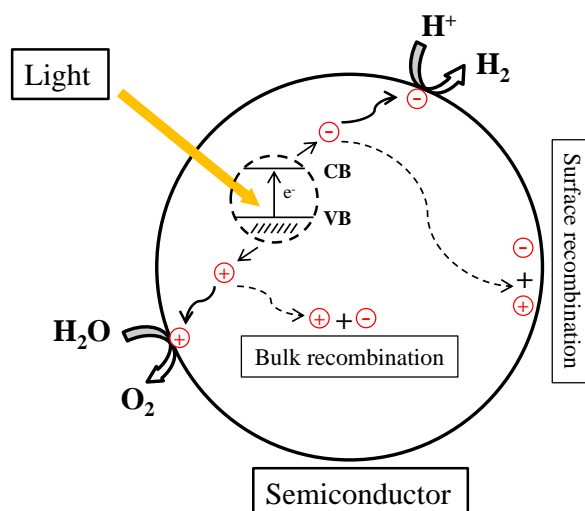


Figure 1.8 Charges recombination. Schematic representation of the recombination of holes and electrons during their migration towards the surface of the semiconductor.

- guarantee a long life and separation of charges (low frequency of recombination events);
- cheap, easy to produce and stable in testing conditions.

All these have to be taken into account when choosing a catalyst for photocatalytic water splitting and often a compromise has to be made.

1.3.2. Improving the activity of the catalyst

The activity of a catalyst can be improved by acting on the charge recombination events and/or the band gap of the material. Charge recombination can be reduced by adjusting the crystallinity and morphology of the semiconductor or with the loading of a co-catalyst.¹⁴ For the band gap (“band gap engineering”), however, a more drastic approach, doping, has to be employed. By doping the catalyst the aim is to increase the absorption in the visible range by narrowing the band gap. A detailed list of photocatalytic systems and their modification by loading of a co-catalyst and/or by doping was published by Chen *et al.* in 2010.¹⁴ Here only few examples are presented and later works are added.

Co-Catalyst loading

Often a co-catalyst is loaded on the surface of the semiconductor to act as an electrons trap and reduce the recombination events (Figure 1.9).^{14, 22} An additional role of the co-catalyst is to introduce reaction sites that may not be available on the native surface of the catalyst.¹⁶ The most employed co-catalyst is platinum and numerous examples are

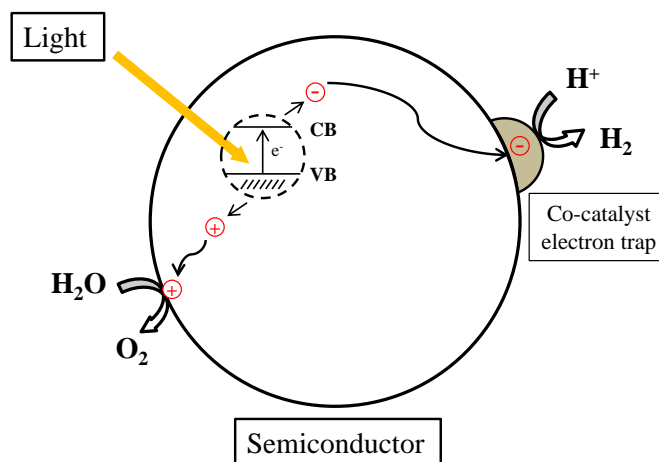


Figure 1.9 Role of a co-catalyst as an electron trap. Schematic representation of the role of the co-catalyst in reducing the charges recombination events.

reported in literature on its ability to enhance the photocatalytic performances of different catalysts.^{14, 23-28} One of the earlier examples of the effect of Pt was reported in 1978 by Kraeutler and Bard²⁹, when they photodeposited platinum on TiO₂ for the photodecomposition of organic acids to methane. Other metals/metals oxides, for example Ru³⁰, Ag³¹, Au³², NiO³³; showing the same effect of reducing charge recombination, have also been employed in the past years.^{14, 34}

To further improve the effect of a traditional transition metal co-catalyst, a co-loading approach can be applied to form independent particles, mixed oxides and core/shell structures.¹⁴ Different effects can be produced. In the first case, the separation of the charges is enhanced by forming sites for the electrons and for the holes with different co-catalysts.^{35, 36} An example of this is the co-loading of Pt and RuO₂ on TiO₂ where Pt acts as an electron trap and RuO₂ as the holes trap.^{35, 37} Mixed oxides of Rh and Cr on (Ga_{1-x}Zn_x)(Ni_{1-x}O_x) have been reported by Maeda *et al.*³⁸ The role of the mixture is that of improving the charge transfer from the catalyst to the co-catalyst.^{38, 39} They also reported the improved photocatalytic activity of the same catalyst when a core/shell structure of noble metal and Cr₂O₃ was employed. In this case the effect produced is the inhibition of the back reaction between H₂ and O₂ to form water.⁴⁰

Crystallinity and particle size

As already mentioned (Section 1.3.1) defects in the structure of a semiconductor can act as recombination centres, therefore a higher level of crystallinity can favour a higher photocatalytic activity.¹⁴ A typical example is the difference in activity between anatase

and rutile in the case of TiO_2 , where anatase has proven to be the most active among the two.¹⁴ This has been ascribed to its higher crystallinity and lack of defects.⁴¹

Particle size, similarly, has been found to have a great influence on the photocatalytic activity of catalysts.^{42, 43} It affects the number of recombination events in the particle. Lowering the size of the catalyst decreases the length of the pathway to the surface, reducing the probability of *bulk recombination*.⁴² On the other hand, however, a too small particle size increases the surface area, increasing the possibility of *surface recombination* events.⁴³ It is therefore important to find a balance for each catalyst.¹⁴

Doping or “band gap engineering”

In order to increase its activity, an oxide semiconductor can be doped with metal or non-metal ions.¹⁴ In both cases a change in the band structure is produced with the aim of increasing visible light absorption.¹⁴ However, the effect generated on the band structure is different. In the case of metal doping the band gap of the original catalyst is not narrowed but an impurity level is introduced either as a donor (VB) or acceptor (CB) level (Figure 1.10). One of the first examples of metal doping was reported in 1982 by Borgarello *et al.*⁴⁴ when they doped TiO_2 with Cr^{5+} ions. Subsequently, TiO_2 has been the most investigated photocatalyst and has been doped in many ways¹⁴ and still today a lot of research focuses of new TiO_2 doped materials with enhanced photocatalytic activity.⁴⁵ The second type of doping is carried out with non-metal ions like: N, B, S, C. In this case no impurity levels are formed but a shift of the valence band to more negative values is

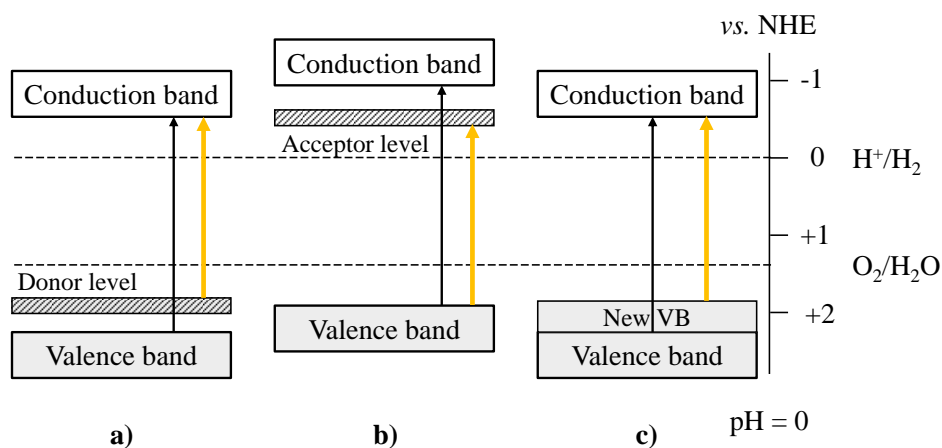


Figure 1.10 Doping options for band engineering. Schematic representation of different kinds of doping: a) metal-doping with formation of a donor level; b) metal-doping with formation of an acceptor level and c) non-metal doping with formation of a new valence band. Black arrows represent UV-promoted excitations and yellow arrows visible-promoted excitations.

achieved (Figure 1.10), narrowing the band gap of the catalyst and allowing visible light absorption.¹⁴ Again TiO₂ has attracted great attention.⁴⁶⁻⁴⁸

1.3.3. Overall water splitting

Overall water splitting can be achieved in two different ways: *via* single or two photons systems. The single photon system was illustrated in Section 1.3.1. In this system, only one catalyst is involved and upon absorption of one photon simultaneous production of H₂ and O₂ from water is achieved. The simultaneous production of H₂ and O₂ with only one catalyst is very challenging.^{20,49} This is because a catalyst would have to fulfil all the band gap requirements discussed above (Section 1.3.1). A more successful option is the two photons process, also referred to as Z-scheme.^{11, 13, 14, 20, 50} In this case two photocatalysts are involved to carry out the two reactions separately (Figure 1.11). Both catalysts absorb the light irradiation and their electrons are promoted to the conduction band. However, due to the unsuitable position of one of their band edges they can carry out only one of the reactions, either the reduction of water (H₂-evolving catalyst) or its oxidation (O₂-evolving catalyst).^{11, 13, 14, 20, 50} The excited electrons left in the O₂-evolving catalyst are then transferred to the second catalyst, to quench its holes, by mean of a redox couple with appropriate redox potential, the mediator (Fe³⁺/Fe²⁺, IO₃⁻/I⁻).^{14, 50} This allows the electron catalytic cycle to be completed.^{11, 13, 20, 50}

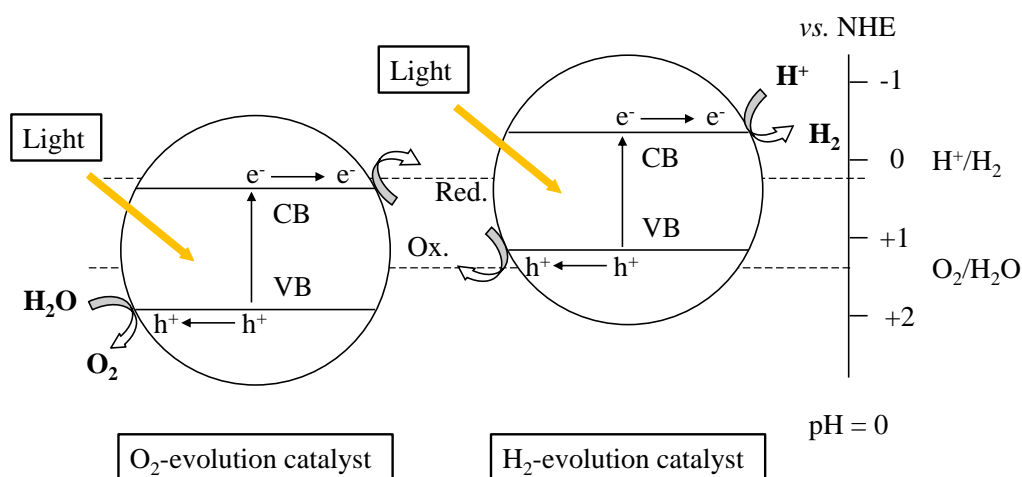


Figure 1.11 Z-scheme photocatalytic water splitting. Schematic representation of overall water splitting employing a two-photon configuration. Two catalyst are involved: O₂-evolution and H₂-evolution catalyst. The electron flow is ensured by employing an electron mediator (Redox couple).

Even though, the Z-scheme is more achievable than the one photon process, it still presents some challenges: finding two catalysts that can successfully carry out the two reactions and a redox couple that can be suitable for both catalysts.

1.3.4. Half reaction and sacrificial reagents

Due to the difficulties associated with the Z-scheme, usually only one of the two catalysts is employed and only the activity for H_2 or O_2 production is investigated. In this case only half of the water redox process is investigated, from here the definition of half reactions. To replace the missing reaction and guarantee an electron flow to and from the catalyst, a *sacrificial reagent* is employed. The chosen reagent sacrifices itself in the process instead of water.^{13, 14} The concept is very similar to that of mediator seen for the Z-scheme, but while the mediator is regenerated by the second catalyst, the sacrificial agent is consumed, posing a limit to the duration of the process. There are two different kinds of sacrificial reagents: electron acceptor (EA) and electron donor (ED) (Figure 1.9).¹³ The EA is employed when the CB of the catalyst is not in the right position to reduce water (it is more positive than H^+/H_2 reduction potential: 0 eV vs. NHE, pH = 0). Hence it is reduced by the photoexcited electrons allowing the formation of holes in the VB for the production of O_2 .¹³ The ED, on the other hand, is needed when the VB of the catalyst is not suitable for the oxidation of water (it is more negative than $\text{H}_2\text{O}/\text{O}_2$ oxidation potential: 1.23 eV vs. NHE, pH = 0). In this case it is oxidised and provides electrons to the catalyst. The electrons will be then photoexcited to produce hydrogen.¹³

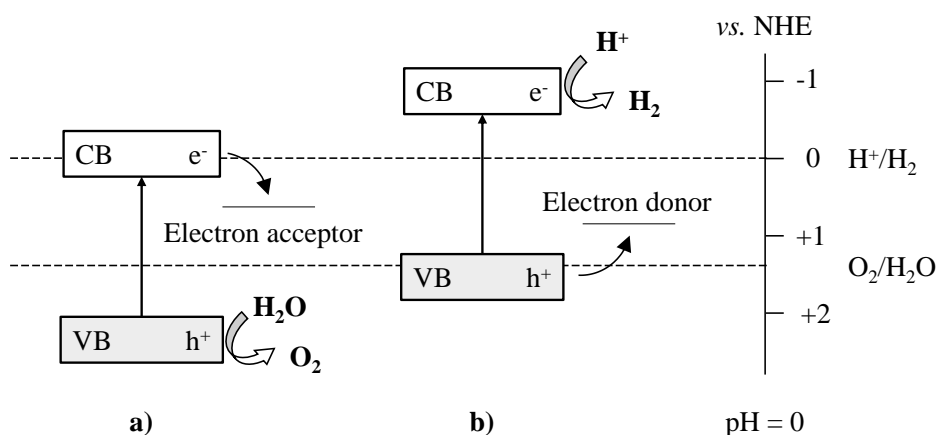


Figure 1.12 Sacrificial reagent systems. Representation of the role of the sacrificial agent in photocatalytic water splitting. Two possible configurations are illustrated: a) electron acceptor and b) electron donor system.

If organic compounds are employed as electron donors, the H₂-evolution half-reaction could be coupled with the decomposition of water pollutants. In this instance, the green fuel of the Hydrogen Economy (Section 1.2) can be produced with high efficiencies with simultaneous purification of water,^{14, 51} and many examples of these processes can be found in the literature.¹⁴ Some of the sacrificial agents employed are: methanol,⁵² oxalic acid,⁵³ triethanolamine,⁵⁴ formaldehyde,¹⁴ etc. Additionally, to integrate this process in the sustainable energy economy, photoreforming of biomasses such as algae, cellulose, insects, have also been investigated.¹⁴

1.4. Graphitic carbon nitride

1.4.1. General description

Most of the catalysts used today for photocatalytic water splitting or hydrogen evolution are metal oxides.^{13, 14, 20, 55, 56} But unfortunately they usually require laborious and expensive synthesis methods to prepare. Recently an organic polymeric material has attracted attention as suitable visible-active photocatalyst for hydrogen evolution from water: graphitic carbon nitride, g-C₃N₄.^{54, 56} A smaller polymeric form of g-C₃N₄ named “melon” was synthesised for the first time by Jöns Jakob Berzelius and reported in 1834 by Liebig before being investigated in more details by Franklin in 1922.⁵⁶⁻⁵⁸

Graphitic carbon nitride is considered to be the most thermodynamically stable among the allotropes of C₃N₄ (α -, β -, cubic- and pseudocubic-C₃N₄).^{54, 56, 57, 59} The name “graphitic” is due to the layered nature of the polymer reminiscent of that of graphite.⁵⁴

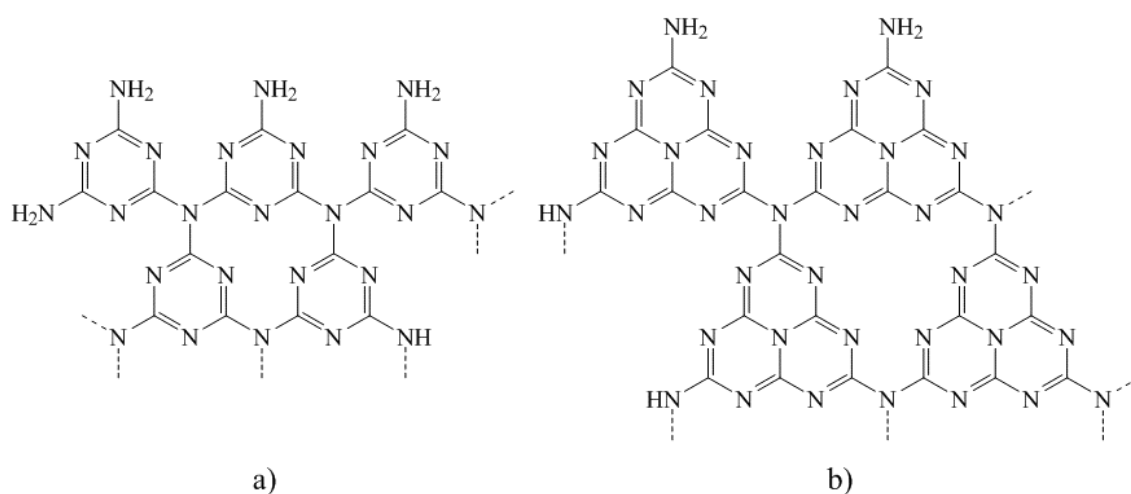


Figure 1.13 Possible g-C₃N₄ structures. Two possible structures of g-C₃N₄ based on a) triazine and b) tri-*s*-triazine repeating units.

Graphitic C_3N_4 (g- C_3N_4) is a conjugated polymer composed mainly of carbon and nitrogen atoms. Figure 1.13 shows two possible structures of g- C_3N_4 : triazine and tri-*s*-triazine (heptazine) based polymer.^{56, 57} The nature of the repeating unit in the polymer has received a lot of attention in the literature, and to date the heptazine based g- C_3N_4 is considered to be the most stable form.^{56, 57} The ideal g- C_3N_4 is an infinite polymeric sheet characterised by a C:N ratio of 0.75 and the absence of protons in the structure.^{57, 60} The real graphitic carbon nitride is instead a finite polymer which includes amino group terminations (-NH- and NH₂-). This lowers the ratio between carbon and nitrogen atoms to a value of ca. 0.60-0.70, and introduces 1-2 wt.% of hydrogen.^{57, 60} These values are highly variable according to the synthetic methods applied to obtain g- C_3N_4 .^{57, 58} In the Franklin study, he stated that it was not possible to obtain the same composition when synthesising the material; he also mentioned that the same issue was encountered by Liebig.⁵⁸

In both possible polymeric structures, the atoms are characterised by sp^2 hybridisation, giving aromatic character to the network and forming a π -cloud of electrons.⁵⁴ This, similarly to graphite, allows the formation of a stack of 2D layers through π - π interactions. This is reflected in an XRD pattern very similar to that of graphite with a main peak at 27.4°, corresponding to the inter-layer d-spacing.⁶¹ However, the presence of nitrogen atoms in the network gives g- C_3N_4 unique properties. Indeed, unlike graphite, graphitic C_3N_4 is a semiconductor, with a direct band gap of 2.7 eV. The direct band gap is due to the uniform distribution of the π -electrons over the network (Figure 1.14⁵⁴).^{54, 55, 59} The

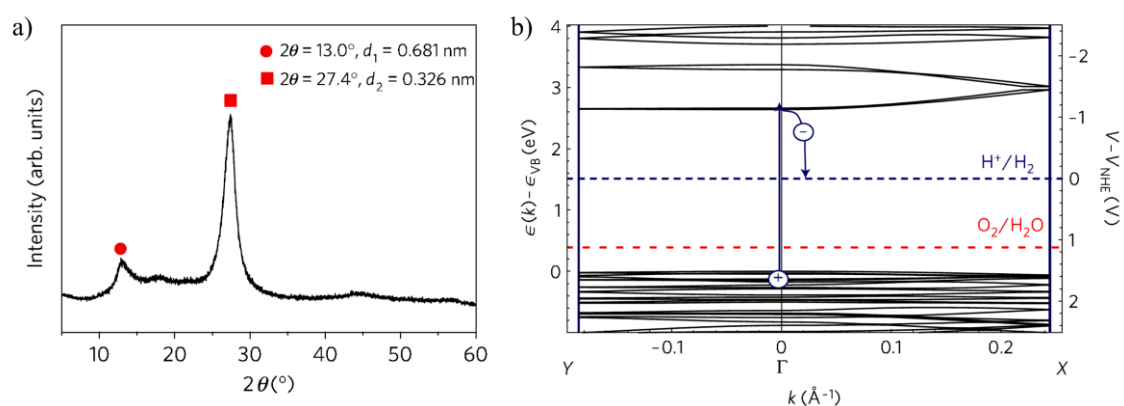


Figure 1.14 g- C_3N_4 XRD pattern and DFT calculations of band structure.⁵⁴ Graphitic carbon nitride XRD pattern (a) shows the characteristic graphitic structure. DFT calculations of its band structure (b) show a direct band gap fulfilling the requirements of a suitable photocatalyst for water splitting. Both pictures are reproduced with permission from ref.54.

HOMO (Highest Occupied Molecular Orbital) is composed of the p_z orbitals of the nitrogen atoms, whereas the LUMO (Lowest Unoccupied Molecular Orbital) is composed of the p_z orbitals of carbon atoms.⁵⁴ The band edges of graphitic carbon nitride (Figure 1.14) and its relatively narrow band gap which allows it to absorb visible light, make g-C₃N₄ a suitable candidate for photocatalytic hydrogen evolution.^{54, 56}

In addition to the interesting electronic structure of this yellow semiconductor, a characteristic that attracts attention is the chemical stability of this material. Graphitic carbon nitride is insoluble in most of the conventional solvents and stable in the whole pH range, from very acidic (pH = 0) to very basic solutions (pH = 14).⁵⁴ It is also characterised by a high thermal stability. Depending on the preparation method it is stable up to 600 °C.⁵⁶ These characteristics make g-C₃N₄ an interesting catalyst able to withstand drastic operating conditions.

1.4.2. State of the art: synthesis

As previously mentioned, the real graphitic carbon nitride is a finite polymer with amino terminations, a variable C:N ratio and hydrogen content. The synthetic procedure has a great effect on these values as shown in the review by Thomas *et al.*⁵⁷ Their work collects some examples of the different synthetic methods reported in the literature over the last twenty years.⁵⁷ A comparison of the C:N ratios obtained with each method is also provided.

The main synthetic methods listed are hydrothermal and solid state reactions.⁵⁷ Only few of the examples provided show a C:N ratio close to the ideal value (0.75).^{62, 63} Gu *et al.* applied a solid state synthesis between calcium cyanamide and cyanuric chloride and achieve a C:N ratio (0.75). However, it is important to point out that this procedure also leads to a high amount of graphite as a by-product.⁶² Guo *et al.*, on the other hand, used a solvothermal method using 1,3,5-trichlorotriazine and sodium amide in benzene.⁶³ The C:N ratio obtained is 0.72 and the sample presents good crystallinity and a graphitic-like structure (XRD pattern).⁶³ All of these procedures as well as others do achieve excellent results but unfortunately involve toxic precursors which combined with high pressure conditions give rise to a number of safety concerns.

A better alternative that is now often used to synthesised g-C₃N₄ is the thermal polycondensation of small organic precursors.⁵⁷ This method is still a solid state synthesis but the precursors used are less toxic than those mentioned earlier. The small organic molecules that can be employed for the synthesis are: urea,⁶⁴⁻⁶⁷ cyanamide,^{68, 69}

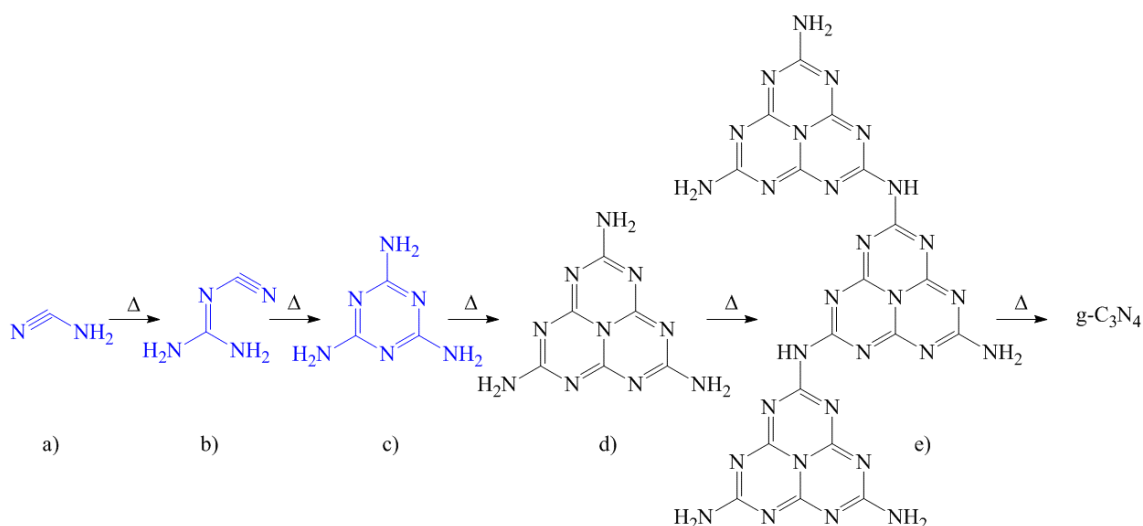


Figure 1.15 Reaction pathway to g-C₃N₄. Reaction steps of the thermal polycondensation of small organic monomer to graphitic carbon nitride. In blue are the molecules that are often used as starting materials. a) Cyanamide, b) dicyandiamide, c) melamine, d) tri-*s*-triazine or melem, e) results of partial polymerisation of melem.

dicyandiamide⁶⁹⁻⁷¹ and melamine^{54, 60, 69, 72, 73}. The C:N ratio obtained from these procedures is lower than the ideal one, with a value of ca. 0.65-0.70. Although less efficient as a chemical reaction, this type of synthesis is preferred for the preparation of g-C₃N₄ to be used in photocatalytic applications^{54, 72} since it has been found out that a catalyst with defects is more active.⁵⁶ The suggested mechanism for the thermal polycondensation is illustrated in Figure 1.15. The reaction proceeds through subsequent polymerisation and condensation reactions of smaller organic precursors.⁵⁷ If the starting materials are cyanamide and dicyandiamide, upon heating, they polymerise to form melamine which then condenses with other melamine molecules or with remaining cyanamide derivatives to form melem. Further heating allows polycondensation of melem into bigger polymeric fragments until formation of graphitic carbon nitride.^{54, 57} It is, therefore, possible to use any of the small organic precursors to synthesise g-C₃N₄ to achieve formation of highly polymerised networks (polymeric melem and g-C₃N₄).

1.4.3. State of the art: photocatalytic applications

In 2009 graphitic carbon nitride was reported for the first time to be a viable visible-active photocatalyst for hydrogen evolution from water.^{54, 68} From the DFT calculations of the HOMO-LUMO position (Figure 1.14),⁵⁴ g-C₃N₄ should be able to produce both H₂ and O₂. However, an electron donor is still needed. According to Wang *et al.*, the reason for

this is ascribed to the fact that the VB is very close to the oxidation potential which implies a small driving force, preventing graphitic carbon nitride from oxidising water.⁵⁴ In their paper they demonstrate that g-C₃N₄ in the presence of a sacrificial agent (triethanolamine, TEOA) can produce hydrogen without the aid of a co-catalyst.⁵⁴ The effect of the co-catalyst was also investigated with platinum loaded on the surface of g-C₃N₄ as a H₂-evolution co-catalyst. They observed that the loading of the metal not only increases the performances but also helps in decreasing N₂ evolution (from the catalyst itself) and in stabilising the activity for hydrogen production.⁵⁴ By loading an O₂-evolution catalyst (RuO₂) they demonstrated that, even if with low activity, oxygen production is indeed achievable with g-C₃N₄ under visible light.

Following this initial work by Wang *et al.*,⁵⁴ g-C₃N₄ has received a significant amount of attention to further improve its activity for hydrogen evolution under visible light. To reach this goal approaches similar to the one previously introduced in Section 1.3.2 have been adopted: the influence of co-catalyst loading, doping and morphology modification). Here is an overview of the main achievements.

Co-catalyst loading

Just after the initial study by Wang *et al.*⁵⁴ Maeda *et al.* published an investigation on graphitic carbon nitride and different co-catalysts.⁶⁸ A screening of a few transition metals was carried out and the study shows that the best co-catalyst is indeed platinum followed by palladium.⁶⁸ After selecting platinum as the optimum co-catalyst they investigated the influence of loading amount and they reported that a 1 wt.% loading *via* an impregnation method gave the best performance.⁶⁸ Other metals have since then been tried as co-catalysts in order to improve the performance of the g-C₃N₄ for hydrogen or oxygen evolution, as well as for the degradation of organic compounds.⁷⁴ Another approach has been the use of noble metals such as Au⁷⁵ and Ag⁷⁶⁻⁷⁸, but none of them showed a catalytic activity higher than platinum on g-C₃N₄. The attention has very recently been directed towards bimetallic alloys,^{78, 79} but significant work is still needed in this area.

Doping and composites

Another approach to improve the activity of g-C₃N₄ is doping with other elements.^{56, 80} Since graphitic carbon nitride is an organic polymer, the concept of doping is slightly different from the traditional concept for inorganic materials. In this case one of the atoms in the network will have to be replaced, and the new atom will have to be able to form

covalent bonds if the structure is to be retained. For this reason non-metallic elements, like boron and sulphur, are employed for doping g-C₃N₄.

Graphitic carbon nitride so far has been doped with boron, sulphur, phosphorus and fluorine.⁸⁰ The aim has been to produce changes in the band structure in order to improve its performance. There are only few examples reported in literature (summarised by Zheng *et al.*),⁸⁰ but unfortunately not all of them were investigated for hydrogen evolution. In 2010 Wang *et al.* reported that the introduction of fluorine atoms on the network brings a change in the hybridisation of the carbon atoms (sp^2 to sp^3), and therefore a change in the HOMO-LUMO structure, which resulted in a small decrease of the band gap (absorption shifted towards longer wavelengths) and an increase in hydrogen evolution compared to un-doped g-C₃N₄.⁸¹ In the same year Liu *et al.* doped g-C₃N₄ with sulphur by a post-synthesis treatment in H₂S.⁸² Again, the sulphur doped g-C₃N₄ showed a significantly higher hydrogen evolution than the one of pristine g-C₃N₄. The substitution of nitrogen atoms in the network with sulphur brings in this case to a negative shift of the VB and CB; with the greatest shift for the CB, and therefore an enlargement of the band gap.⁸² Alternatively, in 2011 Zhang *et al.* introduced S in the graphitic network using an *in-situ* method, with trithiocyanuric acid as organic monomer.⁸³ Contrary to the work by Liu *et al.*⁸², Zhang *et al.* reported a narrowing of the band gap and a shift to more positive value of VB.⁸³ Nonetheless this material did show a higher hydrogen evolution than graphitic carbon nitride.⁸³ A slightly different doping approach was also reported by Zhang *et al.*⁸⁴ in 2010. In this case a co-polymerisation method was adopted in order to increase the content of carbon atoms in the graphitic network. Dycinamide together with barbituric acid was employed to synthesise a carbon rich version of g-C₃N₄.⁸⁴ A decrease in the band gap by an up-shift of the VB was successfully achieved. As a consequence an increased H₂ evolution activity was produced.⁸⁴

The formation of composites between g-C₃N₄ and other photocatalysts has also been investigated. The aim of the combination of graphitic carbon nitride with other materials is that of improving the charge separation, similarly to the loading of a co-catalyst. The difference, however, is in the amount employed. An example of this was reported by Xu *et al.* who prepared a composite between g-C₃N₄ and SrTiO₃.²⁵ The authors suggested that some of the photoexcited electrons are transferred from the graphitic carbon nitride to the strontium titanate.²⁵ A similar behaviour can also be found between the organic polymer and TaON.⁸⁵ In this case the electrons flow from g-C₃N₄ to the TaON which carries out the reduction reaction.⁸⁵ In 2011 Xiang *et al.* showed that by coupling g-C₃N₄

with graphene a substantial increase in hydrogen evolution can be achieved. Graphene did not cause modifications in the network of g-C₃N₄ but helps to reduce charge recombination.⁸⁶

Different strategies can be adopted in order to increase the photocatalytic activity of graphitic carbon nitride, either by changing the band gap or seeking the assistance of other materials to reduce the charge recombination events.

Morphology modification

As previously mentioned (Section 1.4.1), the modification of the morphology of a catalyst can have a positive effect on its photocatalytic performance. Applied to g-C₃N₄ a change of morphology is mainly carried out by increasing the porosity of the material through the use of templates or by exfoliation of its graphitic layers. Wang *et al.* in 2009 reported the enhancement of the performances of mesoporous g-C₃N₄ (mpg-C₃N₄) as a consequence of the significant increase of the surface area after synthesis in the presence of silica templates. However, they observed that an excessive increase of surface area can lead to the introduction of defects in the material and a decrease in performance.⁸⁷

A second strategy to modify g-C₃N₄ morphology is its exfoliation. An example of this method was reported in 2013 by Xu *et al.*⁸⁸ Graphitic carbon nitride monolayers were formed by sonication of the bulk catalyst in an acidic solution. The authors observed an increase in the band gap accompanied by an increase in performance, a discrepancy that was explained by the lower frequency of recombination events.⁸⁸

1.5. Aim of the work

The use of graphitic carbon nitride as a new photocatalyst is only recent, reported for the first time in late 2008 by Antonietti and co-workers.^{54, 89} Despite a growing interest since then, several questions remain unanswered.

The motivation of this work is to increase the understanding of g-C₃N₄; first from a structural perspective, and second, from its activity for hydrogen evolution under visible light and its interaction with the co-catalyst. Hence in the following chapters attention will focus on different aspect of this photocatalytic system.

In the literature the structure of graphitic carbon nitride has been investigated with different techniques, such as solid state nuclear magnetic resonance (SSNMR), electron diffraction, x-ray diffraction (XRD) and, as already mentioned, a tri-*s*-triazine repeating unit is considered to be the most stable.⁵⁷ This is for the intra-layer structure of the

polymer. However, its packing in layers has only be addressed with electron diffraction models.⁹⁰ Chapter 3 addresses the structure of graphitic carbon nitride. The effect of the synthesis conditions on the structure and electronic properties of the material is investigated with a variety of techniques, but mainly with x-ray diffraction. Additionally, neutron diffraction, together with XRD is employed with the intent of confirming the tri-*s*-triazine main unit and some of the proposed models of its 3D structure.

Chapter 4 focuses on the g-C₃N₄ and platinum as co-catalyst. The system is investigated from the loading procedure of platinum to its influence on the photocatalytic process itself. Pt-g-C₃N₄ is prepared and exposed to different treatments in order to achieve a better understanding of the whole process and to improve the photocatalytic performance.

Chapter 5 looks at the proposition of using bimetallic alloys as co-catalysts. The aim is to reduce the platinum content by introducing a cheaper metal and at the same time increase the performance for photocatalytic hydrogen evolution. Different PtMe-g-C₃N₄ are synthesised and tested for their photocatalytic activity. The benefits and limitations of this approach are presented.

Chapter 2

Experimental

2.1. Synthesis

2.1.1. Graphitic Carbon Nitride synthesis

Graphitic carbon nitride ($g\text{-C}_3\text{N}_4$) is synthesised *via* solid state synthesis through thermal polycondensation of melamine (Sigma-Aldrich, 99 %). The white precursor is weighed in a crucible and covered with aluminium foil (Figure 2.1a) to restrict the loss of the gases evolved during the reaction within the vessel. Melamine is then heated in a muffle furnace at temperature ranging from 450 °C to 650 °C for different lengths of time (2.5 h to 15 h). Ramping and cooling rate is set at 5 °C/min for each experiment. At the end of the reaction (Figure 1b-c) the sample appears as a porous mass. The yellow $g\text{-C}_3\text{N}_4$ is then ground in an agate mortar until a fine powder is obtained.

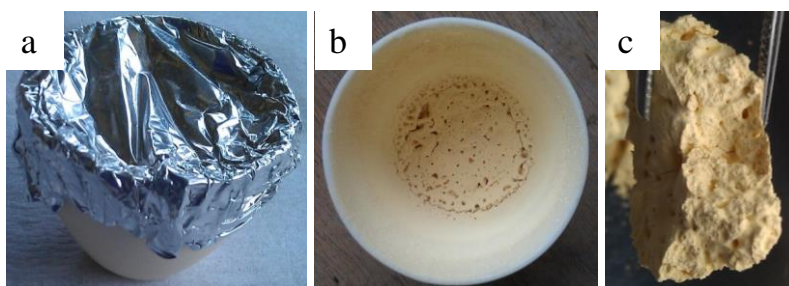


Figure 2.1 Images of $g\text{-C}_3\text{N}_4$ preparation. Images representing different stages of the synthesis of $g\text{-C}_3\text{N}_4$: a) crucible closed with an aluminium foil before synthesis in the furnace, b-c) $g\text{-C}_3\text{N}_4$ after reaction in the muffle furnace.

2.1.2. Platinum loading and reduction

Platinum is loaded on the catalyst by following different procedures. Chloroplatinic acid is used as precursor.

Impregnation: graphitic carbon nitride is suspended in an aqueous solution ($1 \text{ g}\cdot\text{L}^{-1}$) of $\text{H}_2\text{PtCl}_6\cdot 6\text{H}_2\text{O}$ and is left stirring overnight. After evaporation of the water, the loaded catalyst is left drying overnight in an oven at $80 \text{ }^\circ\text{C}$.

Impregnation followed by calcination: after impregnation of the chloroplatinic acid the sample is exposed to thermal treatment at $180 \text{ }^\circ\text{C}$ for 2 hours.²⁵

Photodeposition: no pre-treatment of the catalyst is carried out and the deposition is performed *in-situ*. The chloroplatinic acid solution ($1 \text{ g}\cdot\text{L}^{-1}$) is added directly, with g- C_3N_4 , into the reaction chamber used for the photocatalytic performance evaluation and visible light irradiation is started.

Reduction under H_2 flow: after impregnation of the platinum precursor, Pt-g- C_3N_4 is placed into a tube furnace and reduced at $300 \text{ }^\circ\text{C}$ under flowing 5 % H_2/Ar gas for different lengths of time.⁹¹

Chemical reduction by sodium borohydride (NaBH_4): g- C_3N_4 is suspended in a solution of $\text{H}_2\text{PtCl}_6\cdot 6\text{H}_2\text{O}$ and an aqueous solution of NaBH_4 (in excess of 10 times) is added slowly.⁹² After 2 h the stirring is stopped and the catalyst is left depositing at the bottom of the flask. Once the powder is fully deposited, the solution is removed and fresh, degassed water is added in order to wash the sample (filtration was avoided in order to maintain all the platinum on the catalyst). The depositing procedure is then repeated and after removal of the washing water the sample is dried at room temperature under flowing argon. During the whole procedure an argon flow is maintained in order to guarantee an inert atmosphere.

2.1.3. Synthesis of supported bimetallic alloys

The metal precursors employed in the preparation of bimetallic alloys of composition $\text{Pt}_{0.5}\text{Me}_{0.5}$ (Me = Cu, Ag, Ni, Co) are: H_2PtCl_6 , $\text{Cu}(\text{NO}_3)_2$, AgNO_3 , $\text{Ni}(\text{NO}_3)_2$ and $\text{Co}(\text{NO}_3)_2$.

The alloys are synthesised following the procedures used for platinum. In the specific: co-impregnation of the metal precursors, reduction under H_2 and chemical reduction with NaBH_4 . In all cases the atomic ratio is kept 1:1 and the total amount of metal atoms is equivalent to that of 1 wt.% Pt loaded g- C_3N_4 .

Impregnation: graphitic carbon nitride is suspended in a mixture of aqueous solutions of $\text{H}_2\text{PtCl}_6 \cdot 6\text{H}_2\text{O}$ and $\text{Me}(\text{NO}_3)_x$ ($1 \text{ g} \cdot \text{L}^{-1}$). After overnight stirring the water is evaporated at $90 \text{ }^\circ\text{C}$ and the powder is left drying into an oven at $80 \text{ }^\circ\text{C}$.

Reduction under H_2 flow: after impregnation of the metal precursors, $\text{PtMe-g-C}_3\text{N}_4$ is reduced at $300 \text{ }^\circ\text{C}$ for 24 h under flowing 5 % H_2/Ar gas in a tube furnace.

Reduction by sodium borohydride (NaBH_4): after suspending $\text{g-C}_3\text{N}_4$ into a mixture of solutions of $\text{Me}(\text{NO}_3)_x$ ($1 \text{ g} \cdot \text{L}^{-1}$) and $\text{H}_2\text{PtCl}_6 \cdot 6\text{H}_2\text{O}$ ($1 \text{ g} \cdot \text{L}^{-1}$), fresh NaBH_4 aq. (10 fold molar excess) is slowly added. The same procedure as for the platinum is followed (Section 2.1.2).

2.2. Characterisation methods

2.2.1. Powder x-ray diffraction

X-ray diffraction (XRD) employs electromagnetic radiation (monochromatic X-rays) to characterise the structure of crystalline solids (powders or crystals) by exploiting the scattering power of matter.¹⁷

The monochromatic X-rays are produced by accelerating a beam of electrons which will then collide with a metal target, usually copper. When an accelerated electron hits the metal it can ionise one electron from the $1s$ orbital of a Cu atom. In order to fill the electron vacancy a second electron from the $2p$ orbital will take its place moving to the lower energy level. By doing so it will release the excess of energy in the form of X-ray.¹⁷ Depending on the metal and which electron will fill the gap, the X-ray will have different wavelengths. The most frequent transition, and the one of interest, for copper is the $2p$ to $1s$, the K_α radiation, characterised by a wavelength λ of 1.5405 \AA . A less frequent and therefore less intense is the $3p$ to $1s$ transition, K_β with $\lambda = 1.3922 \text{ \AA}$. They are simultaneously produced in the process and the K_β removed with a filter (usually a nickel foil) to obtain a monochromatic radiation.¹⁷

Once the monochromatic X-ray is obtained it strikes the sample and it is scattered by the electrons of the atoms. This can happen if the wavelength of the radiation is close in value to the interatomic distances of the material, usually few \AA .¹⁷

Bragg's law is used to explain the relation between the wavelength, λ , of the incident beam, the scattered angle, θ , and the interatomic distance, d (Figure 2.2).

If a crystal is considered as made of layers (planes), when the x-ray reaches its surface it will be reflected with an angle θ . In some cases the angle of the reflected beam will be the same as that of the incident beam. Some others will be transmitted by the first layer to be reflected by the second layer and so forth. In order to have constructive interferences between the two reflected beams they have to be in phase, therefore the additional distance ($\overline{AB} + \overline{BC}$) that the second beam will have to travel has to be equal to $n\lambda$. From this condition and applying trigonometry to Figure 2.2 the Bragg's law can be derived (Eq. 2.3).¹⁷

$$\overline{AB} = \overline{BC} = d \sin \theta \quad \text{Eq. 2.1}$$

$$\overline{AB} + \overline{BC} = 2d \sin \theta \quad \text{Eq. 2.2}$$

$$n\lambda = 2d \sin \theta \quad \text{Eq. 2.3}$$

where n is a whole number (1, 2, 3...) and d is the distance between adjacent planes and it is called the d -spacing.¹⁷ When this condition is verified the reflected X-rays are in phase, in all the other cases they are out of phase and destructive interferences occur bringing to cancellation of the radiation.¹⁷

In a powder diffraction experiment the crystals in the sample are distributed randomly in order to assume different orientations so that some of the planes will be able to satisfy Bragg's law.¹⁷ These will diffract the beam with an angle θ and will be detected and counted by a detector. The output is an XRD pattern which is characteristic and unique for the material. Figure 2.3 illustrate as example the XRD pattern for a silicon standard

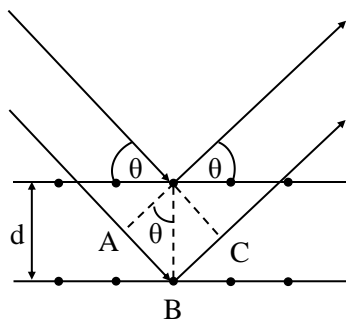


Figure 2.2 Bragg's law. Schematic representation of the interaction between a x-ray and the plane of a crystal. θ : Angle of the incident x-ray.

used to calibrate the diffractometer. Each peak correspond to a Bragg's reflection of the beam and their position represents the angle of the reflected beam.¹⁷

In an XRD pattern the peak position depends on the size and shape of the unit cell of a material, the d -spacing are related to the scattered angle by the Bragg's law (Eq. 2.3). Unit cells with the same shape but different size will generate two similar patterns with a shift in the peak positions. The intensities of the peaks are dictated by the type of atoms in the unit cell. This is because the scattering power of an atom is proportional to the atomic number (Z).¹⁷ Therefore heavier atoms like Pt, will scatter more than lighter atoms like C, N or H. Furthermore, light atoms give origin to inelastic scattering, *i.e.* the X-rays lose or gain energy after being scattered and they are not in phase anymore. This may result in destructive interferences and a background signal in the XRD pattern.¹⁷

For a highly crystalline material the peaks in the pattern are very sharp (Figure 2.3), however in some cases these can be broader. Reasons for this can be found in the crystallite size and/or level of disorder in the material.

In the first case, the X-ray beams will be diffracted with the angles that satisfy the Bragg's law but also with angles that will put the beams out of phase. In this case there will be destructive interferences.⁹³ The extreme case is when $n = 1/2$ and the beams cancel out completely. However if $n < 1/2$, for example $n = 1/4$, the sum will not be zero, but just a

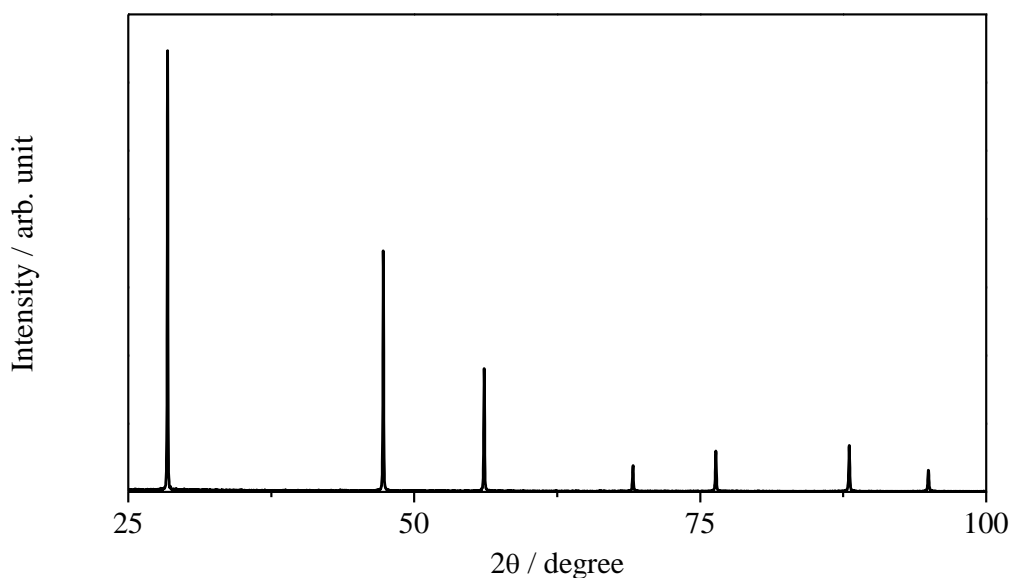


Figure 2.3 XRD pattern of a silicon standard. XRD pattern of the silicon standard used to calibrate the diffractometer. The peaks position is characteristic of the material and it is used to verify the calibration of the instrument by comparing the acquired spectra with the PDF card # 27-1402.

reduced amplitude beam, which will still be recorded at a slightly different angle.⁹³ If more planes are considered and each beam is out of phase of a quarter, the first and the third beam will cancel out. If n is even smaller it will take more planes before a completely destructive interference occurs. In a big crystal the total cancellation of the out of phase beams has more probability to happen than in a small crystal where the number of planes will be lower.⁹³ Therefore in the latter case beams with reduced amplitude and slightly different angles will be detected and will produce a broadening of the peak in the XRD pattern. The equation that expresses the relation between the width of the peak and the size of the crystallite is the Scherrer formula (Eq. 2.4):⁹³⁻⁹⁵

$$D = \frac{k\lambda}{\beta \cos \theta} \quad \text{Eq. 2.4}$$

Where D is the crystallite size (Å), λ is the wavelength of the X-ray (Å), k is the Scherrer constant associated to the shape of the crystallite (usually for unknown shape, $k = 0.9$), β is the FWHM (full width at half maximum) of the peak after subtracting the instrumental line broadening (rad) and θ is the scattered angle (rad).

The second reason for the broadening of a peak is the presence of crystallites with slightly different d -spacing and therefore slightly different θ . This is called strain, a deformation of the crystallites as a consequence of a stress. If the change is the same for all the crystallites (uniform strain) a shift of the peak (or peaks, depending which planes are effected by the deformation) is produced. If the change is different, then a similar effect to that of particle size is produced and many peaks of lower intensity will be generated around the main one resulting in a broadening.⁹³

Both, particle size and strain can have the same effect on the peaks. The Scherrer equation only accounts for size. A Williamson-Hall plot however can separate the two factors. This is particularly useful in the case of nanoparticles where the effect of the smaller size can mask the effect of the strain. The equation to be used in this case is:^{96, 97}

$$\beta \cos \theta = 4\varepsilon \sin \theta + \frac{k\lambda}{D} \quad \text{Eq. 2.5}$$

where all the variables are the same as defined above, with the addition of ε which is the strain due to the imperfections in the crystals. This equation is an example of $y = ax + c$

function, therefore, by plotting $\beta\cos\theta$ vs. $4\sin\theta$ for the peaks in the pattern, the particle size will be given by the intercept with the y axis and the stain by the slope of the line.

The X-ray diffractometer employed for this work is an Empyrean PANalytical series 2 diffractometer with a Cu K α radiation source ($\lambda = 1.5406 \text{ \AA}$). The patterns were analysed with the PANalytical software DataViewer. XRD patterns in the present document are shown as square root of normalised intensities. Theoretical patterns were generated with Fullprof suite and Highscore Plus was employed for indexing of the pattern.

2.2.2. Neutron scattering

Neutron scattering is a complementary technique to x-ray diffraction. In addition to the diffraction spectra it provides information about the diffuse components which makes it a suitable technique for the investigation of the structure of disordered, amorphous and liquid materials.⁹⁸ The basic working principle of neutron scattering is very similar to that of X-ray diffraction and the Bragg's law (Eq 2.3) can still be applied. A beam is sent to the sample and after it has been scattered of an angle 2θ it is detected (Figure 2.4). The difference between the two techniques is the source of radiation employed. In a neutron experiment, as the term says, neutrons are used in place of x-ray.

The advantage of using neutrons is that they are more penetrating, allowing for sample containers or special experimental set-ups, and are scattered by the nuclei rather than the electrons of the atoms.¹⁷ This remove the dependence from the atomic number typical of X-ray sources.¹⁷ Additionally, it is possible to distinguish between neighbouring atoms on the periodic table and isotopes, making neutron diffraction a more sensitive technique.

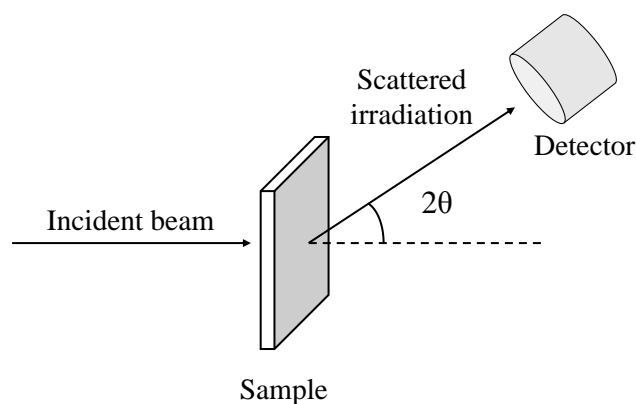


Figure 2.4 Schematic of a Neutron diffractometer. Basic schematic representation of a neutron diffractometer. Image modified from ref. 99.

Two ways are in use to produce neutron beams: nuclear reactor and pulsed sources.^{17, 99} In the first case the neutrons are produced by nuclear fission, where a nuclei is split in two and releases at least two highly energetic neutrons which will be passed through a moderator (usually water) to slow them down. The second option is the spallation source, where the neutrons are produced by an accelerated beam of protons colliding with a heavy metal nucleus. This can be uranium, tantalum or tungsten.⁹⁹ The generated neutrons are passed through a moderator and then concentrated by reflecting them into the target by means of a beryllium reflector. The advantages of this second source is that it is safer and it can be pulsed. This allows to have the neutrons leaving the source all at the same time. Therefore, by measuring the time required to reach the detector (time of flight, TOF) it is possible to calculate the energy and the wavelength, λ of the neutrons. As a consequence, a pulsed spallation source does not require the use of a monochromator.

The two types of neutron source differ in terms of measured variables in the experiment. In the case of a nuclear reactor the wavelength is constant and the angle is varied, in the same way as an x-ray diffraction experiment. In the case of a spallation source the angle is fixed and the wavelength is the variable.^{17, 99} This is determined by measuring the TOF ($1/v$, $\mu\text{s}\cdot\text{m}^{-1}$) of the neutron and applying the de Broglie equation (Eq. 2.6):^{17, 99}

$$\lambda = \frac{h}{mv} \quad \text{Eq. 2.6}$$

where h is the Planck constant (6.626×10^{-34} J·s), m the mass of the neutron (1.675×10^{-27} kg) and v is its speed.

In a typical neutron diffraction output the data are expressed in Q and not 2θ as in an x-ray diffraction experiment. Q represents the magnitude of the momentum transfer vector of

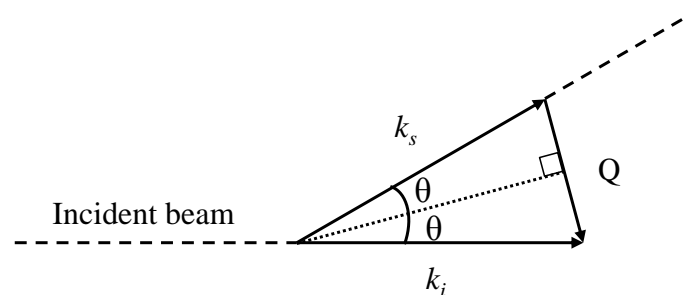


Figure 2.5 Physical meaning of Q . Representation of Q as a momentum transfer vector, the difference between the wave vector of the incident beam, k_i , and the wave vector of the scattered beam, k_s .

the neutron after it has been scattered by the sample. More simply, it represents the difference between the wave vectors of the beam before and after the collision (Figure 2.5). With trigonometric equations and given the wave vector as $k = 2\pi/\lambda$, its magnitude is given by:¹⁰⁰

$$Q = \frac{4\pi}{\lambda} \sin \theta \quad \text{Eq. 2.7}$$

where λ is the wavelength of the incident beam and θ the scattering angle.

The measured values of Q are then used to calculate the total structure factor, $F(Q)$, which mathematically is defined as in Eq. 2.8 which can be seen as a weighted sum of partial structure factors, $S_{\alpha\beta}(Q)$.¹⁰¹

$$F(Q) = \sum_{\alpha \leq \beta} (2 - \delta_{\alpha\beta}) c_{\alpha} c_{\beta} b_{\alpha} b_{\beta} [S_{\alpha\beta}(Q) - 1] \quad \text{Eq. 2.8}$$

This equation shows that the structure factor of a material depends on the concentration of the different atoms and their neutron scattering lengths, expressed as c_{α} , c_{β} , and b_{α} , b_{β} respectively. To avoid counting the same kind of interaction twice the Kronecker function, $\delta_{\alpha\beta}$, is employed.¹⁰¹

The application of a Fourier transform on the total structure factors, yields the total radial distribution function, $g(r)$.^{99, 101} This is a measure of the number of atoms that are at a distance r from an atom of reference.⁹⁹ This can be more usefully converted into a differential pair correlation function, $D(r)$, where the correlation happening at longer distances, r , are weighted by their length scale (Eq. 2.9), graphically enhancing them without decreasing the correlations happening at shorter distances.

$$D(r) = 4\pi r^2 [g(r) - 1] \quad \text{Eq. 2.9}$$

An example of outputs of $g(r)$ and $D(r)$ for melamine are illustrated in Figure 2.6. The intensities are plotted against the atomic distances, r (Å). The effect of weighting the $g(r)$ by the length at which the interaction occurs, is evident and results in an increased intensity for the peaks at higher r . This does not compromise the features at lower distances. This is very useful to obtain information for interatomic distances which are longer than simple bond lengths.

There are however some difficulties in a neutron scattering measurement. Light atoms, especially hydrogen where the nucleus is close in size to the neutron, can cause gain or loss in the energy of the incident beam ($k_i \neq k_s$). This is the inelastic scattering as opposed

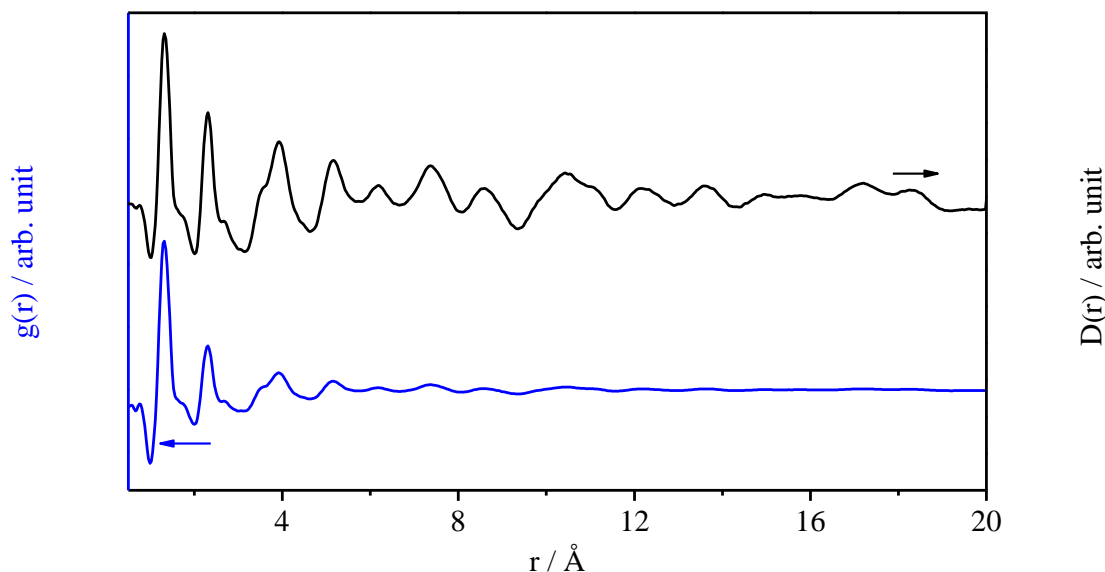


Figure 2.6 Examples of $g(r)$ and $D(r)$ for melamine. Comparison between the total radial distribution function, $g(r)$ (blue) and the differential pair correlation function, $D(r)$, (black).

to the elastic scattering described in Figure 2.5 where $k_i = k_s$.⁹⁹ The measured data will have to be corrected for the incoherent scattering by using complex equations.^{99, 102} This process is more accurate for heavy atoms, therefore, in the case of hydrogen or deuterium the correction will introduce some uncertainty in the $g(r)$ and consequently the $D(r)$.^{99, 102} The diffractometer used for the current investigation is the Near and InterMediate Range Order Diffractometer (NIMROD) at the ISIS facility of the Rutherford Appleton Laboratory.¹⁰¹ It is specifically designed to study amorphous materials and its length scale goes from below 1 Å to above 300 Å with a resolution of ~ 0.1 Å.¹⁰¹ It is specifically designed to minimise inelastic scattering, therefore it is particularly suitable for organic materials containing light elements (H, C, N).¹⁰¹

For a powder neutron scattering experiment few extra measurements other than the sample have to be taken. These are: the empty instrument as a background, the empty sample container and vanadium. The latter is used to calibrate the instrument and has to be scanned in the same beam conditions of the sample, therefore its neutron scattering data will be acquired each time. Vanadium is chosen because of its small coherent scattering length, which means weak Bragg diffraction, and due to its size will have low inelasticity effect which will be easy to correct for.⁹⁹ The container can be made out of vanadium or TiZr alloy. The reason for choosing vanadium has already been explained. TiZr is chosen because the two metals scatter neutrons with opposite phase which will cancel out.⁹⁹

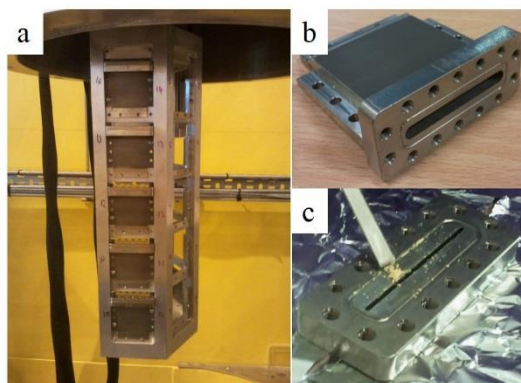


Figure 2.7 Sample holder for a neutron scattering experiment. Images of a) samples rack for automatic sequence of scans on NIMROD; b-c) examples of sample container, c) 1 mm opening.

In the experiments for this study the sample holder was a flat plate TiZr can with sample thickness of 1 and 2 mm (Figure 2.7). The beam area was $30 \text{ mm} \times 30 \text{ mm}$. Each sample was scanned five times to average the data. Data analysis was carried out using the software GudronN and modelling was performed with PDFGui.¹⁰³

2.2.3. Solid State Nuclear Magnetic Resonance (SSNMR)

The NMR technique measures the effect that an external magnetic field has on the nuclei of a molecule. A nucleus is characterised by a magnetic moment, μ . The sum of all the nuclei magnetic moments in a molecule gives the net bulk magnetisation of the molecule.¹⁰⁴

$$\mathbf{M} = \sum_i \mu_i \quad \text{Eq. 2.10}$$

In the absence of a magnetic field all the nuclei magnetic moments can be randomly oriented bringing the net bulk magnetisation to zero. When an external magnetic field of magnitude \mathbf{B}_0 is applied the magnetic moments will start aligning along its direction and \mathbf{M}_0 will now be a vector parallel to \mathbf{B}_0 (Figure 2.8).¹⁰⁵

In a static magnetic field \mathbf{M}_0 will rotate around the axes of the field, which by convention is the z axes in a coordinate system. The frequency of rotation (precession) is called the Larmor frequency and it is defined as:^{104, 105}

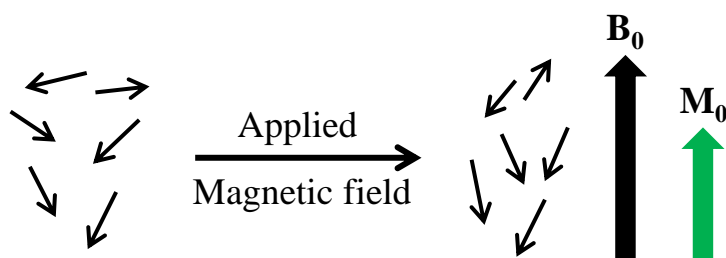


Figure 2.8 Effect of a magnetic field on magnetic moments. The nuclei magnetic moments are represented by the small arrows. B_0 is the magnetic field and M_0 is the net bulk magnetisation generated by the alignment of the magnetic moments.

$$\omega_0 = -\gamma B_0 \quad \text{Eq. 2.11}$$

which shows its dependency from the gyromagnetic constant, γ , characteristic of a nucleus.^{104, 105}

In a basic NMR experiment a pulsed magnetic field, B_1 , is applied along a different direction (x or y) from B_0 .¹⁰⁵ If its frequency, ω_{rf} is equal to ω_0 , the new magnetic field will move M_0 from the z direction towards the xy plane.¹⁰⁴ An example with a 90° pulse is illustrated in Figure 2.9. The new vector representing the bulk magnetisation, M_1 will rotate around z with a new frequency ω_1 , dependent on B_1 . It is this frequency that is measured as a free induction signal (FID) during a NMR experiment. By Fourier Transform (FT) the FID is translated into the spectra of intensities *vs.* frequencies.¹⁰⁵

It is not only the applied field that influence the resonance frequencies of the nuclei, but also their chemical environment. The electrons of the atoms, once exposed to a magnetic field, generate themselves a secondary field which is felt by the neighbouring nuclei and

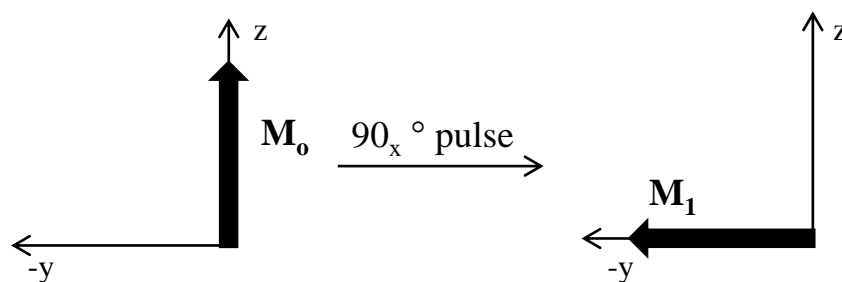


Figure 2.9 Effect of a 90_x° pulse on the bulk magnetisation vector. Graphic representation of the effect on the vector M_0 of an RF pulse applied along the x direction.

will influence their frequency. This gives origin to the chemical shift in a NMR spectra.¹⁰⁴
¹⁰⁵ Since the electrons present around a nucleus depend on the bonds of the atoms, the same nucleus can give different resonances depending on its chemical bonds.

In a solid state NMR the effect of the surrounding atoms in space can also have an effect on the resulting spectra. In solution the dipolar-dipolar interactions are averaged to zero due to the mobility of the molecules (isotropic value). In solid state the reduced mobility of the atoms prevent the averaging (anisotropy). The strength of these interactions is related to the distance r by $1/r^3$.¹⁰⁴ Therefore more information can be obtained by a solid state NMR, on the other hand this makes the analysis of the spectra more complicated.

In a SSNMR experiment, for reasons of nuclear spin, only specific nuclei can be investigated (especially spin 1/2 nuclei such as ^{13}C , ^{15}N , ^1H). Some of these nuclei are naturally very diluted ($^{13}\text{C} = 1.11\%$, $^{15}\text{N} = 0.37\%$)¹⁰⁶. This makes the signal-to-noise ratio on a spectra very low and their relaxation times (time needed for the bulk magnetisation to reach equilibrium) are very long requiring long pauses between scans. To overcome these issues a cross-polarisation experiment is usually carried out. It exploits the magnetisation of a more abundant nucleus (^1H), which is magnetised by applying a pulse as in a normal experiment, and transfers it to a diluted one (^{13}C) of which the resonance frequency is measured. The signal obtained for the diluted nucleus will depend on the amount of abundant atoms in its surrounding.¹⁰⁴ However, a drawback of this experiment is the non-quantitative nature compared to a direct polarisation experiment, where it is the nucleus of interest to be magnetised.

NMR characterisation was carried out on a Bruker Avance III spectrometer (9.4 T magnet, 400.13 MHz). MestReNova 7.1 was used to analyse the data.

2.2.4. Thermal Gravimetric Analysis

Thermal gravimetric analysis (TGA) measures the mass changes in time of the specimen when this is exposed to specific experimental conditions (temperature and atmosphere). The sample is weighed in a crucible and it is inserted in a furnace where it is heated. During the experiment the sample is simultaneously weighed and heated to record changes of weight with changing temperature. Different temperature profiles can be chosen to satisfy specific experimental requirements. The temperature can be constantly ramped to a specific value and immediately ramped down to room temperature or, in an isotherm configuration, it can be ramped up to a specific value and kept constant in order to monitor the changes over time. The composition of the atmosphere in the furnace can be chosen

according to experimental needs and can be both static and flowing.¹⁰⁷ The results of the analysis is a profile of the mass loss or gain *vs.* temperature or *vs.* time in case of an isotherm experiment.

TG analysis for this study were carried out on a RheoTherm TGA 1000M+ Different conditions have been used during the investigation, this will be described for each experiment in due course.

2.2.5. Brunauer-Emmet-Teller Analysis

Brunauer-Emmet-Teller (BET) analysis measures the surface area of solids employing the physical adsorption of a gas on the surface of a solid material. The sample is initially cleaned from any impurity by heating and degassing of the atmosphere. After cooling of the sample a gas that can be adsorbed on the surface of the sample (usually N₂) is introduced into the chamber and by measuring the pressure of the gas is possible to deduce the amount of gas adsorbed and therefore the surface area of the sample.

BET measurement for this work were carried out on a Micromeritics TriStar II.

2.2.6. Elemental Analysis

Elemental analysis (CHN analysis) is used to determine the carbon, nitrogen and hydrogen content in organic compounds. This is given as mass % of the single elements. To do so a high temperature decomposition of the organic material is carried out. The sample is heated to 900 °C under oxygen and a series of steps follow for the identifications of the gaseous compounds evolved during the decomposition process. These are: hydrogen, nitrogen and nitrogen oxides, carbon dioxide and monoxide and finally water. The first step is a reduction/oxidation step at 750 °C by copper which will reduce NO_x into nitrogen and then the copper oxide so formed will reduced the CO to CO₂. The new mixture of gases will go through three detectors which will, in order, remove water and analyse H₂, analyse carbon and remove CO₂ and finally analyse N₂.¹⁰⁷

For this investigation the CHN analysis was carried out at the London Metropolitan University with a Carlo Erba Flash 2000 Elemental Analyser.

2.2.7. Solid UV-Vis spectroscopy

Ultraviolet-visible spectroscopy is employed to investigate the electronic properties of a material. UV-Vis light is employed to excite electrons to higher energy levels.¹⁰⁷

Different wavelengths of light correspond to different energy through Equation 2.12 where h is the Planck constant, c the speed of light and λ the wavelength of the radiation.

$$E = \frac{hc}{\lambda} \quad \text{Eq. 2.12}$$

Hence, by knowing the wavelength of the absorbed radiation it is possible to determine the energy required for the electronic transition.

A typical UV-Vis spectrometer measures the intensity difference between the incident and the final detected radiation. The absorbance is then calculated by:

$$A = \log(I_0 / I) \quad \text{Eq. 2.13}$$

where I_0 is the intensity of the incident beam and I of the measured one. In a classical liquid UV-Vis absorption experiment it is the beam transmitted through the solution that is measured. When the sample is a solid (powder or pellet) transmitted light cannot be measured. In a solid state UV-Vis spectrometer an integrated sphere is placed between the beam source and the sample, this allows for collection of all reflected and scattered light to be collected and measured.

The UV-Vis spectra were acquired with a JASCO-V-650 spectrophotometer equipped with an integrated sphere coated with barium sulphate. The Band Gap energies were calculated *via* Kubelka-Munk transformation with a dedicated software (SpectraManager, JASCO).

2.2.8. Transmission Electron Microscopy (TEM)

Transmission electron microscopy is a technique used for the characterisation of small features in solid samples. It is particularly useful in the characterisation of nanosized samples, *i.e.* nanoparticles. Information obtainable from TEM imaging can vary from shape and simple size distribution to crystal structure determination according to the resolution of the image. In high resolution TEM it is also possible to see features at the atomic scale.¹⁰⁸ The technique is based on scattering of waves by matter, in the specific scattering of electrons. When a homogeneous electron beam reaches a sample it can be scattered in many ways, these are illustrated in Figure 2.10a. Two main groups of scattered electrons can be identified, those that are scattered with an angle $\theta > 90^\circ$ called backscattered, and those with an angle $\theta < 90^\circ$ called forward scattered electrons.¹⁰⁸ The latter are the ones exploited in a transmission electron microscope to produce magnified

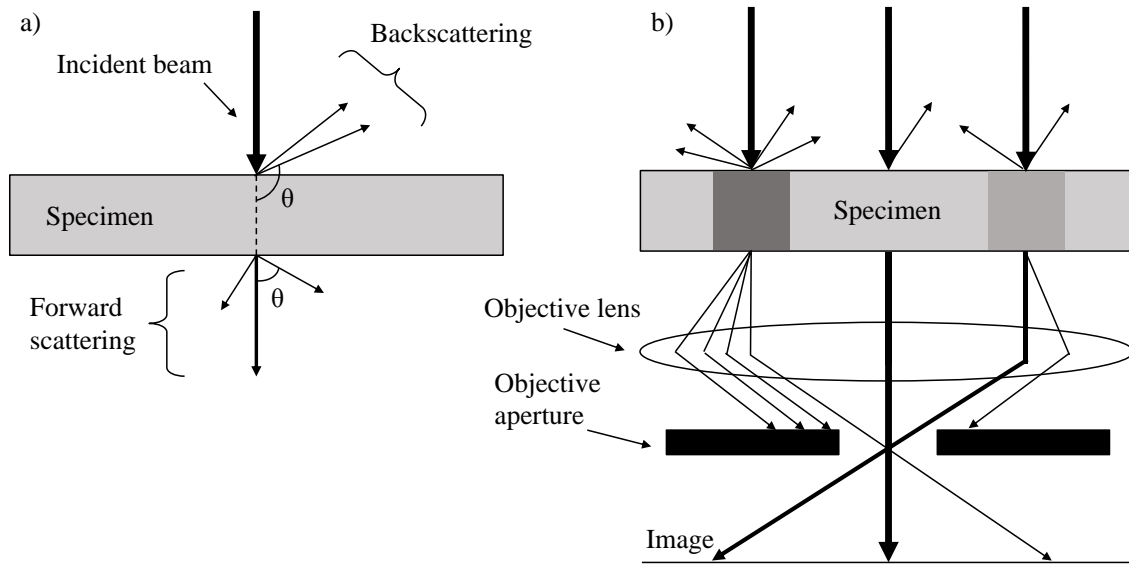


Figure 2.10 Schematic of TEM working principles. Schematic representation of a) electron scattering of a thin specimen and b) of its exploitation in a TE microscope.

images of the specimen.¹⁰⁸ After some of the electrons are backscattered the electron beam that goes through the specimen will be reduced in intensity. This can further be reduced during forward scattering since the electrons can be scattered parallel to the original beam direction (direct) or at an angle θ . The direct beam is what gives the image on the TEM screen and its intensity is important to obtain details of the sample surface. Different beam intensities will result in different contrast area in the image. Lower intensity of the direct beam will correspond to darker areas. Figure 2.10b describes in a simple way the basic working principle of a transmission electron microscope and how the contrast in the image is obtained. To better understand is important to mention that the scattering power of the atoms depend on the atomic number Z , heavier atoms will scatter more than lighter ones. Additionally, for equal Z , in a thick area of the specimen the number of scattering events will be higher than in a thinner area. The dark grey areas in Figure 2.10b represent heavier atoms (for example metal nanoparticles on a carbon support) or thicker areas of same composition.

When the homogeneous electron beam hits the specimen, backscattering will occur and the electrons will be backscattered more by the darker areas leading to lower intensity of the forward scattered beams (in Figure 2.10b the intensity of the beam is expressed *via* the thickness of the arrows).¹⁰⁸ As mentioned, further scattering will occur for the beams that are transmitted through the sample.¹⁰⁸ This will be more intense for the darker areas

in Figure 2.10b and the intensity of the direct beam is decreased even further. Within the microscope a series of lenses and apertures will allow only the direct beams to reach the screen. The direct beams will have different intensities according to the area of samples they went through and this information is translated in an image with different contrasts.¹⁰⁸ An example, acquired with a CCD (charged-couple device camera), is provided in Figure 2.11a where metal nanoparticles are loaded on a carbon-based support. The difference of atomic number and therefore scattering behaviour of metal and carbon produces clear contrast in the image and allows to distinguish the NPs from the support. From images similar to that of Figure 2.11a is possible to obtain information about shape and size of the nanoparticles. At higher magnifications, however, information about the structure of the nanoparticles can be obtained. Figure 2.11b shows lattice fringes for platinum nanoparticles obtained at high magnification. This information can be obtained by analysing the image with the dedicated software (Gatan Digital Micrograph). The lattice fringes distance is measured from the diffractogram (Figure 2.11b inset) obtained by Fourier transform of the image. In the specific a lattice fringe of 0.225 nm is measured which correspond to the d_{111} of Pt⁰.

When using this information to distinguish between different metallic nanoparticles, care has to be taken especially for small NPs.¹⁰⁹ When measuring d -spacing from lattice fringes errors can be generated by the irregular shape of the particle and its orientation.¹⁰⁹ If the particle is slightly tilted compared to the view axis then the lattice fringes seen can be smaller or bigger than the standard ones.¹⁰⁹ Following the example of Tsen *et al.*¹⁰⁹ a measurement of the d_{111} of various platinum nanoparticles (59 NPs of different size and shape) is carried out to determine the statistical distribution of d -spacing value

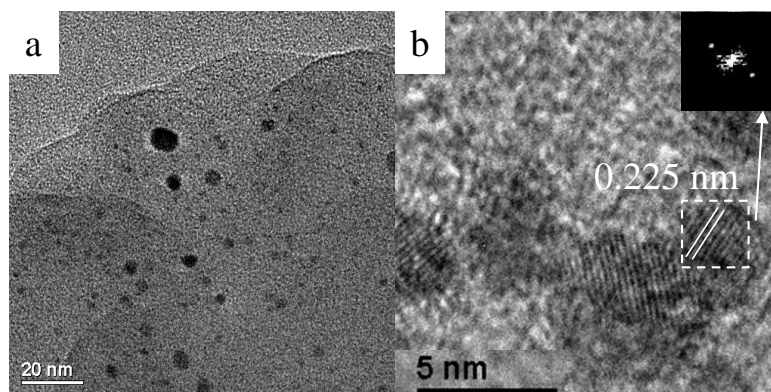


Figure 2.11 Example of (HR)TEM images. TEM images of Pt nanoparticles on carbon-based support: a) low magnification and b) high magnification with visible lattice fringes.

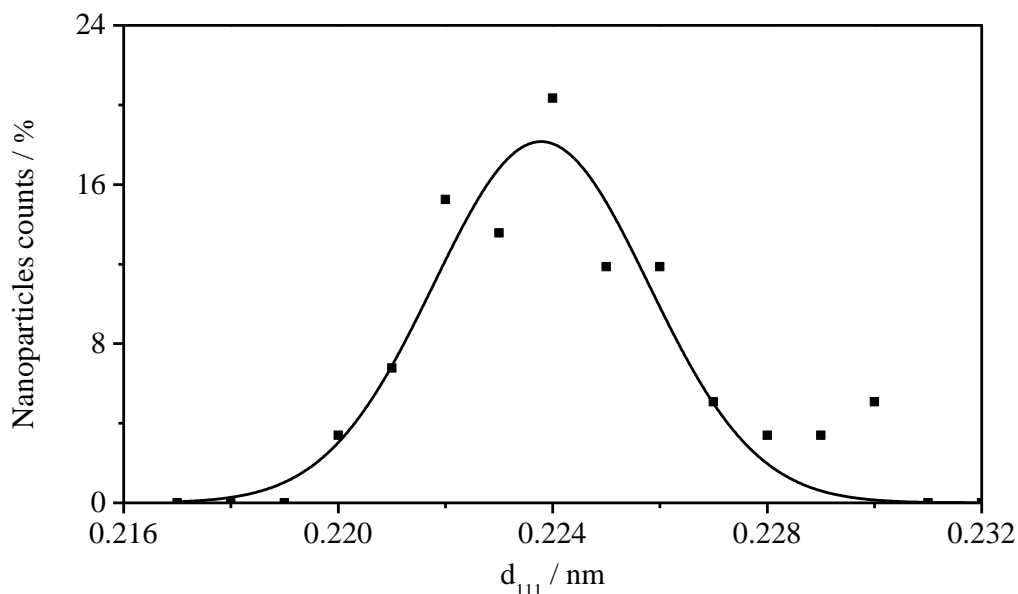


Figure 2.12 Distribution of Pt d_{111} from HRTEM measurements. Gaussian distribution of the d_{111} of Pt NPs. 59 NPs of different shape and size were analysed.

(Figure 2.12). This will provide a tool to critically analyse the d-spacing of different metals NPs (Chapter 5). The measured lattice fringes can be fitted with a Gaussian function¹⁰⁹ of maximum 0.224 nm and FWHM of 0.005 nm. Statistical analysis of the data points shows an average of 0.224 nm with a standard deviation of ± 0.002 nm.

Even though a powerful tool to characterise nanomaterials, TEM imaging presents some drawbacks. Due to the high magnification compared to other techniques only a small part of the whole sample can be analysed.¹⁰⁸ Therefore the information obtained may not be representative of the real situation. For this reason it is important to acquire as many images as possible of different areas, to have a better statistic. In addition, the TEM provides 2D images of 3D features,¹⁰⁸ this inevitably brings to some artefacts and limitations in the determination of characteristics along the third axis. Hence, TEM has to be used together with other techniques if a complete characterisation is to be achieved. (HR)TEM images were acquired on a JEOL-2011 microscope operated at 200 kV with tungsten filament electron source. The specimen was prepared by suspension in acetone of the powder sample. This was, then, deposited on a carbon coated copper grid. Digital images were recorded using a Gatan 794 CCD camera and the dedicated software, Gatan Digital Micrograph was employed to analyse the images. Particle size distribution was obtained by using ImageJ, an image editing software.

2.2.9. Scanning Electron Microscopy (SEM)

Scanning electron microscopy is a technique employed to characterise the morphology and composition of solids. As in the case of TEM, it is based on the interaction of an electron beam with the sample. The type of interaction provides specific information about the specimen. When an electron beam (primary electrons) reaches the surface of a sample it can be backscattered or it can interact with the atoms and ionize them by removing electrons (secondary electrons). By detecting one or the other it is possible to obtain different information, in the first case morphology and composition characterisation is obtained, in the second only morphological.¹¹⁰

The secondary electrons are low in energy and they are produced by the very outer surface of the specimen, and their collection is carried out by a detector with a small bias applied.¹¹⁰ The number of electrons collected and their intensities will be translated into images with different contrast. Figure 2.13 illustrate the basic principle that generates contrast in SEM images. Once generated, the secondary electrons will travel to the detector, however, some will encounter obstacles on their path, especially on a rough surface, and will not reach the detector (Figure 2.13a). The lower number of electrons produced by these areas of the samples will be translated in darker details in the picture (Figure 2.13b).

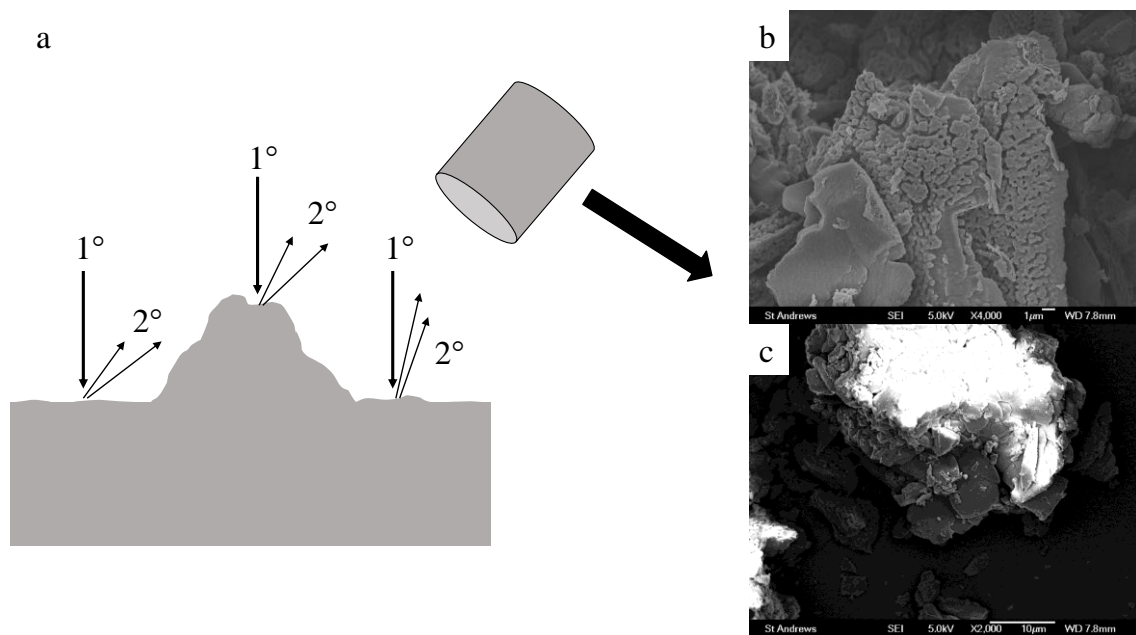


Figure 2.13 Schematic of the principle of SEM imaging. a) Schematic of secondary electrons (2°) generation and detection; effect of surface topography. b-c) examples of SEM images.

If the sample analysed is not particularly conductive this can cause charging effect (Figure 2.13c) due to the accumulation of secondary electrons. The result is an image where areas of the surface result particularly bright. To prevent this usually a metal is sputtered to improve the conductivity during imaging.¹¹⁰

The images for this investigation were collected on a JEOL JSM-6700F scanning electron microscope. Secondary electron mode was employed to obtain topographical information of the surface. Gold was sputtered on the surface of the sample with the aim of reducing the charging effect.

2.2.10. X-ray Photoelectron Spectroscopy (XPS)

XPS is a characterisation technique that provides information on the chemical composition of the outer surface of a solid sample. In an XPS experiment x-ray of energy $h\nu$ are sent to the sample and cause the removal of core electrons from the atoms on the surface of the specimen.¹¹¹ These are characterised by a kinetic energy, E_k , that depends on the atom of origin, its oxidation state and its environment.¹¹¹ The electrons are then collected by a detector and their kinetic energy is measured. A schematic representation of the working principle is illustrated in Figure 2.14. An XP spectra is usually expressed in counts *vs.* binding energy, E_b (eV) of the detected electrons. This is obtained from the kinetic energy measurement *via* Equation 2.14 where $h\nu$ is the known energy of the x-ray,

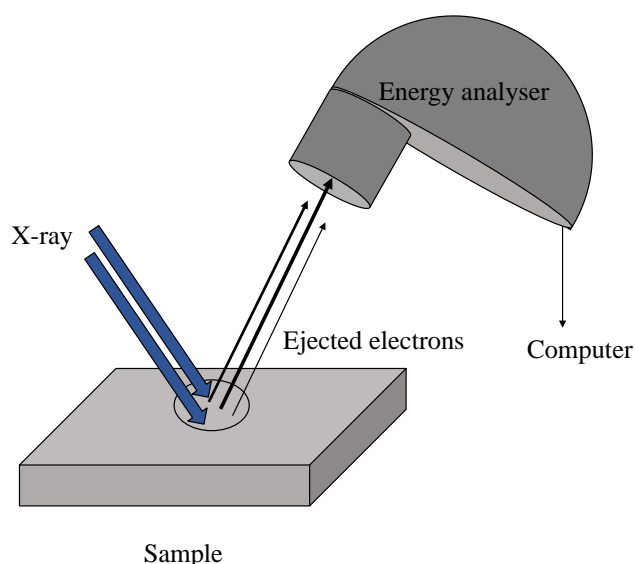


Figure 2.14 Working principle of an x-ray photoelectron spectrometer. Schematic of an XP spectrometer. The electrons of different kinetic energy are presented as arrows of different thickness.

E_k is the measured kinetic energy and ϕ is the work function of the detector of the instrument.¹¹¹

$$E_B = h\nu - E_K - \phi \quad \text{Eq. 2.14}$$

The x-ray beam only interests a small area of the whole specimen, for the instrument used for this study this is 1 mm × 0.5 mm. The depth reached by the beam is only few nanometers, ~ 10 nm. Therefore only the very top layer of the sample is analysed.

The spectrometer used to carry out the analysis for this investigation is a Kratos AXIS Ultra DLD, with a monochromatic Al K α (1486.6 eV) X-ray source and for peak calibration, adventitious C was used at 284.6 eV. Data analysis was carried out on the CasaXPS software. Air sensitive samples were transferred in the spectrometer *via* glovebox specially adapted to allow attachment of the XP spectrometer transfer arm.

2.3. Hydrogen evolution

2.3.1. Reaction vessel

The performances for hydrogen evolution are evaluated by using a custom-made reactor. In details, the vessel is an aluminium circular box (Figure 2.15a, b) with polytetrafluoroethylene (PTFE, Teflon®) lining to prevent photocorrosion of the metal, moreover, PTFE is stable in most drastic conditions allowing easy cleaning. Due to the

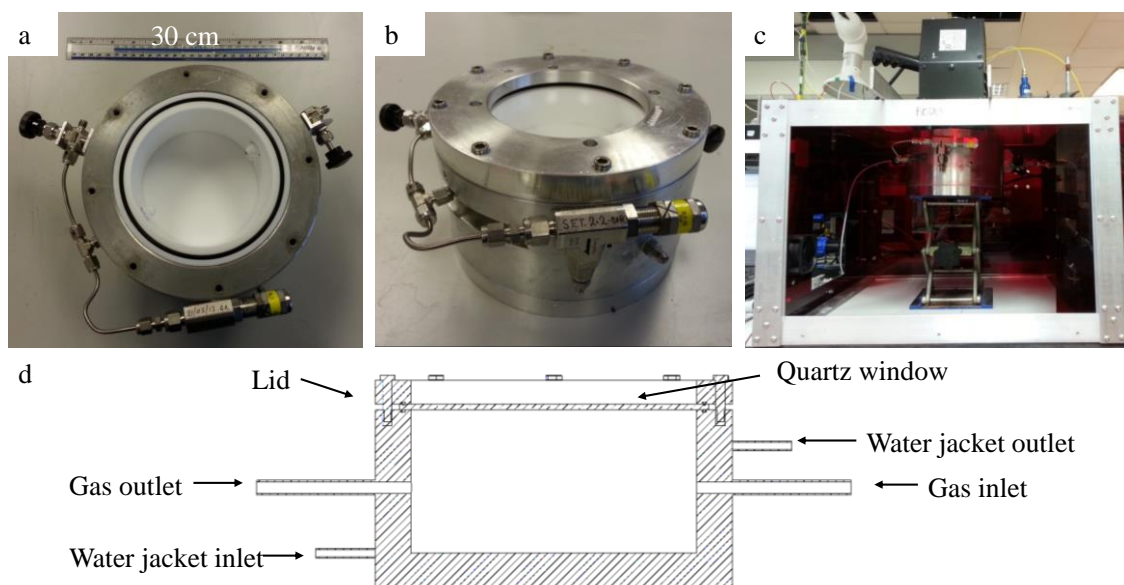


Figure 2.15 Photocatalytic Set-up. Image of the photocatalytic box from top (a) and front (b). Testing set-up with top irradiation (c). Schematic of vessel (d).

gaseous nature of the products of the photocatalytic reaction an optimum seal of the reactor is necessary, therefore O-rings were used to achieve a gas-tight environment. The vessel is equipped with inlet and outlet needle valves for gas sampling and a pressure relief valve for safety reasons. To allow the light to reach the catalyst, the top of the box consists of a quartz window.

Light irradiation is carried out from the top (Figure 2.15c) with a 250 W iron doped metal halide UV-Vis lamp (≥ 290 nm; UV Light Technology Limited) equipped with a UV cut off filter (≥ 420 nm; Borosilicate Coated Glass, UQG Optics Ltd). Figure 2.16 shows the irradiance spectra of the lamp as provided by the manufacturer compared with the measured (Stellarnet EPP2000 Spectrometer) distribution of wavelengths emitted by the lamp with and without UV blocking filter. The photon intensity of the lamp was measured using an Apogee Quantum Sensor (MQ-200 series) and, at the minimum achievable distance (17 cm) from the light source, the photon flux emitted from the lamp with UV cut-off filter is found to be 1812 ± 44 mmol·m⁻²·s⁻¹, constant throughout the whole experiment time (usually 20 h). This value is employed to determine the apparent quantum yield:

$$AQY = \frac{2 \times \text{Number of H}_2 \text{ molecules}}{\text{Number of incident photons}} \times 100 \quad \text{Eq. 2.15}$$

The irradiation causes the temperature to increase during the photocatalytic process, therefore, the photoreactor was also fitted with a water jacket to allow cooling. A thermosensor (Thermochrome i-Botton) was used to monitor the temperature of the outer

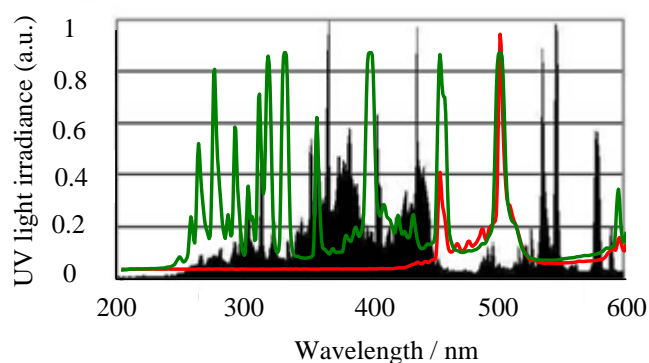


Figure 2.16 UV lamp wavelength distribution. Black: spectrum of wavelength as provided by UV Light Technology Ltd. (reproduced with permission), green: without and red: with cut-off filter.

wall of the box (T_{out}). The temperature of the inner part (T_{in}) can be determined by the relation illustrated in Equation 2.16:

$$T_{\text{in}} = T_{\text{out}} + (27 \pm 1) \text{ } ^\circ\text{C} \quad \text{Eq. 2.16}$$

This relation is valid for temperatures after 30 min from the beginning of the experiment, when a linear correlation between inside and outside T is achieved. Figure 2.17 shows T_{in} and T_{out} as a function of time. The temperature reaches equilibrium at $\sim 70 \text{ } ^\circ\text{C}$ after four hours of visible irradiation. Most of the performance evaluation tests are carried out at the natural temperature of the system.

The pressure was monitored with a pressure sensor (Thermosens Direct, High accuracy, 4~20 mA pressure transmitter).

When single wavelength light was needed for the experiments a LED lamp is used (Modulight, IVIUM Technologies). The available wavelengths are: 460, 525, 590, 623, 660 and 740 nm. When this lamp is employed the temperature within the vessel does not raise and remains constant at room temperature.

2.3.2. Reaction conditions

In a typical photocatalytic experiment the reaction mixture is a suspension of the catalyst ($1 \text{ g}\cdot\text{L}^{-1}$, usually 0.100 g or 0.200 g) in an aqueous solution of sacrificial agent. This was, for most of the experiments, oxalic acid (0.025 M)²⁵ but a different sacrificial agent is

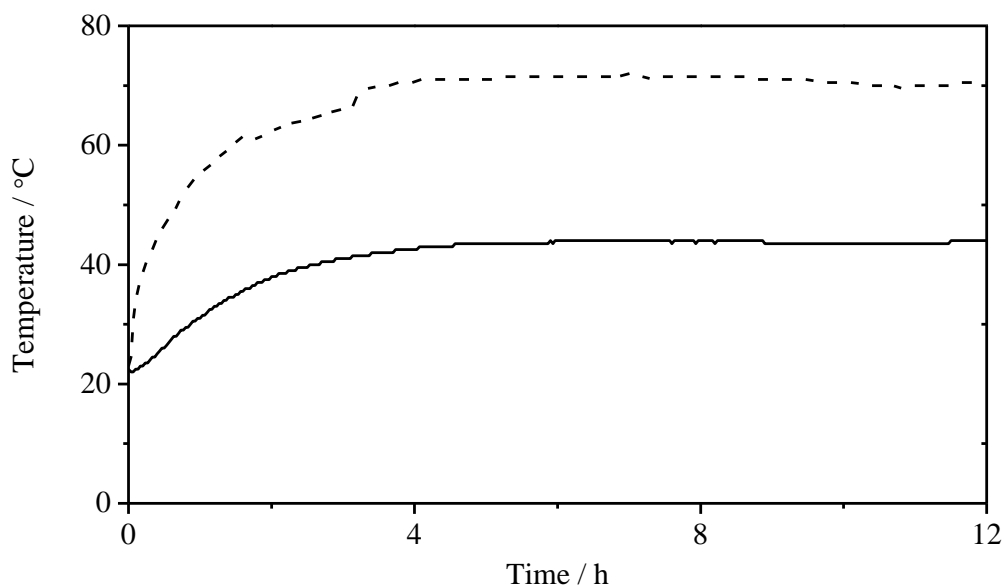


Figure 2.17 Temperature profile. T_{in} (dashed line) and T_{out} (full line) profiles as measured during irradiation time

employed in some of the experiments, this was triethanolamine which is used at 10 v.% (0.75 M)⁵⁴. After sealing the vessel the head space is purged with Argon gas in order to remove air.

2.3.3. Gas sampling

The gas evolved during the photocatalytic test are sampled for chromatographic analysis following three different sampling configurations. These are chosen depending on the activity of the sample and the information needed. These are: batch, semi-batch and continuous.

Batch: one measurement after 20 h of photocatalysis is carried out. This is used for less active materials, when H₂ evolution is not sufficient to have a more frequent sampling, for fast screening and for more general comparisons, when not specific information were needed other than overall activity (Chapter 4, preliminary tests).

Semi-batch: sampling of the product is carried out at regular intervals (1 h or 2 h) during the photocatalytic experiment. This method is applied to active materials when the profile of H₂ evolution rate over time is of interest (most of Chapter 4 and Chapter 5). For this kind of sampling method an automated sampling system is developed: solenoid valves, opened by the gas chromatograph *via* a Labview software, allows the gases to reach the gas chromatograph at a fixed time interval. Figure 2.18 shows a schematic representation of the automatic sampling system.

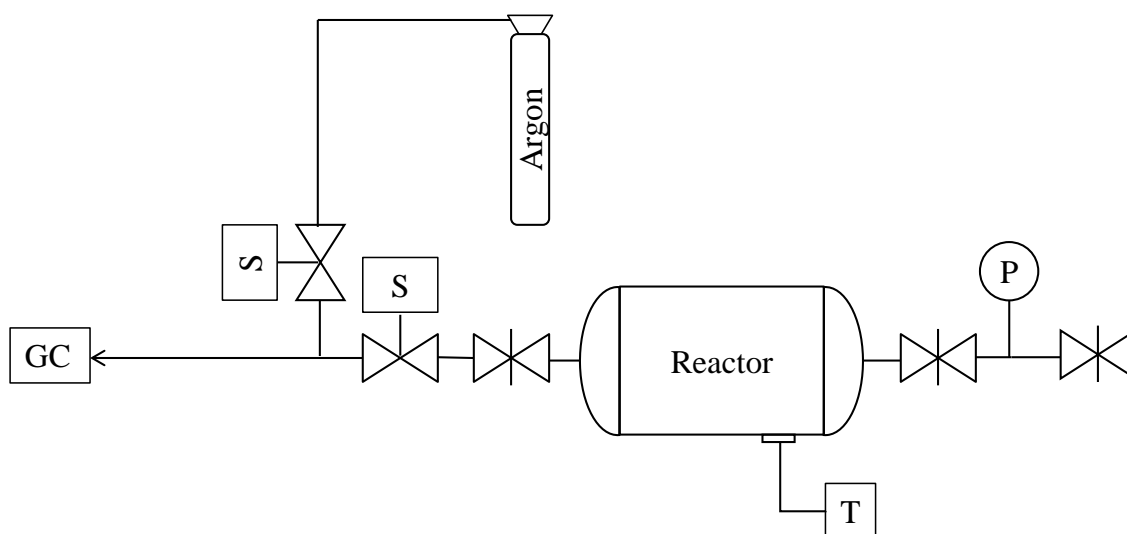


Figure 2.18 Automatic System. Schematic representation of the automated sampling process. S: solenoid valve, P: pressure gauge recording the pressure and T: temperature sensor.

Continuous: a carrier gas (Argon) is used to guarantee a continuous flow through the photocatalytic vessel and the GC. This is used when profile of the evolution of hydrogen over time is necessary for particularly active samples (Chapter 4, reduction pre-treatments). The flow is controlled and kept constant with an Aalborg digital Mass Flow Controller calibrated for an Argon flow of 0-20 sccm/min.

2.3.4. Gas analysis

The gas evolved during the evaluation of the photocatalytic performances were analysed *via* gas chromatography by using an Agilent 3000 Micro GC. Gas chromatography is a useful tool to analyse mixture of gases. These are heated at an appropriate temperature and are carried by a gas (carrier gas) through a column where they will be retained differently according to the interaction with the stationary phase. The retention time is characteristic of a specific component. Once separated by the chromatographic column the different gases will be analysed by a detector. In this specific case the detector consists in a thermal conductivity detector. The carrier gas and the sample gas will pass over different hot filaments and will affect their electric resistance which will be compared to the resistance of the reference column and the carrier gas. Pressure and flow of the sample are automatically controlled by the instrument.

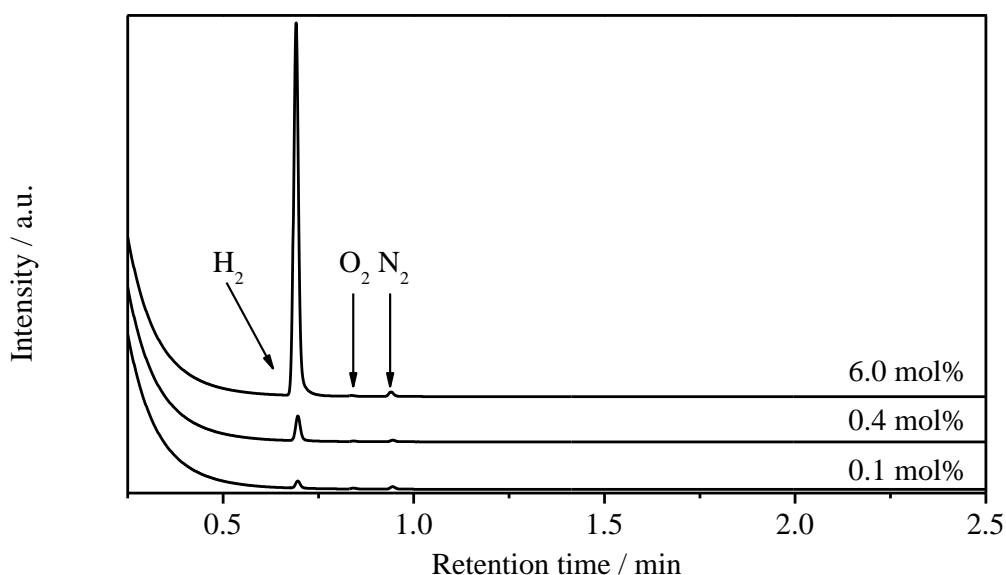


Figure 2.19 Example of Gas Chromatograph. Gas chromatograph taken from actual experiments. Increasing molar concentrations of hydrogen in argon are illustrated.

The instrument was calibrated for hydrogen by using a mixture of pure H₂ in argon. The response of the GC resulted being linear from 0 to 15 mol% H₂ in Ar. Concentrations higher than 15 mol% cause saturation of the detector and therefore no information can be obtained. Figure 2.19 illustrates three chromatographs obtained during a photocatalytic experiment.

The error of photocatalytic measurements is determined for each sampling mode by carrying out the same test a few times on different batches of sample. The deviation from the average value of six measurements for each sampling mode is estimated being $\leq \pm 5\%$.

Chapter 3

The catalyst: Graphitic Carbon Nitride

3.1. Introduction

Graphitic carbon nitride structure has been investigated since “melon”, a small polymeric analogue (Section 1.4), was officially reported for the first time in 1834 by Liebig.^{56, 58} In 1922, Professor Edward C. Franklin published a detailed investigation of the derivatives of cyanamide, dicyanamide and melamine.⁵⁸ Among the studied systems are Melam ($C_6N_{11}H_9$) Melem ($C_6N_{10}H_6$), Melon ($(HC_2N_3)_x$) and Carbonic Nitride ($(C_3N_4)_x$). Regarding Melam and Melem, without providing any details, Franklin said he doubted their existence “*as chemical individuals*”⁵⁸. His opinion about Melon was however different. According to him, in addition to Berzelius synthetic method (heating mercuric thiocyanate), Melon can be synthesised by heating any of the organic compounds he described in his paper.⁵⁸ The only issue was the reproducibility of the obtained product since the hydrogen content was found to vary from 1 wt.% to 2 wt.%.⁵⁸ He also attempted the synthesis of carbonic nitride without being successful in obtaining a pure product.⁵⁸ Few years later, in 1937, Pauling and Sturdivant investigated with x-ray the structure of a crystal provided by Franklin, with supposed formula $NaC_6N_9 \cdot 3H_2O$.¹¹² At the end of their study, they stated that “*remains little doubt as to its correctness*”¹¹², referring to the proposed structure of the crystal: three condensed rings with aromatic character (heptazine unit as in Figure 3.1a, b and c). On the base of Pauling and Sturdivant’s x-ray investigation and Franklin’s study of Melon, in 1940 Redemann and Lucas provided some elucidation on the structure of Melon and the reason why it was so difficult to obtain

reproducible products.¹¹³ They suggested that Melon structure derives from the loss of few amino groups from Melem molecules, and the authors proposed two configurations for this polymeric structure: a linear chain (Figure 3.1a) and a “*symmetrical triangular molecule*”¹¹³ (Figure 3.1b). The higher the number of cyameluric (heptazine) nuclei in the molecules the closer to the ideal Franklin’s Carbonic Nitride (Figure 3.1c). The possible configurations that the molecule can assume were therefore considered responsible for the lack of reproducibility: “*It is probably incorrect to assign any one structure to melon, for it is more than likely a mixture of molecules of different sizes and shapes*”¹¹³.

After 1940 no attention was paid to this compounds until the early 90s when speculations that C_3N_4 could be stronger than diamond directed some of the scientific interest, once again towards Franklin’s Carbonic Nitride.^{114, 115} This led to the discovery of few allotropes with formulation C_3N_4 : α -, β -, cubic-, pseudocubic-, and graphitic- C_3N_4 (g- C_3N_4).¹¹⁴ The latter was found to be the most thermodynamically stable of them all.¹¹⁴ From the late 90s its structure was investigated in many occasions and it was assigned

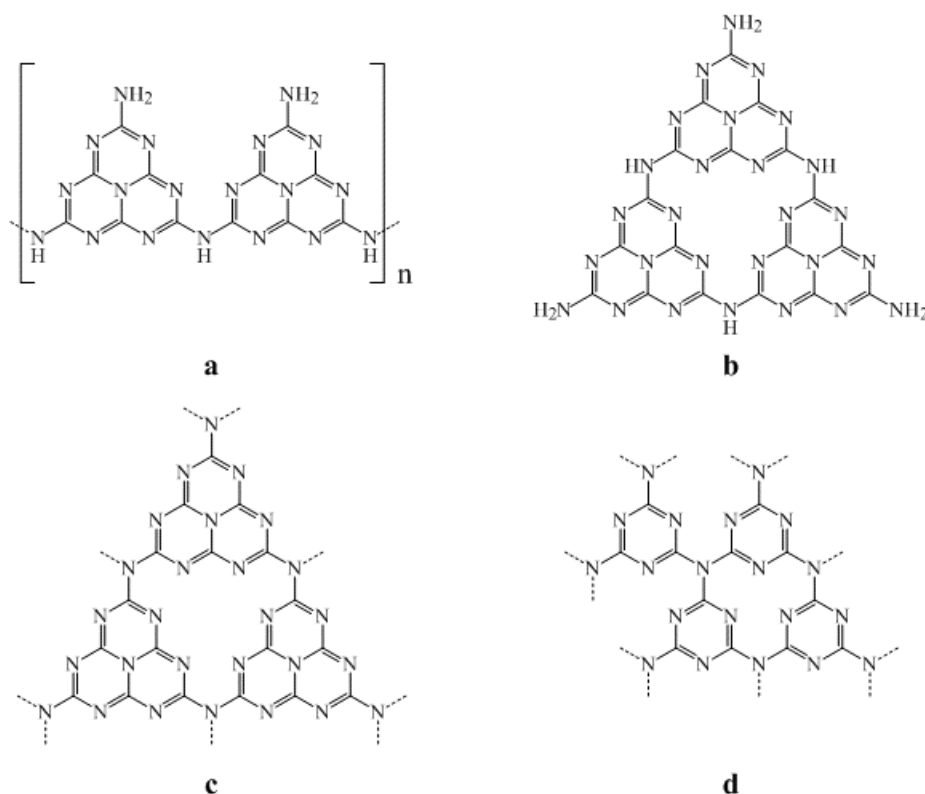


Figure 3.1 Structural representation of Melon and g- C_3N_4 . Redemann & Lucas’ Melon configurations: a) linear chain and b) compact triangular shape.¹¹³ Graphitic carbon nitride possible structures: c) heptazine and d) triazine based.

with a triazine based structure (Figure 3.1d)¹¹⁶⁻¹²⁰, not taking into consideration the work by Liebig^{56, 58} and later by Redemann & Lucas¹¹³.

In the 2000s g-C₃N₄ was described, once again, as composed of heptazine units.^{69-72, 114} Since then, many investigations have been carried out to try to confirm the structure of the most stable allotrope of C₃N₄.^{60, 69, 90, 114, 121, 122} By 2009¹²², with the aid of DFT calculations, electron diffraction and NMR, the 2D structure of g-C₃N₄ synthesised by thermal condensation of small organic polymers was considered solved as a tri-*s*-triazine based polymeric structure. However, due to the highly amorphous character of the material the description of its 3D structure has always proved challenging.

On the basis of the work done so far, this chapter will look at the structural changes of g-C₃N₄ with temperature and will attempt an investigation of the 3D structure of the polymer by means of x-ray and neutron diffraction techniques.

It is important to mention that at the same time this investigation was being carried out a very similar study was published in 2013.¹²³ The investigation described in this chapter however goes beyond the x-ray diffraction by combining it with neutron scattering. The results from Tyborski *et al.* will be used as support to the validity of some of the conclusions of the current investigation and as starting point for the next step which is neutron diffraction.

3.2. Influence of synthesis conditions on structure and morphology

3.2.1. Effect of condensation temperature on the structure

In this study graphitic carbon nitride was synthesised *via* thermal polycondensation of melamine in a closed system, *i.e.* an alumina crucible with a cover was used as the reaction vessel. The reason for this was to retain the gases evolved during sublimation and decomposition of melamine into the system to allow formation of g-C₃N₄. Thermal gravimetric analysis (TGA) (Figure 3.2) shows that at about 300 °C melamine starts decomposing and within 50 °C the weight loss is almost complete. The remaining material (~ 2 wt.% of the starting material) is the result of thermal polycondensation of melamine,⁷² as already shown in 1988 by Costa and Camino.¹²⁴ Upon further heating the condensation product starts decomposing and undergoes two subsequent weight losses (Figure 3.2, inset): first at 480 °C and then at 580 °C, before disappearing completely at ~ 620 °C. The condensation product formed at ~ 350 °C is unlikely to be g-C₃N₄ since this is usually obtained at temperatures above 500 °C.^{54, 125} To try to identify the

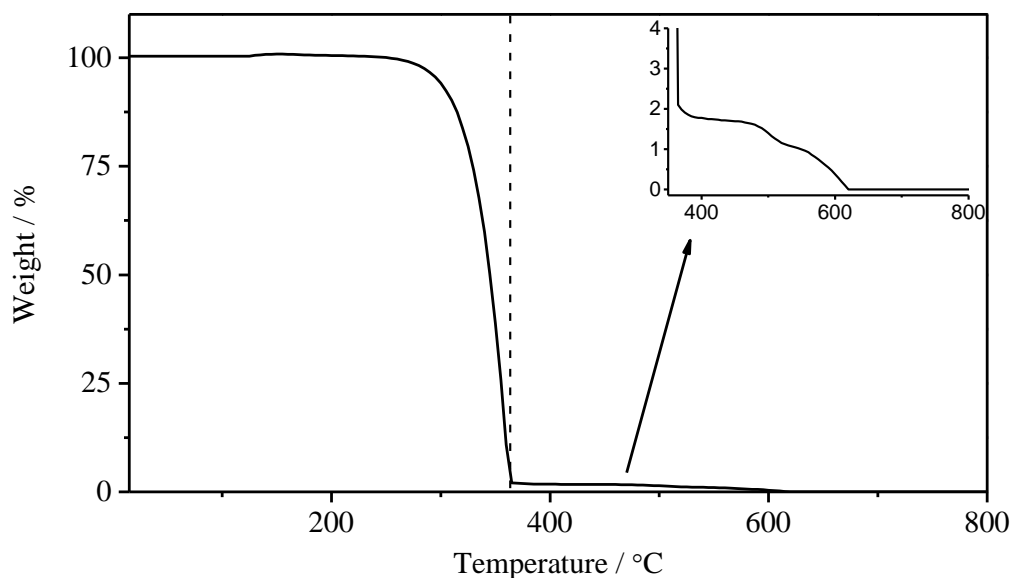


Figure 3.2 TGA of melamine. TGA profile of melamine under air, ramping rate: 5 °C/min. Inset: detail for $T \geq 350$ °C.

intermediates, melamine was synthesised at different temperatures and XRD analysis was carried out. The graphitic carbon nitride was prepared with a 15 h condensation reaction, varying the temperature of the synthesis: 450, 500, 550, 600 and 650 °C (investigation of the influence of the length of condensation will be discussed in Section 3.2.3). For simplicity the samples are, from now on, referred to by the temperature at which they were synthesised; for example, g-C₃N₄ synthesised at 450 °C is identified as C₃N₄-450. Figure 3.3 illustrates the X-ray diffraction patterns of the products obtained from the synthesis carried out at different temperatures. The x-ray diffraction pattern of graphitic carbon nitride is generally characterised by two main reflections.^{54, 72} The main one at $2\theta = 27.4^\circ$, (002) plane, corresponds to a *d*-spacing of 0.326 nm assigned to the distance between the layers of the graphitic material.^{54, 72} The weaker peak at $2\theta = 13.0^\circ$, (100) plane, (*d* = 0.680 nm) is usually associated to the intra-layer *d*-spacing.^{54, 72} For the material synthesised at 450 °C, although it has features that can be attributed to g-C₃N₄, the presence of other multiple peaks strongly indicates the coexistence of other species. Upon heating at 475 °C, the intensity of these extra peaks significantly decreases, they are absent in the XRD patterns up to 600 °C and start reappearing at 650 °C. With increasing temperature up to 600 °C, the (002) and (100) reflections of g-C₃N₄ appear more or less well defined. The (002) reflection is present in all the samples even though there is a progressive shift to higher values of 2θ (Table 3.1) which is also accompanied

by a narrowing of the peak; the FWHM decreases from a value of 1.59 (C_3N_4 -475) to a value of 0.69 (C_3N_4 -650) (Table 3.1). After applying the Scherrer equation on this peak, the crystallite size is found to increase from 6 nm to 15 nm, suggesting a longer range order in the samples synthesised at high temperature. The (100) reflection at 13.0° , on the other hand, seems to become weaker and broader with the increase of the temperature (Figure 3.3). These behaviours suggest an increase in long range order along the (002) plane which could relate to a better organisation of the graphitic layers, and a decrease along the (100) associated to the intra-layer d-spacing.

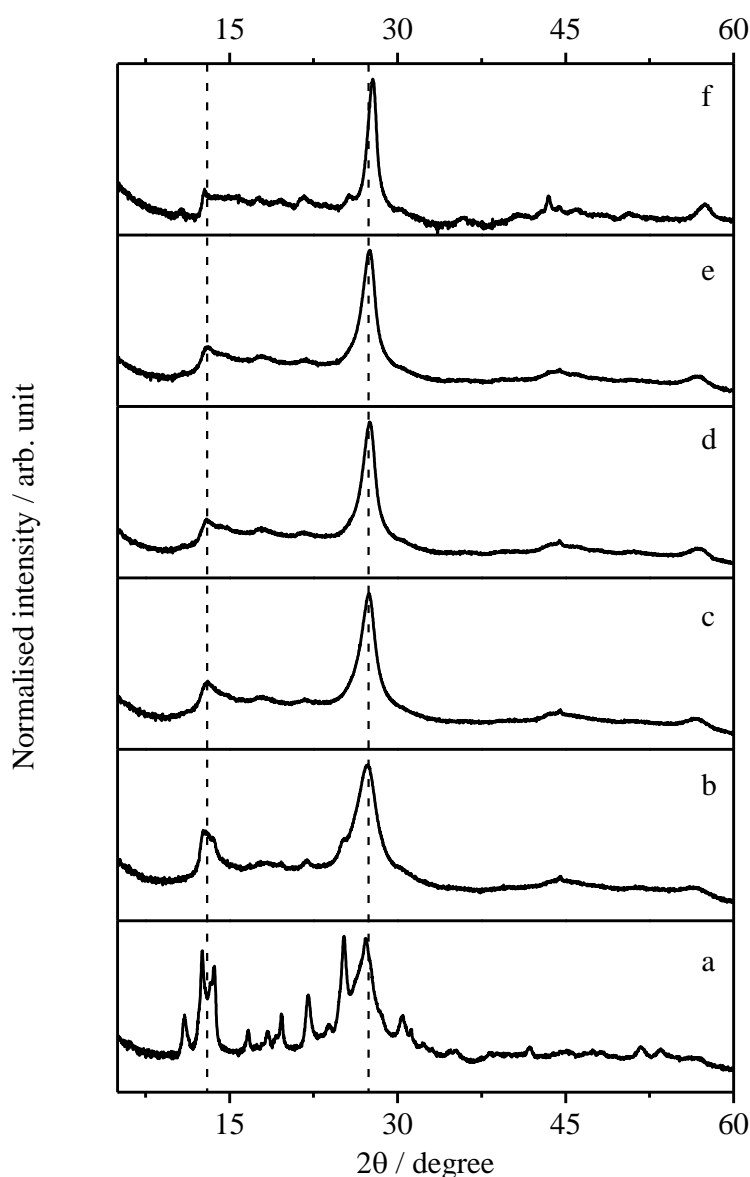


Figure 3.3 Effect of temperature on crystal structure. XRD patterns of the products of reaction carried out at different temperatures: a) 450 °C, b) 475 °C, c) 500 °C, d) 550 °C, e) 600 °C and f) 650 °C.

In 2003 Jürgens *et al.* carried out an extensive investigation on Melem,⁶⁹ organic molecule characterised by a heptazine structure (Figure 1.15d); synthesised at 450 °C. They proposed a refined crystal structure⁶⁹ which is used here to try to understand more about C₃N₄-450 and the synthesis path to g-C₃N₄.

Figure 3.4 shows the comparison between the XRD pattern for C₃N₄-450 and the pattern generated from the crystallographic information provided by Jürgens *et al.*⁶⁹ Most of the reflections of Melem seem to be present in the XRD pattern of C₃N₄-450, however, additional peaks in the C₃N₄-450 can be identified. The preparation method used by Jürgens *et al.* to synthesise the material is different from the one in this study.⁶⁹ Even though, the synthesis was carried out at the same temperature, they used a sealed ampule which allows the formation of an internal pressure that could favour the formation of a more crystalline phase. Furthermore the material was allowed to condense for a shorter amount of time (5 h vs. 15 h). It is reasonable to assume that with a longer condensation period and hence the formation of bigger fragments, C₃N₄-450 is not best represented by the heptazine structure alone.

Elemental analysis (CHN) of C₃N₄-450 (Table 3.1) shows a lower content of hydrogen (2.1 ± 0.1 wt.%) compared to the calculated value for Melem (2.8 wt.%) or the one measured by Jürgens *et al.* (2.98 wt.%)⁶⁹. In addition, the measured C:N ratio for C₃N₄-450 is 0.64 (Table 3.1). If the theoretical C:N ratio for a fully polymerised g-C₃N₄

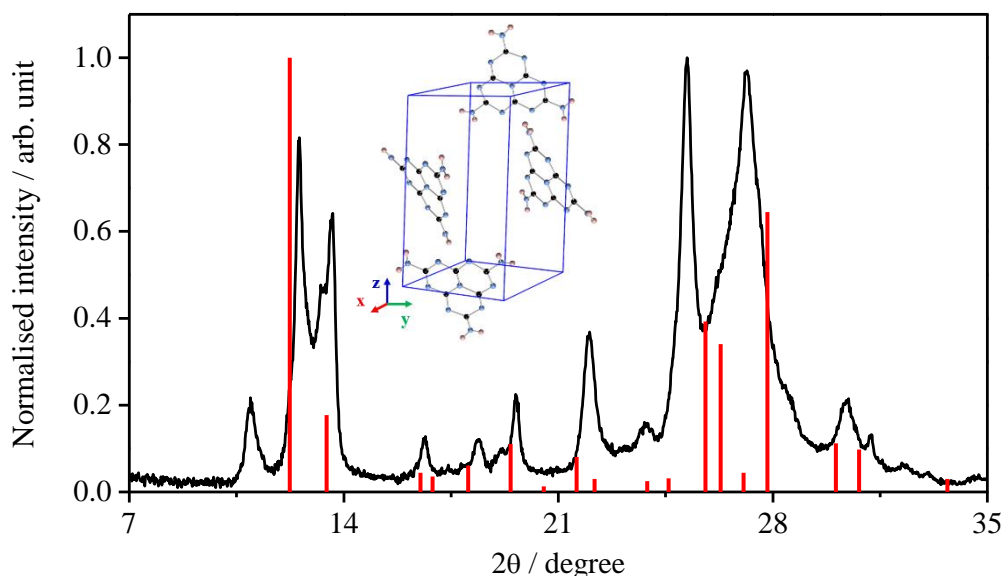


Figure 3.4 XRD pattern of Melem and C₃N₄-450. Comparison of calculated XRD pattern on Melem (red) and measured pattern of C₃N₄-450 (black). Inset: unit cell representation of Melem, generated from the crystallographic information file provided with ref. 69. Space group: P2₁/c; Unit cell: monoclinic, $a = 7.3992$ Å, $b = 8.6528$ Å, $c = 13.3816$ Å, $\beta = 99.912$ °.

(0.75)⁵⁷ and for Melem (0.60) are considered as indication of the maximum and minimum “degree of polymerisation” respectively, it can be stated that the product obtained after calcination at 450 °C is N-rich compared to g-C₃N₄ and therefore characterised by an intermediate “degree of polymerisation”. If Redemann & Lucas’ statement about the variable sizes (*i.e.* number of heptazine units in one molecule) of the polymeric fragments¹¹³ is considered, Figure 3.5 can give an approximated indication of the number of units per fragment by knowing the C:N ratio obtained through CHN analysis. The units polymerised as a linear chain (Figure 3.1a and curve a in Figure 3.5) and the units with the highest level of condensation, as it would be in the ideal g-C₃N₄, (Figure 3.1c and curve b in Figure 3.5), give the lowest and the highest possible C:N ratio, respectively. In between these two values there are many possible ratios due to the different structural combinations of the units in the fragments. In the case of C₃N₄-450 from its C:N ratio of 0.64, it can be assumed that the structure is made of fragments with 2 to 3 heptazine units. While other combinations are possible due to the random nature of the polymerisation process, the CHN analysis agrees with the previous observation made with XRD that C₃N₄-450 has a structure with more than one heptazine unit.

In 2007, using electron diffraction, Lotsch *et al.*⁶⁰ proposed a crystal structure for Melon with chains of heptazine units aligned next to each other. The calculated pattern from this

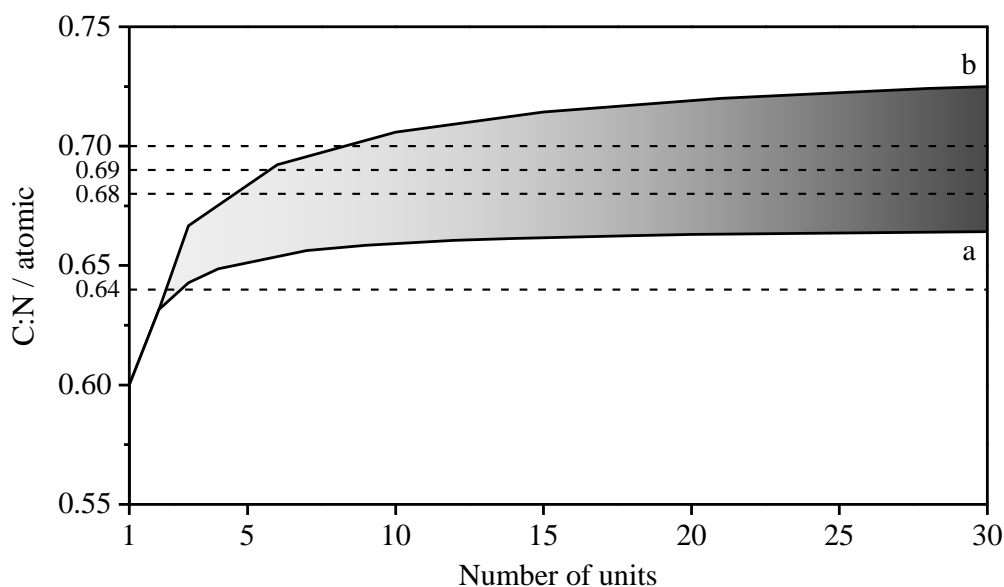


Figure 3.5 C:N atomic ratio vs. number of units per polymeric fragment. Representation of the relationship between C:N ratio and number of heptazine units forming a polymeric fragment. Lines a) and b) represents the minimum and maximum C:N ratio for a fixed number of units. Dashed lines: C:N ratio of the samples (Table 3.1).

structure is compared to that of C₃N₄-450 in Figure 3.6. The atomic coordinates can be found in the PhD Thesis of Bettina Lotsch from which the paper is extracted.¹²⁶ Since Lotsch's study was mainly carried out for a two dimensional structure, the cell parameter *c* is here chosen to match the (002) reflection of the material and an A-A stacking configuration is assumed. The space group used is P2₁2₁2 as suggested in Lotsch's PhD Thesis¹²⁶ and the hydrogen atoms are added. In Figure 3.6 some similarities can be noticed between the two patterns; for example the appearance of a peak at ~ 10 ° which is attributed to the (200) reflection and was not observed in the theoretical pattern of Melem (Figure 3.4). On the other hand, with several peaks still unaccounted for in the measured pattern, it is not possible to identify with certainty the presence of Melon, as intended by Lotsch *et al.*, in C₃N₄-450. This could, nonetheless, be present as a minor phase and with a slightly distorted crystal structure.

It is reasonable to conclude at this stage that C₃N₄-450 is most likely a mixture of phases: possibly Melem combined with bigger polymeric fragments of a structure similar to that of Melon. Even though the structure of C₃N₄-450 has not been solved and may require further investigation, the pathway to the formation of g-C₃N₄ is clearer.

Following the same approach employed for C₃N₄-450, the size of the polymeric fragments for the other graphitic carbon nitride samples can be estimated from the

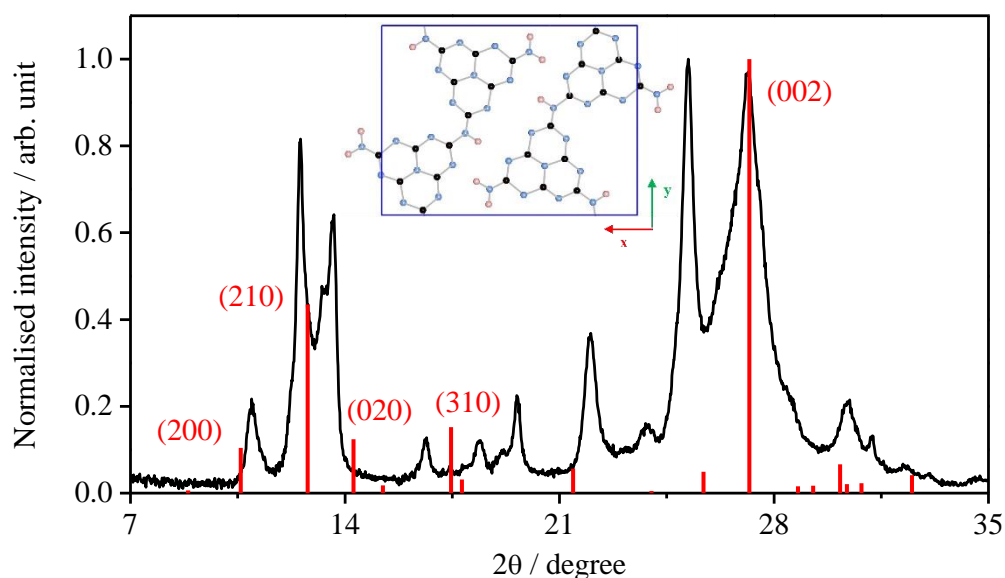


Figure 3.6 Comparison of C₃N₄-450 and Melon. Comparison of calculated XRD pattern of Melon (red) and measured pattern of C₃N₄-450 (black). Inset: unit cell representation of Melon, generated from the information provided by Lotsch²³ and Lotsch *et al.*¹⁵. Space group: P2₁2₁2. Cell parameters: *a* = 16.7 Å, *b* = 12.4 Å, *c* = 6.55 Å, $\alpha = \beta = \gamma = 90^\circ$.^{60, 126}

elemental analysis and Figure 3.5. The CHN analysis of the materials shows a progressive decrease in the nitrogen content for sample synthesised at higher temperatures with a corresponding decrease in hydrogen content (Table 3.1). As a consequence the C:N ratio increases from 0.64 for C_3N_4 -450 to 0.70 for C_3N_4 -650, getting closer to the ideal value for g- C_3N_4 (0.75). From Figure 3.5 it is possible to say that samples C_3N_4 -475 and C_3N_4 -500 (C:N = 0.68) have fragments with at least 5 heptazine units. The increase of the temperature to 500 °C and 550 °C brings to the condensation of about 6-7 units and above 600 °C fragments containing at least 9 units can be assumed. As mentioned earlier, this approach is only a quantitative approximation to provide an easier visualisation of the meaning behind the C:N ratio.

Thermal gravimetric analysis was carried out on all the synthesised materials and the results are presented in Figure 3.7. The decomposition temperature of the nitrides shifts toward higher values for the samples prepared at higher condensation temperatures meaning that the more condensed is the graphitic carbon nitride material the more thermally stable is the compound. The TGA shows that the materials start becoming unstable at 550 °C with the decomposition of tri-s-triazine units. Heating to 700 °C results in the complete disappearance of the materials.

If graphitic carbon nitride is intended to be used for photocatalytic applications, as for the reasons explained in Chapter 1, particular attention should be focused on the band gap

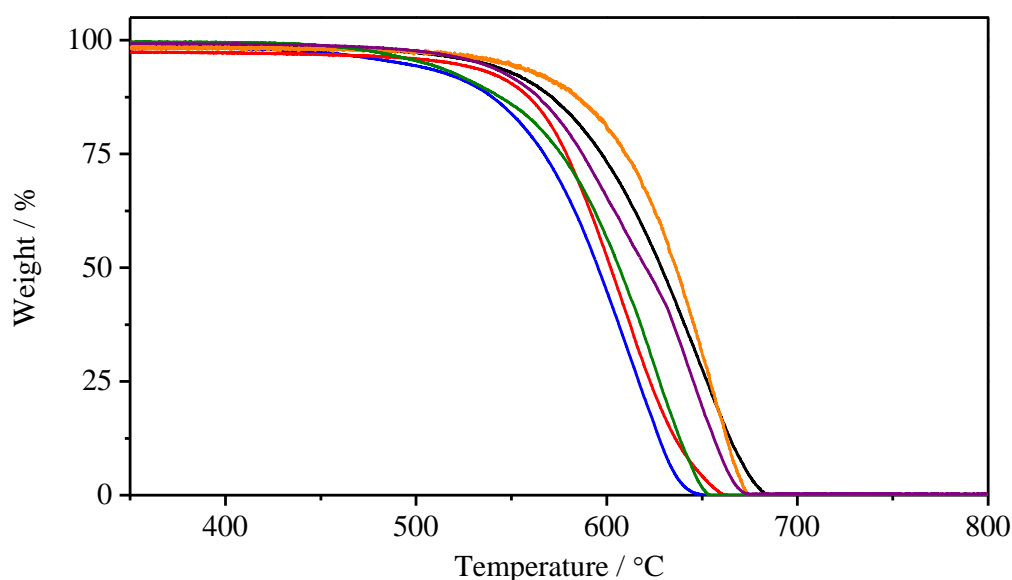


Figure 3.7 Thermal Gravimetric Analysis of different g- C_3N_4 . TG analysis showing the weight loss during heating of C_3N_4 - 450 (green), 475 (purple), 500 (blue), 550 (red), 600 (black) and 650 (orange). Heating step: 5 °C/min; atmosphere: air.

(energy difference between VB and CB, see Section 1.3) of these materials. The UV-Vis spectra of the C_3N_4 synthesised at different temperatures (Figure 3.8) show a shift towards longer wavelengths (visible light) with increasing temperature up to 600 °C, hence a decrease in the values of the band gap (Table 3.1). This change in the band gap can be linked to the degree of polymerisation and C:N ratio. The synthesis at elevated temperature increases the number of tri-s-triazine units taking part in the network and therefore the C:N ratio. Since the presence of sp^2 C-N bonds effects the energy gap, the higher the C:N ratio the larger the size of the sp^2 C-N clusters and the smaller the band gap.¹²⁷⁻¹²⁹ For C_3N_4 -650 the absorption shifts back towards the UV range and a band gap of 3.06 eV. Despite the fact this material has the same C:N ratio as C_3N_4 -600, it is reasonable to assume that the fragmentation in the sp^2 C-N clusters, confirmed by XRD analysis (Figure 3.3f), is responsible for this increase in the Band Gap as this sample as well as polymerising also decomposes at this temperature.

These results suggest that the increase of the condensation temperature favours the formation of bigger molecules. By heating melamine, Melem is initially formed and then polymerised into bigger oligomers (Melon-like) by losing ammonia. The bigger the fragments the more thermally stable they are as shown by TG analysis (Figure 3.7). This is in agreement with what has so far been suggested in the literature regarding the synthesis path starting from organic monomers to polymeric g- C_3N_4 (Figure 1.15).^{54, 57} The increase in size also brings to an increased order in the stacking of the layers which

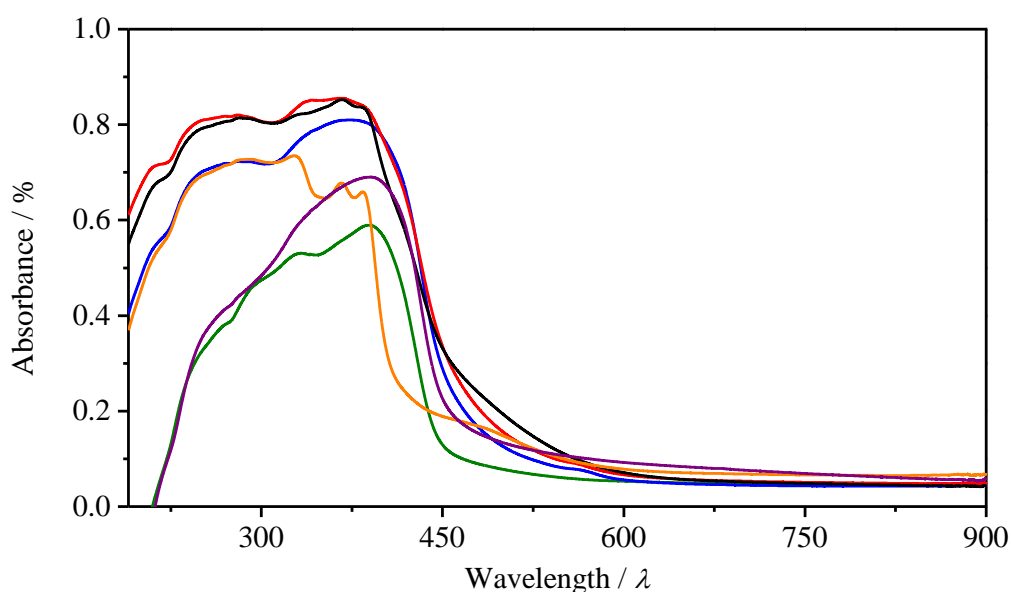


Figure 3.8 UV-Vis absorption spectra. UV-Vis spectra of C_3N_4 - 450 (green), 475 (purple), 500 (blue), 550 (red), 600 (black) and 650 (orange).

Table 3.1 Miscellaneous information about g-C₃N₄ synthesised at different temperatures.

Band gap values, XRD peaks parameters and CHN of g-C₃N₄ obtained after calcination for 15 h at various temperatures.

Temperature (°C)	Band Gap (eV)		(002) position (d/nm)	(002) FWHM (°)	Crystallite size (nm)	C (wt.%) ±0.2	N (wt.%) ±0.9	H (wt.%) ±0.1	C _x N _y H _z (C/N)
450	2.82		27.2° (0.327)	n.a.	n.a.	33.5	60.8	2.1	C _{2.79} N _{4.34} H _{2.15} (0.64)
475	2.77		27.3° (0.326)	1.59	6	34.9	60.0	1.6	C _{2.91} N _{4.29} H _{1.55} (0.68)
500	2.76		27.4° (0.325)	1.17	8	34.6	59.2	1.5	C _{2.88} N _{4.23} H _{1.51} (0.68)
550	2.73		27.5° (0.324)	1.01	10	34.8	58.5	1.4	C _{2.90} N _{4.18} H _{1.40} (0.69)
600	2.70		27.5° (0.324)	1.03	9	34.9	58.1	1.1	C _{2.91} N _{4.15} H _{1.13} (0.70)
650	3.06		27.8° (0.320)	0.69	15	35.4	58.7	0.8	C _{2.95} N _{4.19} H _{0.82} (0.70)

become more densely packed (d_{002} from 0.327 nm for C₃N₄-450 to 0.320 nm for C₃N₄-650, Table 3.1). The reappearance, in the material prepared at 650 °C, of the reflections characteristic of the smaller fragments (C₃N₄-450) indicates that at this temperature the polymeric structure start braking into smaller oligomers. From TG analysis, indeed, at this temperature, most of the samples are completely decomposed (Figure 3.4). Therefore the optimum temperature range to obtain g-C₃N₄ is 500-600 °C.

3.2.2. Effect of temperature on the morphology

In the previous section it was found that g-C₃N₄ is obtained at temperatures going from 500 °C to 600 °C. The effect that the temperature have on the morphology of the material was also investigated. From TG analysis it was seen that a synthesis temperature of 600 °C is close to the temperature of full decomposition of the material (Figure 3.7). This is reflected in the mass loss during the synthesis (Table 3.2) which increases from 50 wt.% for C₃N₄-500 up to 70 wt.% for C₃N₄-600.

Table 3.2 Surface area and particle size of different g-C₃N₄. Effect of reaction temperature on mass loss, surface area and particle size.

Temperature (°C)	Mass Loss (wt.%)	Surface Area (m ² ·g ⁻¹) ± 1	Particle size (µm) ± 2
500	50	8	30
550	55	14	33
600	70	32	35

This mass loss during the synthesis is accompanied by a significant increase in the surface area of graphitic carbon nitride materials. This is higher of a factor four for the material prepared at 600 °C (32 ± 1 m²·g⁻¹) compared to that at 500 °C (8 ± 1 m²·g⁻¹, Table 3.2). This could be associated with a decrease in particle size, which is however not the case since the average particle size remain very similar within experimental error. Scanning electron microscopy images of the samples are illustrated in Figure 3.9. After synthesis at 500 °C the surface of the particles is mainly smooth with minor areas where a more porous and rough surface is exposed. With the increase of the reaction temperature the outer surface is removed, almost peeled off, and reveals an inner part characterised by a rougher surface, especially in the sample synthesised at 600 °C. This change in the surface

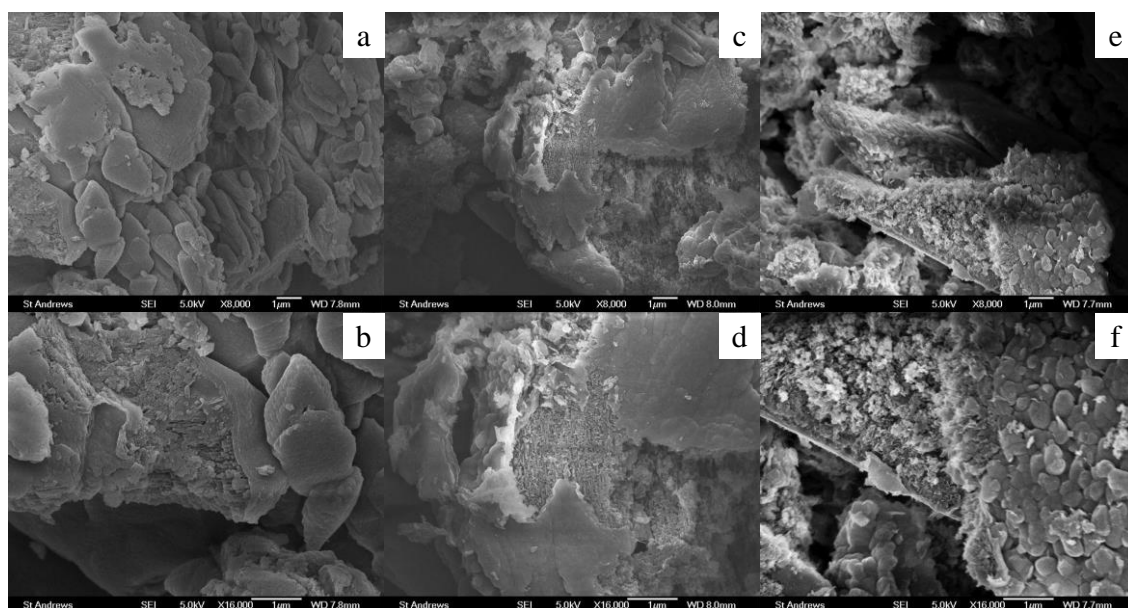


Figure 3.9 SEM images of $g\text{-C}_3\text{N}_4$ synthesised at different temperatures. SEM images at different magnifications (scale bar = $1\mu\text{m}$) of the surface of C_3N_4 - a-b) -500, c-d) -550 and e-f) -600.

texture is responsible for the increased surface area of graphitic carbon nitride and it is produced as a consequence of its thermal decomposition.

3.2.3. Effect of condensation length on the structure and morphology

From the results obtained so far emerged that the minimum temperature required to obtain $g\text{-C}_3\text{N}_4$ is $500\text{ }^\circ\text{C}$. Further increase in temperature brings to a better organisation of the polymeric layers in the structure, until temperatures above $600\text{ }^\circ\text{C}$ cause the decomposition of the material. The previous $g\text{-C}_3\text{N}_4$ XRD patterns presented in Figure 3.3 are for materials synthesised for 15 h. To evaluate the effect of the reaction length, samples synthesised for 2.5, 5, 10 h are also investigated. The XRD patterns of these graphitic carbon nitrides are shown in Figure 3.10. For the samples synthesised at $550\text{ }^\circ\text{C}$ and $600\text{ }^\circ\text{C}$ no changes are observed in the XRD patterns indicating the morphology of $g\text{-C}_3\text{N}_4$ is independent of the synthesis time in this temperature range.

On the other hand, the XRD pattern of graphitic carbon nitride synthesised at $500\text{ }^\circ\text{C}$ for 2.5 h (Figure 3.11a) shows, in addition to the graphitic phase identified by the (100) and (002) peaks, also other multiples reflections. As previously discussed, the presence of those peaks suggests that small carbon nitride fragments, slightly bigger derivative of Melem, are present. The intensity of these reflections are only slightly less intense than

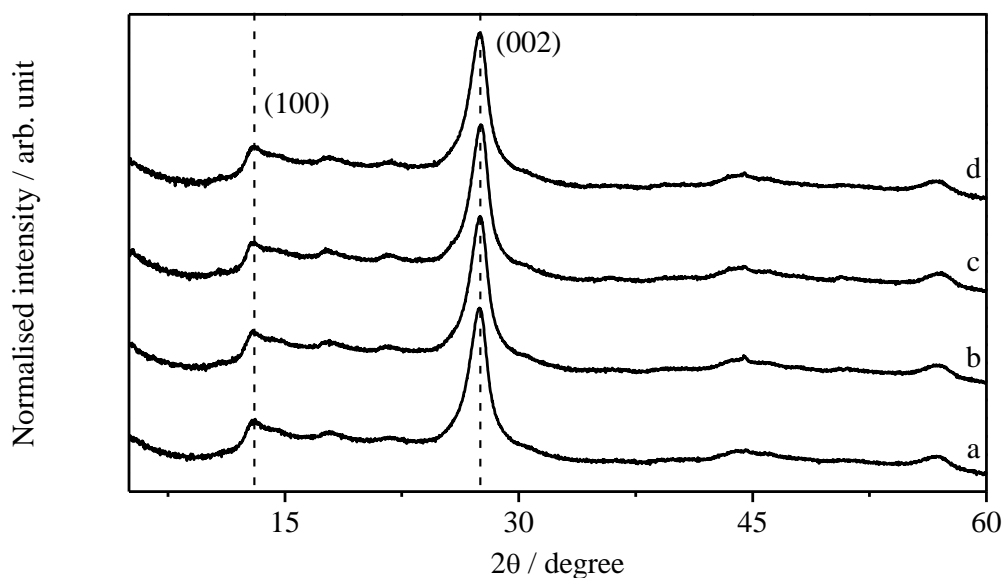


Figure 3.10 Effect of condensation length on the XRD pattern of C₃N₄-550 and -600. XRD patterns of C₃N₄-550 synthesised for a) 2.5 h and b) 15 h; and C₃N₄-600 synthesised for c) 2.5 h and d) 15 h.

the ones seen for C₃N₄-450 (Figure 3.3a), but significantly higher than in the case of C₃N₄-475 (Figure 3.3b). This clearly indicates that despite the higher synthesis temperature a low degree of condensation is obtained for sample C₃N₄-500-2.5 h. Increasing the synthesis time from 2.5 h does result in the disappearance of the multiple reflections, hence providing a material with a higher degree of polymerisation.

The increase of reaction time does not have any effect on the position of the (002) reflection but slightly increases its peak half width (Table 3.2). The change is very small but suggests an increase in the disorder of the structure with synthesis time. This can be explained with the progressive condensation of the remaining smaller fragments, forming more layers which are not yet organised in an ordered stacking. Only the synthesis temperature and not its duration favours a better organisation along the (002) direction as seen with the narrower FWHM for both C₃N₄-550 and C₃N₄-600 in Table 3.1. However this decrease in the FWHM from 1.2 ° for the C₃N₄-500 to 1.0 ° for C₃N₄-550 and C₃N₄-600 can be considered only as a minimal improvement.

An increase in the synthesis time leads to a decrease in the band gap, Table 3.3. The C₃N₄-500 synthesised for 2.5 h has a band gap of 2.80 eV. This is found in between the value for C₃N₄-450 (2.82 eV) and C₃N₄-475 (2.77 eV), Table 3.1; confirming the intermediate degree of polymerisation. Above 5 h of treatment, the physical properties of

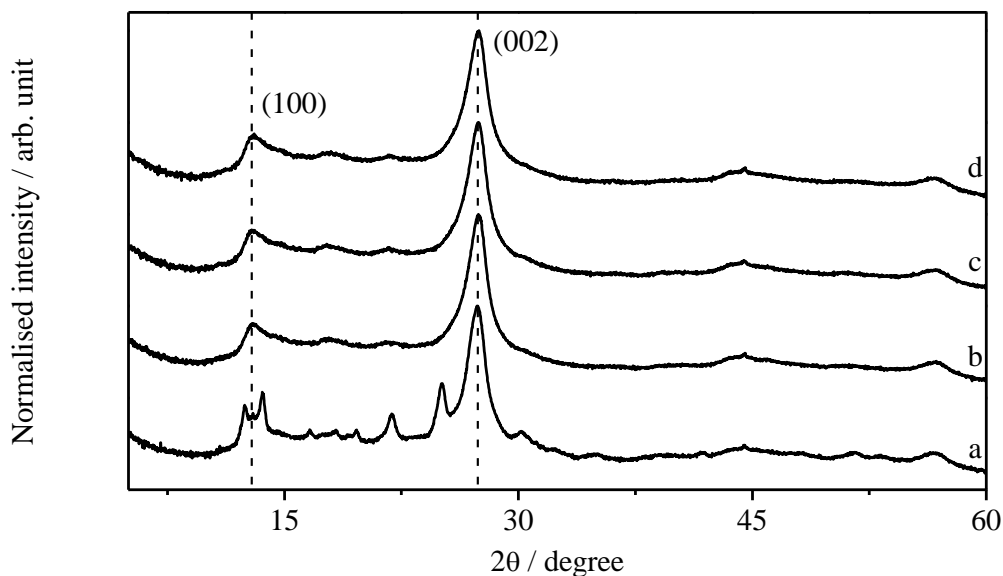


Figure 3.11 Effect of condensation length on the XRD pattern of C_3N_4 -500. XRD patterns of C_3N_4 -500 synthesised for different time length: a) 2.5 h, b) 5 h, c) 10 h, d) 15 h.

the samples remain the same, there is no significant change in the chemical composition, the morphology of graphitic carbon nitride is not altered by the longer thermal treatment, and the measured values of the surface areas for C_3N_4 -500 synthesised at 2.5 h, 5 h and 10 h are $7.8 \text{ m}^2 \cdot \text{g}^{-1}$, $9.1 \text{ m}^2 \cdot \text{g}^{-1}$ and $9.1 \text{ m}^2 \cdot \text{g}^{-1}$, respectively. These values are, within error, the same as for the C_3N_4 -500 synthesised for 15 h (Table 3.2).

In summary, it is found that at low temperature the duration of the synthesis plays an important role in favouring the polymerisation of $g\text{-}C_3N_4$. The minimum synthesis time at $500 \text{ }^\circ\text{C}$ is 5 h and longer syntheses do not improve or deteriorate the produced material. Although marginal, syntheses at $550 \text{ }^\circ\text{C}$ and $600 \text{ }^\circ\text{C}$ lead to an improvement of the ordering of the graphitic layers with the formation of larger sp^2 C-N clusters and a decrease in the Band Gap. On the other hand these syntheses at elevated temperature also result in an increase in the surface area of the material and a significant drop in yield of the reactions.

Table 3.3 Miscellaneous information about C₃N₄-500 synthesised for different time lengths. XRD peaks parameters, band gap values and CHN of g-C₃N₄ obtained after calcination at 500 °C for various time lengths.

Time (h)	(002) 2θ	(002) FWHM (°)	Band Gap (eV)	C (wt.%) ±0.2	N (wt.%) ±0.9	H (wt.%) ±0.1	C _x N _y H _z (C/N)
2.5	27.4°	1.0	2.80	34.5	59.9	1.7	C _{2.88} N _{4.28} H _{1.67} (0.67)
5	27.4°	1.1	2.76	34.7	58.9	1.2	C _{2.89} N _{4.21} H _{1.23} (0.69)
10	27.4°	1.1	2.76	34.9	59.2	1.5	C _{2.91} N _{4.23} H _{1.51} (0.69)
15	27.4	1.2	2.76	34.6	59.2	1.5	C _{2.88} N _{4.22} H _{1.51} (0.68)

3.3. Further characterisation

3.3.1. Solid State NMR

Solid state NMR was carried out on C₃N₄-500, -550 and -600 and the spectra are illustrated in Figure 3.12. Due to the long relaxation time of ¹⁵N and ¹³C nuclei a cross-polarisation (CP) experiment was carried out. In this kind of sequence, the protons in the molecule are magnetised with a pulse and the magnetisation is then transferred to the less abundant nucleus. Therefore the signal obtained is strictly related to the presence of protons in the surrounding of nitrogen and carbon atoms and it is not quantitative. Both nitrogen (Figure 3.12-I) and carbon (Figure 3.12-II) spectra are in agreement with those reported by Lotsch *et al.*⁶⁰ In their work however they employed ¹⁵N labelled precursors to synthesised Melon. This increases the concentration of isotope in the material and therefore allows for higher resolution and/or shorter scanning time. The areas from δ = -170 ppm to δ = -200 ppm correspond to the bridging nitrogen atoms between heptazine (N₇) units and those in the aromatic ring.^{60, 126} The small peak at noise level at δ = -225 ppm is assigned to the tertiary nitrogen atoms in the centre of the heptazine unit. The remaining two features at δ = -245 ppm and δ = -265 ppm are produced by the amino

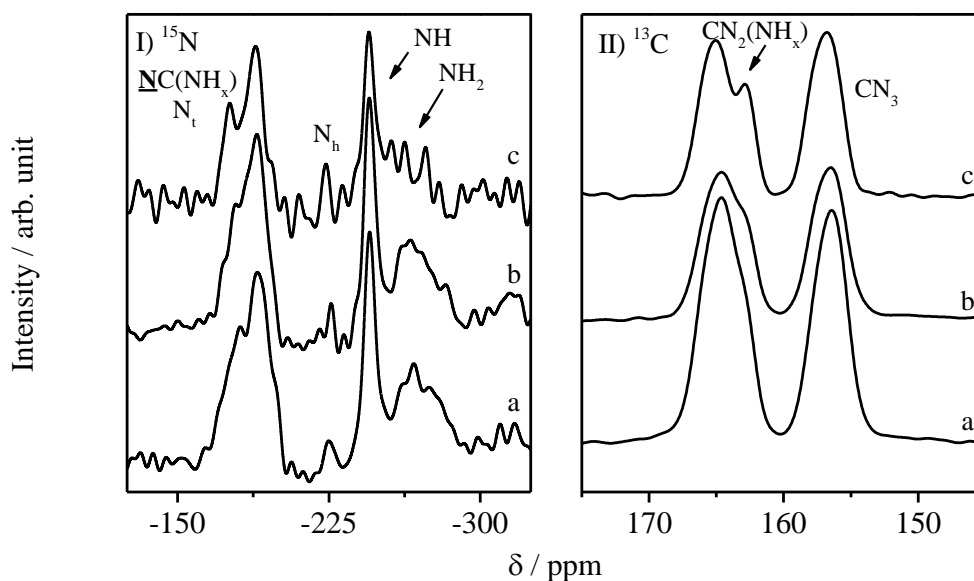


Figure 3.12 Solid state NMR spectra of different C_3N_4 . ^{15}N (I) and ^{13}C (II) solid state NMR spectra for C_3N_4 - a) 500, b) 550 and c) 600.

groups $-NH-$ and $-NH_2$ respectively.^{60, 126} As mentioned, a CP experiment is not quantitative, therefore, is not possible to extract information on the relative amounts. However, the qualitative comparison of the spectra of graphitic carbon nitride synthesised at different temperatures can provide useful information. Despite the difference in the signal-to-noise ratio, after normalisation of the ^{15}N NMR spectra no difference in the relative profiles is noticed.

An easier comparison can be carried out on the ^{13}C spectra (Figure 3.12-II) which are obtained with a higher resolution. Three main peaks can be seen at $\delta = 165$ ppm, $\delta = 163$ ppm (a shoulder in the main peak) and $\delta = 156$ ppm which are assigned by Lotsch *et al.* to $-C-(NH_2)$, $-C-(NH-)$ and CN_3 , respectively.^{60, 126} After Gaussian fitting it is found that the area ratio between the peaks at 163 ppm and 165 ppm (A_{165}/A_{163}) increases with the reaction temperature; with values of 0.15, 0.23 and 0.34 for C_3N_4 -500, -550 and -600, respectively. Even though it cannot be considered quantitative, qualitatively this indicates that the number of terminal secondary amino groups increases as a consequence of further polymerisation at the expenses of the terminal $-NH_2$ groups. This is in agreement with what was concluded in the previous section.

3.4. Structure investigation I: XRD

In the following sections the attention focuses on understanding the structure of g-C₃N₄ obtained from the pyrolysis of melamine. Among the g-C₃N₄ synthesised for this study C₃N₄-500, -550 and -600 present the classical XRD pattern of materials defined as g-C₃N₄.^{54, 57} Since the three carbon nitrides show very similar patterns only the one of C₃N₄-500 will be used as reference. Due to the disordered nature of the material which results in broad peaks, the low number of reflections, and the molecular constrain that the nature of the structure presents, it is not possible to carry out a proper structural refinement. Therefore, theoretical patterns of the proposed structures are generated and these are compared with those acquired experimentally.

3.4.1. Comparison with fully polymerised g-C₃N₄

In 1996 Teter & Hemley¹¹⁶ proposed crystal structures for different allotropes of carbon nitride (C₃N₄) and among them they included the graphitic form.¹¹⁶ The proposed structure is based on triazine repeating units forming layers with a 3D A-B stacking organisation. This structure is characterised by a hexagonal unit cell ($a = b = 4.7420 \text{ \AA}$, $c = 6.7205 \text{ \AA}$, $\alpha = \beta = 90^\circ$, $\gamma = 120^\circ$) with space group $P\bar{6}m2$. In Figure 3.13 the theoretical pattern of Teter & Hemley structure (red lines) is compared with that of C₃N₄-500. The (002) reflection is shifted towards lower angles meaning a larger d-spacing in between the layers; in addition the (100) reflection is significantly shifted compared to that of C₃N₄-500, corresponding to an intra-layer d-spacing of 0.411 nm against 0.680 nm for C₃N₄-500. The poor fit between the Teter & Hemley structure and the measured pattern of C₃N₄-500 indicates that in this case the g-C₃N₄ cannot be represented with a simple triazine based model.

This same conclusion has recently been confirmed by Tyborski *et al.* who in 2013 published an investigation similar to the one subject of this study.¹²³ In their work Tyborski *et al.* attempted the study of the structure of a polymeric carbon nitride (PCN) synthesised by double thermal treatment of dicyandiamide.¹²³ To achieve their goal they followed the same approach as in this study by first starting a comparison of the PCN structure with the one proposed by Teter & Hemley.¹¹⁶ Even though Tyborski *et al.* showed a different set of Miller indices without, however, specifying the space group employed for the simulation, their theoretical pattern matches the one reported by

Teter & Hemley, Figure 3.13 (red lines)¹¹⁶, but not their experimental pattern. Tyborski *et al.* also compared their measured pattern with the structure proposed in 2008 by Bojdys *et al.*,¹³⁰ the most probable 2D structure for g-C₃N₄ composed of heptazine units.^{60, 122, 130} However this direct comparison is surprising since in the Bojdys *et al.* case a completely different synthetic procedure (ionothermal synthesis as opposed to bulk solid state condensation) was applied and a very crystalline material was obtained. Tyborski *et al.* after comparison between the patterns concluded their synthesised PCN did not have either a full polymerised heptazine like structure.¹²³

In this work a theoretical crystal structure for heptazine-based g-C₃N₄ is created to replace the comparison with the structure proposed by Bojdys *et al.*. This is achieved by using the unit cell provided by Teter & Hemley as starting point. The unit cell parameters *a* and *b* need to be increased by a third to take into account the size of the heptazine-unit. In order to remove all the symmetry operators during the generation of the theoretical pattern, the space group is changed to P1. The coordinates of all the atoms in the unit cell need therefore to be specified. The space group P1 is only intended as a processing tool and not as the final space group of the modelled structure. The same approach is employed

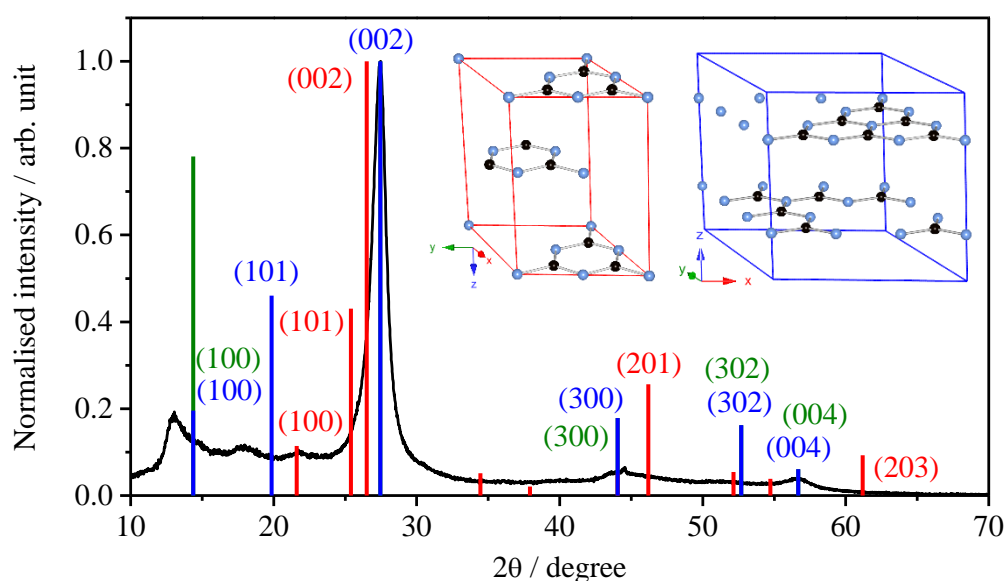


Figure 3.13 XRD: comparison of C₃N₄-500 with triazine and heptazine g-C₃N₄. Comparison of C₃N₄-500 measured pattern (black line) with the theoretical patterns of triazine (red; ref. 116 and PDF#: 83265-ICSD, $a = b = 4.7420 \text{ \AA}$, $c = 6.7205 \text{ \AA}$, $\alpha = \beta = 90^\circ$, $\gamma = 120^\circ$, space group: $\bar{P}6m2$) and heptazine (A-B stacking: blue and A-A stacking: green; space group: P1; hexagonal geometry unit cell parameters: $a = b = 7.113 \text{ \AA}$, $c = 6.490 \text{ \AA}$, $\alpha = \beta = 90^\circ$, $\gamma = 120^\circ$) based g-C₃N₄. Inset: representation of triazine (left, red) and heptazine (right, blue) g-C₃N₄ unit cells.

for all the models of this section (unless specified). An A-B stacking was chosen, not only for comparison reasons, but also because due to the π -cloud of electrons it is more likely that the layers will be organised in order to minimise the repulsion between them.⁶⁰ This is translated into layers where heptazine units are aligned with the holes of the next layers. The unit cell parameter c was once again chosen to match the (002) peak ($d_{002} = 0.325$ nm, $a = b = 7.113$ Å, $c = 6.490$ Å, $\alpha = \beta = 90^\circ$, $\gamma = 120^\circ$, for crystallographic information see Appendix A, Table A.4). The theoretical pattern is compared with the others in Figure 3.13 (blue lines). Having both cells hexagonal geometry the indexes of the reflections are the same for both of them.

The same reflections seen for the triazine-based structure are present but with a shift towards lower angles; however, the (100) reflection is still up-shifted ($2\theta = 14.38^\circ$, 0.615 nm). On the other hand its relative intensities matches that of the measured peak, $I_{100}/I_{002} = 0.19$. Yet the presence of a strong (101) reflection at $2\theta = 19.86^\circ$ does not make this structure configuration probable. It is worth mentioning that when an A-A stacking motif (green in Figure 3.13) is considered the (101) reflection is absent and most of the other peaks retain their positions. Differently, the intensity of the (100) is found to be 0.70 which is too intense to agree with the experimental pattern. Interestingly the reflections corresponding to the (300) and (004) planes provide a possible explanation for the two broad peaks at $\sim 44.0^\circ$ and $\sim 56.5^\circ$. The plane (004) which corresponds to a d-spacing of 0.162 nm and half of the inter-layer d-spacing (0.325 nm, (002) plane) is found in good agreement with measured pattern. There is however a discrepancy between the $d_{100} = 0.680$ nm and $d_{300} = 0.205$ nm where the 3:1 ratio is not verified. Furthermore the lack of the (302) reflection in the C₃N₄-500 pattern has yet to be explained.

3.4.2. Comparison with partially polymerised g-C₃N₄

During the synthesis process it is reasonable to assume that g-C₃N₄ can be polymerised in many other configurations. In 2009 Döblinger *et al.*¹²² investigated an intermediate structure between Melon and the fully polymerised g-C₃N₄. In order to introduce protons in the unit cell some of the heptazine units were removed. In this case the planar symmetry of the carbon nitride layer is hexagonal with $\gamma = 120^\circ$. The unit cell parameters and the fractional coordinates are provided in their work, together with the suggested general space group P1. In this thesis the cell parameter c is fixed to 6.49 Å. The XRD theoretical pattern of the structure by Döblinger *et al.*¹²² is compared with C₃N₄-500 in Figure 3.14. Even though the 3D structure is described by Döblinger *et al.* with an A-A stacking, the

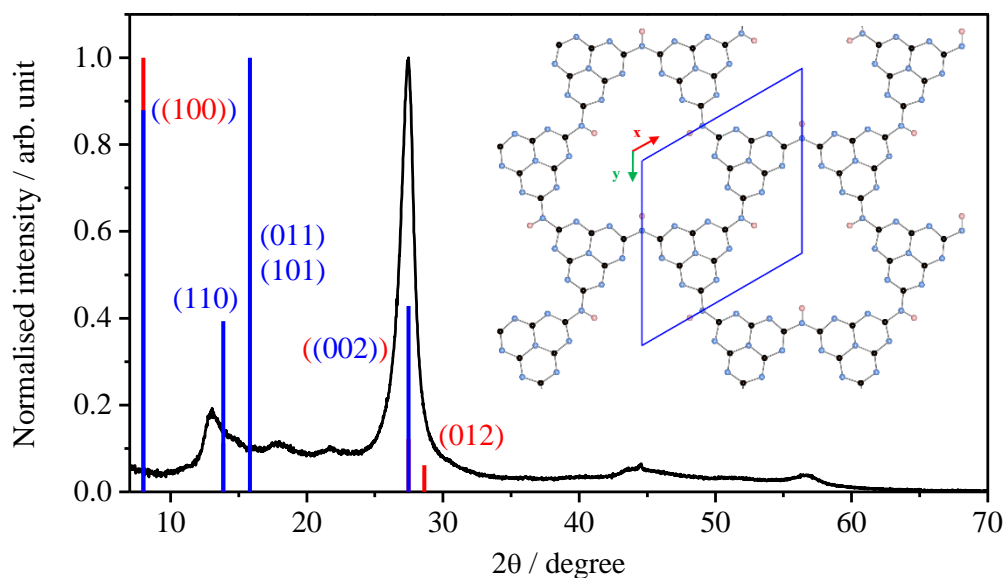


Figure 3.14 Theoretical pattern generated for Döblinger structure.¹²² Theoretical pattern for an alternative structure in stacking configuration A-A¹²² (red) and A-B (blue). Unit cell parameters: $a = b = 12.77 \text{ \AA}$, $c = 6.49 \text{ \AA}$, $\alpha = \beta = 90^\circ$ and $\gamma = 120^\circ$, space group P1 as suggested in ref. 122.

A-B version is also investigated in the work presented here. For both the A-A and A-B stacking the difference between the calculated and measured patterns is significant. The reflection indexed as the (100) is too intense and shifted towards lower angles. When an A-B type stacking is introduced, more reflections appear at angles lower than 20° and with intensities higher than the one of (002).

In addition to the fully and partially polymeric structures found in the literature, other systems can be proposed. In 2 dimensional space there are only few possible combinations theoretically available. On the other hand, in 3D many can be hypothesised. For this study only the simplest possibilities are considered; namely triazine- and heptazine-based graphitic carbon nitride from which, on the example of Döblinger *et al.*,¹²² some repeating units are removed to introduce protons. Both structures are analysed in A-A and A-B stacking configuration. The starting point to create these structures is the unit cell provided by Teter & Hemeley.¹¹⁶ The unit cell parameters a and b are multiplied by a factor two ($a = b = 9.484 \text{ \AA}$) for the triazine-based and a factor three ($a = b = 13.9246 \text{ \AA}$) for the heptazine-based framework. The hexagonal metric of the original cell is retained; the resulting cells are characterised by $\alpha = \beta = 90^\circ$ and $\gamma = 120^\circ$. The general space group P1 is used only to generate the theoretical pattern for all the

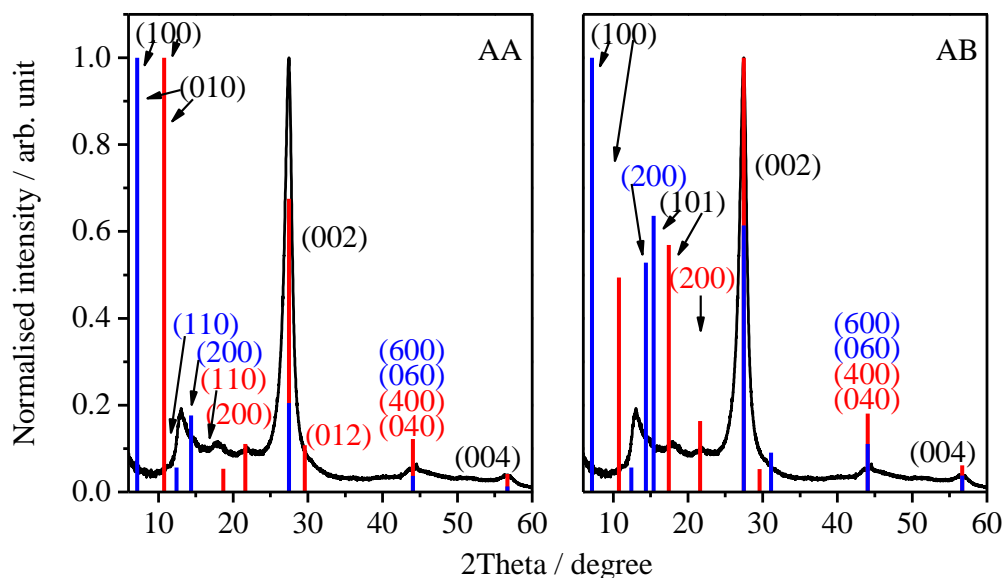


Figure 3.15 Triazine- and heptazine-based partially polymerised structures. Theoretical patterns generated for A-A and A-B stacking of triazine- (red) and heptazine-based (blue) structures. Unit cell parameters: $a = b = 9.484 \text{ \AA}$ (13.9246 \AA for heptazine), $c = 6.49 \text{ \AA}$, $\alpha = \beta = 90^\circ$ and $\gamma = 120^\circ$.

structures. The A-B stacking is generated by shifting one on the layers in order to align aromatic units (triazine or heptazine) of one layer with the holes of the next, in a similar way to the structures seen for the fully polymerised g-C₃N₄ (Figure 3.12). The theoretical XRD patterns for the two type of structures in A-A and A-B stacking configurations are compared to that of C₃N₄-500 in Figure 3.15. These structures have both hexagonal geometry, therefore the same indexing of the reflections is used in both cases.

Figure 3.15a illustrates the comparison between the A-A configuration of both structures, and in Figure 3.15b is the A-B stacking. All four structures present reflections at angles lower than 20° that are too intense compare to the (002), and in addition the (100) is shifted toward smaller angles indicating a d_{100} too big compared to the real material (1.230 nm vs. 0.680 nm). Therefore, unless these structures are present in very low amount in C₃N₄-500 it is not possible to consider them as the main phase in the material. At this point it is not possible to state that any of the investigated structures are found in good agreement with the measured pattern for C₃N₄-500. Although there are major discrepancies, the presence of the (101) reflection in the calculated pattern, makes the heptazine-based fully polymerised g-C₃N₄ (Figure 3.13) with an A-B stacking configuration the best match.

3.4.3. Comparison with Melon

In section 3.2 it was found that the different g-C₃N₄ synthesised for this investigation are not fully polymerised but most likely formed by oligomers of heptazine units. It is therefore reasonable to compare the XRD pattern of C₃N₄-500 with examples of smaller graphitic carbon nitride materials. For this purpose, the structure proposed for Melon (seen in Section 3.2 and Figure 3.6 inset) by Lotsch *et al.*⁶⁰ is initially used. The atomic fractional coordinates are provided in Lostch's PhD thesis, together with the unit cell parameters ($a = 16.7 \text{ \AA}$, $b = 12.4 \text{ \AA}$).¹²⁶ The suggested space group is P2₁2₁2 which corresponds to an orthorhombic unit cell. The unit cell parameter c is not provided by Lotsch *et al.* hence in this investigation it is chosen to match the reflection corresponding to the (002) plane at $2\theta = 27.40^\circ$: $c = 6.49 \text{ \AA}$ (Figure 3.16).

Tyborski *et al.*¹²³ also used the Melon structure proposed by Lotsch *et al.* in their investigation of polymeric carbon nitride (PCN). However, instead of using the atomic coordinates available in Lostch's thesis, the authors used the imaging software ImageJ to extract them from a picture in Lotsch *et al.* manuscript.¹²³ Tyborski *et al.* acknowledged this method could bring some error in the relative position of the atoms. Furthermore they also decided to use a space group with the lowest level of symmetry; P1 and not P2₁2₁2,^{123, 126} while retaining the angles of the suggested unit cell: $\alpha = \beta = \gamma = 90^\circ$.^{123, 126} The reason for the authors to decide on the space group P1 while having a cell with an orthorhombic geometry, may be similar to that explained earlier: using it only as a processing tool. Finally, in order to obtain a better match with the measured XRD pattern as seen in Figure 3.16, Tyborski *et al.* decreased the cell parameters a and b ($a = 16.2 \text{ \AA}$ and $b = 12.1 \text{ \AA}$) allowing to have the (210) reflection at $2\theta = 13.14^\circ$. The reduction of both cell parameters produces a “shrinking” effect on the structure itself and its bonds. The average C=N bond length in Lotsch's structure is 1.324 \AA which is in agreement with values reported in literature for similar systems.^{21, 131} After decreasing the size of the cell, the average bond length in Tyborski *et al.* case is found to be 1.280 \AA ; too short for an aromatic system. Even though Tyborski's idea of reducing the cell does produce an excellent match between the calculated and measured patterns, the position of the different atoms and correct bond lengths within the crystal structure has yet to be resolved. A different approach to the one employed by Tyborski *et al.* is applied in this thesis. While just stated but not explained in the previous paragraph in the unit cell reported by Lotsch *et al.* it is the (210)_{orthorhombic} plane of the orthorhombic cell that is associated to

the peak at $\sim 13^\circ$. This differs from the $(100)_{\text{hexagonal}}$ reflection given in literature for graphitic carbon nitrides synthesised *via* the pyrolysis of smaller organics (Figure 1.14).^{54, 125} The reflections of the structures discussed from this point will be referred to with the orthorhombic indexing.

Since the (210) plane is associated to the distance between the chains of heptazine units in the unit cell (Figure 3.16, inset), the desired position of the generated reflection can be obtained by simply adjusting the distance between the polymeric chains of Lotsch's Melon. The correct position for the (210) reflection is obtained by moving the chains along the x axes, thus reducing only the unit cell parameter a and leaving b unchanged. This allows to keep the C=N average bond distance at 1.325 \AA . Specifically, the distance between the chains, measured as an average between mirroring nitrogen atoms (d_c , Figure 3.13, inset), is reduced from 3.172 \AA to 2.922 \AA . The modified unit cell is now characterised by cell parameters: $a = 16.4 \text{ \AA}$ and $b = 12.4 \text{ \AA}$. The theoretical patterns generated from the three structures: Lotsch *et al.*^{123, 126}, Tyborski *et al.*¹²³ and this work, are compared in Figure 3.16 with the one measured for C_3N_4 -500.

The three unit cells generate very similar XRD patterns and when compared with C_3N_4 -500 (Figure 3.16) most of the observed peaks can be justified by the theoretical

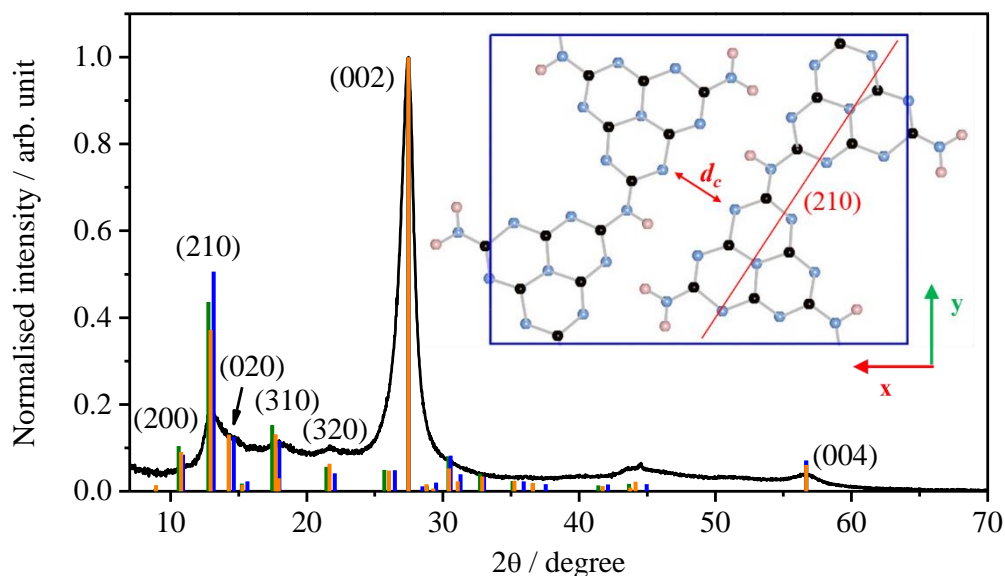


Figure 3.16 Theoretical patterns based on Melon structures.^{123, 126} Comparison of between XRD patterns of C_3N_4 -500 (black), Melon by Lotsch (green, $a = 16.7 \text{ \AA}$, $b = 12.4 \text{ \AA}$, $c = 6.49 \text{ \AA}$, $\alpha = \beta = \gamma = 90^\circ$, Space Group: $\text{P}2_12_12$), Tyborski (blue, $a = 16.2 \text{ \AA}$, $b = 12.1 \text{ \AA}$, $c = 6.49 \text{ \AA}$) and this work (orange, $a = 16.4 \text{ \AA}$, $b = 12.4 \text{ \AA}$, $c = 6.49 \text{ \AA}$). Inset: view along c of unit cell; d_c = distance between the polymeric chains; red line: plane (210) .

ones. The (002) reflection in all three cases is chosen as reference therefore the peaks are perfectly overlapping and normalised to 1. With $d_{002} = 0.325$ nm, the broad peak at $2\theta = 56.68^\circ$ seen in all three unit cell at the same position can be indexed as the (004) reflection, $d_{004} = 0.162$ nm. For some of the other peaks there are however minor differences in position and relative intensities. The peak at $2\theta = 11^\circ$ seems to be either missing from the XRD pattern of C₃N₄-500 or again being too intense in the theoretical patterns. Due to the different unit cell parameters the (210) reflection falls at slightly different angles between the three unit cells: $2\theta = 12.78^\circ$, $2\theta = 13.14^\circ$ and $2\theta = 12.94^\circ$ for Lostch, Tyborski and this work, respectively, they also have different relative intensities $I_{210}/I_{002} = 0.44$, 0.50 and 0.37. The unit cell proposed in this work shows an improvement in the intensity of the (210) reflection, nonetheless, it remains too intense if compared to the experimental ratio of 0.19. The lower intensity of the (210) reflection for the synthesised material could be due to a lower range order along this plane compared to the (002). Additional optimisation of the proposed structure is required to improve the correlation with the experimental results.

Tyborski *et al.* observed that the reflection (210) at $2\theta = 13.14^\circ$ decreased in relative intensity for increasing synthesis temperature of the PCN materials.¹²³ To explain this phenomenon they investigated the effect produced on the XRD pattern by changing the angle γ of their unit cell.¹²³ Tyborski *et al.* observed that by slightly decreasing the angle γ the relative intensity of the (210) reflection could be considerably decreased.¹²³ The optimum value of γ for their structure was found at 87° .¹²³ The influence on the variation of γ on the modified Melon structure proposed in this study is here investigated.

The easiest method to evaluate the variation of γ on the modified Melon is to simply change the angle γ in the unit cell. This changes the geometry of the cell from orthorhombic to monoclinic. Changing this angle inevitably disrupts the organic framework but the error caused by the stretching and compression of the interatomic distances remains very small if the angle range 84° to 90° is considered. Additionally, the volume of the unit cell is also affected by a change of the angle; it goes from a value of 1319.8 Å³ for $\gamma = 90^\circ$ to a value of 1312.6 Å³ for $\gamma = 84^\circ$ corresponding to a 0.5 % decrease. To maintain the volume the same and compare the effect that only the angle has on the pattern, the unit cell parameter b is adjusted accordingly. The changes produced on the reflections (200) and (210) as a function of the angle γ are illustrated in Figure 3.17. The (200) reflection is not affected by the changes in relative intensity (Figure 3.17a) nor in peak position (Figure 3.17b) and at this stage the absence of this reflection in the

measured pattern has to remain unexplained. When changing γ from 90° to 84° the position of the (210) shifts towards lower 2θ angle. From $\gamma = 90^\circ$ to 89° the intensity of the reflection decreases from $I_{210}/I_{002} = 0.37$ to $I_{210}/I_{002} = 0.16$. Further changes to the angle γ sees very little variation of the relative intensity of the (210) which remains between $I_{210}/I_{002} = 0.16$ and 0.17 . While changing the angle γ has the wanted effect of bringing the intensity of the (210) close to the experimental ratio of 0.19, it also results in the appearance of another reflection at about $2\theta = 13^\circ$ which can be attributed to the $(2\bar{1}0)$.¹²³ This reflection is also present in the structure with $\gamma = 90^\circ$ but it perfectly overlaps with the (210). The position of the $(2\bar{1}0)$ is found to shift towards higher 2θ angle with the decrease of the angle γ and the intensity of the $(2\bar{1}0)$ is found slightly higher than the (210); decreasing from 0.20 ($\gamma = 89^\circ$) to 0.18 ($\gamma = 84^\circ$). All this values are more representative of the real situation for C_3N_4 -500 ($I_{210}/I_{002} = 0.19$) than that for $\gamma = 90^\circ$ in the original unit cell ($I_{210}/I_{002} = 0.37$).

As seen in Figure 3.17b, and also mentioned by Tyborski¹²³, the reflections (210) and the $(2\bar{1}0)$ separates from one another as the angle γ decreases. The (210) progressively shifts from $2\theta = 12.94^\circ$ to $2\theta = 12.36^\circ$ with a $\Delta 2\theta = 0.58^\circ$. This is more intense for the $(2\bar{1}0)$ from $2\theta = 12.94^\circ$ to $2\theta = 13.62^\circ$ with a $\Delta 2\theta = 0.68^\circ$. Again the plane (200) is not effected by the change in γ . When choosing the optimum value for the structure both relative intensity and position of the peak have to be considered. From an intensity point of view, since no major changes are present between the different angles lower than 90° , they

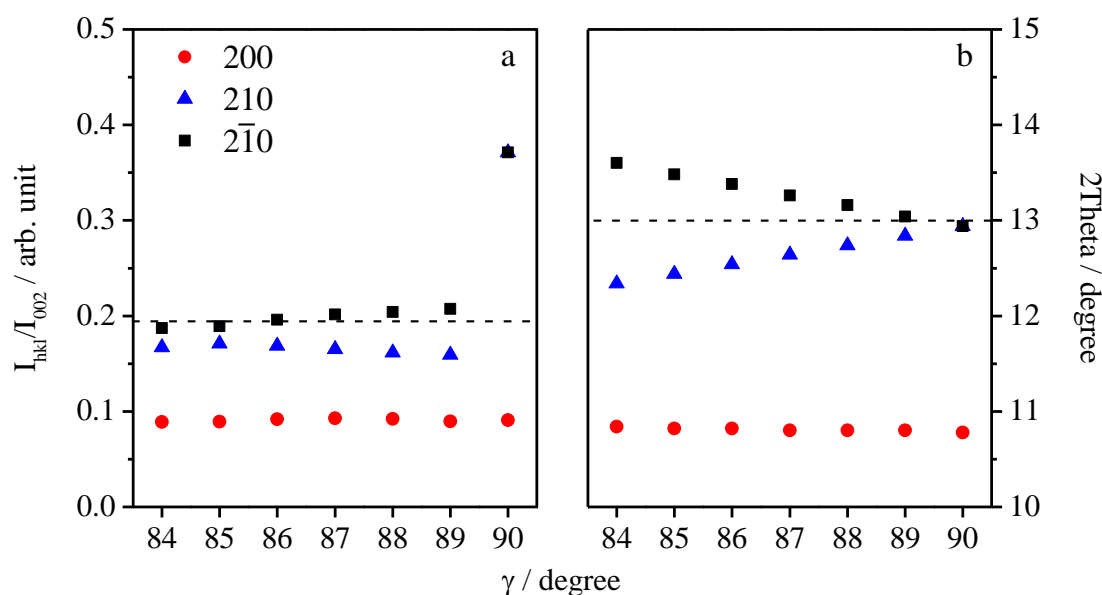


Figure 3.17 I_{hkl}/I_{002} and 2θ vs. γ . Influence of the value of γ on the relative intensity (a) and the position (b) of (200), (210) and $(2\bar{1}0)$ reflections.

could all be considered suitable, however if the peak position is considered, only few can be accepted. Considering the broad nature of the peak at $\sim 13^\circ$ in the measured pattern a slight separation of the (210) and the (2 $\bar{1}$ 0) reflections can be accepted, since it would probably result in one broad peak. However, for $\gamma > 88^\circ$ the separation between the two reflections is too big and two single peaks would probably be generated. Therefore, it is reasonable to conclude that the most probable angle γ of the unit cell is 88° or 89° . However, an angle $\gamma \neq 90^\circ$ would lead to a small deformation of the network, therefore additional modifications are taken into consideration.

Lostch *et al.* reported that a g-C₃N₄ buckled structure would be more stable than a planar one.^{60, 126} Tyborski *et al.* also considered the effect of buckling on the XRD pattern.¹²³ No major differences were found in terms of intensity of the peaks, only the addition of an extra intense reflection at $2\theta = 27.77^\circ$ indexed as (101).¹²³ For comparison the same buckling is applied to the modified Melon investigated in this work. As before the structure is modified to guarantee a (002) reflection at 27.40° by adding a layer (A-A stacking) and setting the cell parameter c at 6.49 \AA . The angles of the unit cell are $\alpha = \beta = \gamma = 90^\circ$. The theoretical pattern and a graphic representation of the unit cell are shown in Figure 3.18. The theoretical pattern is found very similar to the one reported by Tyborski *et al.* including the additional reflection at $2\theta = 28^\circ$ which is, however, indexed as the (102) reflection. This extra reflection is now present because the number of atoms

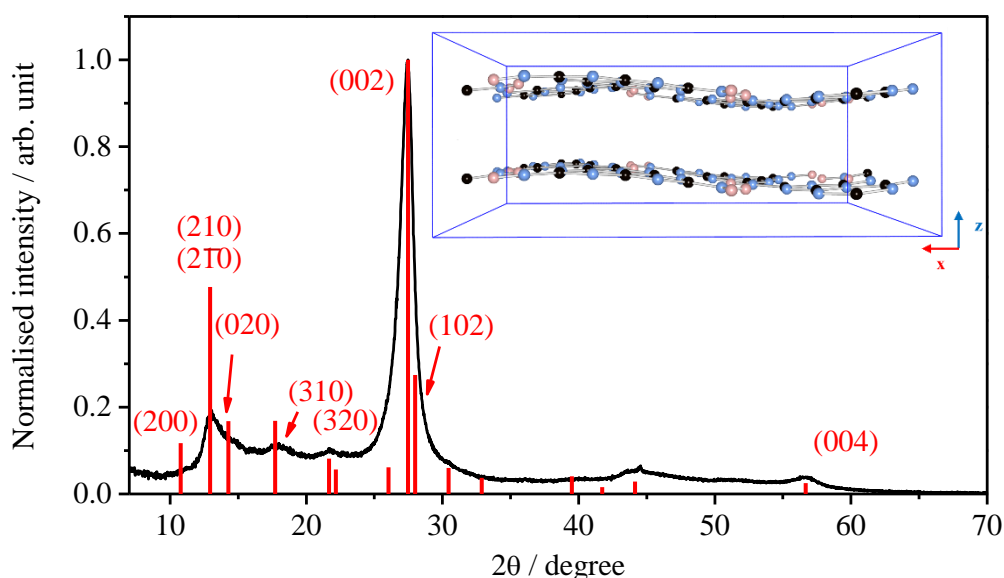


Figure 3.18 Buckled structure for Melon. Theoretical pattern generated for Melon after applying the buckling suggested by Tyborski (red)¹²³. Unit cell parameters: $a = 16.4 \text{ \AA}$, $b = 12.4 \text{ \AA}$, $c = 6.49 \text{ \AA}$, $\alpha = \beta = \gamma = 90^\circ$.

on the corresponding plane is increased compare to the planar structure. Compared to the planar structure (Figure 3.16), the buckling does not produce any changes in the position of the peaks but there is an increase of intensity for the reflections at lower angles. More evident is the case of the peak at $2\theta = 12.94^\circ$ which increases from $I_{210}/I_{002} = 0.37$ for the planar structure to $I_{210}/I_{002} = 0.42$. This increase seems to exclude this structure from the list of possible candidates; on the other hand the position of the peaks well match that of the measured patten. Additionally, a buckled structure is considered more thermodynamically favoured and once again the lower intensity of the experimental peak compared to the (210) reflection can be due to a higher level of disorder.

The crystal structures investigated so far are characterised by A-A stacking. It has been previously mentioned that by being an aromatic network with π - π inter-layer interactions an A-B stacking would be more plausible in order to minimise repulsion between layers. To shift the layers with respect to each other in the unit cell of Melon two approaches can be employed: applying a vector to one of the layer or changing the angles β or α .^{60, 126} Lostch discussed both options pointing out that in the first case a A-B stacking configuration would be introduced but the orthorhombic symmetry of the unit cell would be lost, whereas in the second case the A-A stacking would be retained and the unit cell would become monoclinic.^{60, 126}

Lostch first investigated the effect of three different shifts along the plane a - b and compared them to the electron diffraction pattern of Melon. The first shift (A) was random along both the x and y directions, the second (B) along the diagonal of the cell and the third (C) only along the y axis. The author concluded that none of the electron diffraction patterns generated from the three shift models gave reasonable fit to the observed one.¹²⁶ Despite providing a poor match to the experimental result the structures proposed by Lotsch have only been compared to the electron diffraction and not to the XRD pattern of g-C₃N₄. To study the effect, different shifts are applied to one of the layers of the modified Melon structure (model structure seen in Figure 3.16) investigated in this work. The theoretical patterns generated from those unit cells are presented in Figure 3.19. For comparison an alternative triclinic cell proposed by Lotsch is also included in Figure 3.19. Lotsch did report this cell ($a = 16.389 \text{ \AA}$, $b = 12.635 \text{ \AA}$, $c = 4.065 \text{ \AA}$, $\alpha = 74.704^\circ$, $\beta = 57.067^\circ$ and $\gamma = 89.991^\circ$) as a better match but provided little details explaining this result.¹²⁶ The parameters for this unit cells were determined using Force Field calculations but using the orthorhombic unit cell as a reference the equivalent shift for this structure $(x/a, y/b) = (0.135, 0.085)$ appears like in the case of Shift A, random.

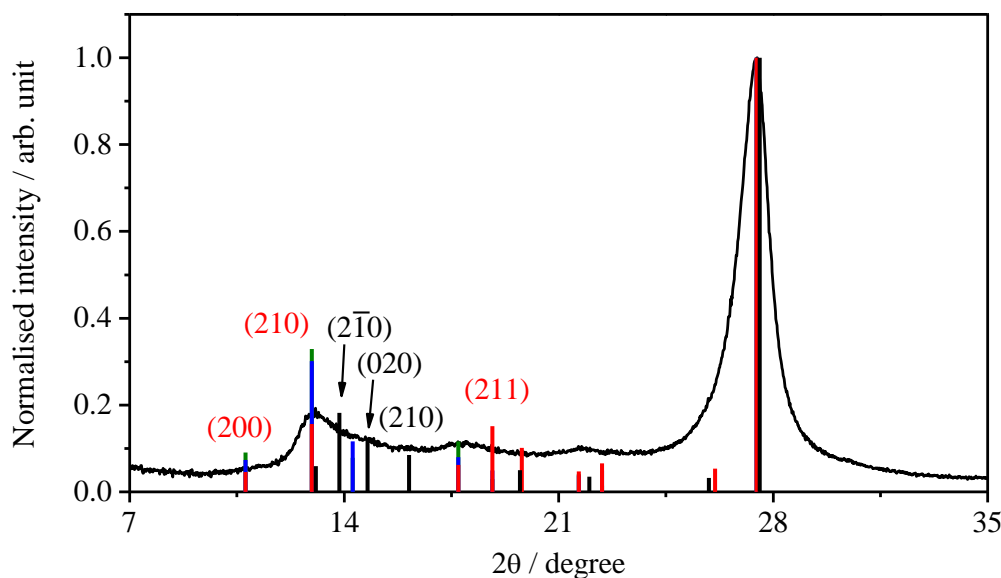


Figure 3.19 Melon structures with shifted layers. Theoretical XRD patterns of Melon with a triclinic unit cell (black, bars, $a = 16.389 \text{ \AA}$, $b = 12.635 \text{ \AA}$, $c = 8.12 \text{ \AA}$, $\alpha = 74.704^\circ$, $\beta = 57.067^\circ$ and $\gamma = 89.991^\circ$) and with a shift of one of the layers ($a = 16.4 \text{ \AA}$, $b = 12.4 \text{ \AA}$, $c = 6.49 \text{ \AA}$, $\alpha = \beta = \gamma = 90^\circ$). Vectors fractional coordinates in (x, y): Shift A (0.124, -0.244) (red), Shift B (0.072, 0.054) (blue), Shift C (0.000, 0.109) (green).

While no major differences in peak position can be observed between the patterns obtained using the different shifts (A, B and C), the relative intensities of some of the reflections, especially the (200) and (210), are found to vary significantly. The reflection (200) has an I_{200}/I_{002} intensity of 0.05, 0.07 and 0.09 for Shift A, B and C, respectively. For the (210) reflection the I_{210}/I_{002} is 0.16 for Shift A and 0.30 and 0.33 for Shift B and C respectively, only marginally decreased from the value of the original structure (0.37). This is due to a change of the 3D structure of the layers which are now differently aligned, this has an effect on the atoms on the different planes. At this stage it is reasonable to assume the structure that the most closely simulates the pattern of C_3N_4 -500 is produced by Shift A. By applying this shift an effect on the theoretical pattern similar to that of the structures with $\gamma \neq 90^\circ$ can be generated but without the separation of the (210) and $(2\bar{1}0)$ and the distortion of the aromatic network. The suggested triclinic unit cell that was determined from the electron diffraction pattern,¹²⁶ on the other hand, does not compare well with the XRD of C_3N_4 -500. The (210) peak is significantly shifted towards higher angles and in its original position the (200) reflection is now found with a very low intensity (0.06). Furthermore, in this case, as well as when the value of γ was modified the separation of the (210) and the $(2\bar{1}0)$ occurs. At this point it is unclear how two

structures (Shift A and the triclinic presented just above) which have been generated from random shifts in the plane a - b can provide such different results.

The second approach suggested by Lotsch *et al.* is the modification of the angles α and β .^{60, 126} This produces shifts along the y (b) and the x (a) direction, respectively. However, the structure is still characterised by an A-A stacking along z (c). The influence that α and β have on the theoretical pattern is, therefore, investigated. Only one of the two angles is changed at a time and while doing so the parameter c is adjusted (increased) in order to retain the (002) reflection at $2\theta = 27.40^\circ$. While changing the angle, the position and the relative intensity of the reflection (210) is monitored. The results are summarised in Figure 3.20 where the variation of I_{210}/I_{002} and 2θ vs. the angle are illustrated. The (200) reflection is not shown since no noticeable change in intensity and position are observed. The effects produced by varying the intensity of α or β are found to be very similar. In both cases the intensity slightly decreases from the original 0.37 to ~ 0.30 . The decrease is greater for β (0.30 for $\beta = 115^\circ$) than for α (0.34 for $\alpha = 115^\circ$) but in both cases this value still remains too high compared to C₃N₄-500 experimental value ($I_{210}/I_{002} = 0.19$). Changing the angle also has an effect on the position of the peak by shifting it towards higher angles. After remaining nearly the same for both α and β up to 95° , once again the change is the largest for β ($= 115^\circ$) with $2\theta = 13.90^\circ$. The effects of the angles below 90° have also been investigated and they were found mirroring the behaviour of $\alpha(\beta) > 90^\circ$.

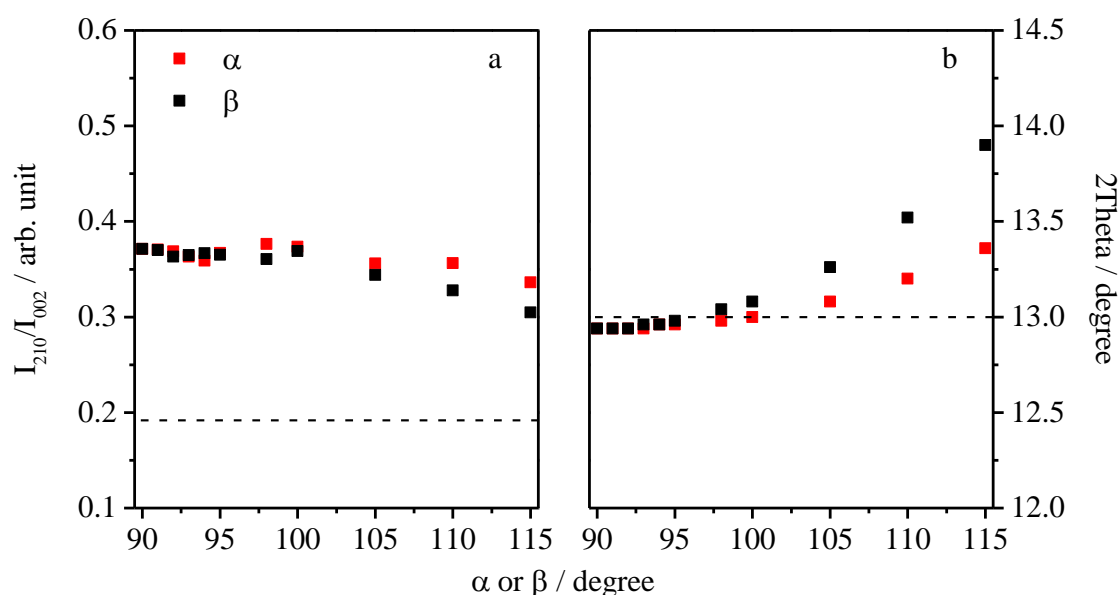


Figure 3.20 I_{210}/I_{002} and 2θ vs. α and β . Influence of the value of α (red) and β (black) on the relative intensity (a) and the position (b) of the (210) reflection. Dashed lines: measured values.

After these considerations, it can be assumed the optimum values of α or β for an A-A stacking of Melon layers can be found between 82° and 98° (with the exception of $\alpha(\beta) = 90^\circ$). Although combinations of α and β are not tested the observation made here helps understanding the behaviour of the structures defined earlier in this section for which a shift to one of the layers is applied. The unit cells labelled Shift A, B and C have equivalent points within the α and β range specified in Figure 3.20. For example, Shift C which has a shifted layer $(x/a, y/b) = (0.000, 0.109)$ shows only a marginal improvement on the intensity; the shift is equivalent to $\alpha = 78.2^\circ$ and $\beta = 90.0^\circ$ included in the range of angles which do not introduce significant changes. In the case of the unit cell Shift A that gives the best match to the XRD patterns, the $(x/a, y/b) = (0.124, -0.244)$ is equal to a cell with $\alpha = 114.809^\circ$ and $\beta = 72.872^\circ$, these values fall in the range of angles that are not considered as optimum. This however shows that the negative effect of modifying only one of the two angles could be decreased by modifying the two at the same time. On the other hand, the triclinic cell calculated by Lotsch from the electron diffraction pattern¹²⁶ has $\alpha = 74.704^\circ$ and $\beta = 57.067^\circ$ which is too far away from 90° and therefore explains the shift in the (210) reflection.

3.4.4. Symmetry considerations

As previously mentioned the space group P1 was employed as a tool to generate the theoretical patterns of the structures considered in the investigation. In this section however the possible symmetry of the structure is evaluated.

The experimental pattern of C₃N₄-500 shows only a limited number of broad peaks. This can in general be ascribed to a structure with short range order along specific planes, preferential orientations or a certain level of symmetry higher than the triclinic considered so far. To evaluate the level of symmetry, the experimental pattern was indexed with the software HighScore Plus which provided possible unit cell parameters and a list of possible space groups. The result of the indexing suggested an orthorhombic cell ($a = 12.1392\text{\AA}$, $b = 8.1570\text{\AA}$, $c = 7.7246$) and orthorhombic space groups. This is in line with the geometry of the cell employed in the previous sections. Among all the space groups suggested by the software few were chosen to generate theoretical patterns and compare them with experimental one (Figure 3.21). The choice of these space groups was made following two criteria: the highest number of indexed experimental peaks and at the same time the lowest number of unexplained lines in the theoretical pattern.

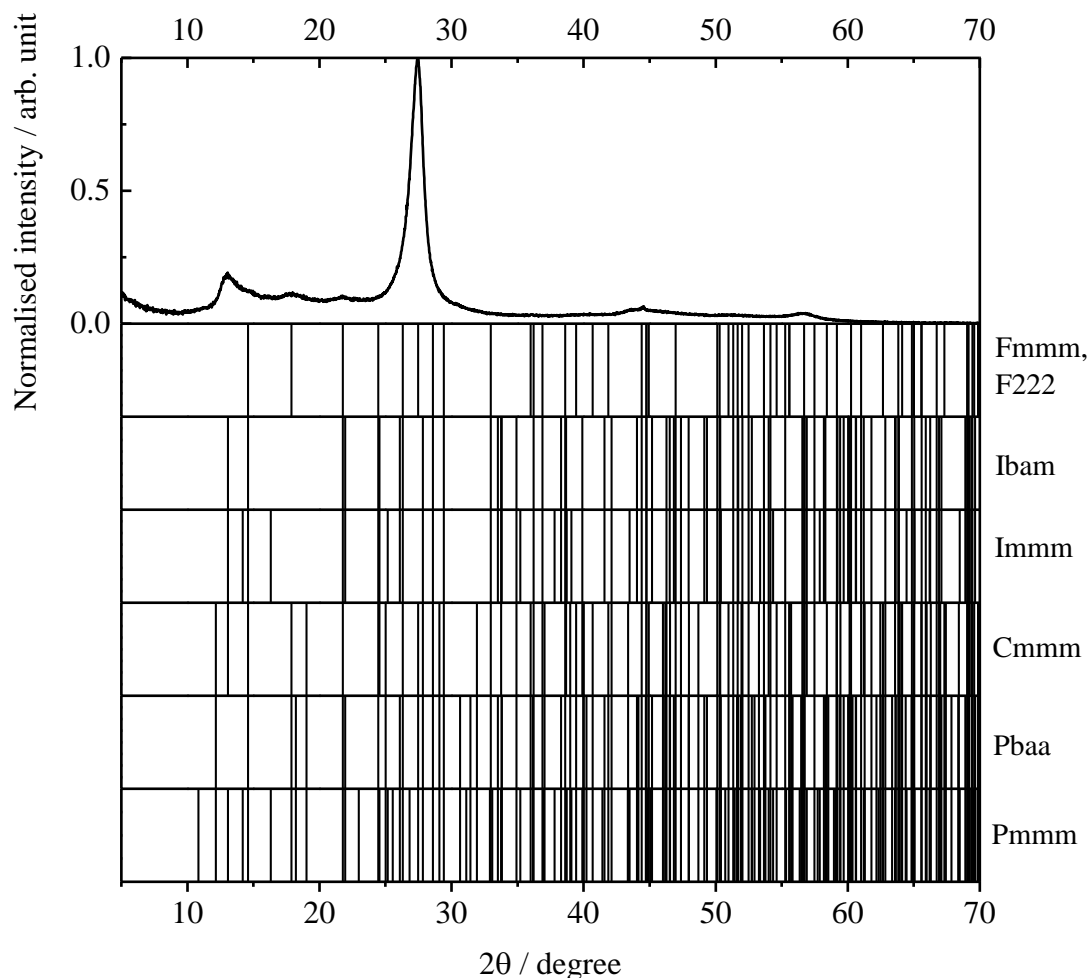


Figure 3.21 Possible space groups. Comparison of the experimental pattern with the theoretical patterns generated from unit cells characterised by different space groups.

All the structures give a high number of reflections, especially at high angles, due to the big unit cell considered. Some however cannot explain all the reflection observed in the experimental pattern, these are: Fmmm, F222, Ibam and Immm. It is only from the space group Cmmm that all the peaks in the XRD pattern of C₃N₄-500 are justified. However, a decrease in the symmetry level increases the reflections (Pmmm), making it difficult to further discriminate between space groups. This findings differ from the suggestion of Tyborsky *et al.*¹²³ of a hexagonal symmetry with space group P $\bar{6}$.

3.4.5. Summary of results

Possible structures for graphitic carbon nitride synthesised from pyrolysis of melamine are investigated by mean of X-ray diffraction. Some structures are taken from previous published studies and modified to generate theoretical XRD patterns to compare with the

one of measured C₃N₄-500. Some other structures were, instead, created on purpose for this investigation to consider new alternatives. During the analysis of the XRD patterns it emerged that not all the proposed structures can be considered suitable candidates to describe graphitic carbon nitride materials or g-C₃N₄, a summary of which is shown in Table 3.4.

Table 3.4 Summary of the modelled structures. Comparison of the peak position and relative intensity of the reflection indexed as (210) for the different structured considered in this work.

	(210) [(100)] 2θ (°)	Δ2θ (°)	I ₂₁₀ /I ₀₀₂
<i>C₃N₄-500</i>	13.00	-	0.19
Triazine	21.62	8.62	0.11
Heptazine A-A	14.38	1.38	0.78
Heptazine A-B	14.38	1.38	0.18
Döblinger A-A	8.00	5.00	8.33
Döblinger A-B	8.00	5.00	2.05
Triaz.-H A-A	10.78	2.22	1.47
Triaz.-H A-B	10.78	2.22	0.49
Heptaz.-H A-A	7.18	5.82	4.90
Heptaz.-H A-B	7.18	5.82	1.64
Melon-Lotsch	12.78	0.22	0.44
Melon-Tyborski	13.14	0.14	0.50
Melon-Thesis	12.94	0.06	0.37
Thesis Buckling	12.94	0.06	0.42
Thesis ShiftA	12.94	0.06	0.16
Thesis ShiftB	12.94	0.06	0.30
Thesis ShiftC	12.94	0.06	0.33
Thesis Triclin.	16.12	3.12	0.09

The triazine based structure proposed by Teter & Hemley¹¹⁶ for g-C₃N₄, and officially recognised (PDF# 83265-ICSD), does not describe, at least from an XRD point of view, the graphitic carbon nitride materials that in the literature is widely addressed as g-C₃N₄.^{54, 72, 125} A better match is obtained for the heptazine-based g-C₃N₄ with an A-B stacking but the slight up-shift and the too high intensity of the (100)_{hexagonal} reflection

still makes this structure a poor representation of synthesised g-C₃N₄. To take into account the protons observed in the TG analysis, other structures both triazine and heptazine based with a lower level of polymerisation were considered but no satisfactory results were obtained.

The theoretical pattern of Melon; a structure proposed by Lotsch *et al.*,^{60, 126} provides a reasonable match to the measured XRD of g-C₃N₄. Following the study by Lostch *et al.*, the compressed structure of Melon reported by Tyborski *et al.* can however be rejected since the C=N bond length is found on average too short. An improved theoretical pattern can be obtained by simply reducing the distance between the heptazine chains. Adjusting the angles α , β and γ of the unit cell is also favourable but only when the angles remain close to 90°.

Despite improving the calculated XRD pattern of g-C₃N₄ compared to the measured one, the proposed unit cells are not found very consistent with the ones reported using other techniques: especially the structures determined with electron diffraction. However it is believed the number of possibilities to represent graphitic carbon materials has been narrowed down. Some of these structures can be used in the case g-C₃N₄ is investigated by other techniques.

3.5. Structure investigation II: Neutron Scattering

In neutron diffraction the neutrons are scattered by the nuclei of the atoms instead of the electrons as in X-ray diffraction. Because of this, the power of diffraction does not depend anymore on the atomic number of the scattering atom. This allows to obtain information about lighter atoms, for example hydrogen.^{17, 132} It is also possible to distinguish between neighbouring atoms on the periodic tables (these will have different scattering cross sections, even though similar atomic number) and different isotopes.

The characterisation for this study was carried out on the Near and InterMediate Range Order Diffractometer (NIMROD) at the ISIS Facility of the Rutherford Appleton Laboratory. This specific instrument provides high resolution (~ 0.1 Å) structural information on a wide scale of lengths (< 1 Å - >300 Å).¹⁰¹ Due to its high resolution and its specific geometry able to minimise the inelastic scattering,¹⁰¹ NIMDROD is particularly suitable for the investigation of organic compounds containing light atoms (hydrogen), liquids and disordered materials; hence ideal for the study of amorphous compounds with covalent bonding such as graphitic carbon nitride materials.¹⁰¹

As already discussed (Chapter 2), from a neutron diffraction experiment the total structure factors $F(Q)$ is obtained after a series of corrections of the raw data. These corrections include background, sample container and inelastic scattering.^{102, 132, 133} Inelastic scattering is particularly important for light atoms like hydrogen and deuterium for which the effect is the strongest. Even though the method used for the subtraction is becoming more and more accurate with time,¹⁰² some errors and artefacts may still be introduced in the data for the correlations involving hydrogen or deuterium.^{102, 132} Once the $F(Q)$ is obtained the data contains information on d -spacing similarly to the X-ray diffraction. After applying Fourier transform and a series of mathematical operations, the result can also be presented as a differential correlation function $D(r)$ which provides direct information on the actual atomic distances (Chapter 2).

Figure 3.22 illustrates the total structure factor $F(Q)$ obtained for C_3N_4 -500, C_3N_4 -550 and C_3N_4 -600 synthesised at 500, 550 and 600 °C, respectively. In neutron diffraction the position of the peaks are expressed in Q (\AA^{-1}) instead of 2θ as for x-ray diffraction. The two are, however, mathematically related (Chapter 2), and through the equation $d = 2\pi/Q$ it is possible to obtain the d -spacing from a specific value of Q .¹⁰¹ No significant differences can be noticed between the three neutron diffraction patterns obtained which also resemble the one obtained by X-ray diffraction (Figure 3.3). The reflection (210), labelled according to the results of the previous section, is assigned to the peak at $Q = 0.87 \text{ \AA}^{-1}$ which corresponds to a d -spacing of 0.722 nm while the peak at 1.89 \AA^{-1} is

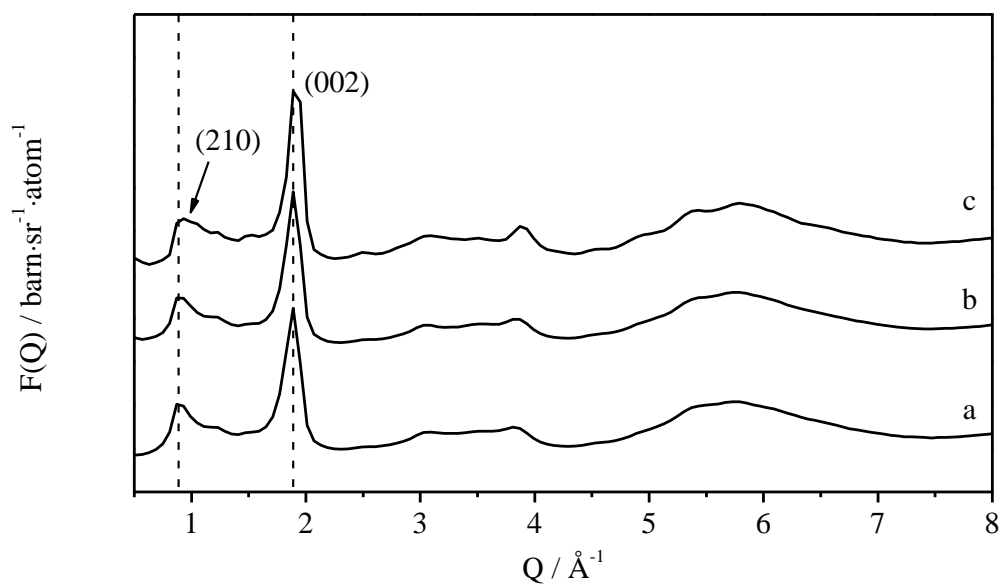


Figure 3.22 Total structure factor, $F(Q)$. Neutron diffraction patterns obtained for a) C_3N_4 -500, b) C_3N_4 -550 and c) C_3N_4 -600.

equal to a d -spacing of 0.332 nm and associated with the inter-layer distance (002). Both peaks results in larger d -spacing than the equivalent ones from the XRD. In the specific the Δd are 0.042 nm and 0.006 nm, respectively. This is due to errors of both instruments and the broad nature of the peaks, especially the one associated to the (210) reflection. The peaks in the x-ray pattern at $2\theta \sim 44^\circ$ and 56° can be seen in the neutron diffraction pattern between $Q = 3$ and 4 \AA^{-1} . Extra features can also be noticed especially at higher Q values due to the higher resolution of the technique compared to X-ray diffraction, and the instrument itself. No additional information can be directly extrapolated from the total structure factor as it is. A more useful representation of the data is the differential correlation function, $D(r)$, from which it is possible to look at differences in the distribution of the atoms at specific distances.

Neutron diffraction offers the possibility to obtain structural information on light atoms and distinguish between isotopes which is particularly useful when information about hydrogen atoms are needed. Hydrogen is characterised by a negative coherent scattering length while for deuterium it is positive;¹³⁴ translating as negative and positive peaks in the $D(r)$ plot. The differential correlation function of C_3N_4 -500 and its deuterated equivalent are shown in Figure 3.23.

The most evident effect of isotopic labelling is visible at 1 \AA which corresponds to the N-H bond distance;²¹ seen with a negative peak for the original (hydrogen) C_3N_4 -500 and

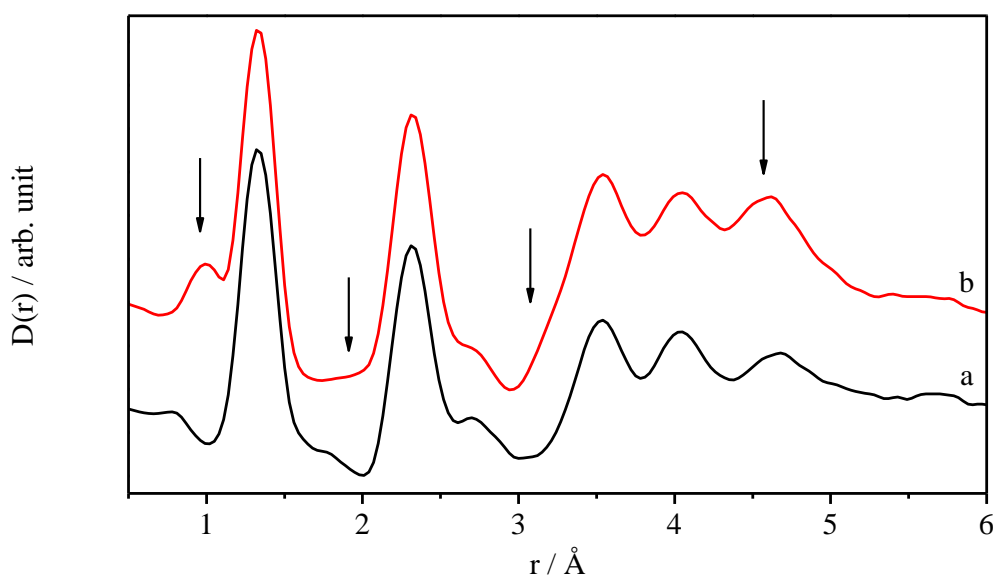


Figure 3.23 Effect of H and D on the $D(r)$ of C_3N_4 -500. Differential correlation function for C_3N_4 -500 (a) and deuterated C_3N_4 -500 (b). Arrows indicates atomic correlations involving hydrogen.

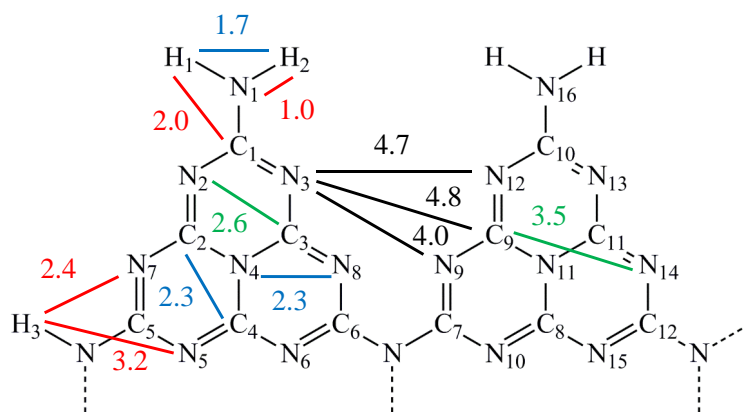


Figure 3.24 Inter-atomic distances in heptazine units. Some examples of inter-atomic distances in a heptazine-based graphitic carbon nitride.

positive peak in the labelled (deuterated) version. At 2 Å a similar less pronounced effect is visible, assigned to the second-neighbour distance H-(N)-C (from H₁ to C₁ in Figure 3.24). Less obvious differences can also be noticed at longer distances: at ~ 3.2 Å in the form of a small shoulder and at ~ 4.6 Å as a change in the peak intensity. The shoulder at ~ 3.2 Å can be associated with the distance between the hydrogen from an amino group to the first nitrogen encountered in the aromatic ring (H₃ to N₅ in Figure 3.24). The peak at ~ 4.6 Å is more difficult to assign to any specific atomic correlation. The large width of this peak could be associated to many intra- and inter-layers distances and not all of them involving hydrogen since a positive peak is observed in both correlation functions.

Figure 3.25 shows the differential pair correlation function of the three graphitic carbon nitride materials synthesised at 500, 550 and 600 °C. The spectra can be divided into three main sections (I, II and III). Area I includes the distances from 0 to 3 Å, these are atomic correlations within the layer of the graphitic carbon nitride materials, more specifically, within a heptazine unit. The second area (II) can be found between 3 and 6 Å, where the inter-layer distances contributes to the signal, for example the inter-layer *d*-spacing at 3.25 Å together with other long intra-planar distances. Above 6 Å (III), systematic ripples can be noticed. These can be attributed to the same moieties found in area II which are repeated in space. This suggests a certain degree of long range order but the low definition of the peaks in this area (ill-defined bumps) also indicate some disorder in the positions of the layers. The attention of this study focuses mainly on areas I and II.

Gaussian fitting of the peaks in area I and II is performed to determine peaks position and area. The main positive peaks at 1.33 Å is the C=N partial double bond in the aromatic

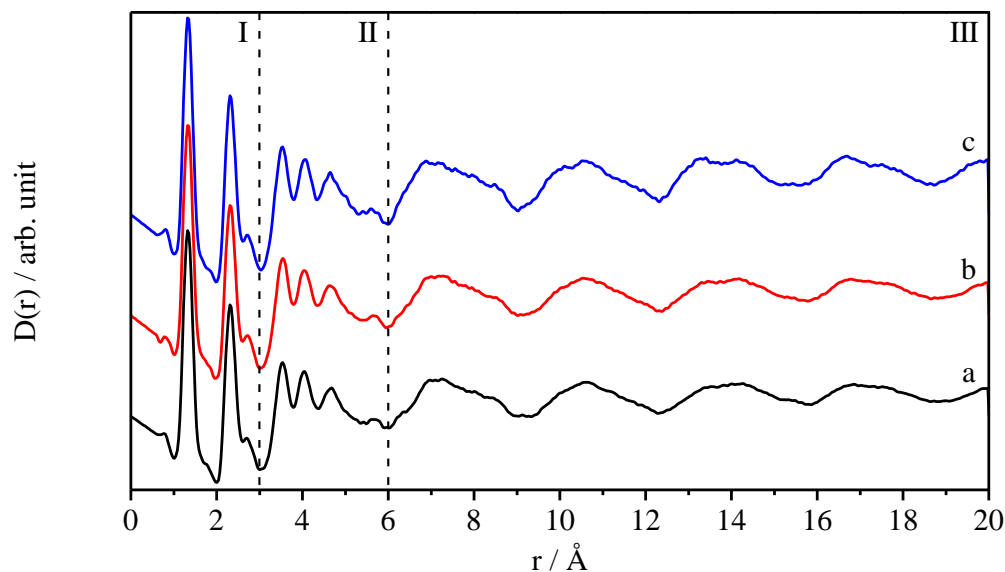


Figure 3.25 Differential pair correlation function for different C_3N_4 . $D(r)$ for a) C_3N_4 -500, b) C_3N_4 -550 and c) C_3N_4 -600. I, II, III: different sections in which the $D(r)$ profile can be divided in.

network.^{21, 131, 135} The high symmetry of the peak (Figure 3.23) suggests the absence of a component at 1.41 Å which would indicate the presence of a Csp^2-Nsp^3 correlation¹³⁵ for the C-N bonds bridging the heptazine units. Therefore, the bridging nitrogen atoms, most likely, feature a sp^2 hybridisation resulting in a shorter bond. At 2.32 Å the second-neighbour correlation for carbon and nitrogen atoms (C_2 to C_4 and N_4 to N_8 , Figure 3.24) is present. The small peak at 2.70 Å could instead be associated with the correlation between mirroring carbon and nitrogen atoms in the aromatic ring (N_2 to C_3). The density and atomic ratio of the material are required in order to obtain the $D(r)$ from the Fourier transform of the total structure factor (Chapter 2). However it is important that the entered values accurately represent the material of interest (within 0.1 at.%) to generate a differential scattering cross section that falls within 10 % of the expected value. While the total structure factors $F(Q)$ of C_3N_4 -500, C_3N_4 -550 and C_3N_4 -600 are found similar, the differential pair correlation functions $D(r)$ of the three materials are expected to show some differences that take into account the small variations reported in Table 3.1. The ratio between the areas of the N-H (1.03 Å) and the C=N (1.33 Å) bond slightly decreases with increasing temperature, with values of 0.07 for C_3N_4 -500, 0.05 and 0.04 for C_3N_4 -550 and 600, respectively. This confirms the higher degree of polymerisation of the samples synthesised at higher temperature.

The inter-layer d -spacing in the XRD for the (002) is reported at 3.25 Å. In the differential pair correlation functions $D(r)$ however no peak is seen at 3.25 Å but instead at 3.52 Å. In the case of a graphitic material with an A-A stacking configuration the atomic distance observed in the differential pair correlation functions would be expected to correlate the inter-layer d -spacing with a peak at 3.25 Å. On the other hand a shift of the layers as for example in a case of an A-B staking would lead to a longer inter-atomic distance while retaining the same inter-layer d -spacing. The result presented here are found in good agreement with the XRD analysis that proposed the A-B structure being one of the best possible candidates (Section 3.4).

The area ratio between the peak at 3.52 Å and the one of C=N (1.33 Å) is found to increase with the synthesis temperature: 0.63 for C₃N₄-500, 0.65 for C₃N₄-550 and 0.71 for C₃N₄-600. This result suggests the presence of a higher number of inter-layer distances, and therefore an increase in the stacking of the layers with temperature. The same conclusion was obtained from XRD analysis where a sharpening of the (002) reflection with increasing temperature was observed (Figure 3.3 and Table 3.1). The peaks at longer distances do not shows any significant variation between the three samples. Any specific assignment of these peaks is made difficult by the presence of long atomic correlations both within and between the layers.

The differential correlation function is used to verify and discriminate between the possible structures for graphitic carbon nitride materials that were selected after X-ray diffraction investigation. This is achieved by generating theoretical $D(r)$ plots with the software PDFGui¹⁰³ from the crystallographic information file (CIF), used for the XRD investigation, and comparing them with the measured one. The software subtracts the differential correlation function from the measured data and provides a residual value R_w . During the refinement the intensity of the calculated plot is adjusted in order to have normalised intensities for the peak labelled (A_{II} , Figure 3.26) at 1.33 Å. The area of this peak is, therefore, used to normalise the other peak areas. The ratios A_{peak}/A_{II} is used for the comparison between structures, together with the R_w values. An R_w value of 0 is considered a perfect fit and 1 a poor representation of the structure. While R_w values are reported for the whole range of r (up to 20 Å), the fitting of an amorphous material becomes less accurate at large distances. For this reason the R_w values are also given for the shorter range 0-6 Å and used in the discussion in this work. Finally to remain coherent with the XRD analysis the calculated $D(r)$ are only compared to the one of C₃N₄-500.

3.5.1. Single phases

The theoretical $D(r)$ calculated from the structure proposed by Tyborski *et al.* and its modified version with the applied shift to the heptazine chains (Section 3.4.3 and Figure 3.16) are compared to the measured $D(r)$ of C_3N_4 -500 in Figure 3.26. In order to help with the discussion, after the Gaussian fitting with a linear background, the main peaks in the differential correlation function of C_3N_4 -500 are labelled I to IX.

The unit cell proposed by Tyborski *et al.* (Figure 3.26c), a structure obtained by decreasing the cell parameters of the original Melon structure (Lotsch, Section 3.4.3), generates a profile with a $R_w = 0.75$. This poor fit is due to the main peaks being shifted towards shorter r distances as a result of the “shrinking” effect previously discussed. This confirms the importance of retaining the bond length in the aromatic network. In addition, the areas of some of the peaks are found very different from the experimental values; especially peaks A_{VII} (4.03 Å) and A_{VIII} (4.62 Å), but also ratios between them. The A_{VII}/A_{VI} gives a value of 1.43; significantly higher than the experimental value 0.94 for C_3N_4 -500 (Table 3.4), while the theoretical ratio A_{VIII}/A_{IX} is found is too small (1.11 vs. 3.85). Since the peak areas can be associated to the relative amount of the inter-atomic distances present in the structure, the recorded excesses and shortages are a good indication this model does not accurately represent the real material.

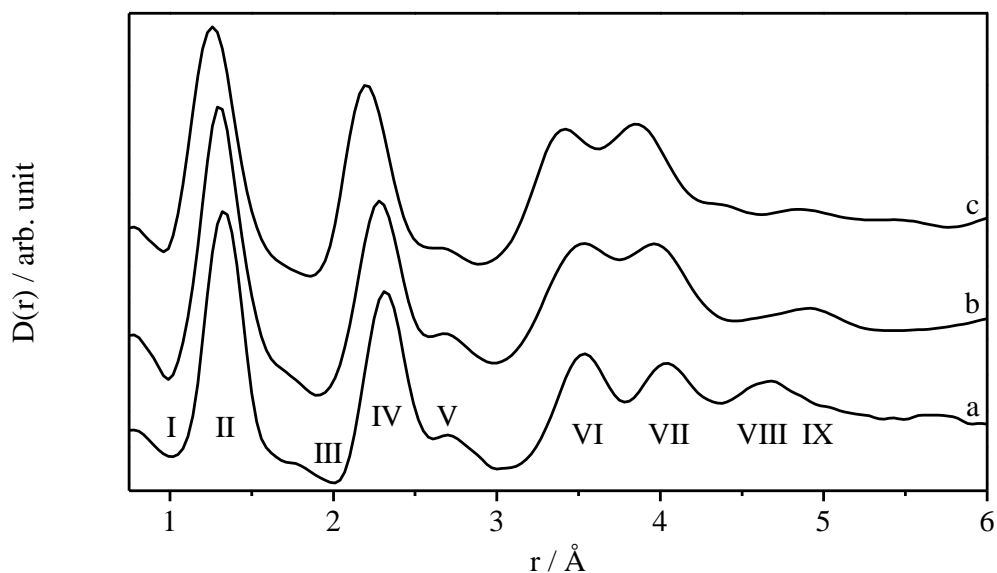


Figure 3.26 Calculated $D(r)$ for modified and Tyborski's Melon. Theoretical differential correlation function for a) C_3N_4 -500, b) modified Melon and c) Tyborski's structure. The main peaks are labelled from I to VIII to help in the discussion. For the residual $D(r)$ see Figure A.1 and A.2.

The theoretical $D(r)$ of the modified version of Melon with the shift applied to the heptazine chains (Section 3.4.3) is now characterised by peak positions and intensities that are more consistent with the one of C_3N_4 -500 (Table 3.4); with an $R_w = 0.41$. The area $A_{IV}/A_{II} = 1.23$ is comparable to the 1.25 of C_3N_4 -500. However, the correlation at 4.62 \AA ($A_{VIII}/A_{II} = 0.39$) is found significantly lower than the experimental value of 0.77. Therefore despite making some progress, the observed discrepancies between the results suggest this modified version of Melon cannot be considered as satisfactory.

The effect of a buckled structure was also found, to some extent, to be beneficial on the calculated XRD pattern (Section 3.4.3). For the differential correlation function as well, introducing buckling in the layers brings to a better fit and better ratios A_{peak}/A_{II} . However, this is only limited with an R_w of 0.38.

From XRD analysis (Section 3.4.3) it was found that applying a small change to the unit cell angle γ could better describe the measured X-ray diffraction pattern. However, it was pointed out simply changing the angle of the cell causes a small distortion of the structure. Figure 3.27b and c show the $D(r)$ obtained for Melon with $\gamma = 88^\circ$ and 89° , respectively. No shift is observed for the peaks at low values of r which indicates that despite having generated an error in the bond length by changing with the angle γ such small distortions of the aromatic network do not appear theoretically. Compared to the original Melon structure (Table 3.4) the R_w slightly increases to 0.43 for $\gamma = 89^\circ$ and 0.45 for $\gamma = 88^\circ$. Overall the majority of the peaks are found in good agreement with the experimental

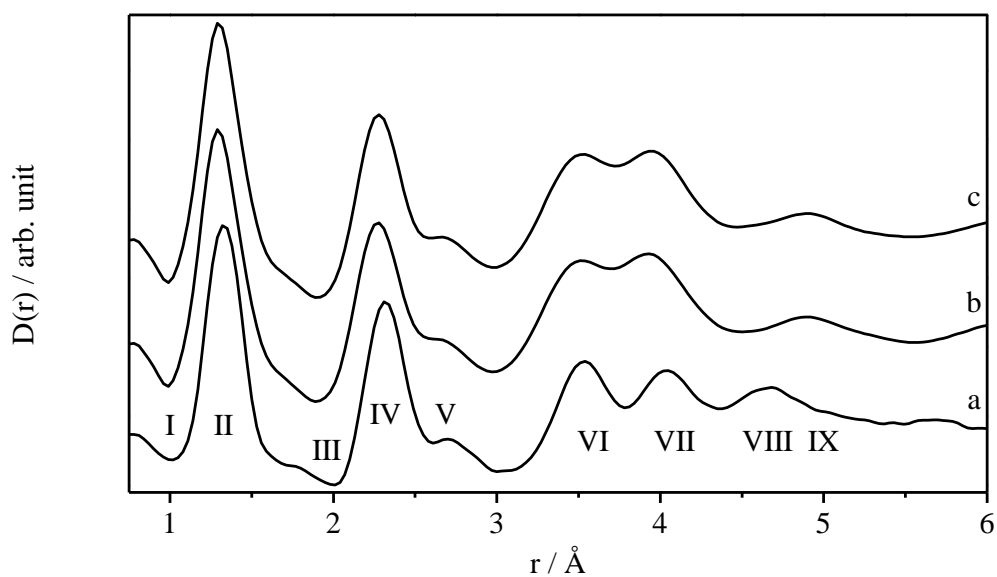


Figure 3.27 Effect of unit cell angle γ on $D(r)$. Differential correlation function for a) C_3N_4 -500, melon with γ b) 88° and c) 89° . For the residual $D(r)$ see Figure A.3 and A.4.

values or remaining mostly constant between the two structures, with the exception of peak VI and VII. Peak VI has a lower area than expected while the opposite is observed for peak VII, giving very different ratios A_{VII}/A_{VI} : 1.70 for $\gamma = 88^\circ$ and 1.33 for $\gamma = 89^\circ$. Even though they are comparable, based on the neutron diffraction analysis carried out so far and contradictory to the XRD results, the angle γ at 90° is the best solution for the structure of C_3N_4 -500.

Looking at the effect of changing the angles α and β in the unit cell (Section 3.4.3), two sets of three angles (92° , 95° and 98°) were used to generate the theoretical $D(r)$. The results of the Gaussian fitting and the R_w obtained for the six structures are listed in Table 3.4. The R_w values for the six structures are very similar (Table 3.4) with the lowest of 0.40 for α and β at 98° , which are shown in Figure 3.28. Increasing the angle (α or β) also results in the increase of the area of the peak VIII. The angles are modified with the intention of simulating a shift of the layers (along a for $\beta \neq 90^\circ$ and along b for $\alpha \neq 90^\circ$) while retaining the A-A stacking configuration. In order to compensate for the change the c parameter of the unit cell has to be adjusted to ensure the inter-layer spacing remains at 3.25 \AA (Section 3.4.2). It is therefore possible to associate the peak around 4.62 \AA to the atomic distances between atoms present in the different layers.

An actual shift of the layers is then introduced to evaluate its effect on the differential correlation function. The calculated $D(r)$ for a structure with a shift on the plane a - b ; $(x/a, y/b) = (0.124, -0.244)$ Figure 3.18, is presented in Figure 3.29. Overall the normalised

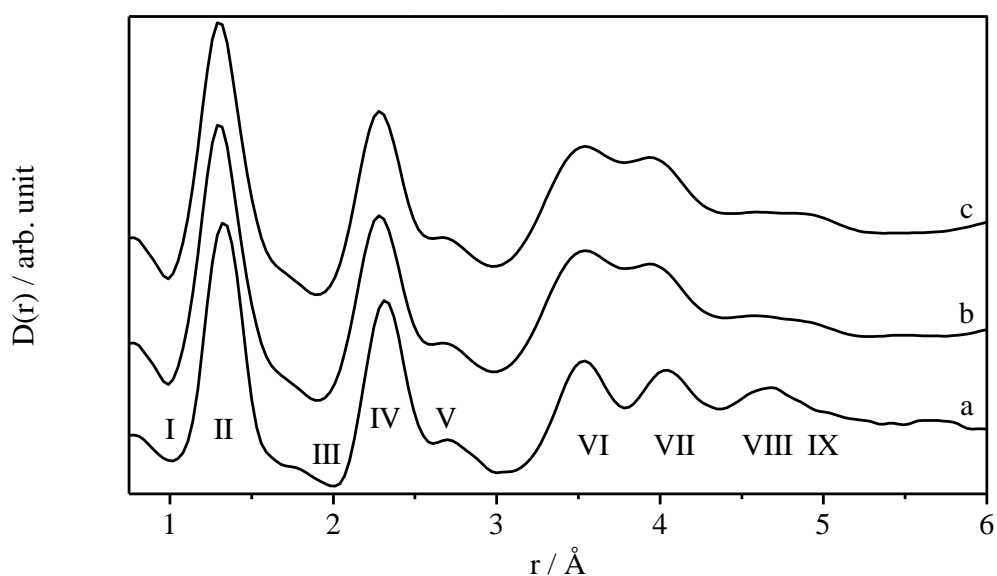


Figure 3.28 Effect of unit cell angles α and β on $D(r)$. Differential correlation function for a) C_3N_4 -500, melon with b) $\alpha = 98^\circ$ and c) $\beta = 98^\circ$. For the residual $D(r)$ see Figure A.5 and A.6.

areas of the peaks are found in good agreement with the observed values (Table 3.4), bringing the R_w down to a value of 0.32. This, together with the results discussed for the modified angles α and β , suggests that indeed a shift between the layers could be present in the real graphitic carbon nitride materials as it was suggested in the XRD analysis. The crystal structure of the Melon with shifted layers is illustrated in Figure 3.30. A shift of the layers simulates a higher level of disorder along the (210) plane. This disorder is repeated in space as shown by the ripples in the $D(r)$ (Figure 3.25).

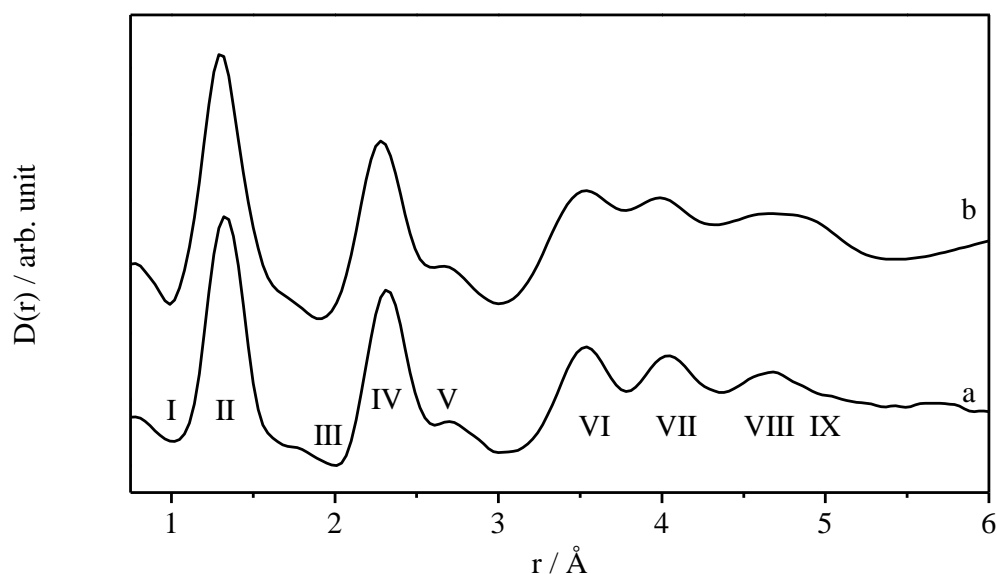


Figure 3.29 Effect on the $D(r)$ of shifted layers. Differential correlation function of a) C_3N_4 -500, Melon after b) shifting the layers. For the residual $D(r)$ see Figure A.7.

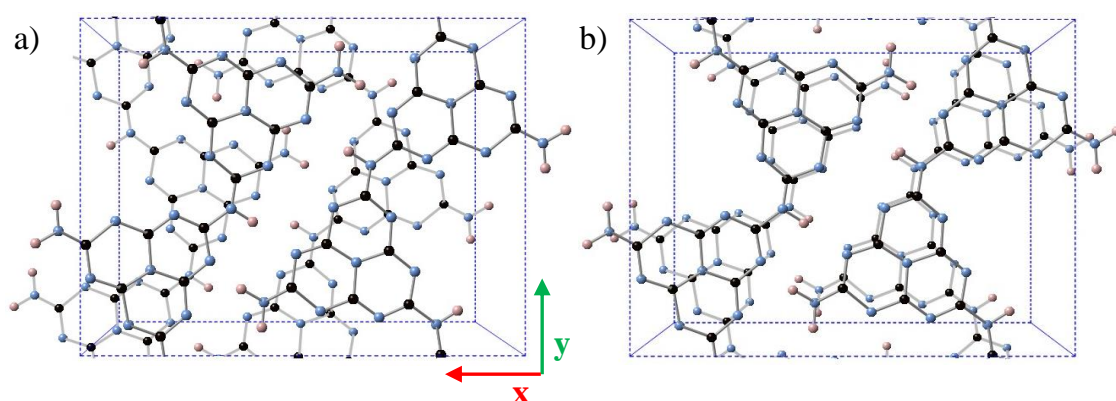


Figure 3.30 Crystal structure of Melon. The crystal structure of Melon with shifted layers (a) is compared with that of Melon with an A-A configuration (b).

Table 3.5 Summary of peak areas from D(r) of single phase. Summary of the peak areas normalised vs. A_{II} and obtained from the D(r) generated for different structures. The peak position and the values for the measured differential correlation function are also listed for comparison. R_w values are provided for the range 0-6 Å and in brackets for the whole range 0-20 Å.

	A_{peak}/A_{II}								R_w
	I	III	IV	V	VI	VII	VIII	IX	
r (Å)	1.03	2.07	2.31	2.72	3.52	4.03	4.62	5.14	-
C_3N_4 -500	0.07	0.14	1.25	0.14	0.63	0.59	0.77	0.20	-
Melon T	0.15	0.07	1.50	0.05	0.58	0.83	0.19	0.17	0.75(0.80)
Melon	0.15	0.09	1.23	0.12	0.64	0.72	0.39	0.05	0.41(0.61)
Buckled	0.15	0.10	1.19	0.13	0.53	0.59	0.49	0.02	0.38(0.59)
$\gamma = 88^\circ$	0.16	0.11	1.24	0.14	0.51	0.87	0.39	0.09	0.45(0.62)
$\gamma = 89^\circ$	0.15	0.10	1.23	0.13	0.59	0.78	0.44	0.05	0.43(0.61)
$\alpha = 92^\circ$	0.15	0.09	1.23	0.12	0.66	0.68	0.41	0.06	0.41(0.60)
$\alpha = 95^\circ$	0.15	0.09	1.23	0.12	0.66	0.66	0.52	0.02	0.41(0.60)
$\alpha = 98^\circ$	0.14	0.09	1.24	0.12	0.69	0.60	0.54	0.06	0.40(0.60)
$\beta = 92^\circ$	0.16	0.09	1.23	0.12	0.67	0.65	0.40	0.08	0.41(0.61)
$\beta = 95^\circ$	0.15	0.09	1.22	0.12	0.65	0.67	0.49	0.04	0.41(0.61)
$\beta = 98^\circ$	0.15	0.09	1.23	0.12	0.65	0.64	0.64	0.02	0.40(0.60)
Shift	0.15	0.08	1.29	0.15	0.67	0.61	0.80	0.23	0.32(0.55)

3.5.2. Multiple phases

So far only single phase structures have been considered to model the data obtained by neutron analysis. However, it has been mentioned (Section 3.4.2) the disorder in graphitic carbon nitride materials may be due to the presence of polymeric fragments that differ in size and shape. As seen with the XRD analysis many combination of structures are possible. Therefore in this section only the structure that provided best fit to the measured D(r) of C_3N_4 -500, the Melon with shifted layers previously discussed, is used as the main phase and is combined with others.

As seen in Table 3.4, the area contribution of the peak at 1.03 Å for Melon is too intense meaning the hydrogen content in that modelled structure is too high. To reduce the hydrogen level fully polymerised structures are used as secondary phases. The ratio of

the phases is left floating until a constant R_w is obtained. The peak area ratios and R_w for the different combinations are summarised in Table 3.5.

The Melon structure combined with the heptazine-based g-C₃N₄, with a 70:30 contribution, provides the lowest R_w value, and the peak area contribution of the N-H bond is found identical to the experimental one. While in a first instance these observations could be indicative of a material with a degree of polymerisation higher than Melon, this high level of heptazine-based g-C₃N₄ in this intermediate system is surprising since the atomic concentration for Melon is found coherent with the measured value. It is possible the peak at 1.03 Å is artificially enhanced by the correction for inelastic scattering, an effect which also applies to all the other peaks involving hydrogen in the D(r).

Table 3.6 Summary of peak areas from D(r) of mixed phases. Summary of the peak areas normalised vs. A_{II} and obtained from the D(r) generated from missed phases of Melon with shifted layers and fully polymerised g-C₃N₄. The peak position and the values for the measured differential correlation function are also listed for comparison. R_w values are provided for the range 0-6 Å and in brackets for the whole range 0-20 Å.

	A_{peak}/A_{II}								
	I	III	IV	V	VI	VII	VIII	IX	R_w
r (Å)	1.03	2.07	2.31	2.72	3.52	4.03	4.62	5.14	-
C ₃ N ₄ -500	0.07	0.14	1.25	0.14	0.63	0.59	0.77	0.20	-
Shift	0.15	0.08	1.29	0.15	0.67	0.61	0.80	0.23	0.32(0.55)
Heptazine A-B	0.07	0.07	1.29	0.17	0.77	0.78	0.75	0.23	0.27(0.52)
Heptazine A-A	0.10	0.08	1.29	0.16	0.74	0.70	0.79	0.23	0.28(0.86)
Triazine A-B	0.14	0.09	1.33	0.15	0.67	0.64	0.86	0.25	0.32(0.55)

3.6. Summary and preliminary conclusions

Graphitic carbon nitride is prepared *via* thermal polycondensation of melamine. The effect of the synthesis conditions on graphitic carbon nitride materials are investigated by mean of, among others, x-ray diffraction (XRD), elemental analysis (CHN) and solid state NMR. After evaluating the effect of the condensation temperature and the length of the reaction, it is found that the minimum required conditions for the formation of the desired product are 500 °C for at least 5 h (Section 3.2). Elemental analysis of samples

synthesised at different conditions shows a decrease in hydrogen content and an increase in C:N ratio with increasing temperature synthesis. This, together with the increase of the terminal secondary amino group shown by NMR, allows to confirm the general synthesis path that was proposed in the literature. Upon heating, melamine reacts and heptazine based molecules are formed as Melem. With further increase of temperature and time the polymerisation of these units bring to formation of bigger fragments, characterised by higher thermal resistance, up to the formation of graphitic carbon nitride above 500 °C. When the temperature is further increased the stacking of the polymeric sheets becomes more organised and densely packed which is translated in a sharper and shifted (002) reflection in the XRD pattern. The size of the fragments is not uniform since only a broad and weak peak at about $2\theta = 13$ is observed in the XRD pattern. This is in agreement with the results obtained from CHN and NMR analysis which shows a partially polymerised g-C₃N₄.

In the past years, graphitic carbon nitride structure has been investigated by mean of electron diffraction and NMR and it was described as a heptazine-based polymer. The proposed models provided information about the 2D structure of the material, leaving the 3D packing unexplored. In this study, x-ray and neutron diffraction techniques are used together to further confirm the validity of the proposed models and to obtain more information about the relative organisation of the layers.

From an XRD point of view the most likely structure is found to be that of Melon. The peak at $2\theta = 13^\circ$ corresponds to the (210)_{orthorhombic} reflection and not the (100)_{hexagonal} as it was previously reported in the literature. By introducing some modification to the structure it is found possible to control the intensity of this peak. The best results are obtained by introducing some elements of disorder in the alignment of the layers. The most promising structure is found to be the Melon where the layers are shifted with respect to each other resulting in an A-B stacking configuration. This is also confirmed by neutron diffraction. Graphitic carbon nitride materials can be described as heptazine-based polymeric fragments organised in regular layers stacked along the *z* axis and with an off-set along the *x* and *y*. The possible symmetry of the crystal structure of graphitic carbon nitride was evaluated by indexing of the experimental pattern. It emerged that the symmetry that would justify all the observed peaks is orthorhombic with a space group Cmmm.

Finally the label for the class of materials that is produced by the thermal polycondensation of small organics should not be g-C₃N₄ since, as seen in this chapter, a

fully polymerised product is not obtained. A more accurate representation is $g-C_xN_yH_z$. However, since it has become customary in literature to refer to them as $g-C_3N_4$, for simplicity in this work the same notation is employed.

Chapter 4

The co-catalyst: Platinum

4.1. Introduction

As already seen (Chapter 1) the co-catalyst has an important role in photocatalytic processes, especially water splitting. Its role is that of acting as an electron trap and preventing charge recombination. Graphitic carbon nitride is among those catalysts that benefit from the assistance of a co-catalyst. Maeda *et al.* in 2009⁶⁸ investigated the performances of graphitic carbon nitride in the presence of different co-catalysts nanoparticles and they concluded that, if H₂ is the desired product, platinum nanoparticles are the best choice. In their study they compared the efficiency of Pt-g-C₃N₄ using different precursors of platinum, loading procedures and amounts. However, more than one parameter was often changed between the experiments making the comparison of the data challenging. Moreover, the study of the chemical composition of the co-catalyst (for example oxidation state or dispersion) was not presented.⁶⁸ Additionally, the variety of loading procedures used in the literature prevents a direct comparison of the results and often the co-catalyst is not well characterised.^{24, 136-138} Another important aspect to consider is the change produced on the nanoparticles during the photocatalytic process. Photocatalytic hydrogen evolution involves many factors: light, sacrificial agents, pH, etc. which can all influence the morphology and composition of the co-catalyst. To be able to maximise the performance of the catalytic system it is important to increase the understanding about all the elements involved in the photocatalytic process and their effect on the co-catalyst.

Additionally to the morphology and composition of the co-catalyst, its actual role in the photocatalytic hydrogen evolution process has to be better understood. It was mentioned (Chapter 1) that the co-catalyst, especially platinum, acts as an electron trap, by receiving the electrons from the semiconductor and preventing the backflow and charge recombination. However, in some cases the co-catalyst is described as having a different role: producing electrons after photoexcitation which will then be injected in the semiconductor.^{139, 140} This is ascribed to the metal surface plasmon resonance (SPR). When the light reaches the nanoparticle (NP) its electromagnetic field causes the free electrons of the metal to move,^{140, 141} this creates a negative and a positive pole in the particle. As a consequence an electric field opposite to that of the light irradiation is generated within the NPs. This brings the electrons to oscillate with a specific frequency: the plasmonic frequency. When the frequency of the light is equal to the plasmonic frequency of the NPs the electrons start to oscillate. In order to move, the electrons have to absorb energy and they do so from the light.^{140, 141} A fast way to detect this plasmonic phenomenon is by UV-Vis spectroscopy. Since usually the plasmonic frequencies of metal nanoparticles correspond to the frequency of UV-Vis light, this is translated in the absorption of a specific wavelength in that region.¹⁴¹

Even though this phenomena is very promising it brings some confusion in its identification and interpretation since each metal has a different resonance which also varies depending on the shape and size of the particle. In addition, in small metal NPs there are other electron transitions (interband transition)¹⁴² that could be easily confused with SPR when using UV-Vis absorption. Plasmonic effect of noble metals like Au and Ag is confirmed, however, platinum seems to arise some debate on its actual role in photocatalytic processes. Some authors consider platinum as a non plasmonic co-catalyst acting as a normal electron trap,¹⁴³ some others instead consider it as the source of electrons due to its surface plasmon resonance.¹³⁸

In this chapter platinum is investigated under many aspects from the loading procedure to the changes during photocatalysis, with the aim to better understand the system Pt-g-C₃N₄. To do so, evaluation of photocatalytic activity and analytical techniques like: transmission electron microscopy (TEM) and x-ray photoelectron spectroscopy (XPS) are employed.

4.2. Preliminary activity investigation

The previous chapter described the characterisation of C₃N₄-500, -550 and -600. In this chapter the catalytic activity of these materials for hydrogen evolution under visible light is evaluated. Initially the activity of the catalyst is evaluated in the absence of the co-catalyst. The measured hydrogen evolution rate for the pristine g-C₃N₄ is found to be 2 $\mu\text{mol}\cdot\text{h}^{-1}\cdot\text{g}^{-1}$ for the one synthesised at lower temperature and 3 $\mu\text{mol}\cdot\text{h}^{-1}\cdot\text{g}^{-1}$ for C₃N₄-550 and -600 (Table 4.1). This shows slightly higher activity for the catalyst synthesised at higher temperature. In the previous chapter it was seen that with increasing synthesis temperature the band gap of the material decreases from 2.76 eV to 2.70 eV (Table 4.1). In terms of wavelength that can be absorbed by the material to excite its electrons, this means a shift of 10 nm towards the visible range ($E = hc/\lambda$), from 449 nm to 459 nm. The lamp used for the investigation (Figure 2.16, red line) emits more light of 459 nm than 449 nm. Therefore more excited electrons are produced in C₃N₄-550 and C₃N₄-600. However, for these low values of hydrogen the error on the GC measurement is too high to state with certainty that there is an actual increase in performance.

Table 4.1 H₂ evolution rates for C₃N₄-500, -550, -600. H₂ evolution rates for pristine g-C₃N₄ and g-C₃N₄ loaded with 1 wt.% Pt *via* calcination method. Surface area (SA) and band gap (E_g) are also listed for clarity. Test conditions: 0.2 g of catalyst in 0.2 L of 0.025 M aqueous solution of oxalic acid, visible light ($\lambda \geq 420$ nm). Value of evolution rates are averaged over a 20 h testing time (batch).

Temperature (°C)	H ₂ evolution rate ($\mu\text{mol}\cdot\text{h}^{-1}\cdot\text{g}^{-1}$)		SA ($\text{m}^2\cdot\text{g}^{-1}$) ± 1	E _g (eV)
	g-C ₃ N ₄	1wt.% Pt-g-C ₃ N ₄		
500	2	1100	8	2.76
550	3	728	14	2.73
600	3	726	32	2.70

When 1 wt.% of platinum⁵⁴ is loaded on the surface of g-C₃N₄ by impregnation followed by calcination the performance is drastically increased (Table 4.1). The measured H₂ evolution rates for C₃N₄-500, -550, -600 are 1100, 728 and 726 $\mu\text{mol}\cdot\text{h}^{-1}\cdot\text{g}^{-1}$ respectively. Despite the band gaps, different from the pristine samples, when platinum is loaded the most active material is the one synthesised at lower temperature. Since this is true only when platinum is loaded the reason must be found in the interaction between catalyst and

co-catalyst. In the previous chapter it was found that higher thermal treatment brings to lower wt.% yields after the synthesis, 50 % for C₃N₄-500, 45 % for C₃N₄-550 and only 30 % for C₃N₄-600 (Table 3.2). This is associated with an increase of surface area from 8 ± 1 to 32 ± 1 m²·g⁻¹ but no change of particle size (Table 3.2). The reason for this was ascribed to the progressive decomposition and “peeling-off” of the outer layer revealing a rough surface (Figure 3.9). The higher surface area could be the reason for the lower performance of the catalyst once platinum is loaded on its surface. The process of hydrogen evolution is driven by light absorption by the catalyst and electron transfer to the co-catalyst. The walls of the channels in the catalyst will see less light than the outer surface, therefore if the platinum precursor, during the impregnation procedure, enters those channels it is possible to assume that the electron transfer will not be as efficient as on areas directly exposed to light irradiation and the effective amount of co-catalyst participating in the photocatalytic hydrogen evolution reaction is reduced.

For its higher activity only C₃N₄-500 will be employed for further investigations on the interaction between platinum and g-C₃N₄. For simplicity it will be referred to as g-C₃N₄ and Pt-g-C₃N₄ when loaded with platinum.

4.3. Effect of the loading procedure

The traditionally employed loading procedures for platinum in photocatalytic applications are: impregnation of a solution of the precursor followed by mild thermal treatments^{25, 54, 68} and photodeposition.^{54, 68, 144} The former method is done *ex-situ* before the catalytic test while the latter approach is carried out *in-situ* the testing reactor and it is driven by light irradiation.^{54, 68} These procedures are employed in the current investigation to load platinum from chloroplatinic acid (H₂PtCl₆·6H₂O) and investigate the effect on its morphology and composition. An additional third procedure is investigated: a simple impregnation of the platinum precursor solution on the catalyst without further treatment. To allow a comparison between the three loading procedures the same amount of platinum (1 wt.%)⁶⁸ is used and the samples are tested for hydrogen evolution under visible light. In Table 4.1 the hydrogen evolution rates for the three different Pt-g-C₃N₄ are summarised. The results are expressed in both μmol·h⁻¹·g⁻¹ and in ml·h⁻¹·g⁻¹ (the normalisation is per g of catalyst) to allow a more direct appreciation of the amount produced. Also included in Table 4.2 is the apparent quantum yield (AQY) which considers the amount of photons introduced into the reaction chamber (Chapter 2). The apparent quantum yield aims to normalise the performance by the light source

employed. It does not, however, account for mass of catalyst or geometry of the reactor. For these reasons and because the light source employed throughout this study is the same, a normalisation by mass of catalyst ($\mu\text{mol}\cdot\text{h}^{-1}\cdot\text{g}^{-1}$) is preferred. Nonetheless, for clarity the AQY values will also be presented.

Table 4.2 Comparison of loading methods. H₂ evolution rates and apparent quantum yield for Pt-g-C₃N₄ prepared using three different loading methods. Test conditions: 0.2 g of catalyst in 0.2 L of 0.025 M aqueous solution of oxalic acid, visible light ($\lambda \geq 420$ nm). Value of the evolution rates are averaged over a 20 h testing time (batch).

Loading method	H ₂ evolution ($\mu\text{mol}\cdot\text{h}^{-1}\cdot\text{g}^{-1}$)	H ₂ evolution ($\text{ml}\cdot\text{h}^{-1}\cdot\text{g}^{-1}$)	Apparent Quantum Yield (%)
Impregnation	1280	31	0.69
Impregnation and calcination	1100	27	0.59
Photodeposition	732	18	0.39

The Pt-g-C₃N₄ samples prepared employing the traditional methods (*via* impregnation followed by calcination and photodeposition) give the lowest hydrogen evolution under visible light with the photodeposited material giving the worst performance out of the two. When the platinum precursor is simply impregnated on the catalyst a ~16 % improvement is found compared to the calcined Pt-g-C₃N₄ (Table 4.2). This shows that the post impregnation calcination step can be a limiting factor in the final performance of the material. The better performance of the thermally treated sample against the photodeposited one has been reported by Maeda *et al.*⁶⁸. The authors explained that the photodeposition method results in the formation of large agglomerates of platinum nanoparticles and therefore less active sites. The proposed mechanism sees the platinum precursor being reduced on the surface of g-C₃N₄ during the photodeposition; the newly formed platinum metal nanoparticles becomes an electron trap and therefore favourable site for the next reductions, leading to large Pt⁰ clusters.⁶⁸ However, in the preparation of their materials Maeda *et al.* used two different precursors and loading amounts: 1 wt.% Pt from H₂PtCl₆ for the photodeposition method and 3 wt.% Pt from Pt(cod)₂ for the impregnation followed by calcination, making the results of the two methods difficult to compare. Nonetheless a 100 % increase in hydrogen evolution was achieved, which is above the ~50 % increase presented in Table 4.2. This indicates at this stage that the

performance of the material is more affected by the loading procedure than the choice of precursor and/or the Pt loading.

To investigate the influence of the loading procedure on the morphology and composition of the co-catalyst the materials are studied by XPS and TEM. In a first series of experiments the starting materials, which can only include the two Pt-g-C₃N₄ prepared *via* the impregnation routes (*ex-situ*), are analysed. The N 1s and C 1s XP spectra of the two samples are presented in Figure 4.1.

In both cases the typical peaks of graphitic carbon nitride can be identified. For the N 1s region the nitrogen atoms characterised by sp^2 hybridisations (C-N=C, within the triazine ring)^{57, 145-147} are identified by the peak at binding energy of 398.7 eV which is supported by the presence of a π -excitation signal at 404.5 eV; characteristic of aromatic compounds.^{145, 148} The bridging nitrogen atoms and the amine groups are identified by the components at 400.0 eV and 401.2 eV, respectively.¹⁴⁵⁻¹⁴⁷ For the C 1s region, four peaks are identified. A binding energy of 288.3 eV corresponds to the sp^2 carbon atoms (C-N=C).^{86, 146, 148, 149} As in the nitrogen region, the presence of aromatic character is supported by the presence of the π -excitation signal at 293.7 eV.¹⁴⁸ Two extra small peaks are present at binding energies of 284.6 eV and 289.8 eV. These can be attributed to C-C and C-O species, respectively.¹⁵⁰ The presence of oxidised carbon could be caused by a slightly oxidation during the synthesis of graphitic carbon nitride which is carried out under air. A similar explanation could be given for the C-C bonds, formed as by-products

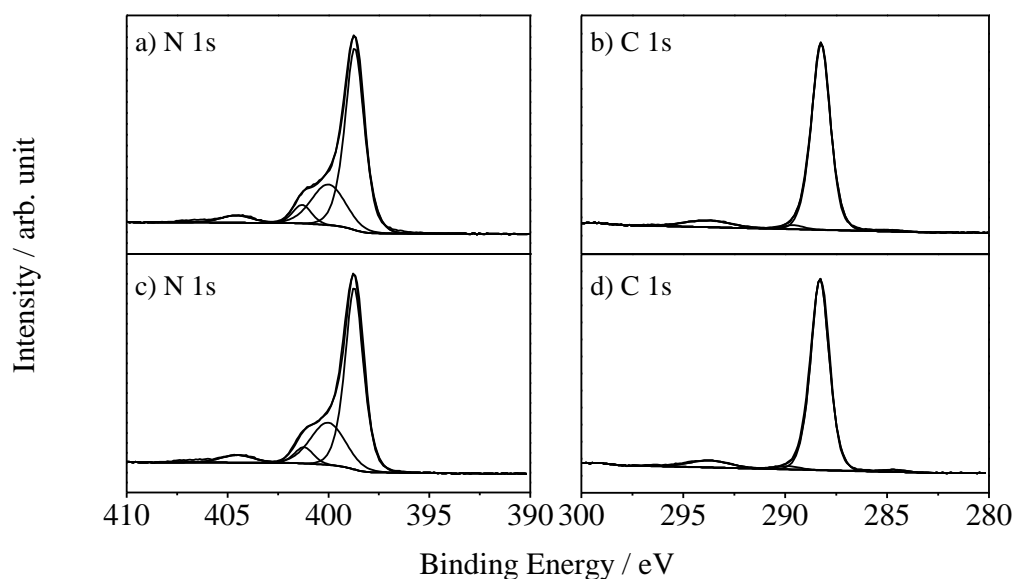


Figure 4.1 N 1s and C 1s XP spectra of samples before test. XP spectra of N 1s and C 1s regions for Pt-g-C₃N₄ a, b) simply impregnated and c, d) thermally treated.

of the thermal poly-condensation. These, however, are in small quantities and do not compromise the nature of the material. Furthermore, they are also present in examples described in literature, even though not discussed.⁵⁷ With the XP N 1s and C 1s spectra for Pt-g-C₃N₄ remaining identical to the as-made g-C₃N₄ scanned under the same conditions, it is reasonable to conclude that the loading of the co-catalyst has no effect on the surface chemical composition of the catalyst.

XPS Pt 4f spectra for these materials are shown in Figure 4.2. Two main species of platinum can be identified for each Pt-g-C₃N₄. The peak at binding energy 72.8 eV is assigned to Pt^{II}O^{91, 136, 151} and the peak at 75.0 eV to PtCl_x species. The presence of chlorides is confirmed by a peak at 198.1 eV in the Cl 2p region (Figure 4.2 inset). In the case of calcined Pt-g-C₃N₄ a higher content in platinum oxide could be expected, due to the thermal treatment being carried in air. However, in both cases the ratio between PtO and PtCl_x is 0.8. This indicates that the mild thermal treatment is not enough to bring any significant change in the composition of the platinum on the surface of graphitic carbon nitride, and therefore not responsible for the difference observed in hydrogen evolution. The Pt:N ratios, calculated using the total peak areas of platinum and nitrogen, for the simply impregnated and the impregnated followed by calcination samples are 0.030 and 0.037, respectively. These values are within the average of 0.04 ± 0.01 estimated for the impregnated Pt-g-C₃N₄. At this stage the difference between the two sets of

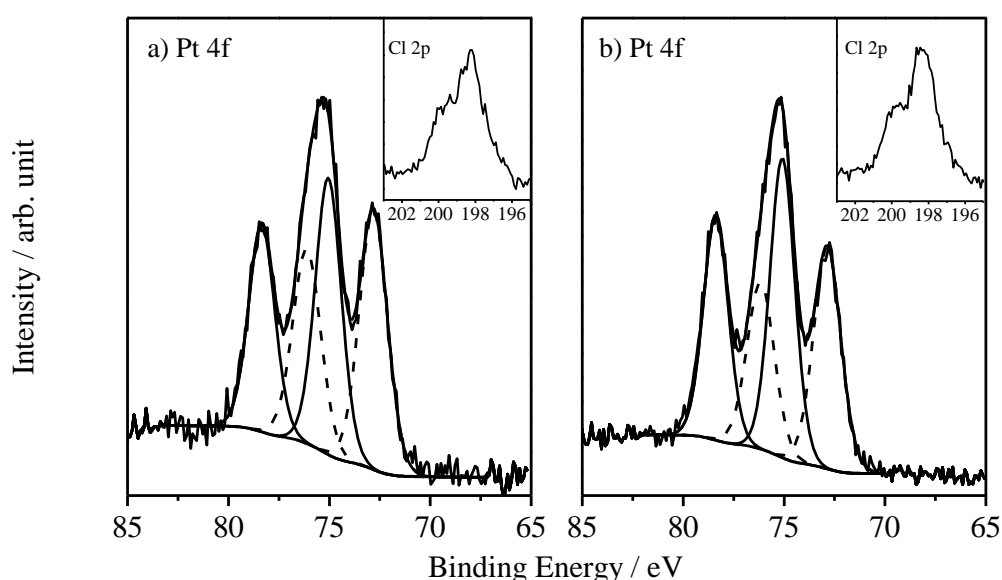


Figure 4.2 Pt 4f XPS spectra before photocatalysis. Pt 4f XPS spectra of Pt-g-C₃N₄ a) impregnated and b) thermally treated before photocatalysis. PtO: dashed line; PtCl_x: solid line. Inset: Cl 2p spectra.

measurements is not thought to be significant, suggesting that the Pt NPs morphology is not effected by the thermal treatment.

Figure 4.3 shows TEM and high resolution TEM images for the samples before photocatalytic test. The chloride species identified from XPS analysis are expected to be in a monoatomic layer dispersion on the surface of the catalyst, therefore no particles should be seen. However, the platinum (II) oxide can be expected to be present in the form of particles. It is important to mention that, for both samples, during the preparation of the TEM specimen the nanoparticles are removed from the support and can be detected on the copper grid used for the analysis. This indicates that the contact between the catalyst and co-catalyst is not strong enough to withstand suspension in solvents, making the identification of the nanoparticles, on the actual support, challenging.

As expected, for both Pt-g-C₃N₄ samples nanoparticles can be identified on the surface of graphitic carbon nitride. The HRTEM images reveal lattice fringes for the nanoparticles of both samples (Figure 4.3b and d). For the impregnated Pt-g-C₃N₄, however, these are less clear than for the calcined one, probably due to an increased level of crystallinity of the latter, achieved after thermal treatment. The measured values are

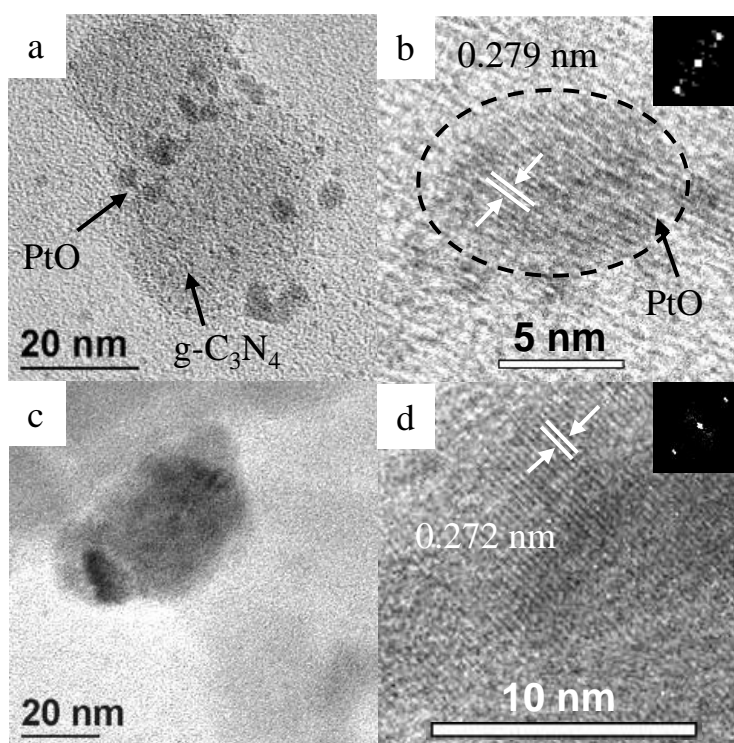


Figure 4.3 TEM and HRTEM images of Pt-g-C₃N₄ before photocatalytic test. TEM and HRTEM images of Pt-g-C₃N₄ a) and b) simply impregnated, c) and d) after thermal treatment at 180 °C for 2 h. Insets b) and d) shows diffractograms obtained for the nanoparticles.

0.279 nm and 0.272 nm for the impregnated and calcined respectively, and correspond to the (002) plane of PtO.¹⁵² The higher values compared to the tabulated one (PDF card # 42-0866)¹⁵² can be associated to the error of TEM measurements (Chapter 2) but also to a not well crystallised phase. Nonetheless, these findings are in agreement with the XPS results which identified PtO as one of the main species. When simple impregnation is employed as the loading procedure, particles sized 3-10 nm are formed (Figure 4.3a). Due to the difficulties in identifying the particles it is not possible to estimate an average particle size. After the thermal treatment the nanoparticles join together forming bigger agglomerates characterised by a size of 20-40 nm. Sintering of nanoparticles after thermal treatment has also been observed for other systems in the literature.¹⁵³ However, the presence of big particles in the TEM images is not coherent with the XPS results discussed earlier which seem to indicate that the Pt NPs distribution remains the same between the simply impregnated sample and the impregnation followed by calcination. It is important to remember that TEM only provides two-dimensional images, hence the particles seen in Figure 4.3 c-d could be considered as the result of the migration of the PtO NPs into a thin layer agglomerate rather than the formation of large three dimensional platinum structures. This would not produce an effect on the Pt:N ratio and be coherent with the XPS data. Nonetheless, the performance for hydrogen evolution are found to be decreased for the calcined material (Table 4.2). An unchanged Pt:N ratio suggests that the contact surface between platinum species and carbon nitride is not modified. On the other hand, since the amount loaded is the same, a fusion of the NPs would produce a decrease in the surface area of the nanoparticles, hence the active sites for the reaction would be less.

As previously discussed (Table 4.1), the simply impregnated sample is also more active than the photodeposited one. Since the photodeposition of the co-catalyst is an *in-situ* method, a comparison between the two loading procedures before photocatalysis is not possible. XP spectra of Pt 4f regions of the impregnated and photodeposited samples after photocatalytic evaluation of performance are shown in Figure 4.4.

After photocatalysis the curve fitting of the Pt 4f envelopes for both the impregnated and photodeposited samples shows the presence of two main species. The peak at 72.8 eV is representative of PtO^{91, 136, 151}, and the peak at 70.8 eV is associated to Pt^{0 24, 91, 136, 151}. It appears that as a result of exposure to visible light the platinum chloride that was originally observed for the impregnated sample reduces to platinum metal and this

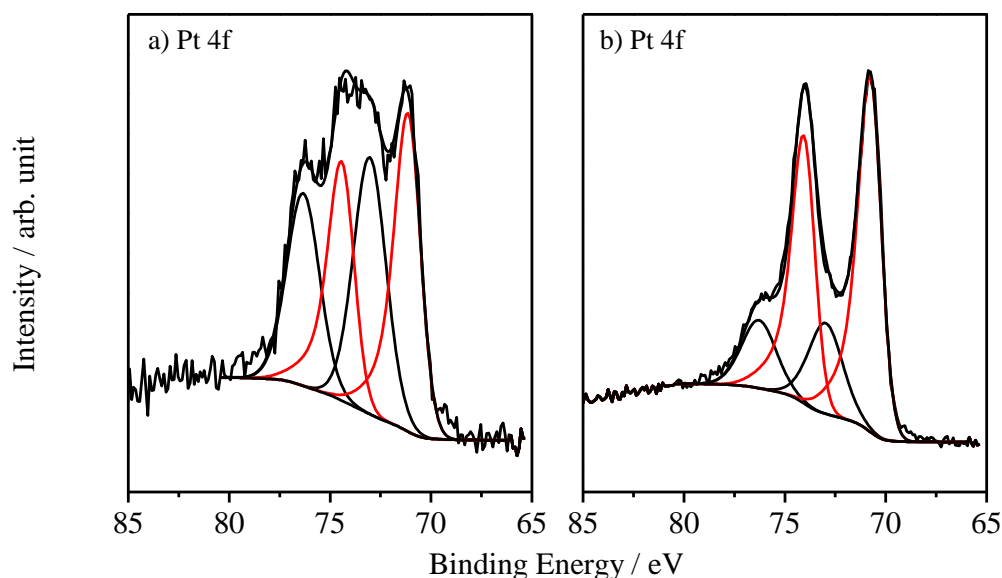


Figure 4.4 Pt 4f XPS spectra after photocatalysis. Pt 4f XPS spectra of Pt-g-C₃N₄ a) impregnated and b) photodeposited after photocatalysis. PtO: black line; Pt⁰: red line¹⁵⁴.

reduction happens for both loading procedures. At this stage, the mechanism behind the reduction of platinum chloride is not yet known.

Also in term of terminology a distinction needs to be made between the two loading procedures. It is correct to talk about photodeposition because the platinum precursor is in solution in the presence of the catalyst and by light irradiation this is simultaneously photoreduced and deposited on the surface of the g-C₃N₄. For the impregnated material the platinum precursor is already deposited on the surface of g-C₃N₄ and during the photocatalytic process it is photoreduced. This loading method can therefore be seen as a *photoreduction*.

Even though the two samples in Figure 4.4 show the same platinum species on the surface, they are present in different relative amounts. For the impregnated sample (Figure 4.4a) the ratio between PtO and Pt⁰ is 1:1.3 (42.6 % PtO; 57.4 % Pt⁰), for the photodeposited sample (Figure 4.4b), on the other hand, the ratio is 1:3 (25.2 % PtO; 74.8 % Pt⁰). This difference may be explained by the fact that for the impregnated sample some PtO is already present on the g-C₃N₄ leaving less PtCl_x available for photoreduction. However, when the platinum precursor (*i.e.* chloroplatinic acid) is added in the reaction chamber it is all available to be reduced, bringing to a higher content of metal compared to the oxide. The two samples also show to be different in the platinum to nitrogen ratio. For the impregnated method the Pt:N ratio is 0.04, and for the photodeposited it is 0.08. As

mentioned earlier, for the same amount of platinum, a higher Pt:N ratio is indicative of a more uniform distribution of the platinum on the surface of the support, with the formation of smaller particle size. In order to confirm this, TEM is used to look at the morphology of the nanoparticles.

Figure 4.5 shows TEM and HRTEM of the impregnated and photodeposited sample after photocatalysis. The impregnated Pt-g-C₃N₄ (Figure 4.5a and 4.5a inset) shows nanoparticles sized 2.3 ± 1.2 nm with formation of some clusters. When the platinum is photodeposited (Figure 4.5c and 4.5c inset) the average particle size is smaller with a value of 1.3 ± 0.6 nm. These results agree with the observations made from the C:N values obtained from XPS analysis and discussed in the previous paragraph. In both cases lattice fringes can be seen at higher magnification (Figure 4.5b and 4.5d) in the TEM images. They correspond to the (111) plane of platinum metal^{151, 155} with a d-spacing of 0.224 nm and 0.227 nm (PDF card # 04-0802).

It was previously mentioned that during the TEM specimen preparation of Pt-g-C₃N₄ before photocatalysis the nanoparticles were removed from the support. After photocatalysis, this phenomenon is not observed and the NPs are more easily spotted.

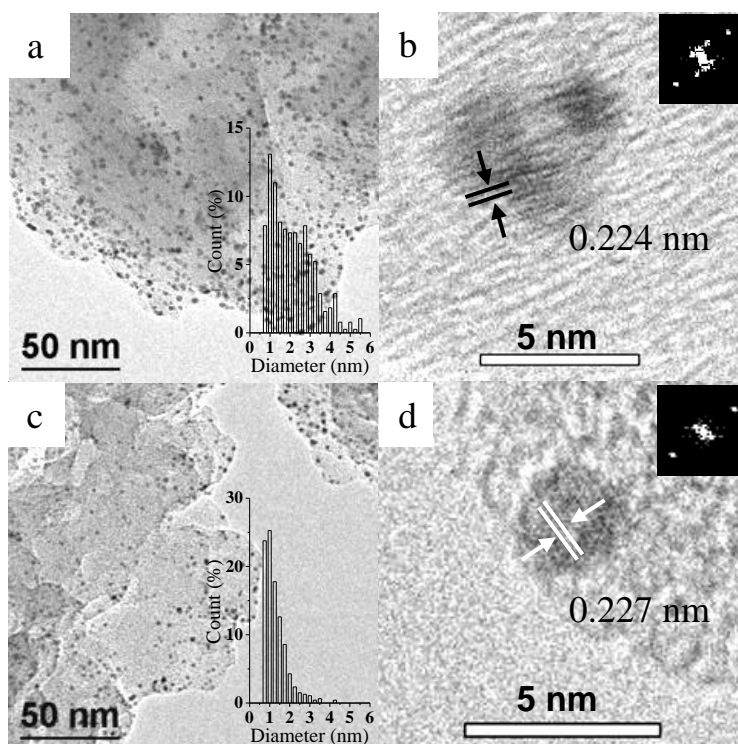


Figure 4.5 TEM and HRTEM of Pt-g-C₃N₄ after photocatalysis. TEM and HRTEM images of a, b) impregnated and c, d) photodeposited Pt-g-C₃N₄ after photocatalysis. Insets a, c) particle size distribution, b, d) diffractograms of the nanoparticles.

This clearly indicates a stronger interaction between the platinum and graphitic carbon nitride. This has been explained with the interaction between the Pt nanoparticles and the nitrogen atoms contained in the polymer structure.¹⁵¹ Examples of this behaviour have been reported for other metallic nanoparticles, for example Ni¹⁵⁶ and Ag¹⁵⁷.

The impregnated and photodeposited samples are also analysed *via* XRD after photocatalysis. To acquire the diffraction patterns the used catalysts are collected, transferred into a flask and let deposit at the bottom. After removal of the water the samples are dried under argon flow. The diffractograms are compared in Figure 4.6. The low amount of platinum loaded and the small size of the nanoparticles, make the detection of the Pt⁰ challenging. However, a weak peak at 39.8° (0.226 nm) characteristic of the (111)^{136, 151, 155, 158, 159} reflection plane can be seen in the case of impregnated Pt-g-C₃N₄ after photocatalysis. This confirms the d-spacing of 0.224 nm seen in the HRTEM images. The platinum peak is weaker and barely identifiable in the case of the photodeposited sample. Since the loading amount is the same and the relative platinum metal content is higher than for the impregnated Pt-g-C₃N₄, the less defined peak can find explanation in the smaller particle size seen from TEM imaging.

From the results presented so far, two main factors emerged that could be causing the lower activity of the photodeposited sample. The first is its higher content in platinum metal (Pt⁰/PtO = 3) compared to the impregnated sample (Pt⁰/PtO = 1.3). This may

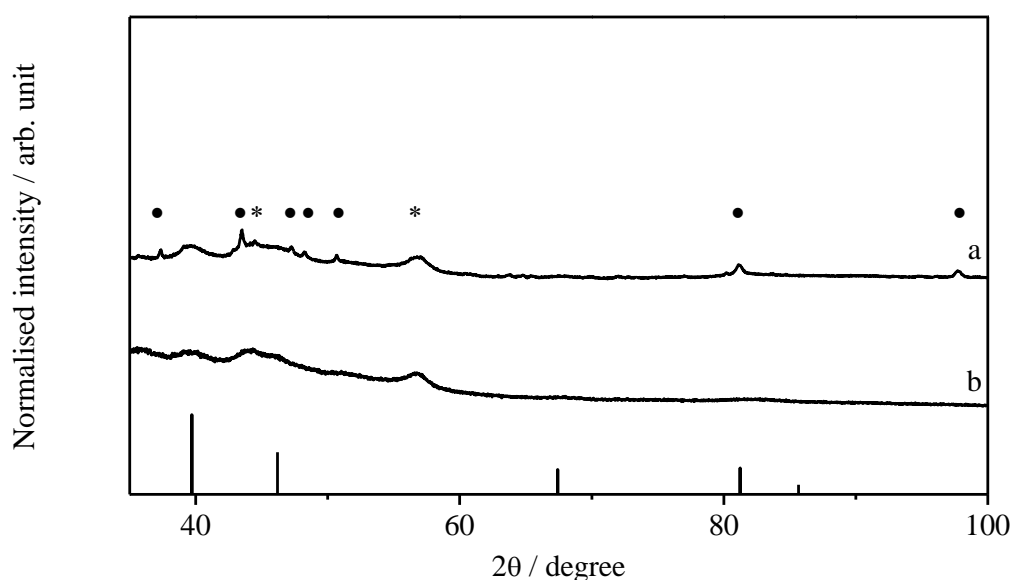


Figure 4.6 XRD patterns of sample after photocatalysis. XRD patterns of a) impregnated and b) photodeposited Pt-g-C₃N₄ after photocatalysis. ●) Holder, *) g-C₃N₄, bars) Pt⁰ XRD pattern as from ICDD database (PDF card # 04-0802).

suggest that the two species are both needed to maximise the hydrogen evolution and a possible synergistic effect could be hypothesised. The second factor is the size of the Pt NPs. Smaller particle size, for the same amount of platinum, brings to a higher coverage of the surface of g-C₃N₄, *i.e.* higher Pt:N ratio from the XPS analysis. This leads to less graphitic carbon nitride surface to be exposed to light irradiation or to the adsorption and oxidation of the sacrificial agent (oxalic acid). At this point it is not yet possible to state which one of the two factors, or if both are responsible for the difference in performance. Further investigations are therefore needed to better understand the dynamics of the process. This study will start with looking at the changes of the co-catalyst during the photocatalytic process.

4.4. Interaction with light

To gain a better understanding on the evolution of the platinum oxidation state during the photocatalytic process and try to elucidate the reason for the difference in activity between impregnated and photodeposited Pt-g-C₃N₄, the profile of hydrogen evolution of the most active material is followed hour by hour and at specific stages XPS analysis is carried out. Figure 4.7 illustrates the hydrogen evolution rate *vs.* time. In order to allow XPS characterisation to monitor the platinum species throughout the photocatalysis,

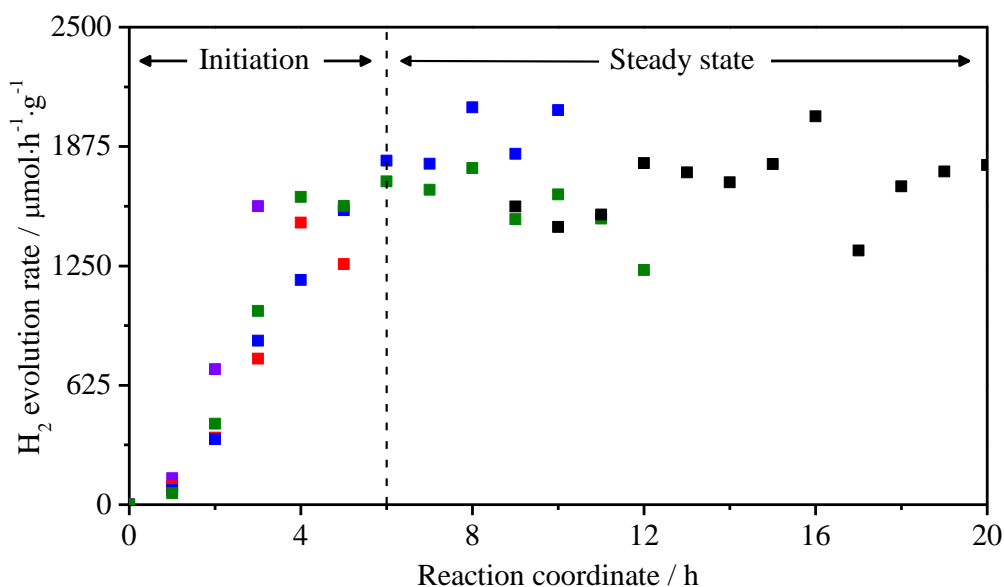


Figure 4.7 H₂ evolution rate *vs.* time. H₂ evolution rate for the impregnated Pt-g-C₃N₄. Five different photocatalytic test of different time length are shown. (■) 3 h, (■) 5 h, (■) 10 h, (■) 12 h, (■) 20 h. Test conditions: 0.2 g of catalyst in 0.2 L of 0.025 M aqueous solution of oxalic acid, visible light ($\lambda \geq 420$ nm). Reactor configuration: semi-batch, measurement every 1 h.

experiments of different time length are carried out. The catalyst is collected, dried under argon and transferred to the XPS machine through a glove box in order to minimise the effect of exposure to air on the oxidation state of the platinum. The hydrogen evolution rate is not linear over time. In the first six hours of the process it increases until reaching a constant value of $\sim 1691 \mu\text{mol}\cdot\text{h}^{-1}\cdot\text{g}^{-1}$ (AQY = 0.91 %). Therefore, the photocatalytic process can be divided in two main stages: initiation and steady state.

The first step to explain the time needed to reach a constant hydrogen production is to exclude a thermal factor. The reaction chamber is exposed to direct light and this brings to an increase in the temperature of the system. As shown in Chapter 2 (Figure 2.17), the temperature profile has a very similar trend to that of hydrogen evolution. To eliminate the temperature influence, the performance is evaluated while cooling the photocatalytic reactor and keeping the temperature constant during the test. Figure 4.8 shows the H_2 evolution rate and T profile vs. time.

When the system is cooled down the performance is lower ($642 \mu\text{mol}\cdot\text{h}^{-1}\cdot\text{g}^{-1}$, AQY = 0.34 %). This decrease in performance may be caused by a change in the kinetic of the reaction. Another possible explanation is found in the decrease of the semiconductor character with decreasing temperature. Interestingly, the initiation period of six hours is still present even though the temperature reaches a constant value (38°C)

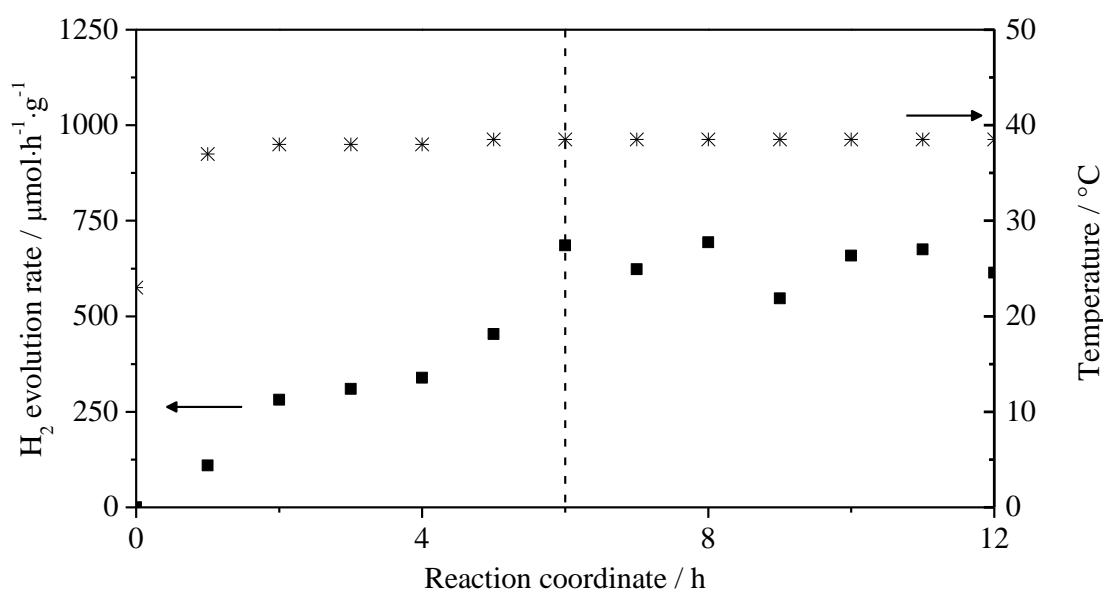


Figure 4.8 H_2 evolution rate and T vs. time upon cooling. ■) H_2 evolution rate in $\mu\text{mol}\cdot\text{h}^{-1}$ and *) temperature profile over time. Test conditions: 0.2 g of catalyst in 0.2 L of 0.025 M aqueous solution of oxalic acid, visible light ($\lambda \geq 420 \text{ nm}$). Reactor configuration: semi-batch, measurement every 1 h.

after 1 h from the beginning of the photocatalytic experiment. This demonstrates that the temperature has no effect on the profile of the hydrogen evolution rate but only on its magnitude.

Figure 4.9 show the XPS spectra of impregnated Pt-g-C₃N₄ analysed after 1.5 h, 3 h and 20 h of photocatalytic test, they are compared with the sample before photocatalysis (t = 0 h). By looking at the graph it is evident that the chlorides (75.0 eV) present before photocatalysis disappear and are replaced by metallic platinum (70.8 eV), as already discussed earlier. More importantly it is observed that the intensity of the Pt⁰ peak increases with time. However, the disappearance of PtCl_x is not as gradual as the appearance of Pt⁰ suggesting that the chlorides are instantaneously removed and slowly reduced to form metal. Since, the Pt:N ratio is constant, within error (0.04 ± 0.01), throughout the photocatalytic test, a different explanation has to be provided. The binding energy of Pt(OH)₂ is equivalent to that of PtO¹⁶⁰ and a distinction between the two in the XP spectra is not possible. Therefore, it can be assumed that once in solution the chloride species are converted in hydroxides and these are then gradually reduced to form Pt⁰.

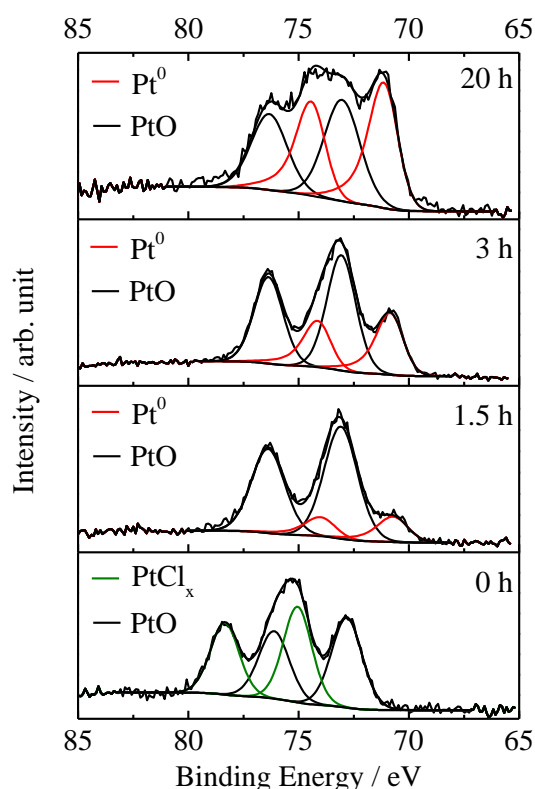


Figure 4.9 Pt 4f spectra of Pt-g-C₃N₄ at different test lengths. Pt 4f XP spectra of impregnated Pt-g-C₃N₄ before, during (1.5 h, 3 h, 20 h) and after photocatalysis. PtCl_x: green line; PtO: black line; Pt⁰: red line¹⁵⁴.

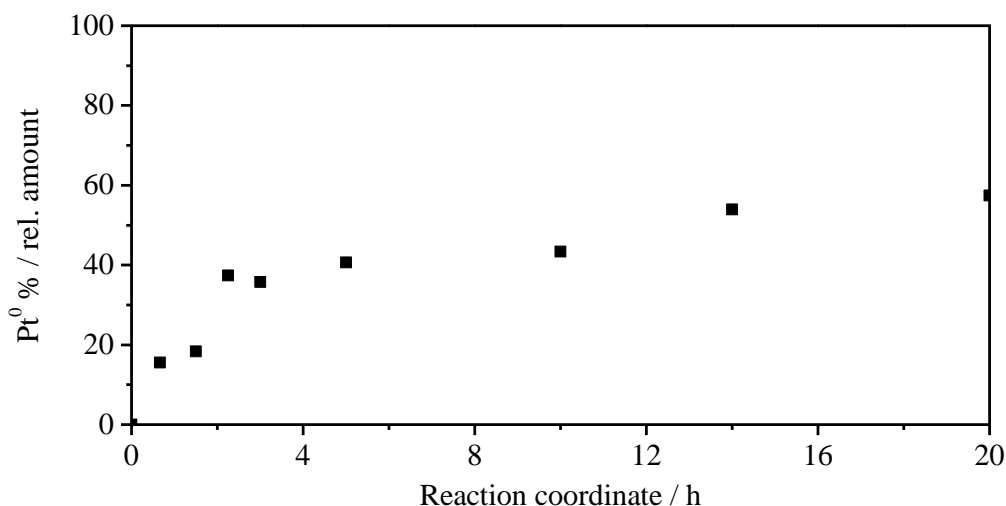


Figure 4.10 Pt⁰ relative amount vs. time. Pt⁰ % of total platinum content as obtained by XPS analysis.

Figure 4.10 shows the relative amount of Pt⁰ ($Pt^0 / P_{tot} * \%$) vs. time as obtained from XPS analysis. The platinum metal content increases in the first few hours and becomes almost constant with a value of ~ 57.4 %. This trend strongly resembles the profile of H₂ evolution rate shown in Figure 4.7. The results indicates that in the first few hours of the photocatalytic process the excited electrons produced in g-C₃N₄ by light absorption are partially employed for the reduction of platinum chloride/hydroxide to platinum metal. The initial low activity can be ascribed to less electrons being available to reduce water or, more likely, to the absence of enough metal to trap the electrons and produce hydrogen. These results, together with those illustrated in the previous paragraph, again seem to suggest that an equal amount of Pt⁰ and PtO both present on the surface of the catalyst would favour hydrogen production more than an excess of platinum metal. Implication of this would be a synergistic effect between the metal and the oxide. In order to confirm this hypothesis and decide if the lower performance of the photodeposited sample (~43 % lower) is indeed due to the amount of Pt⁰, the coverage or both, reduction pre-treatments are investigated.

4.5. Reduction pre-treatment

In an attempt to achieve reduction of the co-catalyst, two different reduction procedures are evaluated: reduction in 5 % H₂ / Ar at 300 °C⁹¹ and chemical reduction with sodium borohydride (NaBH₄)⁹². In the case of reduction under flowing hydrogen, the sample is initially reduced for different amounts of time to find the optimum condition to achieve

maximum reduction. For a fast evaluation the reduced samples are compared for hydrogen evolution. Figure 4.11 shows the H₂ evolution rates at the steady state for the samples reduced in H₂ for 12 h, 24 h, 36 h and 48 h. For comparison the hydrogen evolution rate of the simply impregnated sample is also shown. The performance of the catalyst increases from 1430 $\mu\text{mol}\cdot\text{h}^{-1}\cdot\text{g}^{-1}$ (AQY = 0.38 %) to 3150 $\mu\text{mol}\cdot\text{h}^{-1}\cdot\text{g}^{-1}$ (AQY = 0.84 %) after 12 h of reduction under hydrogen. Further increase in activity can be obtained by increasing the reduction time to 24 h (3900 $\mu\text{mol}\cdot\text{h}^{-1}\cdot\text{g}^{-1}$, AQY = 1.05 %), while longer treatments do not result in further improvement. After 36 h and 48 h the H₂ evolution rate at the steady state is 3860 and 4020 $\mu\text{mol}\cdot\text{h}^{-1}\cdot\text{g}^{-1}$, respectively. This suggests that after 24 h a maximum reduction level of the platinum is reached.

In order to verify this assumption and estimate the amount of platinum species present on the surface of the pre-reduced Pt-g-C₃N₄ materials, XPS analysis is carried out on the samples reduced for 24 h and 48 h. In both cases only platinum metal and platinum oxide are detected. The relative amounts of Pt⁰ and PtO are summarised in Table 4.3. For both samples total reduction of the chloride species is achieved. The ratio between Pt⁰ and PtO is found 1.3 after 24 h and 1.7 after 48 h reduction. The small increase in platinum metal content is not reflected in the performance of the material, which remain within the $\pm 5\%$ variation estimated for the experiments. Additionally, the Pt:N ratio is unaffected by a

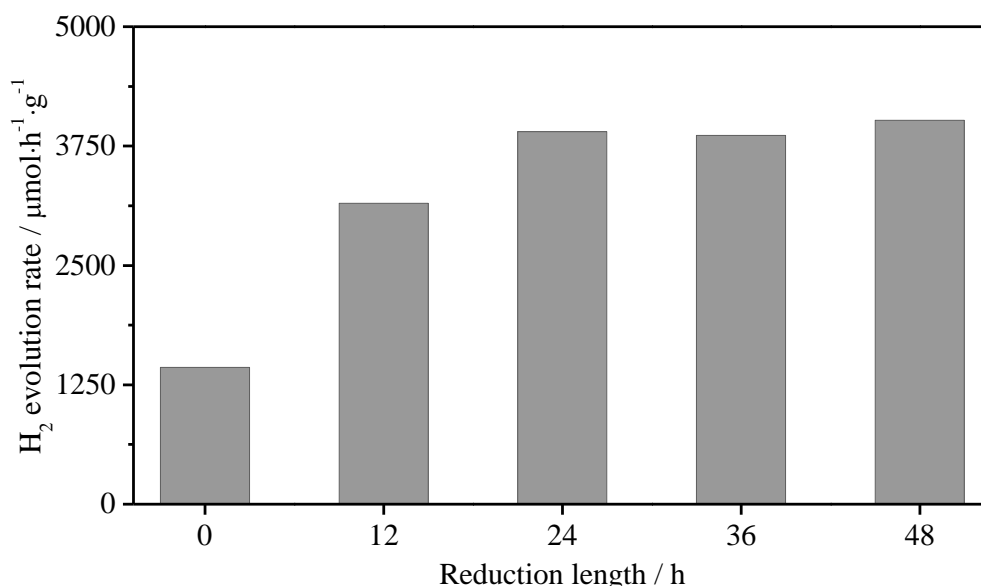


Figure 4.11 H₂ production steady state for reduced Pt-g-C₃N₄. Steady state H₂ evolution rates for Pt-g-C₃N₄ reduced in 5 % H₂/Ar at 300 °C for different lengths of time. Test conditions: 0.1 g of catalyst in 0.1 L of 0.05 M aqueous solution of oxalic acid, visible light ($\lambda \geq 420$ nm). Reactor configuration: continuous; argon flow, measurements every 20 min.

longer thermal treatment (Table 4.3), suggesting that there is no change in the morphology on the platinum nanoparticles. From these results it is possible to consider 24 h as the optimum reduction time. Further characterisation are therefore carried out on the sample reduced for 24 h. It is also interesting to notice that Pt⁰:PtO ratio for the pre-reduced samples are found in the range of the one observed for the impregnated sample after photocatalysis (1.3, Figure 4.10).

Table 4.3 XPS Pt 4f summary for Pt-g-C₃N₄ reduced in H₂. Platinum species relative amounts and Pt:N ratio for samples reduced in 5 % H₂/Ar at 300 °C for 24 and 48 h.

Reduction length (h)	PtO %	Pt ⁰ %	Pt:N
24	44.2	55.8	0.051
48	37.7	62.3	0.052

In Section 4.4, after monitoring the Pt⁰ content over time, it was concluded that in the first 6 h of the photocatalytic process the excited electrons produced in g-C₃N₄ by light absorption are partially employed to reduce the platinum cations to platinum metal. Therefore it can be assumed that since the pre-reduced material already presents the “final” Pt⁰:PtO ratio, no initiation period should be noticed. Figure 4.12 shows the performance over time of the reduced catalysts. It clearly shows that an initiation period

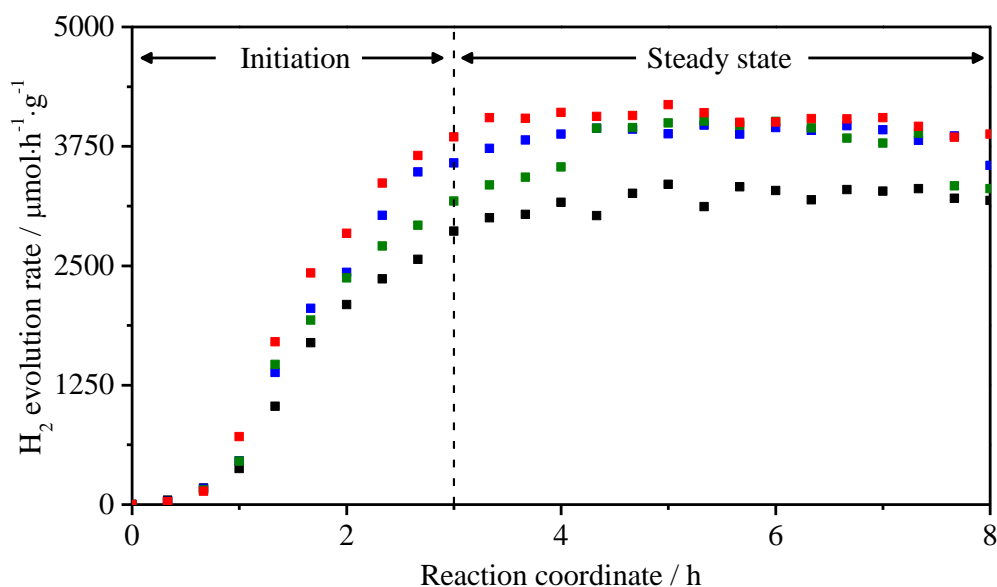


Figure 4.12 H₂ evolution rate profile for reduced Pt-g-C₃N₄. H₂ evolution rate profile for Pt-g-C₃N₄ reduced for 12 h (■), 24 h (■), 36 h (■) and 48 h (■). Test conditions: 0.1 g of catalyst in 0.1 L of 0.05 M aqueous solution of oxalic acid, visible light ($\lambda \geq 420$ nm). Reactor configuration: continuous; argon flow, measurements every 20 min.

can still be observed, but instead of 6 h (seen in Figure 4.7) it is now reduced to 3 h. Since XPS analysis shows that the ratio of PtO and Pt⁰ characteristic of the steady state production for the impregnated sample (Figure 4.10) is successfully achieved during reduction pre-treatment there is no apparent explanation for the remaining initial 3 h of increasing rate.

TEM images give information on the morphology of the platinum nanoparticles on the pre-reduced sample before and after the photocatalytic test (Figure 4.13). Figure 4.13a shows that reduction at 300 °C forms particles of irregular shape and size of 20-60 nm. Thermal treatment brings to coalescence of the platinum nanoparticles, as already seen in Section 4.2. The average particle size is found to be 4.9 ± 4.7 nm. This value is more than double the average particle size estimated for the Pt NPs formed after photocatalytic test of the impregnated sample (2.3 ± 1.2 nm) and the wider distribution well represent the formation of bigger agglomerates/nanoparticles. High resolution images (Figure 4.13b-c) show the lattice fringes of values 0.223 nm and 0.195 nm, characteristic, within error (Chapter 2), of the (111) and (100) planes of platinum metal (PDF card # 04-0802). After irradiation with visible light no big agglomerates can be found on the surface of the catalyst (Figure 4.13b). The average particle size is now 2.7 ± 1.9 nm, closer to the value of the impregnated Pt-g-C₃N₄ after photocatalysis. These findings indicates that during photocatalytic performance evaluation of the pre-reduced sample, the platinum

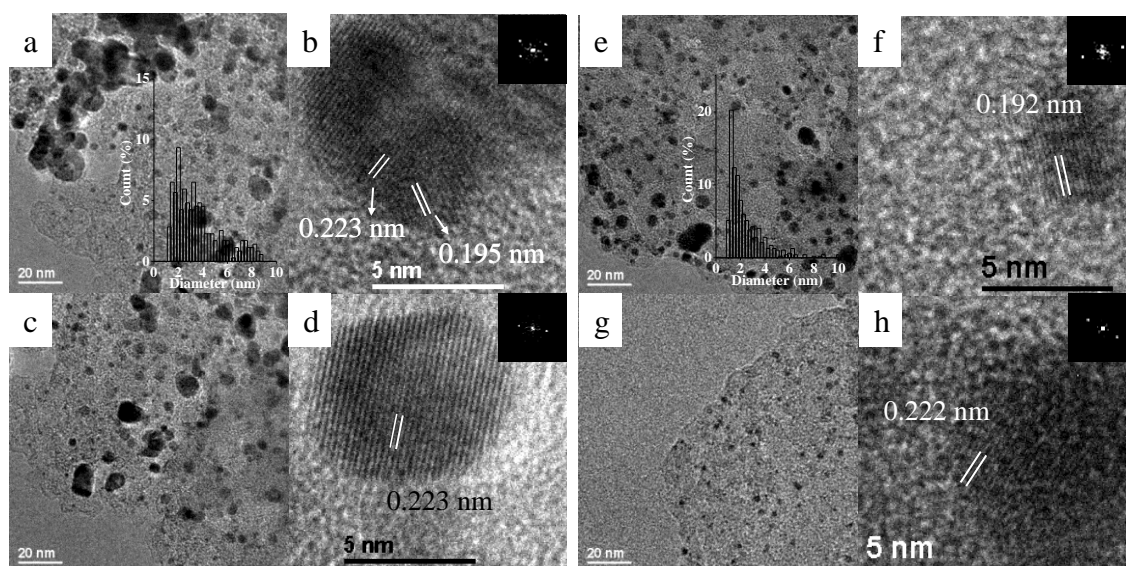


Figure 4.13 TEM images of Pt-g-C₃N₄ reduced under 5 % H₂. TEM and HRTEM images of Pt-g-C₃N₄ reduced under flowing 5 % H₂/Ar a-d) before and e-h) after photocatalysis. Insets: particle size distribution and diffractogram of selected nanoparticle.

nanoparticles rearrange forming smaller ones. This could provide the explanation for the 3 h of initiation time, and suggests that to obtain the maximum evolution rate the nanoparticles have to adopt an optimum particle size. Since the Pt⁰:PtO ratio of the two materials are very similar as well as the nanoparticles size after photocatalysis, the results obtained so far do not yet provide an explanation for the higher activity of the pre-reduced sample compared to the simply impregnated.

The x-ray diffraction pattern of pre-reduced Pt-g-C₃N₄ is shown in Figure 4.14a. In this case differently from the impregnated sample after photocatalysis (Figure 4.6), the peaks characteristic of the fcc crystal structure of Pt⁰ (PDF card # 04-0802) can be clearly identified at 39.8°, 46.3°, 67.6° and 81.4°. These corresponds to the (111), (200), (220) and (311) planes respectively.^{136, 151, 155, 158, 159} This is in agreement with the lattice fringes observed in the HRTEM images (Figure 4.13). The more visible Bragg's reflection in the XRD pattern of the reduced material compared to the impregnated one (Figure 4.6a) can be due to bigger crystallite size, but also higher level of crystallinity of the nanoparticles. This can be determine by employing the Scherrer equation and the Williamson-Hall plot. By applying the Scherrer equation on the (111), (220) and (311) reflections the crystallite size results in being 16 nm. When the same reflections are used for the Williamson-Hall plot the crystallite size is 15 nm, which is in good agreement with the result obtained from the Scherrer equation. Since the latter only accounts for the crystallite size (Chapter 2) and the former for both size and strain, the matching results indicates that the nanoparticles are well crystallised with reduced strain, which is confirmed by the small slope of the line (strain: $-2.25 \cdot 10^{-4}$) in the plot (Figure 4.14inset a).

It is worth mentioning the discrepancy between the crystallite size value obtained from XRD analysis and the average particle size estimated from TEM images. The two techniques have both limitations. With TEM only a small part of the whole sample is examined even though care is taken to acquire images on different areas of the surface. XRD on the other hand will be more sensitive toward big particles than small ones and only crystalline nanoparticles will be detected. Therefore, direct comparison of particle/crystallite sizes between samples can only be performed within the same characterisation technique. Due to the poor quality of the XRD pattern for the impregnated Pt-g-C₃N₄ is not possible to apply the Scherrer equation or the Williamson-Hall plot and therefore compare the two materials. Nonetheless, since during photocatalysis the average particle sizes determined by TEM and the Pt⁰:PtO ratio are very similar for both impregnated and reduced Pt-g-C₃N₄, it is reasonable to ascribe the

higher activity of the reduced sample to a more crystalline phase achieved by thermal treatment. Higher crystallinity of the platinum NPs could affect their electronic structure and be beneficial in the electronic interaction between g-C₃N₄ and the metal allowing for a more efficient transfer of electrons.

Chemical reduction by NaBH₄ is also investigated. In this case the platinum is reduced in the presence of g-C₃N₄ by adding a solution of sodium borohydride under inert atmosphere. After reduction the sample is dried under argon flow at room temperature and no thermal treatment is performed. The chemically reduced Pt-g-C₃N₄ is tested for hydrogen evolution in the same conditions than those reduced under hydrogen and its hydrogen production at the steady state is found to be 515 μmol·h⁻¹·g⁻¹ (Table 4.4). This value is almost three times lower than the activity of the impregnated sample, indicating that chemical reduction has the opposite effect than reduction under hydrogen.

The XRD pattern for the obtained Pt-g-C₃N₄ is illustrated in Figure 4.14b. In the XRD pattern, Figure 4.14, the typical Pt⁰ fcc peaks are visible. The peaks are broader than those of the reduced in hydrogen Pt-g-C₃N₄. This can be due to smaller crystallites or a less crystalline phase. The crystallite size obtained from the Scherrer equation is 8 nm while from the Williamson-Hall plot (Figure 4.14inset b) it is found 5 nm. The difference of the two value indicates that there is a strain effect to be considered. The slope (-4.98·10⁻³) of

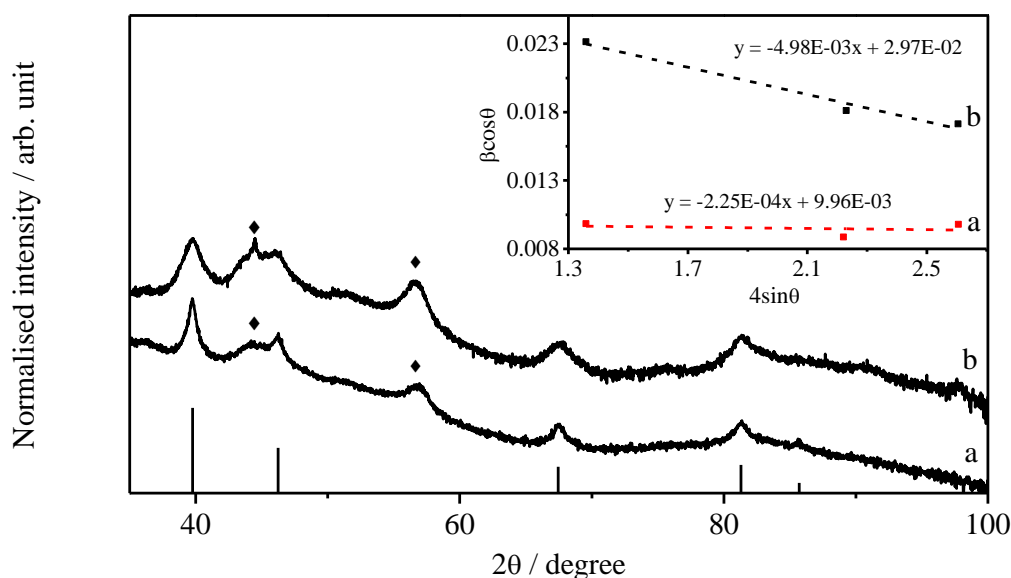


Figure 4.14 XRD pattern of reduced Pt-g-C₃N₄. XRD patterns for Pt-g-C₃N₄ reduced with a) 5 % H₂/Ar and b) NaBH₄. Bars) Pt⁰ XRD pattern as from ICDD database [PDF# 04 0802]. ♦) g-C₃N₄. Inset: Williamson-Hall plot for the two samples, a) reduced in H₂ and b) reduced with NaBH₄.

the Williamson-Hall indicates that indeed the nanoparticles are not very crystalline especially if compared to those reduced in hydrogen at 300 °C (Figure 4.14inset c). Therefore, the crystallite size is 5 nm, which is three times smaller than the one obtained for the reduced sample.

From TEM images (Figure 4.15) the average size of the nanoparticles is found to be 3.7 ± 2.9 nm only slightly smaller than the value obtained from the Williamson-Hall plot. The lower activity for hydrogen evolution could therefore be ascribed to either the lower crystallinity or the different initial particle size, which results being in between the values of the samples impregnated and reduced under flowing hydrogen. At this stage it is not yet possible to establish which factor has the highest influence on the activity.

The Pt 4f XP spectrum of the sample reduced with sodium borohydride is presented in Figure 4.16. After chemical reduction the main species present on the surface of g-C₃N₄ is platinum metal. The Pt⁰:PtO ratio is now 3.6 with a relative amount of platinum metal of 75.9 % and 20.2 % of PtO (Table 4.4). The remaining 3.9 % is identified as platinum chloride left from the reduction process. In addition to the platinum metal content increase, the Pt:N ratio is also found significantly increased to 0.284, more than 5 times that of the Pt-g-C₃N₄ reduced under hydrogen. An increase of this ratio was expected due

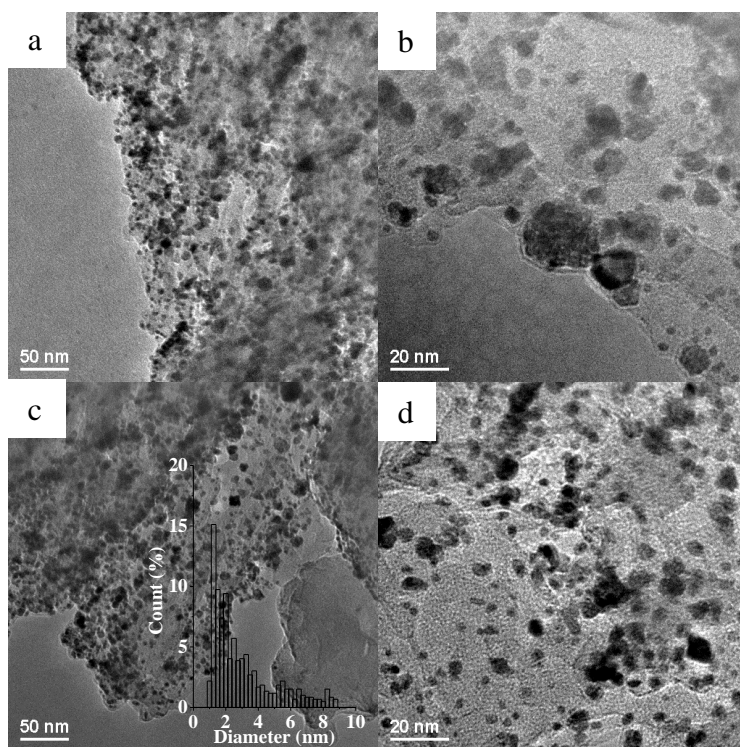


Figure 4.15 Platinum NPs morphology for Pt-g-C₃N₄ reduced with NaBH₄. TEM images of Pt-g-C₃N₄ reduced with NaBH₄. Inset: particle size distribution.

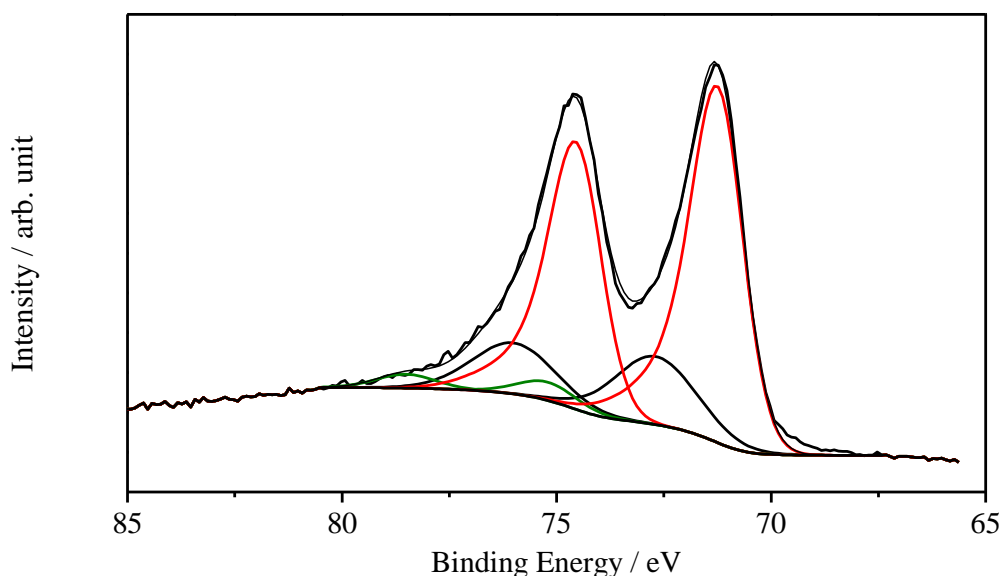


Figure 4.16 XPS spectra of Pt 4f region of Pt-g-C₃N₄ reduced with NaBH₄. Pt 4f region of Pt-g-C₃N₄ reduced with NaBH₄. PtCl_x: green line; PtO: black line; Pt⁰: red line¹⁵⁴.

to the smaller particle size value obtained from TEM and XRD analysis, however, such a significant increase is surprising especially if compared with the impregnated sample after photocatalysis. In this case the nanoparticles size was found smaller with a value of 2.3 ± 1.2 nm but the Pt:N ratio was lower than the one of the chemically reduced sample with a value of 0.04. This seems to be a contradiction since smaller NPs should result in a higher Pt:N ratio. Since the amount of platinum precursor employed is the same for all the samples, the difference in coverage between the impregnated and the chemically reduced Pt-g-C₃N₄ could be caused by an agglomeration of the particles of g-C₃N₄ during the reduction which would lead to less surface exposed during the XPS analysis. However surface area analysis reveals for both samples values ($8.2 \text{ m}^2 \cdot \text{g}^{-1}$ for the simply impregnated and $7.5 \text{ m}^2 \cdot \text{g}^{-1}$ for the chemically reduced) which do not deviate from that of the original g-C₃N₄ ($8 \pm 1 \text{ m}^2 \cdot \text{g}^{-1}$). A different explanation can therefore be provided if the nanoparticles of the chemically reduced sample are considered as very thin or monolayer like. Considering the exponential decay of the XPS signal with depth a monolayer of platinum would provide a stronger signal than spherical nanoparticles. Analysis of a chemically reduced sample loaded with half of the amount of platinum (0.5 wt.%) reveals a Pt:N ratio of 0.131, about half of the ratio measured for the 1 wt.%, confirming that indeed the particles have a monolayer-like configuration.

The average particle size measured from TEM images is representation of the 2D size and do not provide information of the height of the nanoparticles. Therefore, Pt:N ratio can be considered as a measure of the coverage of g-C₃N₄ with platinum, and in this case it provides a more reliable piece of information than the particle size obtained from TEM images.

Figure 4.17 shows the UV-Vis absorbance spectra of impregnated before and after photocatalysis and the reduced Pt-g-C₃N₄ (5 % H₂ and NaBH₄). The presence of metallic platinum increases the absorbance of the material in the visible range without changing the band gap of g-C₃N₄ (2.76 eV). The absorbance due to Pt⁰ is higher in the case of the sample reduced with NaBH₄ than in the other samples. This provides supporting evidence of a higher platinum surface coverage and higher Pt⁰ content for the chemically reduced material.

At this stage three factors can be considered responsible for the difference in hydrogen evolution of the samples: Pt⁰:PtO ratio, Pt coverage/particle size and crystallinity. In order to discriminate between them the chemically reduced sample was further reduced in hydrogen at 300 °C to bring to a coalescence of the nanoparticles and therefore a reduced Pt:N ratio. XPS analysis shows that the content of platinum metal slightly increases to 83.4 % due to the reduction of the chlorides species left from the chemical reduction and partial reduction of PtO. This brings the Pt⁰:PtO ratio up to 5.0 (Table 4.4). Additionally,

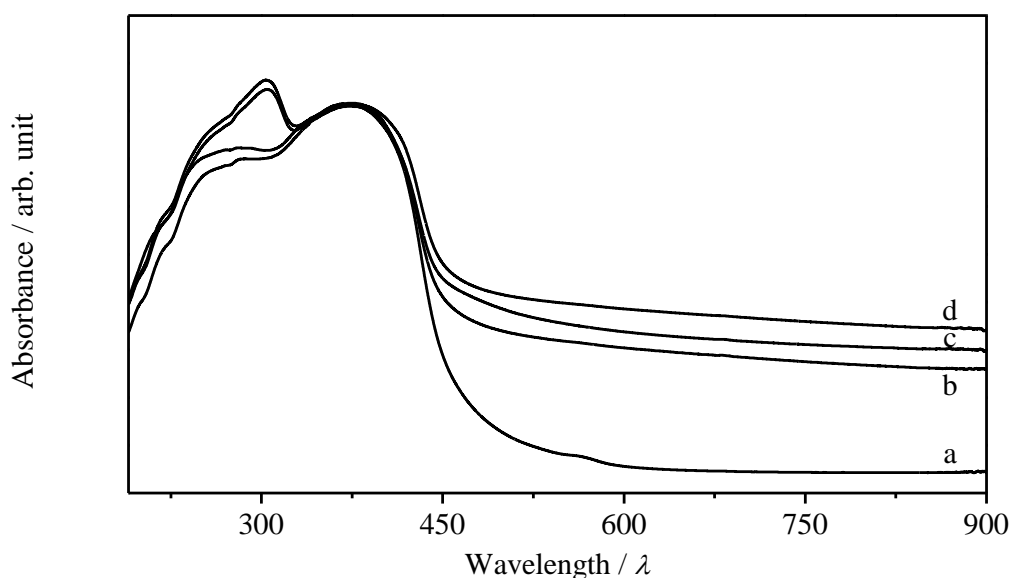


Figure 4.17 UV-Vis spectra of impregnated and reduced Pt-g-C₃N₄. UV-Vis spectra of a) impregnated, b) impregnated after photocatalysis, c) reduced under 5 % H₂ and d) reduced with NaBH₄ Pt-g-C₃N₄. The spectra have been off-set along y to align the max at 400 nm.

the Pt:N ratio is now 0.102, successfully decreased from the 0.284 of the chemically reduced Pt-g-C₃N₄ indication of the coalescence of the nanoparticles with thermal treatment. This is also confirmed by TEM images and particle size analysis (Figure 4.18) which reveals an average particle size of 10 ± 9.6 nm more than twice that of the chemically reduced sample. However, again, after comparing the estimated particle size with those of samples discussed earlier, the obtained Pt:N ratio is higher than expected. This suggests that even after thermal treatment the nanoparticles that are initially reduced with NaBH₄ retain a thinner configuration than NPs obtained with other methods.

The hydrogen evolution rate at the steady state of the double reduced sample is found $1721 \mu\text{mol}\cdot\text{h}^{-1}\cdot\text{g}^{-1}$ (AQY = 0.46 %). The activity increases by a factor 3.3 compared to the Pt-g-C₃N₄ reduced only with NaBH₄ (Table 4.4). Since the total platinum loading and the platinum metal content are very similar the only two factors that can be considered responsible for the increase in performance are the platinum coverage (Pt:N), linked to particle size and thickness, and the crystallinity. The Pt:N decreases of a factor 2.8, suggesting that indeed the coverage effects the activity, with a lower coverage being beneficial. If the surface of g-C₃N₄ is highly covered with metal, less surface is available for light absorption to produce excited electrons. An additional reason can be found in

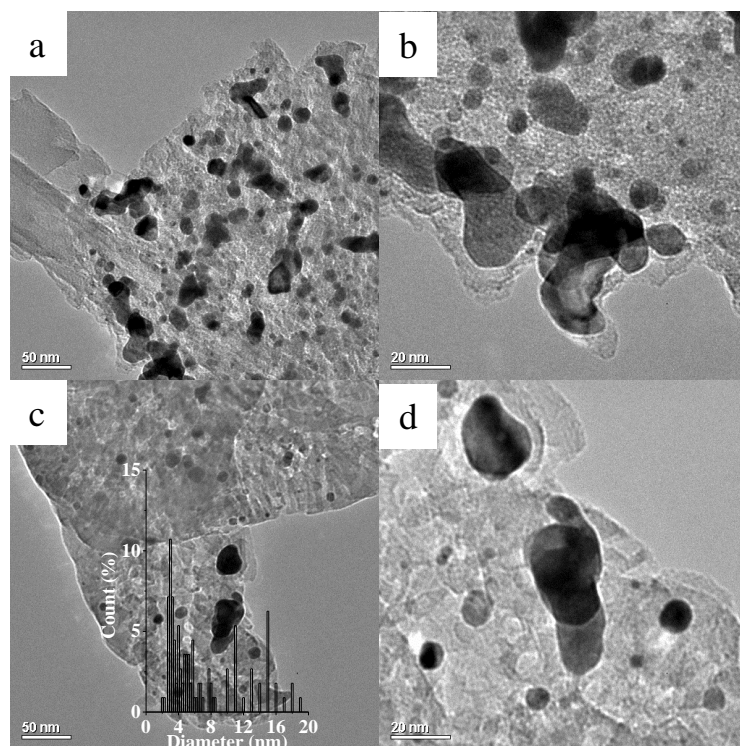


Figure 4.18 Platinum NPs morphology for Pt-g-C₃N₄ after double reduction. TEM images of Pt-g-C₃N₄ reduced with NaBH₄ and with 5 % H₂/Ar.

the configuration of the nanoparticles that causes such a high coverage. In the literature examples have been reported of the increase of metal NPs activity with increasing particle size up to a certain value.¹⁶¹⁻¹⁶³ The effect of the particle size on the activity highly depends on the catalytic process considered. Even though, at this stage is not yet possible to determine the exact effect that the size has on the activity, some assumptions can be made. In the case discussed here, thin nanoparticles may not be efficient enough in trapping electrons and therefore prevent recombination in the catalyst.

Coverage alone does not completely explain the increase in performance of a factor 3.3, the increased crystallinity also plays a role in enhancing the performance. In various catalytic processes involving metal NPs, it has been reported that the facets of the crystals, (111), (100) etc., have different activity depending on the catalytic process.^{164, 165} Applied to the present case, the thermal treatment brings to a better organisation of the atoms in the crystals, this may change the type of surface exposed and the relative amount compared to others favouring the activity for hydrogen evolution. Unfortunately, due to the irregular shape of the nanoparticles is not possible to determine the exposed plane.

Table 4.4 Comparison of reduced with not reduced Pt-g-C₃N₄. H₂ evolution rates at the steady state and relative amount of Pt species (XPS) for reduced and not reduced platinum loaded graphitic carbon nitrides. Test conditions: 0.1 g of catalyst in 0.1 L of 0.050 M aqueous solution of oxalic acid, visible light ($\lambda \geq 420$ nm). Reactor mode: continuous, measurement every 20 min.

	Impregnated	5 % H ₂ / Ar	NaBH ₄	NaBH ₄ + 5 % H ₂
H ₂ $\mu\text{mol}\cdot\text{h}^{-1}\cdot\text{g}^{-1}$	1430	3900	515	1721
(AQY %)	(0.38)	(1.05)	(0.14)	(0.46)
PtO %	42.6	44.2	20.2	16.6
Pt ⁰ %	57.4	55.8	75.9	83.4
PtCl _x %	-	-	3.9	-
Pt:N	0.04	0.051	0.282	0.102

When the double reduced sample is compared with the Pt-g-C₃N₄ reduced only in H₂ the performance is still lower of a factor 2.3 (Table 4.4). Since both samples have been exposed to the same thermal treatment the crystallinity can be considered the same for the two. Therefore the difference in performance could be ascribed to the platinum coverage, its relative amount (synergistic effect mentioned in the previous section) or both. The Pt:N ratio of the double reduced Pt-g-C₃N₄ is twice that of the only reduced in hydrogen sample indicating once again that the coverage of platinum has the biggest

effect on the performance for photocatalytic hydrogen evolution. This suggests that if the synergistic effect between platinum metal and platinum (II) oxide occurs it only has a minor influence.

In summary, different reduction procedures are employed to investigate the effect on platinum morphology and composition and how these influence the activity. It is found that the coverage of platinum on g-C₃N₄ has the major role in the improvement of photocatalytic performance. A lower coverage brings to an enhancement of the activity. Crystallinity as well plays a role in the overall performance by increasing the hydrogen evolution. With the acquired information, however, it was not possible to confirm the synergistic effect speculated in the previous sections. A better control on the nanoparticle size could provide further insight on the actual role of the configuration of the platinum NPs and confirm the findings of this investigation.

4.6. Effect of the sacrificial agent

As already mentioned, photocatalytic systems are very complex, with many aspects and interactions to be considered. In the previous sections, the effect of the loading procedure and of light irradiation on the nature of the co-catalyst were investigated with the aim of understanding more of this complex system. However, there are other elements playing an important role in the process. Among those is the sacrificial agent, *i. e.* the electron donor (ED). Its role is that of providing electrons to the system, by being oxidised, to allow for the electron cycle to be closed (Section 1.3.4). Ideally, when designing a photocatalytic process the ED should be chosen among water pollutants to make the hydrogen evolution process even more appealing by a simultaneous potential waste water treatment. In the literature, a great variety of electron donors are employed¹⁴ and among them are triethanolamine (TEOA)⁵⁴ and oxalic acid (H₂C₂O₄, OA)^{25, 166}. Surprisingly in the literature the effect of the sacrificial agent is not always investigated; comparison between different sacrificial agents is made⁵⁴, but their effects on the performance of the catalyst is not investigated. In this study the two different sacrificial agents (TEOA and OA) are compared to understand the causes that are responsible for the difference in activity. Unfortunately there are some complications associated with this comparison since it is difficult to change only one aspect of the process without affecting some others.

The two EDs are chosen because one is an acid and the other one a base. This is a very important aspect since the different pH can have an influence on the process. Figure 4.19 illustrates the hydrogen evolution rate for impregnated Pt-g-C₃N₄ in the presence of oxalic

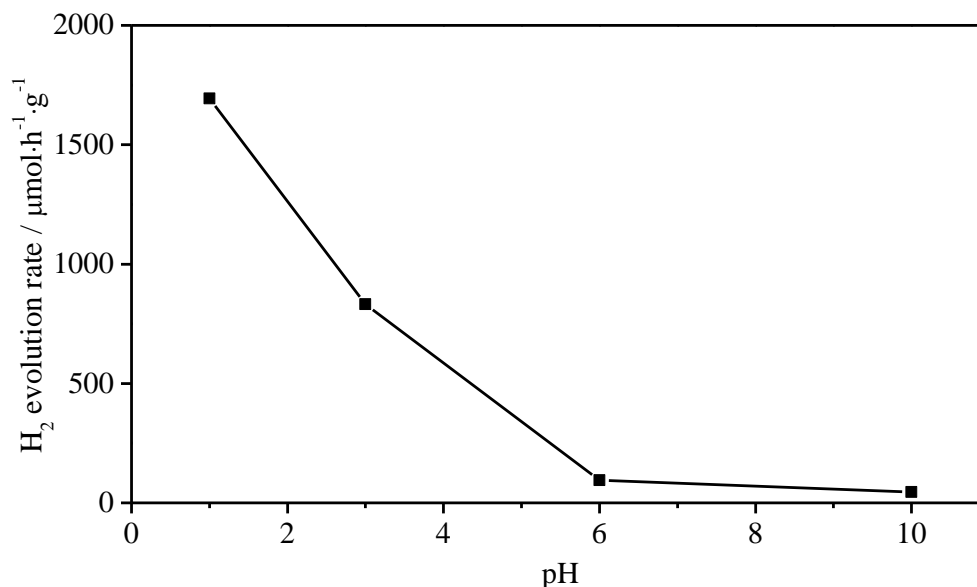


Figure 4.19 H₂ evolution rate vs. pH. H₂ evolution rate of impregnated Pt-g-C₃N₄ at different pH. The pH was adjusted using NaOH solution. Test conditions: 0.1 g of catalyst in 0.1 L of 0.025 M aqueous solution of oxalic acid, visible light ($\lambda \geq 420$ nm). Reactor mode: semi-batch, measurement every 2 h.

acid when NaOH is used to adjust the pH of the solution. The decrease in performance could be explained by the fact that the acid dissociates in water to give protons. The protons are then reduced in place of water. Hence, the sacrificial agent can affect the performance by effecting the pH.

The hydrogen evolution rate of the impregnated Pt-g-C₃N₄ vs. time when using the two different EDs is illustrated in Figure 4.20. When the oxalic acid is used as sacrificial agent the already discussed initiation period is observed, and the steady state hydrogen evolution is $1693 \mu\text{mol}\cdot\text{h}^{-1}\cdot\text{g}^{-1}$ (AQY = 0.45 %). When the employed sacrificial agent is TEOA a drastic decrease in activity is observed with a hydrogen evolution of only $218 \mu\text{mol}\cdot\text{h}^{-1}\cdot\text{g}^{-1}$ (AQY = 0.06 %), but more interestingly the rate is constant, within error, throughout the photocatalytic test.

The XPS analysis of impregnated Pt-g-C₃N₄ after photocatalysis in the presence of TEOA is shown in Figure 4.21 and summarised in Table 4.4. The main platinum species present on the surface of the catalyst is PtO (91.6 %, of total platinum, 73.1 eV) and only 8.4 % is platinum metal (70.5 eV). In Section 4.2 the initiation period was ascribed to the photoreduction of the platinum precursor to metallic platinum. The absence of the initiation period in the performance and the XPS results show that in the presence of TEOA the reduction of platinum cations does not happen, at least not at the same extent.

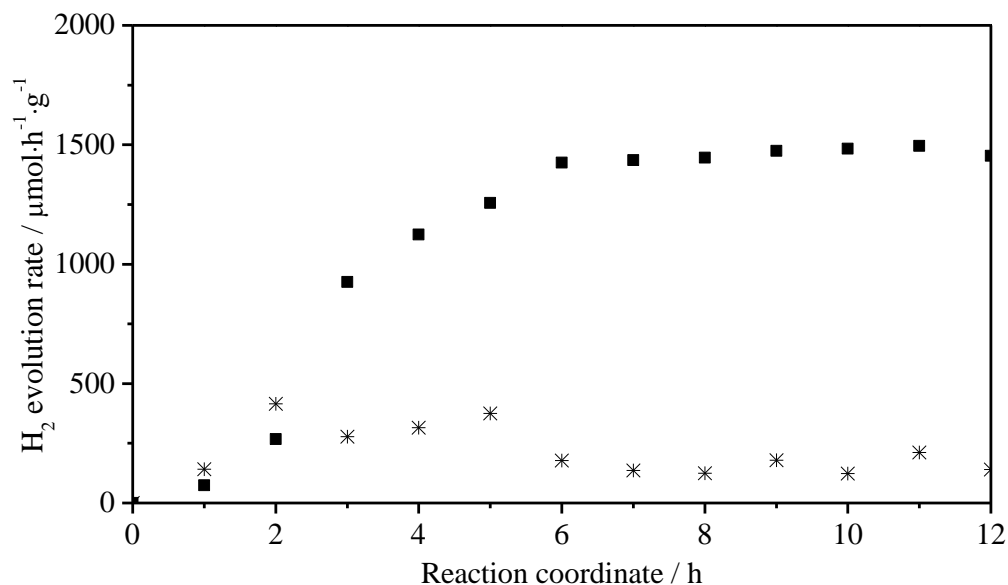


Figure 4.20 Sacrificial agent influence on H₂ evolution rate profile. Profile vs. time of H₂ evolution rate for impregnated Pt-g-C₃N₄ when ■) oxalic acid and *) triethanolamine are used as sacrificial agent. Test conditions: 0.1 g of catalyst in 0.1 L of 0.025 M aqueous solution of oxalic acid or 10 v.% of TEOA, visible light ($\lambda \geq 420$ nm). Reactor configuration: semi-batch, measurement every 1 h.

In a study by Zhang *et al.* the influence of the pH on the platinum photodeposited on TiO₂ was investigated.⁹¹ In their work, it was demonstrated that the pH of the solution during

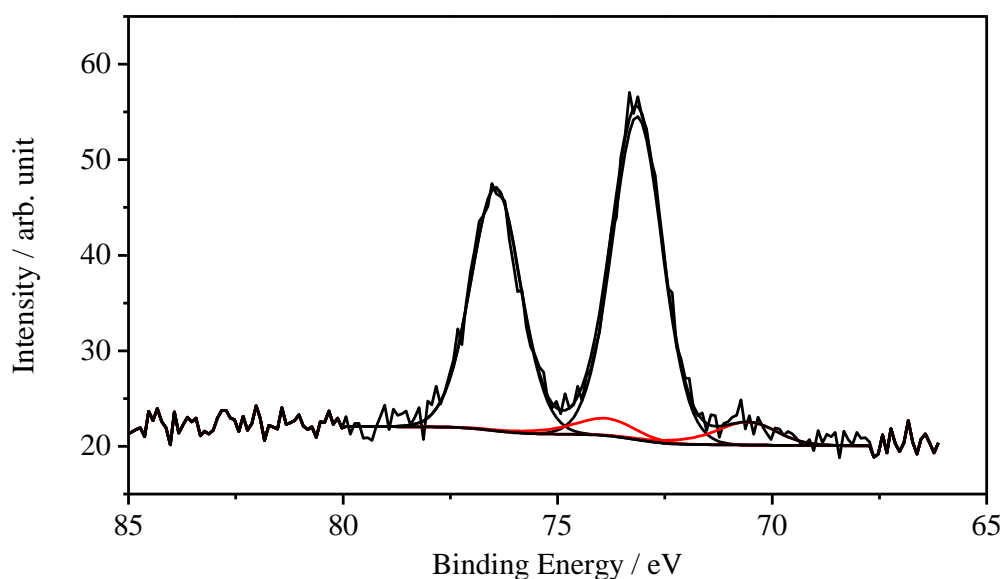


Figure 4.21 XPS Pt 4f spectra of Pt-g-C₃N₄: TEOA. Pt 4f region of Pt-g-C₃N₄ tested in the presence of TEOA as sacrificial agent. PtO: black line; Pt⁰: red line.

Pt photodeposition strongly influences the oxidation state and morphology of the nanoparticles. It was found that acidic pH (< 5) causes the reduction of PtCl_6^{2-} (K_2PtCl_6 as platinum precursor) to Pt^0 while at pH value larger than 7 less metallic platinum was formed and PtO and PtO_2 were the main species.⁹¹ The reason for this is ascribed to the products formed from the hydrolysis of PtCl_6^{2-} in solution at the different pH.⁹¹ At a pH smaller than 5 the main species are PtCl_6^{2-} and $\text{Pt}(\text{OH})\text{Cl}_5^{2-}$ which are then reduced to Pt^0 by the excited electrons produced in the catalyst by light absorption. However, at higher pH the chlorides are further hydrolysed leading to formation of PtO and PtO_2 .⁹¹ Even though their system is slightly different from the one considered in the current study, the authors' findings can still be used to interpret the XPS results of Pt-g- C_3N_4 tested in the presence of TEOA. After impregnation some platinum chloride remain present on the graphitic carbon nitride surface (as seen in Section 4.2). Those platinum chloride species will be hydrolysed in water to different extent depending on the pH. Triethanolamine brings the solution to a pH = 10, and oxalic acid to a pH = 1 (Table 4.4) therefore, in the former case there is more hydrolysis products which explain the formation of PtO while in the latter case Pt^0 is formed.

Table 4.5 Summary of the effect of different sacrificial agents. Summary of the effect of the sacrificial agent on pH, performance, platinum species relative amounts and Pt:N ratio. Test conditions: 0.1 g of catalyst in 0.1 L of 0.025 M aqueous solution of oxalic acid, visible light ($\lambda \geq 420$ nm). Reactor configuration: semi-batch, measurement every 1 h.

Sacrificial agent	pH	H_2 evolution rate ($\mu\text{mol}\cdot\text{h}^{-1}$) (AQY %)	Pt %	PtO %	Pt:N
Oxalic acid	1	1693 (0.45 %)	56.8	43.2	0.050
TEOA	10	218 (0.06 %)	8.4	91.6	0.017
$\text{Na}_2\text{C}_2\text{O}_4$	10	60 (0.02 %)	25.1	74.9	0.073

Another difference that emerges from the XPS results is the ratio Pt:N. For the oxalic acid the ratio is 0.05 and for triethanolamine 0.017. This indicates the NPs on the surface of g- C_3N_4 are larger when triethanolamine is used as sacrificial agent than when oxalic acid is chosen. TEM images of the sample after photocatalysis in the presence of TEOA (Figure 4.22) confirm the XPS analysis by showing clusters of nanoparticles as opposite to the small nanoparticles formed when oxalic acid is employed (Figure 4.5). The presence of these large clusters of nanoparticles seen in Figure 4.22 may be explained by

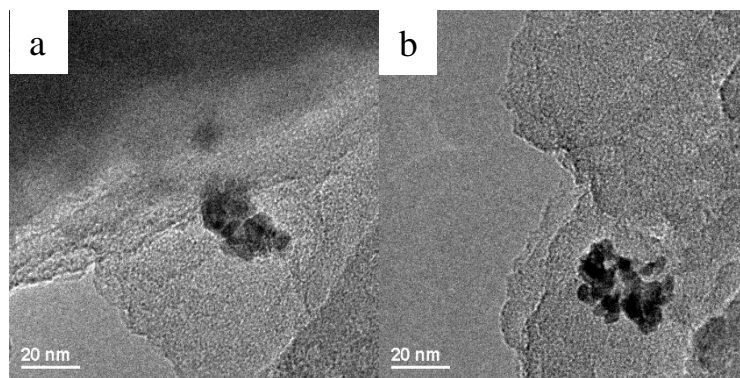


Figure 4.22 TEM images of Pt-g-C₃N₄ tested with TEOA. TEM images (a, b) of different areas of Pt-g-C₃N₄ after photocatalytic test in the presence of TEOA as sacrificial agent.

the formation of complexes between the platinum and the products formed during the oxidation of triethanolamine. Horikoshi *et al.* in 2001 investigated the photooxidation of ethanolamines by TiO₂. They achieved complete mineralisation of the amines which resulted in the evolution of CO₂.¹⁶⁷ In the current investigation, however, no carbon dioxide was detected *via* gas chromatography which suggests that the complete mineralisation was not achieved. As a consequence it can be assumed that other organic decomposition derivatives are formed, for example, mono- and diethanol amine.¹⁶⁷ These compounds have hydroxyl and amino groups which can form complexes with platinum. These organic compounds are bi- or tri-functional, which could lead to bridging phenomena between platinum atoms causing the agglomeration observed in the TEM images. In an XPS spectra a Pt^{II} complex would appear at the same binding energy as PtO, therefore it would not be possible to distinguish between the two.

The pH is found to definitely have an influence on the oxidation state of the co-catalyst, but the nature of the sacrificial agent is also important. As mentioned at the beginning of this section, it is difficult to change only one parameter. In order to try to isolate the effect of the pH from the nature of the sacrificial agent, sodium oxalate (Na₂C₂O₄) was used in place of oxalic acid in order to achieve a pH = 10. XPS Pt 4f region of the sample after photocatalysis and the hydrogen evolution rate profile *vs.* time are shown in Figure 4.23. From the XPS analysis (Figure 4.23a) PtO (72.8 eV) is the main platinum species present on the surface of graphitic carbon nitride with a relative amount of 74.9 %. The remaining 25.1 % corresponds to Pt⁰ (71.0 eV). Therefore, the effect of the pH on the oxidation state is confirmed, even though the platinum metal contribution is slightly higher for sodium oxalate than for triethanolamine. The hydrogen evolution profile when sodium oxalate is

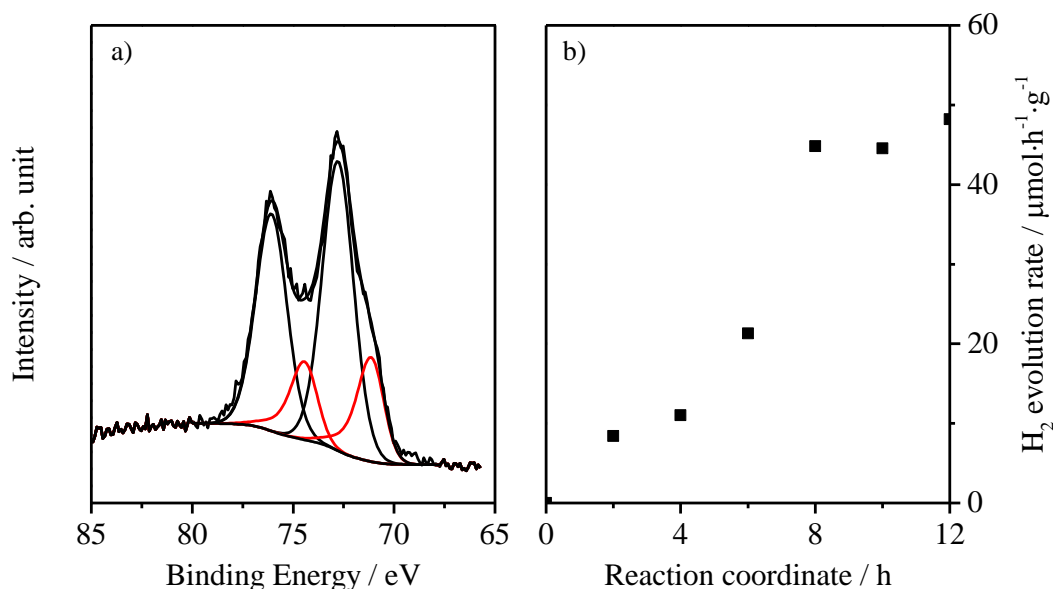


Figure 4.23 XPS and H₂ evolution of Pt-g-C₃N₄ using Na₂C₂O₄ as ED. a) XPS Pt 4f region after photocatalytic test (Pt⁰: red line) and b) H₂ evolution rate profile for Pt-g-C₃N₄. Test conditions: 0.1 g of catalyst in 0.1 L of 0.025 M aqueous solution of sodium oxalate, visible light ($\lambda \geq 420$ nm). Reactore configuration: semi-batch, measurement every 2 h.

used as sacrificial agent is shown in Figure 4.24b. The presence of an initiation period appears surprising given previous discussions. The 8 h period is found slightly longer than the one observed for the oxalic acid: 6 h, Figure 4.7. This specific length of time at the beginning of the experiment could probably be associated to the chemical nature of the sacrificial agent itself, maybe linked to organometallic complex formation. The exact mechanism cannot be given, but one can be suggested. The remaining platinum chloride left on the surface of the catalyst after impregnation may form complexes with the oxalates. However, these oxalates quickly oxidise to CO₂ and the platinum becomes available for reduction.

In this section it is found that the low pH of the testing solution has a positive effect on the performance and it is probably due to the favoured reduction of the platinum precursor. The choice of the sacrificial agent (base or acid) can, therefore affects the photocatalytic process. In addition the chemistry of the sacrificial agent with the co-catalyst also has to be considered. It is shown that the triethanolamine may form organometallic complexes with the platinum preventing its reduction to platinum metal. It is, therefore, very important to take into consideration these aspects when choosing a sacrificial agent, in order to make the best choice to maximise the hydrogen production.

4.7. Role of platinum in the process: plasmonic behaviour?

After investigating some of the parameters that can have an effect on platinum as co-catalyst, the influence of platinum on the process has to be evaluated. It has already been mentioned (Section 4.1) that on the role of platinum in photocatalytic processes there are conflicting opinions.^{138, 142} In most of the cases, it is considered only as an electron trap, capturing electrons from the catalyst and discharging them during a reduction process.¹⁴³ Sometimes, it is reported as having a plasmonic behaviour on the base of the increased absorption in the visible region once it is loaded on the surface of a catalyst.¹³⁸ The two options lead to two different mechanisms. A schematic representation of the two is illustrated in Figure 4.24.

If the platinum based co-catalyst works as an electron trap it will receive excited electrons from the catalyst and use them to carry out the reduction reaction while the holes left in the catalyst will be used for the oxidation of the electron donor (Figure 4.24a). On the other hand, if the co-catalyst has plasmonic behaviour, the pathway is completely the opposite to the one presented above. The light absorbed by the metal produces a separation of charges and the electrons are injected into the g-C₃N₄ catalyst which becomes responsible for the reduction of water. The co-catalyst uses the holes to oxidise the sacrificial agent (Figure 4.24b).¹⁴⁰ Due to the conflicting opinions on this topic, a series of experiments were carried out to understand which role the platinum has in the photocatalytic system Pt-g-C₃N₄.

UV-Vis absorption spectra of platinum loaded graphitic carbon nitride were previously shown in Figure 4.17, where Pt-g-C₃N₄ samples with and without reduction pre-treatment

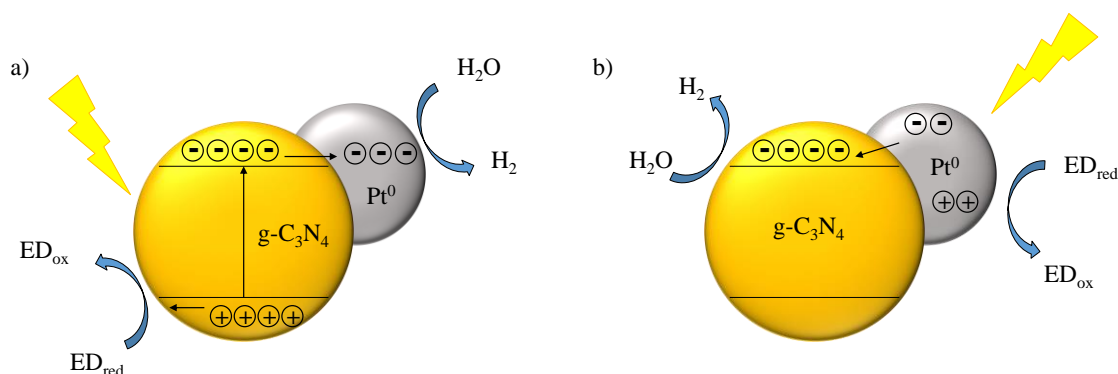


Figure 4.24 Role of Pt⁰ NPs in photocatalytic H₂ evolution. Two possible mechanisms describing the role of the co-catalyst in the photocatalytic H₂ evolution: a) as electron trap and b) as plasmonic co-catalyst.

were compared. From the absorption spectra it was observed that when Pt^0 is present on the surface of the catalyst there is, indeed, a significant increase in absorption due to the platinum itself. If this absorption is related to its surface plasmon resonance,¹³⁸ then under any of those wavelengths, mechanism b in Figure 4.24 could take place, and hydrogen could be produced. To verify this theory photocatalytic tests using single wavelength light are carried out. Light of wavelengths 460 nm (red light), is chosen because it is in the absorption region of g- C_3N_4 (Figure 4.25). Additionally, light of wavelength of 623 nm (blue light) is employed because it is outside the catalyst absorption region but absorbed by platinum metal (Figure 4.25). Impregnated Pt-g- C_3N_4 (no Pt^0 on the surface) was tested under both wavelengths. A reduced Pt-g- C_3N_4 was tested under 623 nm light to ensure the presence of Pt^0 on the surface of g- C_3N_4 and verify the SPR phenomena.

The hydrogen evolution rate for the impregnated sample under 460 nm wavelength is $41 \mu\text{mol}\cdot\text{h}^{-1}\cdot\text{g}^{-1}$ (the lower value compared to previous results is due to a not optimum wavelength, a less powerful light source and lower temperature, Chapter 2). After photocatalysis the UV-Vis spectrum of the sample is collected and an increase in visible absorption characteristic to Pt^0 is observed (Figure 4.25, blue line) meaning that platinum metal nanoparticles are successfully formed under this condition. However, when tested under light at a 623 nm wavelength, the catalyst does not show any hydrogen evolution

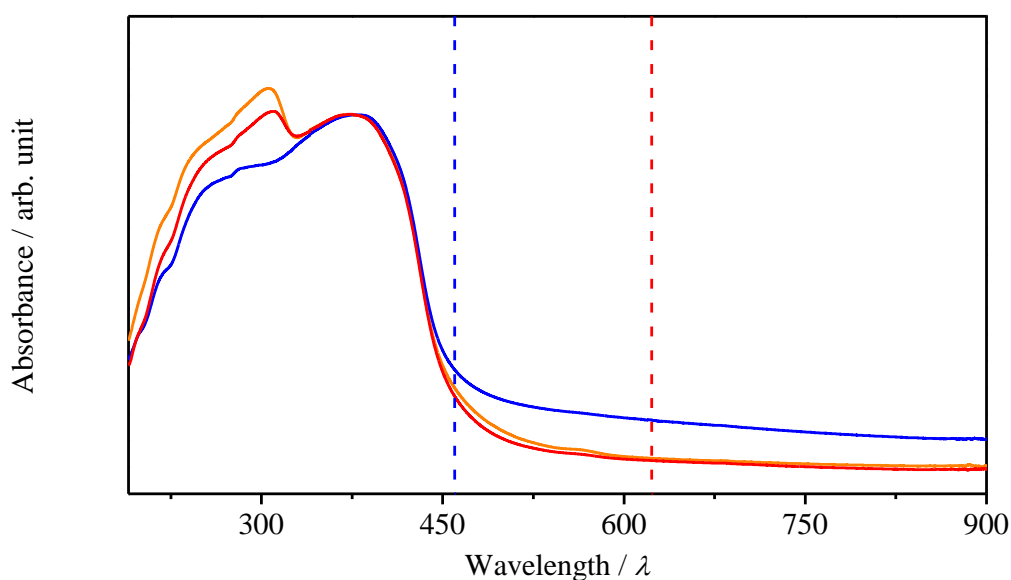


Figure 4.25 Influence of single wavelength-light test on UV-Vis spectra. UV-Vis spectra showing the influence of single wavelength light on the formation of Pt^0 . Impregnated Pt-g- C_3N_4 (orange) before test, (blue) after test under 460 nm, and (red) after test under 623 nm. Vertical lines represent the position of the two wavelengths used in the hydrogen performance tests.

and the absorption in the UV-Vis spectrum is comparable to that of the starting Pt-g-C₃N₄ with no Pt⁰ (Figure 4.25, red line). This indicates that no Pt⁰ is formed when light of 623 nm is employed. The absence of hydrogen is expected. The band gap of graphitic carbon nitride (2.76 eV) is too wide to absorb such a long wavelength characterised by an energy of 1.99 eV, therefore its electrons cannot be promoted to the conduction band. In addition, the absence of Pt⁰ suggests that platinum is formed at wavelength that are absorbed by g-C₃N₄ (460 nm). This confirms that Pt⁰ is reduced by the photoexcited electrons of g-C₃N₄.

To further investigate the plasmonic activity of platinum the reduced sample was also tested using the 623 nm wavelength. Again in this case no H₂ was evolved, suggesting that, even though Pt⁰ can absorb the light of $\lambda = 623$ nm, no electrons are formed and injected into the g-C₃N₄. It is therefore reasonable to conclude that in this specific system the co-catalyst does not show any plasmonic activity and it only acts as an electron trap (Figure 4.24a) reducing the recombination of the charges in the catalyst.

The results show that in the visible range platinum nanoparticles are not characterised by any SPR. It is important to point out however that under UV light platinum could show plasmonic character, specifically at 210 nm¹⁴¹. In the study by Garcia,¹⁴¹ the difference between plasmonic resonance (UV for Pt) and interband transitions (Vis for Pt) was explained. From this review it becomes clear that the platinum plasmonic resonance under visible light reported in the literature is in fact an interband transition which does not contribute to the photocatalytic hydrogen evolution.

4.8. Assessing the catalytic characteristic of Pt-g-C₃N₄

A catalyst to be defined as such has to satisfy some basic requirements. It has to be reusable more than once, and have a specific (ideally long) shelf life. These characteristics are briefly discussed in this section. Impregnated Pt-g-C₃N₄ is employed for this investigation.

An important characteristic of a catalyst to evaluate is its shelf life, how long the catalyst can be stored in normal conditions without losing any activity. Figure 4.26 shows the H₂ evolution rate at the steady state for impregnated Pt-g-C₃N₄. This is monitored over a period of six months. No special care is taken in storing the material. Except a small decrease (10 %) in performance after the first month, probably due to slight hydrolysis of the chlorides species, the activity proves stable (within 5 % fluctuation). It can, therefore,

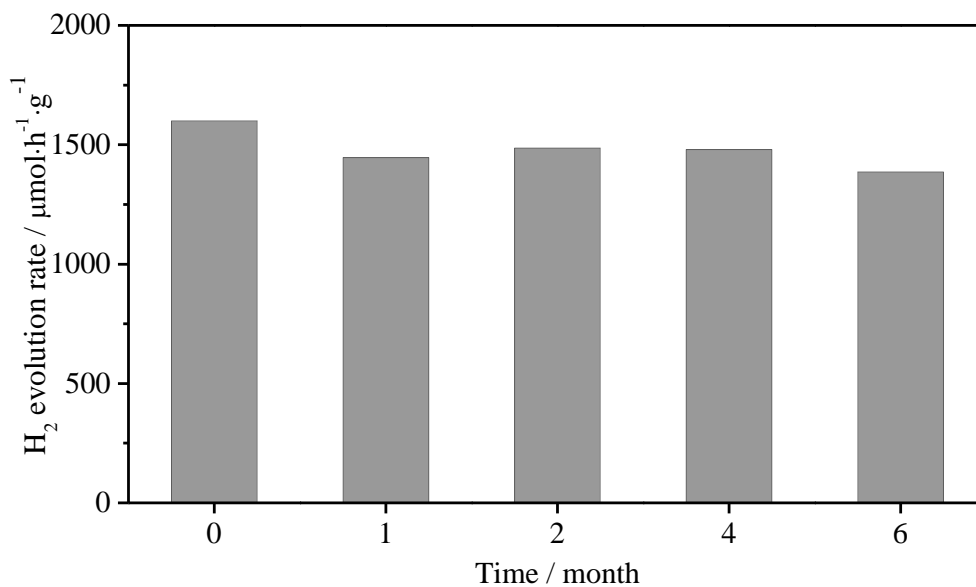


Figure 4.26 Shelf life evaluation. H₂ evolution rates of impregnated Pt-g-C₃N₄ tested at different intervals. Test conditions: 0.1 g of catalyst in 0.1 L of 0.025 M aqueous solution of oxalic acid, visible light ($\lambda \geq 420$ nm). Reactor configuration: batch.

be stated that the sample can be stored in normal conditions for a period of six months without any significant loss in activity.

Impregnated Pt-g-C₃N₄ was tested for photocatalytic hydrogen evolution for more than one cycle. For each test fresh oxalic acid was added to the reaction mixture. Figure 4.27

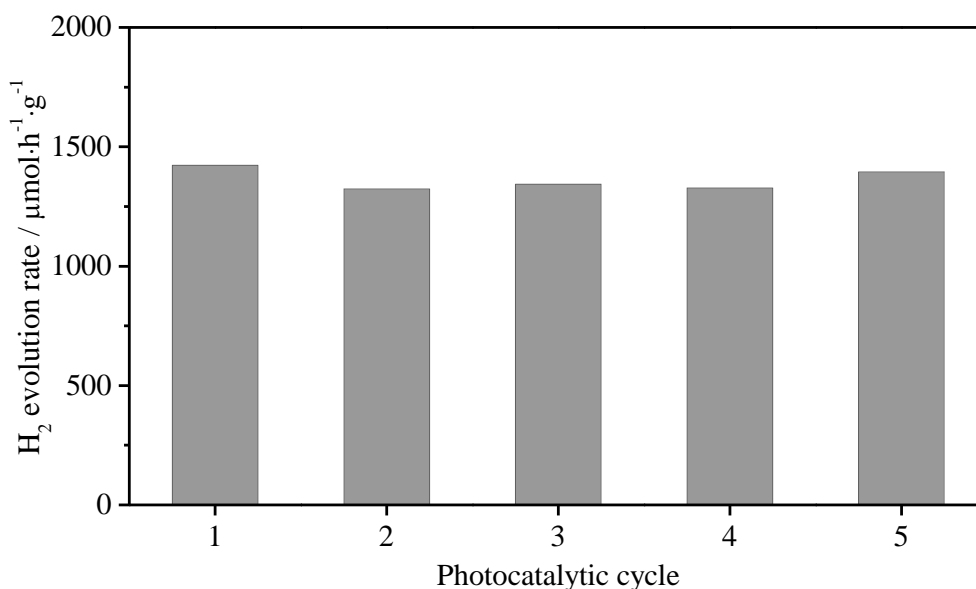


Figure 4.27 Reusability of the catalyst. H₂ evolution rates of re-used impregnated Pt-g-C₃N₄. Test conditions: 0.1 g of catalyst in 0.1 L of 0.025 M aqueous solution of oxalic acid, visible light ($\lambda \geq 420$ nm). Reactor configuration: semi-batch; measurements every 2 h.

shows the H₂ evolution rate at the steady state for photocatalytic cycles. The results show that the catalyst can be reused at least five times without any loss in activity.

4.9. Conclusions

The activity for hydrogen evolution of C₃N₄-500, -550 and -600 have been investigated with and without co-catalyst. It has been found that when g-C₃N₄ is not loaded with a co-catalyst the most active of the three is the one synthesised at 600 °C. Differently, when 1 wt.% Pt is loaded on the surface the highest performance is obtained for C₃N₄-500. This has been assigned to the lower surface area of the material synthesised at low temperature which allows a better interaction between catalyst, co-catalyst and light. Further investigation were carried out on this material. In the specific, the effect of different parameters on co-catalyst and activity.

Investigation of three different procedures (impregnation, impregnation followed by calcination and photodeposition) and reduction pre-treatments (reduction under H₂ and with NaBH₄) has shown significant differences in performance. Among the loading procedures the simple impregnation has shown to be the best of the three. With investigation by TEM and XPS the possible causes have been reduced to platinum metal relative content and coverage of g-C₃N₄ surface. From the investigation of the reduced sample it has emerged that the main factors that govern the activity of Pt-g-C₃N₄ are the level of crystallinity and the dispersion of metal. The higher the crystallinity the higher the performance. The coverage on the other hand has shown to be detrimental, the higher the coverage the lower the activity for hydrogen evolution.

The sacrificial agent employed during photocatalytic test has also been found to have an effect on both morphology and oxidation state of the co-catalyst, and consequently on the performance. In the presence of oxalic acid (pH = 1) platinum metal is formed in the form of small particles. However in the presence of triethanolamine (TEOA) it is mainly formed as what appears to be PtO and in the form of big clusters. This is possibly due to the formation of complexes with amines which are produced during photocatalysis. Additionally the activity in the presence of TEOA is found significantly lower. This has led to the conclusion that acidic pH is more favourable for photocatalytic hydrogen evolution, both because of the protons provided by dissociation of oxalic acid and for the higher metal content obtainable.

Finally, the mechanism of Pt⁰ formation taking place during photocatalysis has been elucidated. When light strikes g-C₃N₄ excited electrons are produced into the conduction

band of the semiconductor, these are employed to reduce the platinum precursor to platinum metal which will act as a simple electron trap by trapping the electrons and will prevent recombination events.

Chapter 5

The co-catalyst: Bimetallic Alloys

5.1. Introduction

Even though platinum is a very active co-catalyst in photocatalytic processes a drawback associated with its use is its prohibitive cost. In other catalytic processes where platinum is widely used, for example oxygen reduction reaction in proton exchange fuel cells, efforts have been made to find cheaper alternatives and at the same time to improve the activity and the stability of the catalysts.¹⁶⁸ One possible method is the use of bimetallic catalysts which could be an alloy of platinum and a non-precious metal.^{168, 169} In recent years the same approach of combining the effect of two different metals to modify the co-catalyst has been applied in photocatalysis.^{78, 79, 170-174} So far only a few examples involving platinum-based alloys for photocatalytic hydrogen production applications have been reported in the literature^{78, 79, 175} and only the work by Di *et al.*⁷⁸ and Yu *et al.*⁷⁹ were carried out on g-C₃N₄.

The choice of combining two metals, which can affect the electronic and/or morphological properties of the final material, is largely dictated by the desired catalytic process. In photocatalysis where a metallic co-catalyst is employed, the interaction between the semiconductor (SC) and the metal is important because it regulates the electron transfer between the two. This process has to be as effective as possible to prevent charge recombination events (Chapter 1). By alloying two metals their electronic properties are modified causing changes in the metal-semiconductor heterojunction. A more detailed explanation is provided below.

When metallic nanoparticles are loaded on the surface of a semiconductor the Fermi levels of the two materials become aligned and as a consequence the valence (VB) and the conduction band (CB) of the semiconductor bend. The band bending for an n-type semiconductor is illustrated in Figure 5.1b. The intensity of the bending (ΔeV) depends on the Fermi level of the metal which corresponds to the metal work function (ϕ_{Me}).¹⁷⁶ The difference between the Fermi level of the metal and the conduction band of the semiconductor is the Schottky barrier (ϕ_B).¹⁷⁶ In addition to the Schottky barrier a slightly smaller potential energy barrier equivalent to the intensity of the band bending (ΔeV) is formed within the SC. Both barriers are particularly important for the photocatalytic process where the electrons have to flow from the conduction band of the semiconductor to the metal. A low barrier within the SC (ΔeV) is beneficial to efficiently transfer the electrons from the semiconductor to the metal,^{177, 178} but a high Schottky barrier would be beneficial in preventing the electrons to flow back and recombine in the semiconductor. Since ΔeV is smaller than ϕ_B it could be assumed that an optimum value exists for which the Schottky barrier remains high enough to prevent backflow but the ΔeV is low enough to promote the transfer of the electrons from the SC to the metal. The used of a bimetallic alloy may offer a way to achieve this goal.

In a bimetallic alloy the work function has an intermediate value between those of the two single metals and it depends on the relative concentrations of the components.¹⁷⁹ Figure 5.2 shows the work functions of silver and some transition metals compared to that of platinum and to the bands position of g-C₃N₄.^{21, 56} Platinum has the highest work function and therefore produces the highest Schottky barrier when loaded on g-C₃N₄. This feature makes Pt the most effective co-catalyst in preventing the back flow of electrons

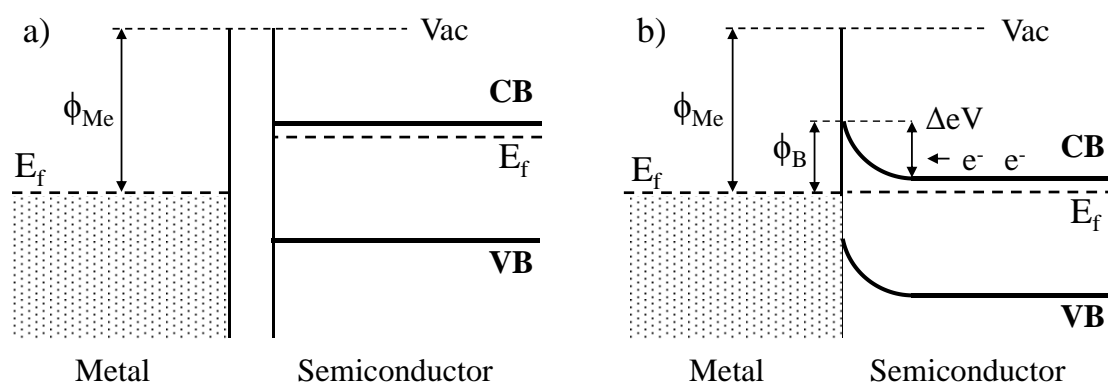


Figure 5.1 Metal-Semiconductor heterojunction. Schematic of the electronic levels at the surface of a metal and a semiconductor a) before and b) after contact. E_f = Fermi level, ϕ_{Me} = work function of the metal, ϕ_B = Schottky barrier.

by acting as an electron trap. On the other hand the electrons from the conduction band of the semiconductor have to overcome the barrier generated within the semiconductor; *i.e.* the ΔE_V in Figure 5.1b,^{177, 178} which is also the highest for platinum. Therefore, it is reasonable to assume that alloying Pt with cheaper transition metals characterised by a lower work function can reduce the potential barrier to facilitate the transfer of electrons from the semiconductor to the metal while at the same time still prevent the backflow of electrons.

As already mentioned, among the examples of bimetallic co-catalyst for photocatalytic application only the works by Di *et al.*⁷⁸ and Yu *et al.*⁷⁹ involve g-C₃N₄. In 2010, Di *et al.* reported the positive effect produced on hydrogen evolution by combining gold with platinum by sequential loading procedure.⁷⁸ The second example looked at the activity enhancement of g-C₃N₄ loaded with PtCu nanoparticles synthesised prior the loading procedure and protected with ligands.⁷⁹ In the present work, different from the previous two examples, the synthesis of the alloy nanoparticles is performed during the loading procedure to maximise the interaction with g-C₃N₄ but also to allow a direct comparison to the work presented in Chapter 4. The metals chosen to synthesise the bimetallic co-catalyst are among those that have proven successful in enhancing platinum activity in processes like oxygen reduction reaction. They are Ni, Co, and Cu. In addition silver is considered because of its plasmonic effect. All these metals have lower work functions than Pt as shown in Figure 5.2 and would bring to a decrease of the Schottky barrier.²¹

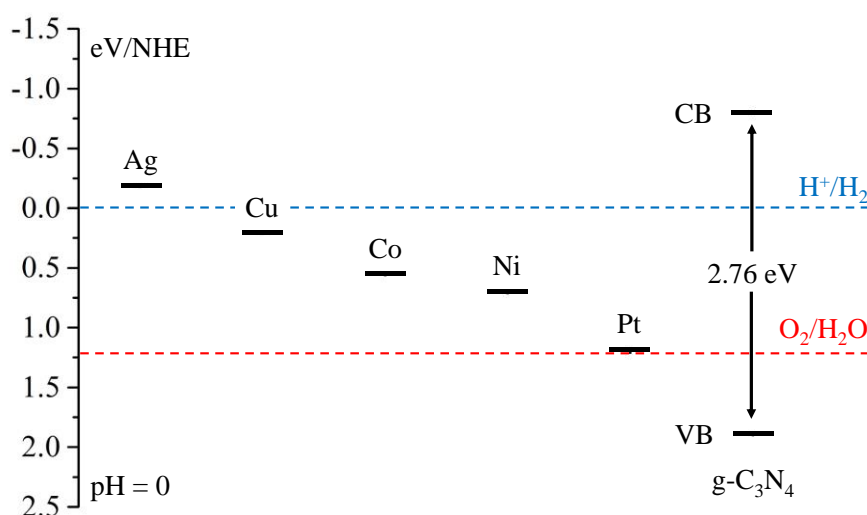


Figure 5.2 Work function of some metals compared to VB and CB of g-C₃N₄. Comparison of the work functions (ϕ , eV) of the metals used in this investigation with the band structure of graphitic carbon nitride⁵⁶. The work functions have been referenced to the NHE at pH = 0 from the values reported in ref. ²¹($\phi_{\text{NHE}} = \phi_{\text{vac}} - 4.44$ eV).

5.2. Synthesis and performance

The first aspect to consider is the synthesis of the binary alloy and the relative amount of metals. In the literature the two most commonly used methods to synthesise bimetallic nanoparticles directly on a support are reduction by calcination in hydrogen and chemical reduction by NaBH_4 ;¹⁸⁰⁻¹⁸³ both have already been applied for the synthesis of Pt NPs and discussed in Chapter 4. However, the synthesis conditions are found to significantly vary in the literature. Examples of the direct synthesis on the support for each bimetallic alloy that are of interest for this work are summarised in Table 5.1. Since to date no specific Pt:Me atomic ratio seems to be preferred, a 50:50 ratio is chosen as starting point in this work. The total number of metal atoms (Pt + Me) is kept constant and equivalent to that of the 1 wt.% Pt-g-C₃N₄. The next important factor is the reduction temperature. In general, as seen in Table 5.1, the reduction in hydrogen occurs at temperatures higher than 400 °C. However, while it has been previously discussed in Chapter 3 that g-C₃N₄ starts decomposing at 500 °C, thermal gravimetric analysis shows that adding the co-catalyst significantly decreases that temperature (Figure 5.3). For all the prepared materials a major weight loss occurs at 400 °C. The extent of decomposition goes from 3.2 wt.% for PtCu-g-C₃N₄ to 23.6 wt.% for PtAg. It is therefore not possible to form and

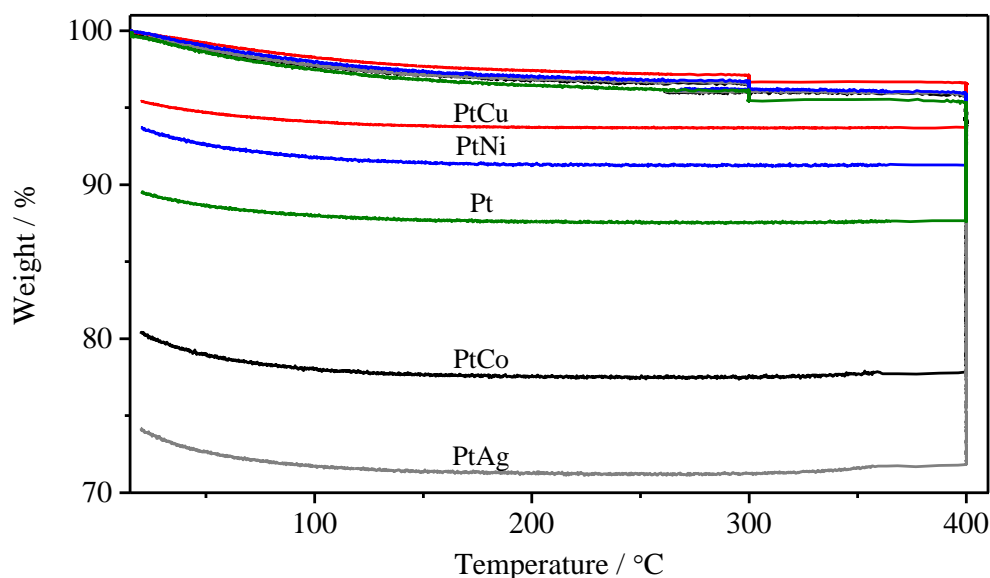


Figure 5.3 TGA of PtMe-g-C₃N₄. Thermal gravimetric profiles of PtMe-g-C₃N₄. Conditions: 5 % H₂/Ar, 5 °C/min up to 300 °C (dwell: 4 h), further 5 °C/min up to 400 °C (dwell: 2 h); cooling to r.t. at 5 °C/min.

Table 5.1 List of synthetic procedures for PtMe alloys. Brief summary of some of the synthetic procedures. Code: &) indicates co-impregnation and /) indicates subsequent loading.

Pt:Me (atomic)	Precursors	Synthesis method	Conditions	Ref.
PtCu				
6:94	Pt(NH ₂) ₄ (OH) ₂ & Cu(NO ₃) ₂	O ₂ + H ₂	450 °C + 260 °C	180
50:50	Pt(NH ₂) ₄ (OH) ₂ / Cu(NO ₃) ₂	O ₂ + H ₂	450 °C + 380 °C	184
~ 30:70	CuCl ₂ / K ₂ PtCl ₄	KBH ₄ + H ₂	300 °C	185
50:50; 25:75	H ₂ PtCl ₆ & CuCl ₂	H ₂	220 °C	181
11:89	H ₂ PtCl ₆ & CuCl ₂	NaBH ₄	-	182
20:80; 50:50	H ₂ PtCl ₆ & Cu(NO ₃) ₂	H ₂	350 °C	186
90:10 to 40:60	H ₂ PtCl ₆ & Cu(NO ₃) ₂	H ₂	400 °C	174
PtAg				
n.a.	H ₂ PtCl ₆ & AgNO ₃	-	-	187
36:64	K ₂ PtCl ₆ & AgNO ₃	NaBH ₄	-	183
PtNi				
n.a.	H ₂ PtCl ₆ / Ni(NO ₃) ₂	H ₂	200 °C	188
3:97 to 74:26	K ₂ PtCl ₄ & NiCl ₂	NaBH ₄	-	189
50:50	H ₂ PtCl ₆ & Ni(NO ₃) ₂	NaBH ₄	-	190
71:29 to 64:36	Pt(acac) ₂ & Ni(acac) ₂	LiEt ₃ BH+H ₂	400 °C	191
PtCo				
75:25	H ₂ PtCl ₆ & CoCl ₂	H ₂	150-400-700 °C	192
85:15	H ₂ PtCl ₆ & Co(OH) ₂	NaBH ₄	-	193
n.a.	Co(NO ₃) ₂ / Pt(NH ₃) ₂ (NO ₂) ₂	H ₂	350 °C	194
75:25	Pt(NH ₃) ₄ (OAc) ₂ & Co(NO ₃) ₂	H ₂	400 °C	195

reduce the co-catalyst at 400 °C and above without decomposing the g-C₃N₄. Therefore, for this reason and in order to still be able to compare the results with those obtained when only platinum is used, the same reduction conditions: 5 % H₂/Ar at 300 °C for 24 h, are employed for all the bimetallic co-catalysts. Finally, to investigate the effect of the loading procedure on the formation of the alloy chemical reduction using NaBH₄ is also employed with the same procedure described in Chapter 4. All the materials are tested for hydrogen evolution under visible light. Structure and morphology of the resulting products are analysed with XRD and (HR)TEM.

5.2.1. PtCu-g-C₃N₄

Three PtCu-g-C₃N₄ materials are prepared following the procedures used to synthesise Pt-g-C₃N₄ (Chapter 2 and 4): simple impregnation, reduction under hydrogen gas and chemical reduction with NaBH₄. The so prepared materials are tested for photocatalytic hydrogen evolution and the performances are compared in Figure 5.4. The results are compared with those of 1 wt.% Pt-g-C₃N₄ and 0.5 wt.% Pt-g-C₃N₄. When the co-catalyst is composed of only platinum, the hydrogen evolution rate at the steady state is found to be 1723 $\mu\text{mol}\cdot\text{h}^{-1}\cdot\text{g}^{-1}$ for the 1 wt.% and 1531 $\mu\text{mol}\cdot\text{h}^{-1}\cdot\text{g}^{-1}$ for the 0.5 wt.%. For the simply impregnated PtCu-g-C₃N₄ the hydrogen evolution rate at the steady state is 1443 $\mu\text{mol}\cdot\text{h}^{-1}\cdot\text{g}^{-1}$, 16 % lower than that of the 1 wt.% Pt, but comparable to the H₂

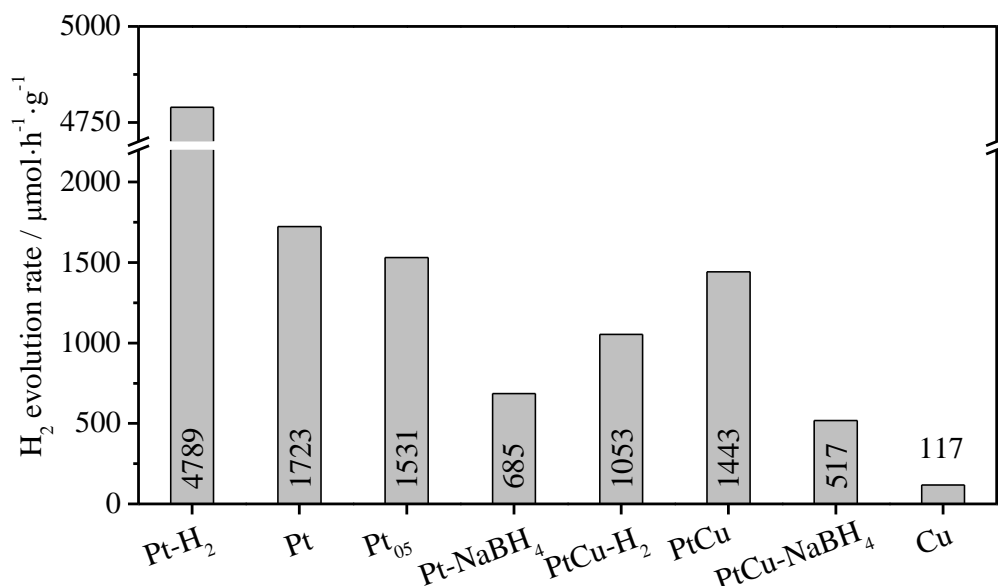


Figure 5.4 H₂ evolution rates of PtCu-g-C₃N₄. Comparison of the hydrogen evolution rates at the steady state for PtCu-g-C₃N₄ prepared by simple impregnation, reduction by H₂ and NaBH₄. For comparison, values for 1 wt.% Pt and 0.5 wt.%-g-C₃N₄ are also included.

production of the 0.5 wt.% Pt loaded g-C₃N₄. The results suggest that if a PtCu alloy is formed no improvement in activity is observed with the substitution of Pt with Cu atoms. On the other hand, if no alloy is formed then the performance is only due to the presence of platinum nanoparticles on their own, considering the negligible activity of Cu NPs (Figure 5.4).

When the catalyst is reduced in hydrogen a detrimental effect is produced on the performance and a H₂ evolution rate of 1053 $\mu\text{mol}\cdot\text{h}^{-1}\cdot\text{g}^{-1}$ is obtained which is 27 % lower than the not pre-treated material. This behaviour is opposite to what has been seen for the 1 wt.% Pt loaded g-C₃N₄ where the reduction in hydrogen brought to an enhancement in performance by a factor 3 (Chapter 4). The H₂ evolution of PtCu-g-C₃N₄ chemically reduced with NaBH₄ is found to be 517 $\mu\text{mol}\cdot\text{h}^{-1}\cdot\text{g}^{-1}$. Compared to the PtCu impregnated material, the drop (64 %) in hydrogen evolution rate is of a similar magnitude to the one observed for the equivalent Pt system (60 %). This suggests that the introduction of copper is not favourable to enhance the performance of the catalyst.

To verify the presence of a PtCu alloy on the surface of g-C₃N₄, XRD analysis is performed on the reduced samples, the patterns are compared in Figure 5.5 with that of Pt-g-C₃N₄ reduced in H₂ under the same conditions (Figure 5.5a). The impregnated sample is not illustrated in Figure 5.5 since, as demonstrated by Figure 4.6 (Chapter 4), in the case of 1 wt.% Pt no well-defined peaks in the XRD pattern could be identified.

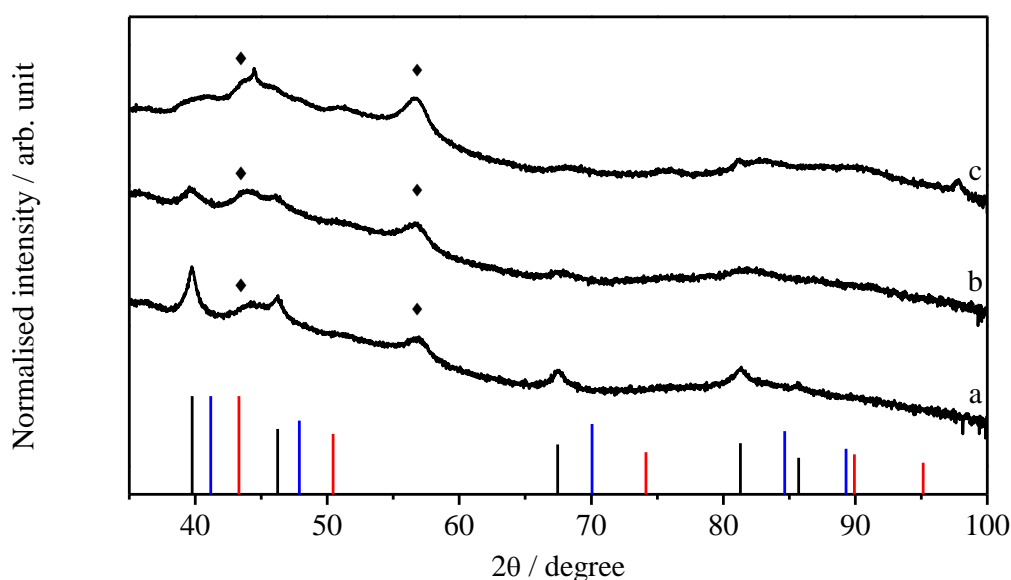


Figure 5.5 XRD of PtCu-g-C₃N₄. XRD patterns of a) Pt-g-C₃N₄ reduced with H₂ and PtCu-g-C₃N₄ reduced with b) H₂ and c) NaBH₄. Bars: XRD patterns of Pt (PDF card #:04-0802, black), Cu (PDF card #: 04-0836, red) and PtCu (PDF card #: 48-1549, blue). ♦: g-C₃N₄.

When the reduction of PtCu-g-C₃N₄ is carried out under hydrogen atmosphere (Figure 5.5b) the peaks are well defined and easy to identify. Only the main peaks characteristic of Pt⁰ can be observed: the (111) reflection at 39.8° and the (200) at 46.2°. Compared to those of Pt-g-C₃N₄ (Figure 5.5a) the peak at 39.8° is smaller and broader. This could be due to the lower content of platinum (only 50 % of the original). The absence of the peaks characteristic of PtCu alloy can either indicate no alloyed particles are formed, they are too small or not crystalline enough, with the last possibility being the least probable.

When the reducing agent is NaBH₄ (Figure 5.5c) the peaks are not well defined and therefore no clear identification is possible. Nonetheless, the broad peak at 2θ ~ 40.0° could be ascribed to the presence of both the (111) reflection of Pt⁰ and the (111) reflection of PtCu alloy (blue bars in figure 5.5, PDF # 48-1549). The peak at 2θ = 50.4° could be assigned to the (200) reflection of Cu⁰ suggesting the presence of copper metal. However, this assumption cannot be confirmed since the (111) reflection (2θ = 43.3°) partially overlaps with the peak of g-C₃N₄.

(HR)TEM images of all the PtCu-g-C₃N₄ samples are illustrated in Figure 5.6. The impregnated PtCu-g-C₃N₄ is analysed after photocatalytic test. As discussed in Chapter 4 this procedure can be seen as a photoreduction, hence coherent with the other loading procedures. After exposing to visible light the impregnated PtCu-g-C₃N₄, the average particle size is found to be 3.5 ± 2.8 nm (Figure 5.6a, inset). This value is higher than when platinum alone is impregnated on the surface (2.3 ± 1.2 nm, Chapter 4). The size distribution is also increased as seen from Figure 5.6a where big particles are accompanied by smaller particles. Figure 5.6b shows nanoparticles characterised by lattice fringes of values 0.219 nm and 0.188 nm which correspond to the (111) and (200) reflections of a cubic PtCu alloy (PDF card # 4-8731). In addition, some nanoparticles with lattice fringes of 0.226 nm characteristic of the (111) reflection of cubic Pt⁰ are also observed. This indicates that the degree of alloying is only partial. (HR)TEM should not be considered a quantitative technique since the analysed area is only a fraction of the overall sample. Nonetheless, in the limited number of TEM images acquired for this particular system the probability of finding PtCu nanoparticles compared to Pt is approximately 2:1.

When the sample is reduced under hydrogen the average particle size is found to be 3.9 ± 2.0 nm (Figure 5.6d, inset) showing no significant increase compared to the impregnated PtCu-g-C₃N₄. This behaviour is once again different from what was

observed in the case of Pt-g-C₃N₄ when the reduction in hydrogen atmosphere favoured the formation of big clusters of NPs and the average size increased by a factor two (4.9 ± 4.7 nm, Chapter 4). From the high resolution TEM images (Figure 5.6be-f) only platinum metal lattice fringes can be seen (0.226 nm). This result is found in agreement with the observation made in the XRD analysis. At this stage it is not possible to confirm the successful formation of the PtCu alloy. However, it is reasonable to believe copper remain present on the surface of g-C₃N₄, but the lack of evidence in both XRD and TEM could either indicate its presence as an amorphous phase or, less likely, monolayer-like configuration. For the reduction by NaBH₄ (Figure 5.6g-i) PtCu alloy coexist with platinum metal NPs at a relative frequency in the TEM images of 1:1. This confirms what has been seen in the XRD, *i. e.* a broad peak suggesting the presence of both alloy and platinum metal. The overall average particle size is estimated to be 2.6 ± 1.5 nm which is lower than the other loading procedures, justifying the low resolution in the XRD pattern. The presence of the PtCu alloy is confirmed *via* HRTEM for both the simply impregnated and chemically reduced (NaBH₄) samples. However, photocatalytic tests shows that no effect on the performance is produced. The absence of any significant change in hydrogen evolution can be explained if the amount of PtCu alloy is too low to have any quantifiable effect and only platinum is responsible for the production of hydrogen. The sample reduced under H₂ does not show any evidence of PtCu alloy formation but still sees a decrease in performance. This indicates that despite not being visible a change is introduced by the Cu in the system. The results presented here are found in disagreement with the literature. Mu *et al.* showed that when PtCu nanoparticles were exposed to reduction treatments at 300 °C a platinum-rich surface was obtained.¹⁸⁸ Furthermore, the Cu@Pt core-shell systems is often reported in the literature with improvement in catalytic activity.^{185, 196} At this stage is not possible to provide a definitive explanation of why such a decrease in performance is observed. Nonetheless, some possible explanations can be speculated. Since only platinum metal is confirmed, it can be assumed that copper metal is present on its own on the surface of g-C₃N₄. Copper has a lower work function than platinum, therefore, it may receive electrons from the semiconductor more easily than Pt but at the same time facilitated their backflow and recombination. Alternatively, since when copper is introduced in the system no big clusters of NPs can be observed after reduction in H₂, this suggests a higher dispersion of nanoparticles. As seen in the previous chapter a higher dispersion may be detrimental for the activity.

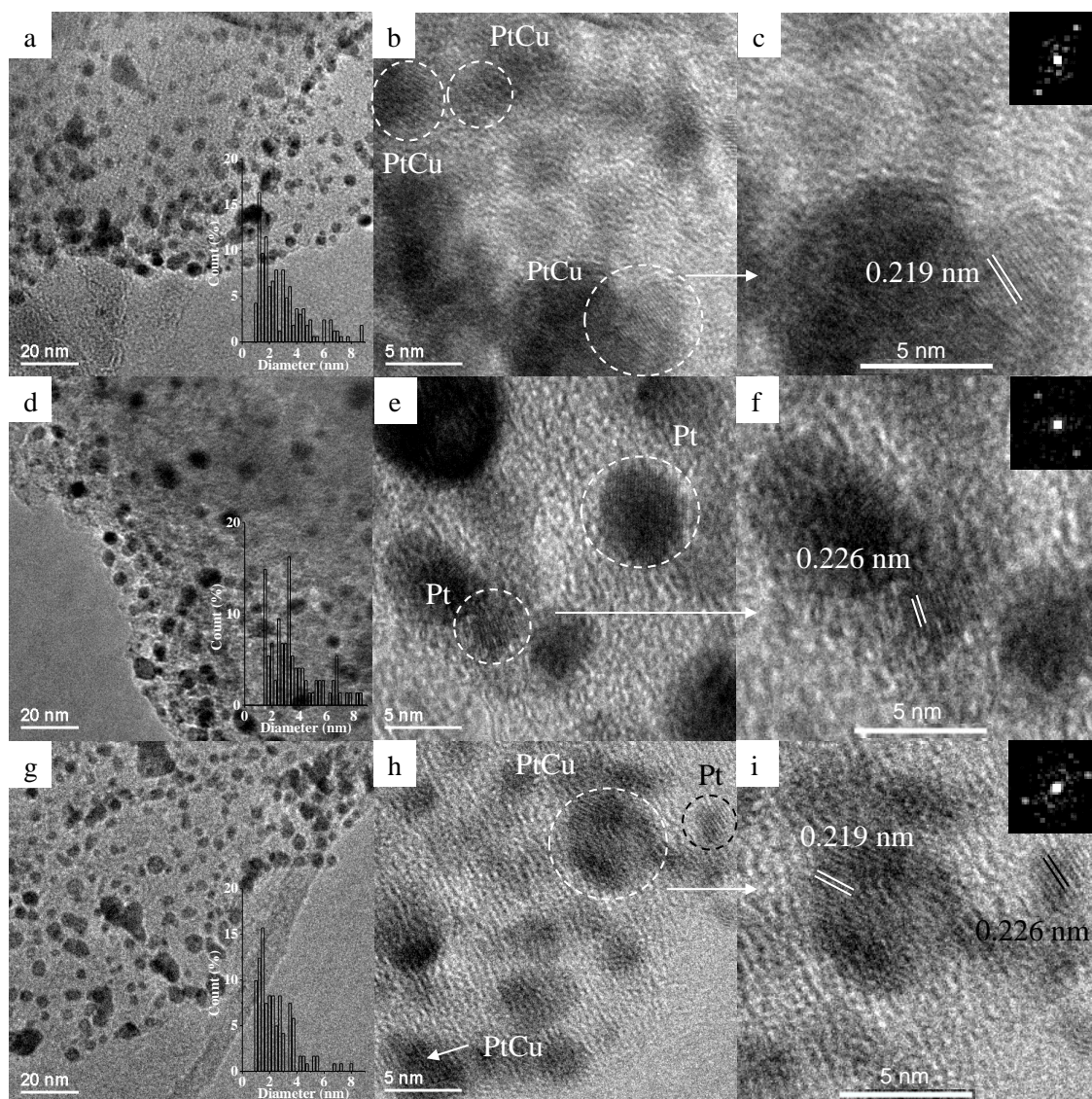


Figure 5.6 (HR)TEM images of PtCu-g-C₃N₄. (HR)TEM images of PtCu-g-C₃N₄ a-c) impregnated after photocatalytic test; reduced with d-f) H₂ and g-i) NaBH₄. Inset: a, d, g) particle size distribution; c, f, i) example of diffractogram of selected nanoparticle.

5.2.2. PtAg-g-C₃N₄

The photocatalytic activities of PtAg loaded g-C₃N₄ prepared following different procedures are compared with the equivalent Pt-loaded samples in Figure 5.7. After simple impregnation of the metal salts the hydrogen evolution rate at the steady state is found to be 1292 $\mu\text{mol}\cdot\text{h}^{-1}\cdot\text{g}^{-1}$, 25 % lower than the production rate for 1 wt.% Pt-g-C₃N₄ indicating that the replacement of the platinum atoms with silver has a negative effect on the activity of the catalyst. Similar effect on the activity is produced by the chemical

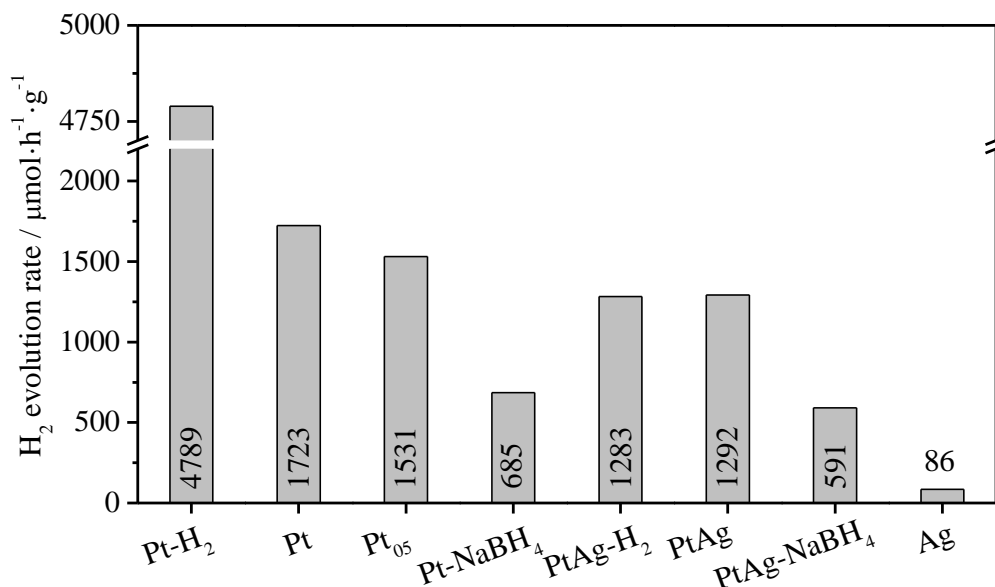


Figure 5.7 H₂ evolution rates of PtAg-g-C₃N₄. Comparison of the hydrogen evolution rates at the steady state for PtAg-g-C₃N₄ prepared by simple impregnation, reduction by H₂ and NaBH₄. Performance of Pt-g-C₃N₄ is also shown for comparison.

reduction treatment (NaBH₄), which brings down the performance by 14 %, (591 μmol·h⁻¹·g⁻¹ vs. 685 μmol·h⁻¹·g⁻¹ for the equivalent Pt-g-C₃N₄). The activity for the PtAg-g-C₃N₄ reduced under hydrogen is 1283 μmol·h⁻¹·g⁻¹; 73 % less than the reduced Pt-g-C₃N₄.

Figure 5.8 illustrated the XRD patterns obtained for PtAg-g-C₃N₄ prepared *via* reduction with hydrogen (Figure 5.8b) and NaBH₄ (Figure 5.8c). After reduction in hydrogen (Figure 5.8b) at 300 °C a clear sharp peak appears at 2θ = 38.1° together with two small but visible peaks at 2θ = 64.4° and 2θ = 77.4°. These are associated to the (111), (220) and (311) reflections of cubic Ag metal (PDF card # 04-0783). The (200) Bragg's reflection of Ag at 2θ = 44.3° overlaps with the peak from g-C₃N₄. Williamson-Hall plot of the three clearly visible peaks reveal a crystallite size of 43 nm which is significantly bigger than the one calculated for the equivalent Pt-g-C₃N₄ (15 nm, Chapter 4). No visible sign of platinum or alloy is present in this case.

After chemical reduction of the metal precursors with NaBH₄, (Figure 5.8c) the broad peak at 2θ ~ 40° indicates the presence of platinum metal, and the broad shoulder at a smaller angle suggests either the presence of silver metal, PtAg alloy or both. The reflection of platinum metal and bimetallic alloy are very close and the small nature of

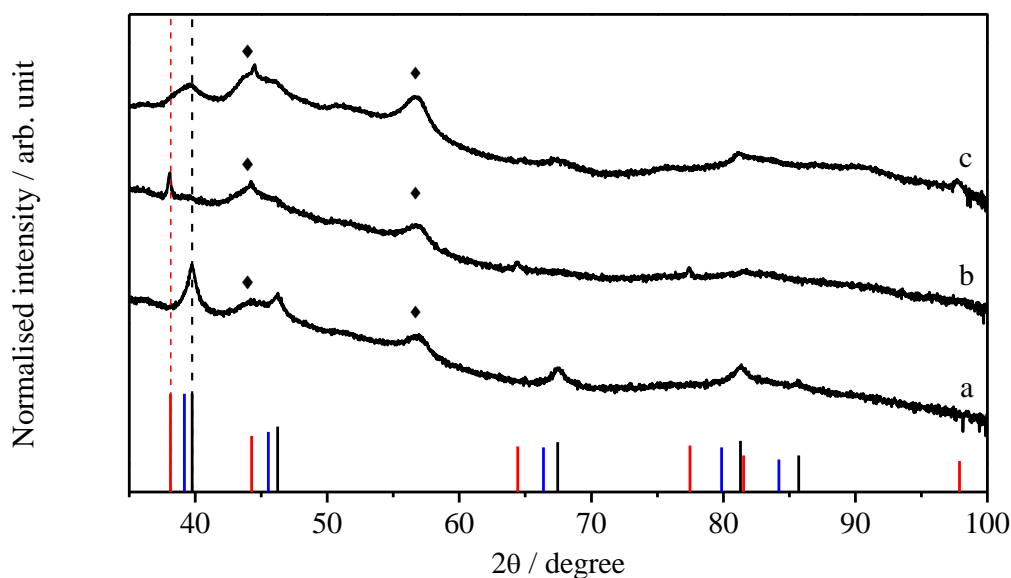


Figure 5.8 XRD of PtAg-g-C₃N₄. XRD patterns of a) Pt-g-C₃N₄ reduced with H₂ and PtAg-g-C₃N₄ reduced with b) H₂ and c) NaBH₄. Bars: XRD patterns of Pt (PDF card #:04-0802, black), Ag (PDF card #: 04-0783, red) and PtAg (PDF card #: 01-1796, blue). ◆: g-C₃N₄

the nanoparticles brings to a broadening of the peaks, making the identification challenging.

(HR)TEM images of the three PtAg-g-C₃N₄ samples are illustrated in Figure 5.9. After photocatalytic test of the simply impregnated material, nanoparticles with an average size of 7.9 ± 7.8 nm are formed (Figure 5.9a). Some of them present a peculiar ring-like shape (Figure 5.9b) which was not observed for the platinum nanoparticles. An example of formation of Ag-based alloy nanorings has been reported by Liu *et al.*¹⁹⁷. In their work they synthesised AgPd nanorings by forming silver nanoparticles and subsequently depositing palladium on its surface. To form the nanorings a mild thermal treatment (100 °C) was carried out in order to promote the dissolution of the silver core into the palladium shell.¹⁹⁷ A similar mechanism can be suggested for the formation of PtAg nanorings during *in-situ* photoreduction. During irradiation the photoexcited electrons of g-C₃N₄ may be used to reduce first the silver which is characterised by a reduction potential of $E_{\text{red}} = 0.7996$ eV²¹, closer to the conduction band position (-0.83 eV)⁵⁶ of g-C₃N₄ compared to that of platinum ($E_{\text{red}} = 1.118$ eV)²¹. Subsequently, the reduced silver may act as an electron trap and provide favourable sites for the reduction of platinum. Since the temperature of the solution during the photocatalytic test reaches 75 °C, it is possible to assume that this temperature is high enough to promote the diffusion of the

silver core into the platinum shell to form the alloy. (HR)TEM image of the nanorings (Figure 5.9c) shows clear lattice fringes with value 0.141 nm. This can be associated to the (220) plane of a PtAg alloy with atomic ratio 1:1 (PDF card # 01-1796). However, the inter-planar distances for the alloy and metallic platinum (0.139 nm, PDF card # 04-0802) are very similar, and due to the intrinsic error in determining inter-planar distances from TEM images (Chapter 2), it is not possible to state with certainty that indeed an alloy is formed. Nonetheless, this peculiar shape has not been observed for the Pt NPs analysed so far, hence it is reasonable to assume that the nanorings are the result of alloying between platinum and silver.

After reduction in hydrogen at 300 °C mainly small particles of 2.9 ± 1.9 nm are observed (Figure 5.9d-f). (HR)TEM images of the smaller particles shows lattice fringes that could be assigned to both Pt and PtAg, for the reasons already explained. It is however possible to identify small Ag NPs with a lattice fringe on 0.232 nm (PDF card # 04-0783). In addition to the many small nanoparticles a few big NPs of diameter larger than 30 nm are identified (Figure 5.9d inset). No lattice fringes could be observed for these NPs and therefore it is not possible to identify their composition. The presence of large spherical nanoparticles was not noticed during the investigation of Pt-g-C₃N₄. Therefore it is most likely the large nanoparticles (Figure 5.9d inset) are mainly containing silver. This assumption would be in agreement with what is obtained from the Williamson-Hall analysis of the XRD pattern.

When the reduction is carried out with NaBH₄ the average particle size is 3.8 ± 3.6 and NPs with a ring-like shape are present. The nanorings are not as well-defined and as frequent as after photoreduction. A similar mechanism to the photoreduction could be proposed for the reduction with NaBH₄ without the thermal treatment. The absence of a thermal treatment could be a reason for the low number of rings present on the surface of g-C₃N₄. The observed lattice fringes (0.227 nm, 0.197 nm) can be attributed to either Pt and/or PtAg.

The presence of the alloy can only be speculated for the simply impregnated sample after photocatalytic test. For the reduced materials, due to the similarities of lattice fringes values and the error in the measurements, it is not possible to state whether the alloy was successfully formed. None of the loading methods produce an improvement on the catalytic activity of Pt-g-C₃N₄. The introduction of silver as a co-catalyst has a detrimental effect on the performance for photocatalytic hydrogen evolution. Excluding the hydrogen reduced method, the largest decrease is observed for the simply impregnated material. If

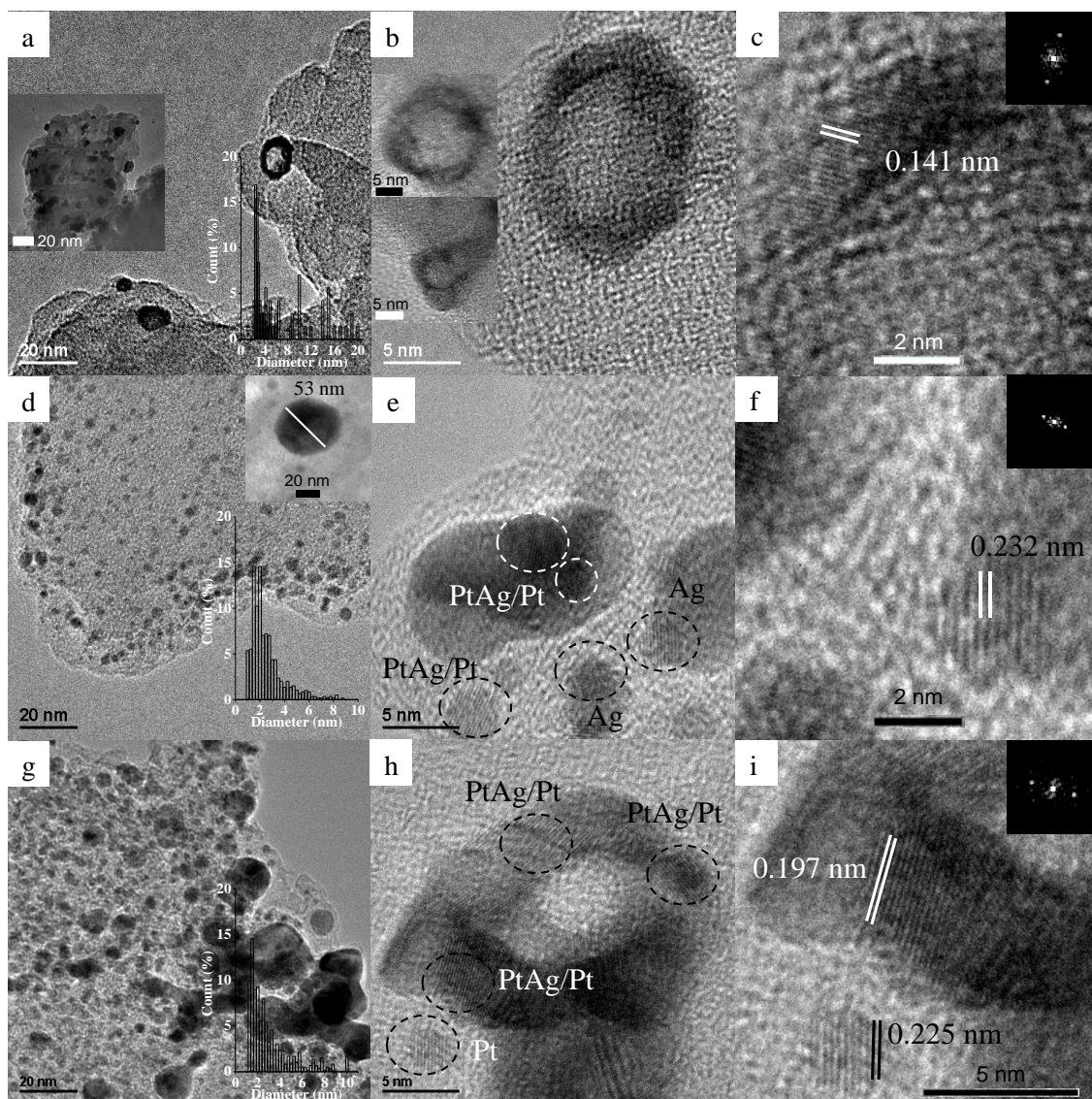


Figure 5.9 (HR)TEM images of PtAg-g-C₃N₄. (HR)TEM images of PtAg-g-C₃N₄ a-c) impregnated after photocatalytic test; reduced with d-f) H₂ and g-i) NaBH₄. Inset: a, d, g) particle size distribution and additional areas of the surface; c, f, i) example of diffractogram of selected nanoparticle.

a PtAg alloy is formed, its lower work function compared to Pt would favour the recombination events.

5.2.3. PtNi-g-C₃N₄

The activity of the PtNi-g-C₃N₄ samples are summarised in Figure 5.10. After simple impregnation of the two metal precursors the H₂ evolution rate is found to be 1716 $\mu\text{mol}\cdot\text{h}^{-1}\cdot\text{g}^{-1}$ which is nearly identical to the activity of the 1 wt.% Pt, and 12 %

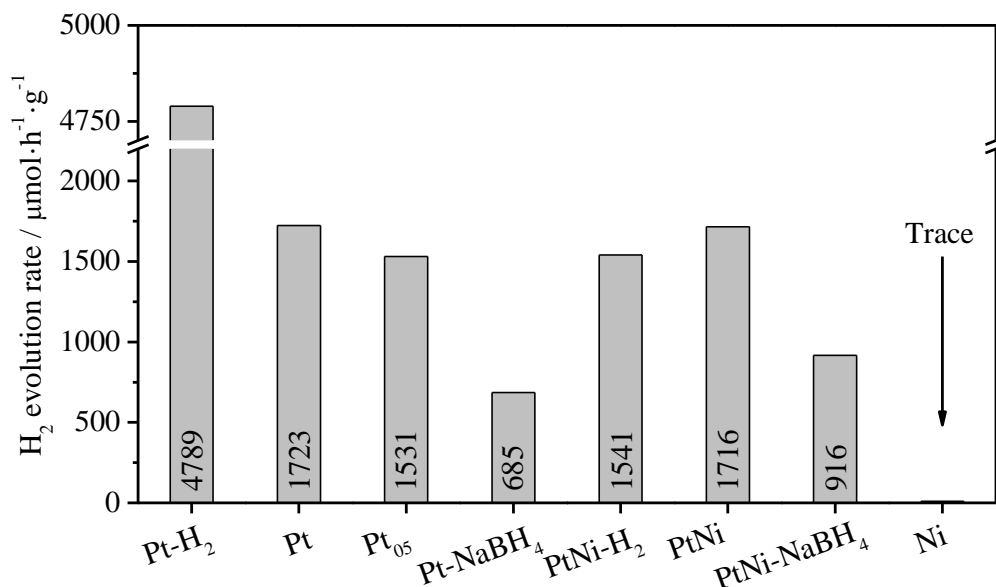


Figure 5.10 H₂ evolution rates of PtNi-g-C₃N₄. Comparison of the hydrogen evolution rates at the steady state for PtNi-g-C₃N₄ prepared by simple impregnation, reduction by H₂ and NaBH₄. Performance of Pt-g-C₃N₄ is also shown for comparison.

higher than the value obtained for the 0.5 wt.% Pt loaded material (Pt₀₅ in Figure 5.10, 1530 μmol·h⁻¹·g⁻¹). The hydrogen evolution rate when only nickel is used as co-catalyst is found to be 9 μmol·h⁻¹·g⁻¹. The performance is, therefore, not the sum of the individual H₂ productions, but a result of a positive interaction between the two metals. A similar effect is noticed when the metal precursors are reduced with NaBH₄. In this case the hydrogen evolution rate is 916 μmol·h⁻¹·g⁻¹ which shows an increase of 34 % in activity when compared to Pt-g-C₃N₄ prepared in the same way (685 μmol·h⁻¹·g⁻¹). A different behaviour is shown by PtNi-g-C₃N₄ after reduction under hydrogen flow. The activity of the reduced material is now lower than that of the impregnated one, with a value of 1541 μmol·h⁻¹·g⁻¹. Once again the reduction under H₂ of the bimetallic co-catalyst produces an effect opposite to that produced on pure platinum loaded graphitic carbon nitride.

The XRD patterns of the reduced samples are compared in Figure 5.11 with the XRD pattern of Pt-g-C₃N₄ reduced under hydrogen (Figure 5.11a). The XRD of the sample after reduction (Figure 5.11b) in hydrogen does not provide any evidence of the presence of a PtNi alloy. A very small and very broad peak can be seen at 2θ ~ 40.0° which can be associated to the (111) reflection of Pt⁰. The low intensity and the broad width of this peak could be due to either a small amount or a very small particle size of Pt NPs. In the

XRD pattern of the chemically reduced sample (Figure 5.911c), a peak at $2\theta = 39.97^\circ$ is observed, an angle that is slightly higher than the one of Pt^0 at $2\theta = 39.76^\circ$. This shift is too small to justify the presence of a PtNi alloy with a 1:1 atomic ratio which has its main diffraction peak, (111) reflection, at $2\theta = 41.69^\circ$ (blue bars in Figure 5.11). However an alloy of composition $\text{Pt}_x\text{Ni}_{1-x}$ with $x > 0.5$ may still be present. The composition of the alloy can be calculated by using Vegard's law¹⁰⁹ (Eq. 5.1) valid for metals with the same crystal structure:

$$d_A = C_{\text{Pt}} d_{\text{Pt}} + C_{\text{Ni}} d_{\text{Ni}} \quad \text{Eq. 5.1}$$

where d_A , d_{Pt} , d_{Ni} are the d-spacing of the alloy, Pt^0 and Ni^0 and C_{Pt} and C_{Ni} are the atomic concentrations of the metals in the alloy. With $d_{\text{Pt}} = 0.226$ nm (PDF card # 4-802), $d_{\text{Ni}} = 0.203$ nm (PDF card #: 04-0850) and $d_A = 0.225$ nm (Figure 5.9c), C_{Ni} is calculated from Eq. 5.1 as 0.04. The resulting alloy composition is $\text{Pt}_{0.96}\text{Ni}_{0.04}$. It is important to mention, this alloy composition is an underestimation of the real Ni content since in Vegard's the metals should have comparable atomic radii. The formation of an alloy can be confirmed by the presence of a broad peak at $\sim 48^\circ$. Since, the initial atomic ratio of the precursors was 1:1, the low amount of Ni in the alloy means that the remaining nickel

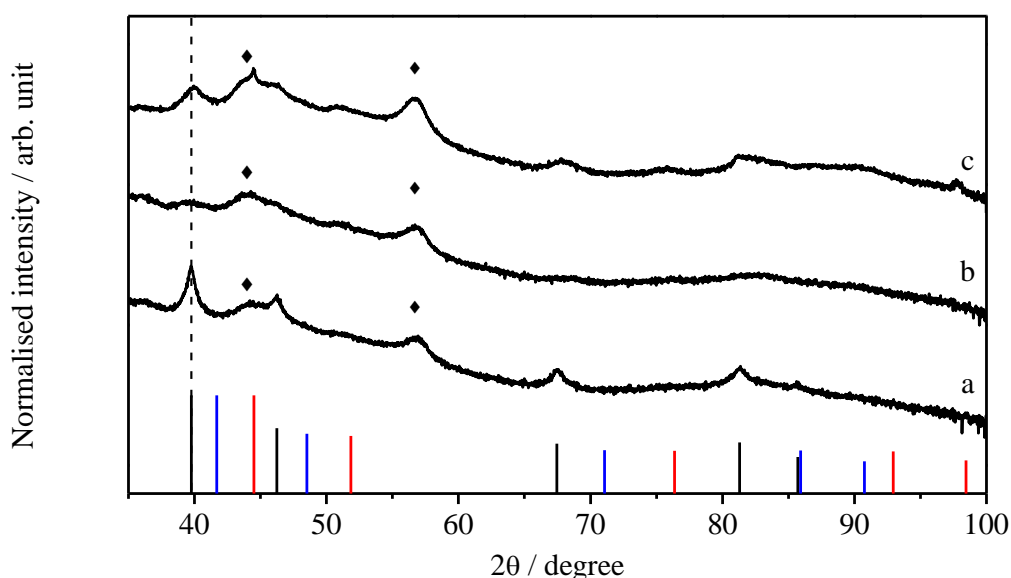


Figure 5.11 XRD of PtNi-g-C₃N₄. XRD patterns of a) Pt-g-C₃N₄ reduced with H₂ and PtNi-g-C₃N₄ reduced with b) H₂ and c) NaBH₄. Bars: XRD patterns of Pt (PDF card #:04-0802, black), Ni (PDF card #: 04-0850, red) and PtNi (PDF card #: 04-8735, blue). ◆: g-C₃N₄

has to be present in other forms. The (111) reflection of metallic nickel overlaps with the peak of g-C₃N₄, but at ~ 76° a very broad peak can be associated to its (220) reflection. The (HR)TEM images for the three samples are illustrated in Figure 5.12. After photocatalytic test of the simply impregnated PtNi-g-C₃N₄ small nanoparticles with an average size of 2.0 ± 1.1 nm are formed (Figure 5.12a). This value is similar to the one obtained for pure platinum loaded g-C₃N₄ (2.3 ± 1.2 nm). From the analysis of high resolution images only lattice fringes characteristic of platinum can be identified (Figure 5.12b-c). When reduction under hydrogen is performed on the impregnated sample formation of bigger particles and agglomerates can be observed similarly to when only platinum is used as co-catalyst (Figure 5.12d). The average particle size is 3.4 ± 2.2 nm. Earlier, the absence of defined peaks in the XRD pattern was associated to a small average particle size but the TEM images show this is not the case. The poor resolution in the XRD can therefore be due to the presence of more species bringing to a decrease of the intensities. High resolution TEM images (Figure 5.10f) show lattice fringes with a distance of 0.217 nm which corresponds to the (111) plane of a cubic PtNi alloy with a 1:1 atomic ratio. However, this is only a minority and most of the analysed particles showed lattice fringes characteristic of platinum metal.

Chemical reduction by NaBH₄ brings to the formation of nanoparticles with a wider distribution of sizes compared to the H₂ reduced sample (Figure 5.10g). The average particle size in this case is 3.7 ± 4.2 nm. This is due to the formation of clusters of nanoparticles. Analysis of the lattice fringes indicates the presence of Pt⁰ and PtNi alloy. Lattice distances of values varying between 0.226 nm (d_{111} of Pt⁰) and 0.216 nm (d_{111} of PtNi, PDF card #: 04-8735) can also be found, for example, 0.220 nm and 0.221 nm. This suggests the presence of alloys composition Pt_xNi_{1-x} with an excess of platinum content ($0.5 < x < 1$) as proposed in the XRD analysis. However, due to the uncertainty in the determination of the lattice fringes distances¹⁰⁹ these values could still be indication of the PtNi alloy with a 1:1 ratio. In addition to platinum metal and the alloy, the presence of Ni⁰ can also be confirmed by lattice fringes of 0.203 nm characteristic of its (111) reflection. This confirms what was discussed for the XRD of this material.

The (HR)TEM results show that it is possible to obtain a PtNi alloy after reduction with hydrogen gas or NaBH₄ with the latter being the most successful. However, with the information at hand it is not possible to quantify the extent of alloying. The presence of platinum metal nanoparticles in both cases indicates that this does not proceed completely. Differently, no alloy nanoparticles are observed for the simply impregnated

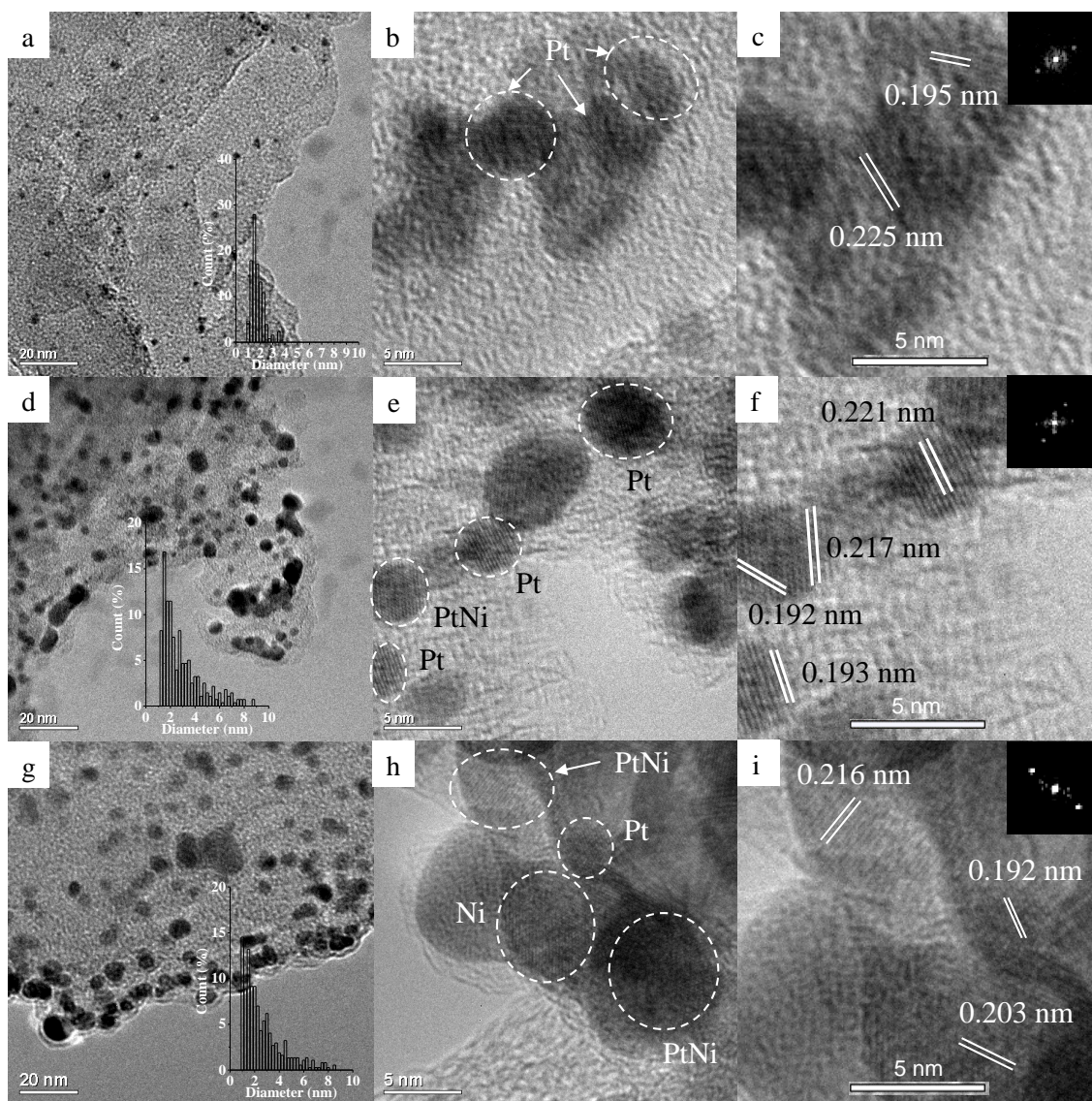


Figure 5.12 (HR)TEM images of PtNi-g-C₃N₄. (HR)TEM images of PtNi-g-C₃N₄ a-c) impregnated after photocatalytic test; reduced with d-f) H₂ and g-i) NaBH₄. Inset: a, d, g) particle size distribution; c, f, i) example of diffractogram of selected nanoparticle.

sample. If individual platinum NPs were present on the surface of g-C₃N₄ the performances would have been expected to be the same as of the 0.5 wt.% Pt loaded g-C₃N₄, but the photocatalytic results show a performance comparable to that of the 1 wt.% Pt. This suggests a synergistic effect between the two metals. Improvement on the performance is also obtained after chemical reduction for which the presence of PtNi NPs is instead confirmed. For the H₂ reduced sample a decrease in performance is observed, opposite to what may have been expected. In this case the presence of the alloy is confirmed. If the alloy is indeed responsible for the increase in performance as seen for

the other two loading procedures, then the sample reduced with hydrogen should have also showed an improvement in activity. This result does not yet find an explanation. It may, however, be related to different crystallisation levels, facets exposed or structures with different level of activities.¹⁹⁸

5.2.4. PtCo-g-C₃N₄

Figure 5.13 shows the hydrogen evolution rates for the different PtCo-g-C₃N₄ loading procedures. When the precursors of the two metals are simply impregnated on the surface of g-C₃N₄ the H₂ evolution rate at the steady state is 1707 $\mu\text{mol}\cdot\text{h}^{-1}\cdot\text{g}^{-1}$, comparable to the one of 1 wt.% Pt and 11.5 % higher than that of 0.5 wt.% Pt. However, in this case the activity of Co-g-C₃N₄ is 190 $\mu\text{mol}\cdot\text{h}^{-1}\cdot\text{g}^{-1}$, therefore the higher activity could be ascribed to a sum of the contributions of the two metals without synergistic effect. Nonetheless, comparable activity is obtained by replacing 50 % of the platinum atoms with cheaper cobalt. The activity of PtCo-g-C₃N₄ reduced under hydrogen is 2159 $\mu\text{mol}\cdot\text{h}^{-1}\cdot\text{g}^{-1}$; 26 % higher than the impregnated equivalent. Even though this performance remains significantly lower than the H₂ reduced 1 wt.% Pt-g-C₃N₄, it shows an opposite behaviour compared to the previously discussed bimetallic co-catalysts which after reduction under H₂ showed a decrease in performance. Reduction with NaBH₄ improves the activity of the catalyst, 827 $\mu\text{mol}\cdot\text{h}^{-1}\cdot\text{g}^{-1}$, 21 % higher than the 1 wt.% Pt-g-C₃N₄. In this case the replacement of half of the Pt atoms with the cheaper Co leads to higher performance.

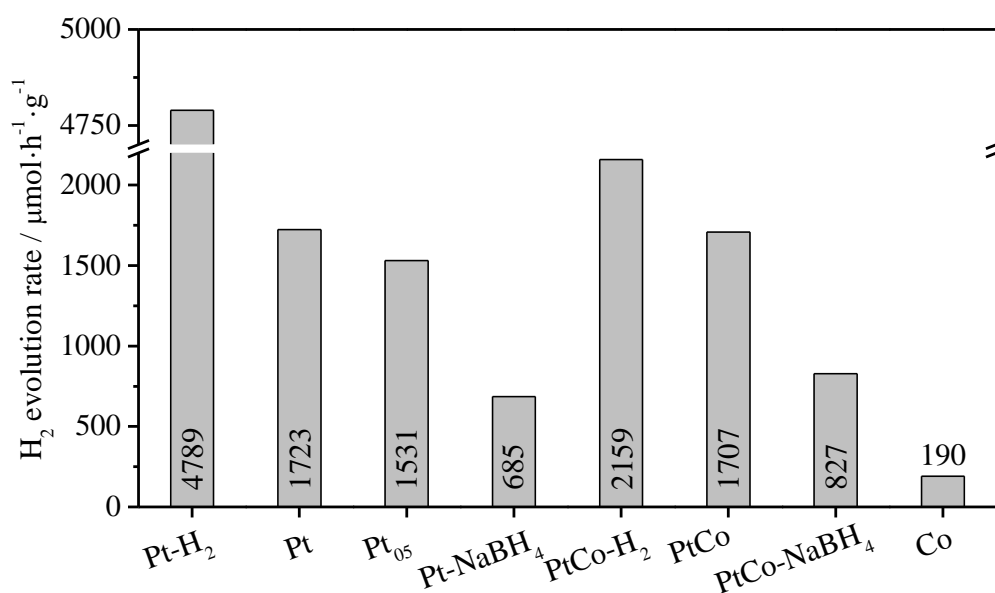


Figure 5.13 H₂ evolution rates of PtCo-g-C₃N₄. Comparison of the hydrogen evolution rates at the steady state for PtCo-g-C₃N₄ prepared by simple impregnation, reduction by H₂ and NaBH₄.

In the XRD pattern of PtCo-g-C₃N₄ reduced under hydrogen (Figure 5.14b) is not possible to clearly identify a peak at $\sim 40^\circ$ or any other angle. The formation of more than one phase (Pt⁰, Co⁰, and various Pt_xCo_{1-x}) may have a detrimental effect on the intensity of the peaks of each species. After chemical reduction with NaBH₄ (Figure 5.14c) the peak at $2\theta = 39.99^\circ$ ($d = 0.225$ nm) appears shifted compare to the (111) reflection of Pt metal ($2\theta = 39.76^\circ$, $d = 0.226$ nm) and can be linked to the alloying with cobalt. This shift is too small to indicate the presence of a Pt_{0.5}Co_{0.5} alloy. After applying Vegard's law the alloy composition is estimated to be Pt_{0.95}Co_{0.05}. This Co content is however underestimated due to the difference in atomic radius of the two metals. Nonetheless, the excess of platinum in the alloy suggests Co⁰ and/or a cobalt rich alloy can also be present to take into account the remaining cobalt loading. This assumption is confirmed with the presence of the broad peak at $\sim 51^\circ$, in between the (200) of the metallic cobalt and the alloy with an atomic ratio of 1:1.

(HR)TEM images of the samples are illustrated in Figure 5.15. After photocatalytic test of the simply impregnated sample, the average particle size of the NPs is 2.7 ± 1.7 nm, only slightly bigger than Pt-g-C₃N₄ (2.3 ± 1.2 nm). High resolution images show nanoparticles with a 0.226 nm lattice fringes (Figure 5.15c) which is characteristic of platinum metal. For the Pt_{0.5}Co_{0.5} alloy a lattice fringe of 0.217 nm would be expected (PDF card # 1-0115), and in the case of platinum rich alloy a value close to 0.226 nm

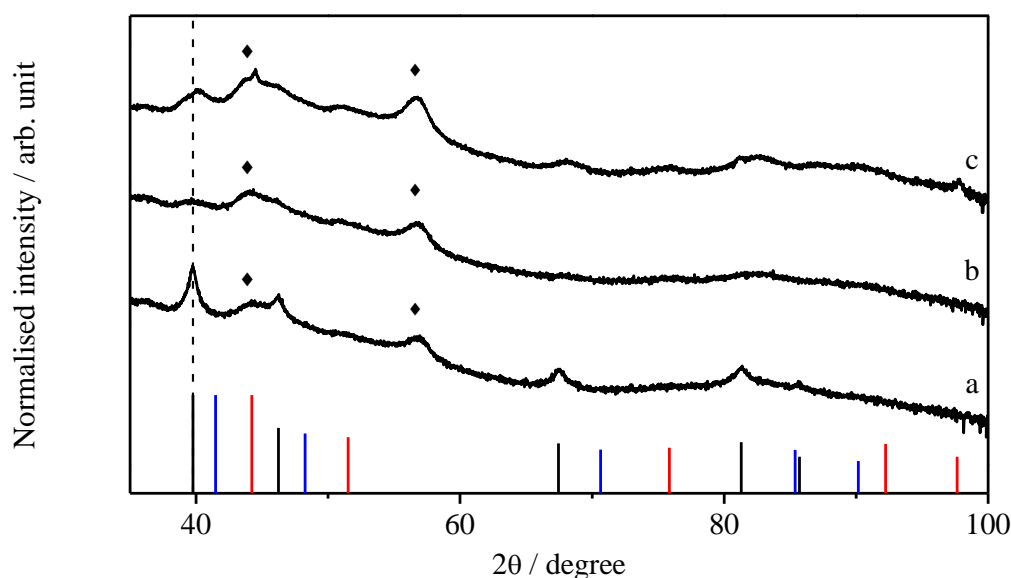


Figure 5.14 XRD of PtCo-g-C₃N₄. XRD patterns of a) Pt-g-C₃N₄ reduced with H₂ and PtCo-g-C₃N₄ reduced with b) H₂ and c) NaBH₄. Bars: XRD patterns of Pt (PDF card #:04-0802, black), Co (PDF card #: 15-0806, red) and PtCo (PDF card #: 01-0115, blue). ◆: g-C₃N₄

would be expected. While the measurement of 0.226 nm in Figure 5.15c is found in good agreement with Pt⁰, the presence of an alloy cannot be excluded.

After reduction under hydrogen the average particle size slightly decreases to a value of 2.3 ± 1.1 nm (Figure 5.13d). The presence of cobalt seems to prevent the agglomeration of the nanoparticles upon thermal treatment, a behaviour that has previously been observed for Pt NPs which formed big clusters after reduction at 300 °C (Chapter 4). The coalescence of PtCo nanoparticles have been reported at temperatures above 700 °C¹⁹⁹, significantly higher than the 300 °C employed in this investigation which is probably too low to promote coalescence. These observations could lead to assume the formation of a

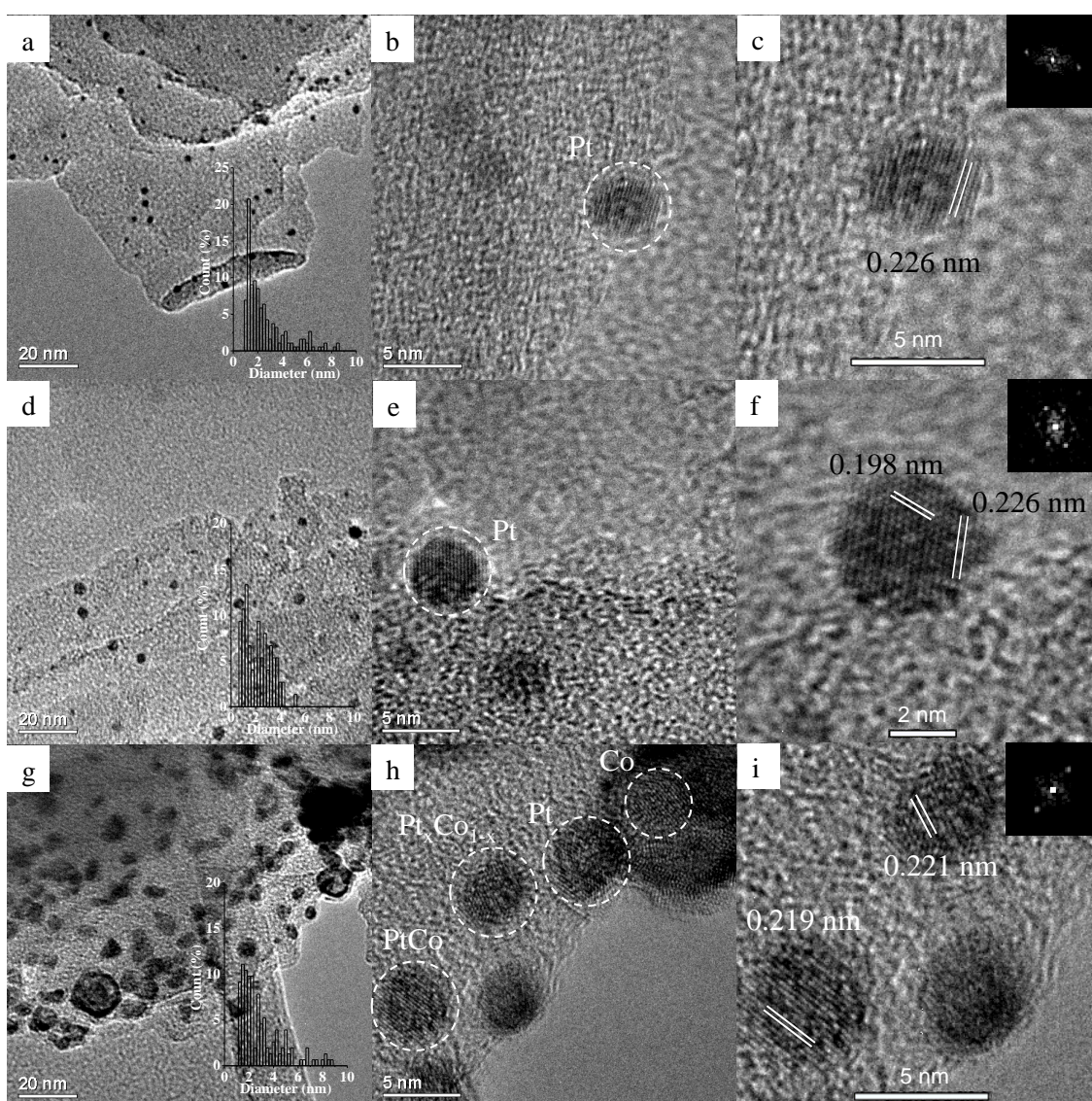


Figure 5.15 (HR)TEM images of PtCo-g-C₃N₄. (HR)TEM images of PtCo-g-C₃N₄ a-c) impregnated after photocatalytic test; reduced with d-f) H₂ and g-i) NaBH₄. Inset: a, d, g) particle size distribution; c, f, i) example of diffractogram of selected nanoparticle.

PtCo alloy. However, after analysis of the high resolution images, only Pt⁰ lattice fringes are observed (Figure 5.15f).

After chemical reduction with NaBH₄ nanoparticles with an average size of 3.5 ± 2.9 nm are formed (Figure 5.15g). Figure 5.15 shows the concomitant presence of PtCo alloy, Pt⁰ and possibly Co⁰. The first can be identified by the d_{111} of 0.219 nm; Pt⁰ by the d_{200} of 0.197 nm. The remaining nanoparticles are characterised by the presence of lattice fringes of values that due to the uncertainty in the measurements could be associated to two different species. For example a d_{111} = 0.221 nm could be associated to Pt⁰ but also to a platinum-rich alloy of generic composition Pt_xCo_{1-x}, with $x > 0.5$. This last case is coherent with what has been discussed in the XRD analysis. Together with small particles it is possible to notice large particles with ring-like shape (Figure 5.16). The centre of the ring is mostly empty and the ring itself is characterised by lattice fringes of 0.219 nm which is indicative of the (111) plane of PtCo alloy. This result is found similar to the one of the impregnated PtAg alloy, hence a similar mechanism of formation can be assumed. Despite the lack of evidence of such mechanism in the literature, it could consist in the formation of Co@Pt core-shell structure with the subsequent dissolution of the Co into the Pt shell during the chemical reduction.

Photocatalytic activity of the impregnated sample is described as the sum of the contributions of the two single metals, suggesting that no alloying takes place during the photoreduction. When the sample is reduced under hydrogen a small improvement in performance can be detected, but not as intense as expected. This indicates that in this case the presence of cobalt does negatively influence the hydrogen production rate. An explanation for this phenomenon cannot yet be provided. As in the previous bimetallic

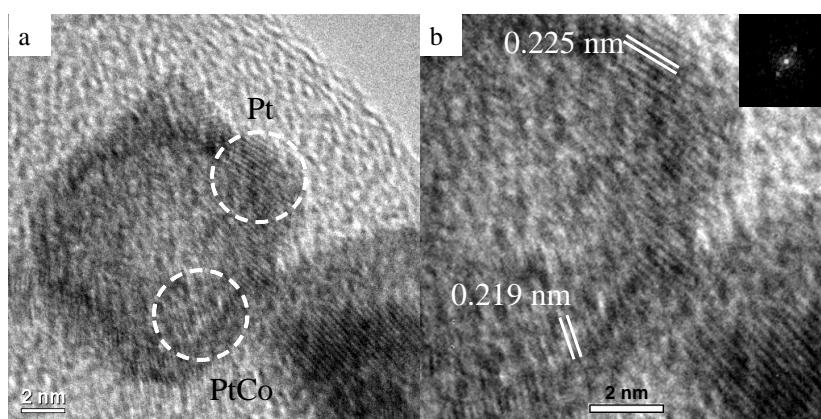


Figure 5.16 HRTEM of ring-like PtCo nanoparticle. a) Example of a ring shapes PtCo nanoparticle, b) details of the lattice fringes.

cases this could be ascribed to a different distribution of the nanoparticles or crystal structure. The highest improvement on photocatalytic activity is achieved after chemically reducing the PtCo-g-C₃N₄, which also sees the formation of a PtCo alloy. This enhancement in photocatalytic activity can be attributed to the lower work function of the alloy which can increase the efficiency of the electron transfer from the catalyst to the metal.

5.2.5. Further discussion

Table 5.2 summarizes the results obtained after a preliminary investigation of the bimetallic co-catalysts PtCu, PtAg, PtNi and PtCo.

Table 5.2 Summary of results obtained for the bimetallic alloys. Summary of the photocatalytic activities, particle sizes and alloy formation for the PtCu-, PtAg-, PtNi-, PtCo-g-C₃N₄. The uncertain presence of alloy is indicated with p.

		Cu	Ag	Ni	Co	Pt
	ϕ_{vac} (eV)	4.65	4.26	5.15	5	5.65
	NPs size (nm)	3.5	7.9	2.0	2.7	2.3
Photo	H ₂ ($\mu\text{mol}\cdot\text{h}^{-1}\cdot\text{g}^{-1}$)	1443	1292	1716	1707	1723
	Alloy	y	y	n	n	-
	NPs size (nm)	3.9	2.9	3.7	2.3	4.7
H ₂	H ₂ ($\mu\text{mol}\cdot\text{h}^{-1}\cdot\text{g}^{-1}$)	1053	1283	1541	2159	4789
	Alloy	n	p	y	n	-
	NPs size (nm)	2.6	3.8	3.4	3.5	3.7
NaBH ₄	H ₂ ($\mu\text{mol}\cdot\text{h}^{-1}\cdot\text{g}^{-1}$)	517	591	916	827	685
	Alloy	y	p	y	y	-

Three different loading procedures were investigated: *in-situ* photoreduction, reduction with H₂ and with NaBH₄. Reduction under hydrogen at 300 °C is found to cause, in all four cases, a significantly lower hydrogen production compared to the equivalent Pt-g-C₃N₄. Despite the lack of evidence in the XRD patterns and the TEM images, the thermal treatment of a bimetallic system may lead to the formation of different crystal structures and/or exposed facets, which are known to have different catalytic properties.^{164, 165, 198} Another possible explanation, can be provided with the assumption that no alloy is formed but only monometallic nanoparticles. Copper, silver, nickel and

cobalt have lower work functions compared to platinum (Figure 5.2) and once loaded on the surface of g-C₃N₄ they generate a lower Schottky barrier (Figure 5.1). This lower potential barrier is likely to be more favourable to the backflow of electrons from the metal to the semiconductor, favouring the recombination of the photoexcited charges within the SC. The total number of electrons that will be effectively used to carry out the reduction reaction will be reduced and with it the hydrogen production.

Photo- but mostly chemical reduction are proven to bring to the formation of the alloy in most of the bimetallic systems. When these procedures are employed an increase in performance is produced only for Ni and Co. A possible explanation is the correlations of H₂ evolution rates with particle size and work function, assuming that the amount and the composition of the alloys formed are the same in all four cases. The change on the work function resulting from the alloying is assumed the same for all the bimetallic systems despite the fact that the work function of an alloy between two metals is not always linear to their relative amounts.¹⁷⁹ Figure 5.17 shows the H₂ evolution rates vs. NPs size (a) and metal work function (b) for the photo and the chemically reduced samples. When *in-situ* photoreduction is employed as the synthesis method the performance decreases with increasing particle size. No conclusion can be reached for the chemically reduced samples which present similar average diameters.

The catalytic performance of the materials obtained with the two loading procedures are found related to the work function. Copper and silver have the lowest work functions

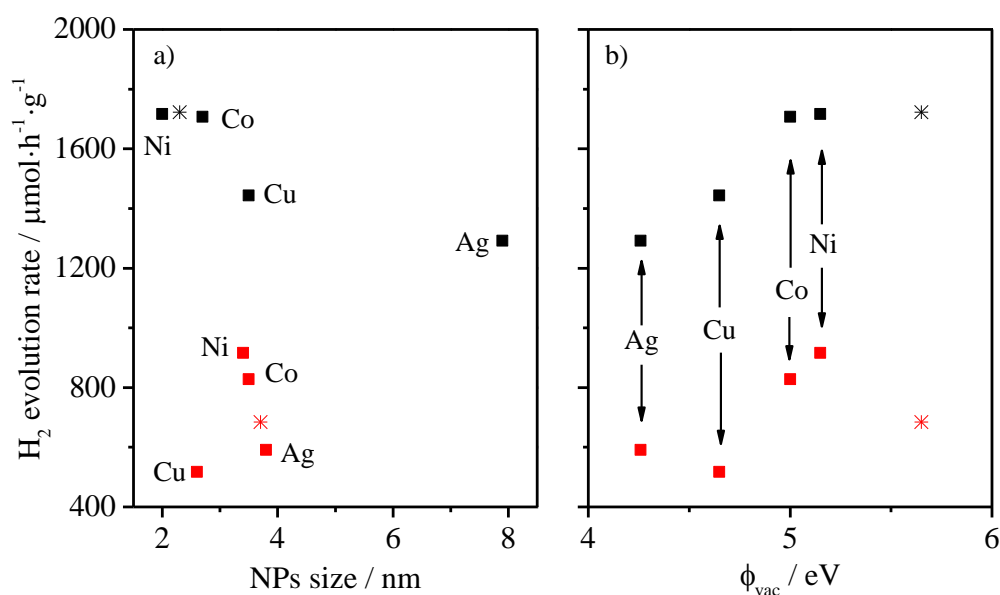


Figure 5.17 H₂ evolution rate vs. NPs particle size and metal work function. Photoreduced (black) and chemically reduced: NaBH₄, (red). *) 1 wt.% Pt.

among the metals employed for this investigation (Figure 5.2), therefore, provided the assumptions and approximation made, the resulting alloys have lower work functions compared to the others. As a consequence the Schottky barrier generated at the metal-semiconductor interface is the lowest. In the introduction of the chapter it was said that an optimum barrier height could improve the performance of the catalyst by facilitating the electron transfer to the metal but, at the same time, preventing the backflow. It is therefore, possible that PtCu and PtAg generate a barrier that is too low and the electrons can easily flow back into the SC. In the case of PtNi and PtCo the barrier may be only slightly lower than that of platinum and, therefore, can facilitate the passage of the electrons to the metal but still prevents the re-injection into graphitic carbon nitride. To confirm this theory proper characterisation of the co-catalyst is necessary to determine the amount of alloy and its composition.

5.3. Conclusions and future works

A preliminary investigation of four Pt-based bimetallic alloys as co-catalyst for g-C₃N₄ has been carried out using three loading procedures. The activity for photocatalytic hydrogen evolution of the different PtMe-g-C₃N₄ has been evaluated and compared to the platinum-only system. It has been found that an enhancement in performance compared to the Pt-g-C₃N₄ can be obtained but only for PtNi and PtCo co-catalysts when loaded by simple co-impregnation or by chemical reduction. Treatment in hydrogen at 300 °C has brought, in all cases, to a lower performance than expected which indicates that this loading procedure is only suitable to achieve catalytic improvement in the case of a Pt only system. Chemical reduction, in the case of PtNi and PtCo, sees the most significant improvement in hydrogen evolution and therefore proves to be the most promising approach to a bimetallic co-catalyst.

During this preliminary investigation, the performance of the catalyst has been successfully improved by replacing 50 % of Pt atoms with cheaper Ni and Co atoms. Even though, the presence of the alloy has been confirmed mainly by (HR)TEM images, a quantification of the alloying extent and the composition of the bimetallic nanoparticles has not been possible due to the low amount loaded on graphitic carbon nitride. Further investigation is necessary especially on PtNi and PtCo-g-C₃N₄ to better understand the effect of the alloy on the performance for hydrogen evolution. The influence of the alloy composition also has to be studied by using different initial metal ratios. To allow for a clearer characterisation by XRD, higher loadings may be necessary. For the most

promising materials the characterisation could also be extended to a wider range of techniques: chemisorption, XPS or low energy ion scattering (LEIS) in order to gain additional information on the chemical composition of the surface.

Chapter 6

Conclusions and Future Work

6.1. Conclusions

The need of clean and renewable energy has directed the attention in developing processes to convert intermittent energy sources like solar into fuels. An example is photocatalytic water splitting through which hydrogen can be produced and employed as green, carbon free fuel. After the first example of light driven water splitting by TiO_2 reported by Fujishima and Honda in 1972 much effort has been made to find new and more active materials. Particular attention has been addressed to those materials able to absorb visible light, since this composes most of the solar spectrum. Since late 2008, graphitic carbon nitride ($\text{g-C}_3\text{N}_4$) is among those visible-active materials able to photocatalytically produce hydrogen from water.

The structure of $\text{g-C}_3\text{N}_4$ has been investigated since its discovery in the 19th century. To date satisfactory results have been obtained for its 2D structure defining it as a heptazine-based polymer, as opposite to the triazine-based initially proposed. Nonetheless, its 3D configuration has never been solved and it is generally defined as graphitic-like layered structure. Reason for this is the disordered nature of the polymer; its XRD pattern shows only two broad features with the main one being the inter-layer distance. In this investigation additionally to XRD, neutron diffraction was employed to obtain more information about the 3D structure of this catalyst.

In a first instance the synthesis path and the effect that the synthesis conditions have on graphitic carbon nitride structure were investigated with XRD, elemental analysis and

solid state NMR. The material was synthesised by thermal polycondensation of melamine, therefore, temperature and condensation time were varied and the XRD patterns compared. Temperature from 450 ° up to 650 ° and length from 2.5 h to 15 h were employed. It was found that the minimum requirement to obtain the so called g-C₃N₄ is a condensation at 500 °C for at least 5 h. Below 500 °C the desired product is not obtained. Additionally, from the results it emerged that in the low temperature range the condensation length is more important than the temperature itself and longer time favour the polymerisation more than the temperature. For example, the product obtained at 475 °C after 15 h was more polymerised than the product obtained at 500 °C for 2.5 h. Higher temperatures caused higher mass loss (g-C₃N₄ starts decomposing at 550 °C) with a consequent increase in surface area, which was associated to an increase in the roughness of the surface (peeling-off) and not to a decrease in the particle size. Higher temperature also favoured a higher level of order in the stacking translated in a sharper (002) reflection in the XRD pattern. Another effect produced by the increasing temperature was the decrease of the band gap, ascribed to the increase in polymerisation and *sp*² hybridisation.

Furthermore, during this investigation it was possible to confirm and better understand the reaction path from melamine to g-C₃N₄. Upon heating, melamine reacts to form heptazine based molecules, Melem. With further increase of temperature and time these units polymerise into bigger fragments, but not yet graphitic carbon nitride. Above 500 °C g-C₃N₄ is formed as a heptazine-based polymer organised in layers. Higher temperature brings to a slightly higher level of polymerisation but mainly the stacking of the polymeric sheets becomes more organised and densely packed which is translated in a sharper and shifted (002) reflection in the XRD pattern. However, the shape and size of the fragments remain irregular giving in the XRD the weak and broad peak at $2\theta = 13^\circ$.

In a second phase of the investigation modelling of the 3D structure of g-C₃N₄ was performed with XRD to narrow down the possibilities and subsequently with neutron diffraction. Fully polymerised structure were initially employed and was demonstrated that the measured XRD pattern of g-C₃N₄ does not justify their presence. Among the partially polymerised structures proposed in the literature, Melon proved the most likely. After modification of the unit cell by shifting the heptazine chains closer to each other the position of the peaks well matched those of the measured pattern. However, the intensity of the, now, (210) reflection was too high, therefore different modifications of the unit cell were introduced to decrease it. The angles of the unit cell were modified one

by one and the effect on the XRD pattern monitored. It was found that a small change (2°) of γ could decrease the intensity by separating the (210) and the (2 $\bar{1}$ 0). However, this could introduce a distortion of the aromatic network. The same decrease in intensity without the separation of the reflections and the distortion was obtained by introducing a shift, along both y and x , of the layers with respect to each other. This was ascribed to the introduction of a simulated disorder in the alignment of the layers. Neutron diffraction analysis also confirmed that the structure that better described the differential pair correlation function, $D(r)$, of g-C₃N₄ was the one with layers shifted in both directions. It was therefore possible to conclude that the 3D structure of g-C₃N₄ is a regular stacking of heptazine-based layers which are not aligned and this introduces disorder along the (210) plane. The possible symmetry of the structure was also investigated by indexing of the experimental XRD pattern. It was found that Cmmm space group represent the highest symmetry level that would justify all the observed reflections.

The three materials (C₃N₄-500, -550 and -600) that proved, from XRD, to be graphitic carbon nitride were tested for photocatalytic hydrogen evolution. From the structural investigation it was found that the higher the synthesis temperature the smaller the band gap. This was reflected in a higher activity of C₃N₄-600 in the absence of a co-catalyst. However, when platinum was loaded on the surface C₃N₄-500 showed the best performance. The explanation was found in the lower surface area for the material synthesised at low temperature than those at high. An explanation was proposed: a high surface area causes the platinum precursor to deposit in the channels of the catalyst which will not be exposed to the light as much as the outer surface. This could reduce the positive interaction between catalyst and co-catalyst and the electron transfer.

After selecting the most active material this was employed to carry out further investigation on the co-catalyst and how this was affected by the loading procedure. Three different loading method were applied: simple impregnation, impregnation followed by calcination and photodeposition. The best method for photocatalytic hydrogen evolution was found to be the simple impregnation, when the precursor of the co-catalyst was only impregnated. During the investigation it was observed that before photocatalytic test the main platinum species on the surface of g-C₃N₄ were PtO and PtCl_x; during photocatalytic test the chlorides were reduced to platinum metal and a Pt⁰:PtO ratio of 1.3 was achieved. The impregnation method was therefore described as a photoreduction. During

photodeposition, on the other hand, excess of platinum metal and a higher dispersion was observed, both possible reasons for the lower performance.

Through the investigation of pre-reduced (5 % H₂ and NaBH₄) samples it was found out that a third additional factor could have an effect on the activity: crystallinity of the nanoparticles. With TEM and XPS characterisation it was possible to discriminate between this factors and it was concluded that the dispersion of the nanoparticles (measured as Pt:N ratio from XPS analysis) had the major effect. The reason was ascribed to a high coverage of the surface of g-C₃N₄ preventing light absorption and interaction with the sacrificial agent. Additionally, the electron transfer of electrons between catalyst and metal could also be affected and be less efficient for smaller/thinner nanoparticles. Therefore a high coverage is detrimental for the performance

The effect of the sacrificial agent on the platinum was also subject of investigation. Additionally to oxalic acid, triethanolamine was also employed. It was found that by producing two different pH they influenced the oxidation state of the platinum and as a consequence the activity for hydrogen evolution. With acidic pH platinum metal was formed (to different extents according to the loading procedure) and the hydrogen production was high. When TEOA was employed and the pH was basic, mainly Pt^{II} in big agglomerates were obtained. The reason was ascribed to possible formation of Pt^{II} complexes with the decomposition products of TEOA. As a consequence the activity of the material was found drastically decreased. Therefore, the choice of the sacrificial agent has to be carefully made.

The interaction during photocatalysis between the catalyst and the co-catalyst was also elucidated with single wavelength experiments. Platinum metal formation was observed (UV-Vis) only by using light absorbed by g-C₃N₄. This confirmed that the reduction of platinum was carried out by the photoexcited electrons of the catalyst. During the investigation the plasmonic effect of platinum metal was excluded and its role as an electron trap confirmed.

In order to improve the activity of Pt-g-C₃N₄ and reduce the amount of platinum (reduced cost) bimetallic co-catalyst were investigated. Platinum-based alloy of Cu, Ag, Ni and Co were chosen for an initial study. To promote the formation of the alloy the same reduction treatments employed for the platinum were applied for the bimetallic alloys: photoreduction, reduction in H₂ and NaBH₄. Of the three procedures photoreduction and reduction by NaBH₄ proved to be suitable for the formation of the alloy in all four cases.

When these two procedures were applied an increase in performance was obtained only for the systems PtNi and PtCo. In an opposite way to Pt-g-C₃N₄ reduction in hydrogen for all the samples did not bring the expected increase in activity by a factor three. Overall the highest relative improvement was obtained when NaBH₄ was employed as the reducing agent showing it as the most suitable method for this kind of system.

Due to the limitation of the analytical techniques employed it was not possible to quantify the extent of alloying for each case and relate it to the performance. Nonetheless, on the assumption of a uniform degree of alloying, the activity of the bimetallic alloys showed an increasing trend with increasing metal work function. This suggested that including a metal with lower work function (Ni and Co) could lower the Schottky barrier and improve the activity by promoting the electron transfer from the semiconductor to the metal while still preventing their backflow. However, metal characterised by a too low work function (Cu and Ag) could decrease the barrier too much and increase the backflow. This investigation proved that by alloying platinum with a transition metal it is possible to successfully increase the performance of the catalyst and reduce the platinum content.

6.2. Future work

Further investigation is needed on the effect on the performance that the particle size and platinum coverage for the system Pt-g-C₃N₄. To be able to do so control of size during the reduction is indispensable, this can be achieved by employing organic stabilisers.^{198, 200} This however would require the removal of the stabiliser before photocatalysis in order to allow a better interface between catalyst and co-catalyst. Removal is often carried out by thermal decomposition which may affect particle size and morphology, in addition of leaving some carbon contaminations. Additionally, the effect on activity of different platinum exposed facets in terms of interaction with the reaction media but also with g-C₃N₄ and therefore electron transfer will be investigated. This can be achieved by shape control of the nanoparticles.

With regard to the bimetallic nanoparticles the effort will be addressed in the accurate characterisation of the alloy by means of XRD, TEM and especially XPS. To do so however, the amount of metal loading will have to be increased to ensure detection, especially by XRD and XPS. This will allow to understand in more details the difference between the three loading methods. Subsequently attention will be mainly addressed to PtNi and PtCo-g-C₃N₄ to further improve, if possible, the activity by changing the ratio of the metals and controlling the size.

Appendix A

Crystallographic information and D(r) plots

A.1. Crystallographic information

Below the most significant crystallographic information are listed. Easily derivable CIF are not tabulated. For these structures a mathematical transformation of the provided coordinate can be applied. For example, for that of Melon with shifted layer, a vector can be applied to the coordinates in Table A.10.

Table A.1 Melem crystallographic information as from ref. ⁶⁹ Unit cell information: Space group: P2₁/c; Unit cell: monoclinic, $a = 7.3992 \text{ \AA}$, $b = 8.6528 \text{ \AA}$, $c = 13.3816 \text{ \AA}$, $\beta = 99.912^\circ$. (Figure 3.4)

Atom	x	y	z	Uiso
C1	0.765(2)	0.203(2)	0.447(1)	440(20)
C2	0.675(2)	-0.069(2)	0.453(1)	440(20)
C3	0.867(2)	0.046(2)	0.593(1)	440(20)
C4	0.602(2)	0.093(1)	0.3119(9)	440(20)
C5	0.773(2)	-0.195(1)	0.5924(9)	440(20)
C6	0.959(2)	0.294(1)	0.5903(8)	440(20)
N1	0.771(1)	0.065(2)	0.5019(9)	320(10)
N2	0.695(1)	0.221(1)	0.3509(7)	320(10)
N3	0.581(1)	-0.044(1)	0.3644(8)	320(10)
N4	0.659(1)	-0.196(1)	0.5017(8)	320(10)
N5	0.870(1)	-0.083(1)	0.6515(9)	320(10)
N6	0.956(1)	0.169(1)	0.6443(8)	320(10)
N7	0.883(1)	0.315(1)	0.4956(7)	320(10)
N8	0.511(1)	0.1046(8)	0.2226(6)	320(10)
N9	0.766(1)	-0.3282(9)	0.6460(7)	320(10)
N10	1.056(1)	0.413(1)	0.6356(7)	320(10)

H1	0.542(5)	0.164(4)	0.183(1)	250
H2	0.427(3)	0.047(3)	0.204(1)	250
H3	0.679(4)	-0.384(4)	0.633(2)	250
H4	0.846(3)	-0.349(2)	0.692(2)	250
H5	1.081(5)	0.416(2)	0.696(7)	250
H6	1.091(4)	0.479(2)	0.602(1)	250

Table A.2 Melon from Lotsch¹²⁶ Unit cell information: space group: P2₁2₁2, unit cell: orthorhombic, $a = 16.7 \text{ \AA}$, $b = 12.4 \text{ \AA}$, $c = 6.49 \text{ \AA}$, $\alpha = \beta = \gamma = 90^\circ$. (Figure 3.6)

Atom	x	y	z
C1	0.338	0.472	0.25
C2	0.217	0.798	0.25
C3	0.264	0.63	0.25
C4	0.133	0.648	0.25
C5	0.988	0.683	0.25
C6	0.071	0.82	0.25
N1	0.139	0.762	0.25
N2	0.086	0.935	0.25
N3	0.222	0.904	0.25
N4	0.277	0.733	0.25
N5	0.194	0.588	0.25
N6	0.056	0.608	0.25
N7	0.998	0.788	0.25
N8	0.327	0.568	0.25
N9	0.923	0.638	0.25
C7	0.338	0.472	0.75
C8	0.217	0.798	0.75
C9	0.264	0.63	0.75
C10	0.133	0.648	0.75
C11	0.988	0.683	0.75
C12	0.071	0.82	0.75
N10	0.139	0.762	0.75
N11	0.086	0.935	0.75
N12	0.222	0.904	0.75
N13	0.277	0.733	0.75
N14	0.194	0.588	0.75
N15	0.056	0.608	0.75
N16	0.998	0.788	0.75
N17	0.327	0.568	0.75
N18	0.923	0.638	0.75
H1	0.3778	0.6109	0.25
H2	0.9186	0.5576	0.25
H3	0.8704	0.6783	0.25
H1	0.3778	0.6109	0.75

H2	0.9186	0.5576	0.75
H3	0.8704	0.6783	0.75

Table A.3 Teter & Hemley triazine-based g-C₃N₄ crystallographic information.¹¹⁶ Unit cell information: Space group: P $\bar{6}m2$; Unit cell: hexagonal, $a = b = 4.7420$ Å, $c = 6.7205$ Å, $\alpha = \beta = 90^\circ$, $\gamma = 120^\circ$. PDF#: 83265-ICSD. (Figure 3.13)

Atom	x	y	z
C1	0.3518	0.1759	0
C2	0.0198	0.5099	0.5
N1	0	0	0
N2	0.6667	0.3333	0.5
N3	0.1694	0.3387	0.5
N4	0.5026	0.4974	0

Table A.4 Heptazine-based g-C₃N₄ crystallographic information. Unit cell information: Space group: P1; Unit cell: hexagonal, $a = b = 7.113$ Å, $c = 6.490$ Å, $\alpha = \beta = 90^\circ$, $\gamma = 120^\circ$. (Figure 3.13)

Atom	x	y	z
N1	0	0	0.25
N2	0	0.33333	0.25
N3	0	0.66667	0.25
N4	0.33333	0	0.25
N5	0.33333	0.66667	0.25
N6	0.66667	0	0.25
N7	0.33333	0.33333	0.25
N8	0.66667	0.66667	0.25
N9	0	0	0.75
N10	0	0.33333	0.75
N11	0	0.66667	0.75
N12	0.33333	0	0.75
N13	0.66667	0.33333	0.75
N14	0.66667	0	0.75
N15	0.33333	0.33333	0.75
N16	0.66667	0.66667	0.75
C1	0.2222	0.1111	0.25
C2	0.2222	0.4444	0.25
C3	0.2222	0.77778	0.25
C4	0.55553	0.77778	0.25
C5	0.88887	0.77778	0.25
C6	0.88887	0.1111	0.25
C7	0.2222	0.1111	0.75
C8	0.55553	0.4444	0.75

C9	0.88887	0.4444	0.75
C10	0.55553	0.1111	0.75
C11	0.88887	0.77778	0.75
C12	0.88887	0.1111	0.75

Table A.5 Heptazine based g-C₃N₄ as from Döblinger.¹²² Unit cell information: space group: P1, unit cell: hexagonal, $a = 12.77 \text{ \AA}$, $b = 12.77 \text{ \AA}$, $c = 6.49 \text{ \AA}$, $\alpha = \beta = 90^\circ$, $\gamma = 120^\circ$. For second layer, same coordinates with $z = 0.75$. (Figure 3.14)

Atom	x	y	z
H1	-0.00014	0.29888	0.25
H2	0.70113	0.70113	0.25
H3	0.29888	-0.00014	0.25
C1	0.88673	0.36735	0.25
C2	0.68449	0.23365	0.25
C3	0.63274	0.51949	0.25
C4	0.76644	0.45101	0.25
C5	0.48049	0.11324	0.25
C6	0.5491	0.3155	0.25
C7	0.36735	0.88673	0.25
C8	0.23365	0.68449	0.25
C9	0.51949	0.63274	0.25
C10	0.45101	0.76644	0.25
C11	0.11324	0.48049	0.25
C12	0.3155	0.5491	0.25
N1	0.87661	0.46575	0.25
N2	0.79636	0.25198	0.25
N3	0.53426	0.41084	0.25
N4	0.74809	0.54453	0.25
N5	0.58904	0.12345	0.25
N6	0.45548	0.20353	0.25
N7	0.46575	0.87661	0.25
N8	0.25198	0.79636	0.25
N9	0.41084	0.53426	0.25
N10	0.54453	0.74809	0.25
N11	0.12345	0.58904	0.25
N12	0.20353	0.45548	0.25
N13	0.66667	0.33338	0.25
N14	0.33338	0.66667	0.25
N15	-0.00007	0.37903	0.25
N16	0.62097	0.62097	0.25
N17	0.37903	-0.00007	0.25

Table A.6 Triazine-based partially polymerised graphitic carbon nitride (A-A). Unit cell information: Space group: P1, Unit cell: hexagonal, $a = b = 9.484 \text{ \AA}$, $c = 6.49 \text{ \AA}$, $\alpha = \beta = 90^\circ$ and $\gamma = 120^\circ$. For second layer: $z = 0.75$ and same x,y coordinates. (Figure 3.19)

Atom	x	y	z
C1	0.16667	0.58333	0.25
C2	0.66667	0.58333	0.25
C3	0.41667	0.58333	0.25
C4	0.91667	0.08333	0.25
C5	0.91667	0.58333	0.25
C6	0.41667	0.83333	0.25
C7	0.91667	0.33334	0.25
C8	0.91667	0.83333	0.25
C9	0.66667	0.08333	0.25
H1	0.12067	0.06033	0.25
H2	0.43967	0.06033	0.25
H3	0.43967	0.37933	0.25
N1	0	0	0.25
N2	0.75	0.5	0.25
N3	0.25	0.75	0.25
N4	0.75	0.25	0.25
N5	0.75	0.75	0.25
N6	0	0.5	0.25
N7	0.5	0	0.25
N8	0.5	0.5	0.25
N9	0	0.25	0.25
N10	0	0.75	0.25
N11	0.5	0.75	0.25
N12	0.25	0.5	0.25
N13	0.75	0	0.25

Table A.7 Triazine-based partially polymerised graphitic carbon nitride (A-B). Fractional coordinates of the shifted layer. For first layer see Table A.6. Unit cell information: Space group: P1, Unit cell: hexagonal, $a = b = 9.484 \text{ \AA}$, $c = 6.49 \text{ \AA}$, $\alpha = \beta = 90^\circ$ and $\gamma = 120^\circ$. (Figure 3.19)

Atom	x	y	z
C1	-0.3333	0.58333	0.75
C2	0.16667	0.58333	0.75
C3	-0.0833	0.58333	0.75
C4	0.41667	0.08333	0.75
C5	0.41667	0.58333	0.75
C6	-0.0833	0.83333	0.75
C7	0.41667	0.33334	0.75
C8	0.41667	0.83333	0.75

C9	0.16667	0.08333	0.75
H1	-0.3793	0.06033	0.75
H2	-0.0603	0.06033	0.75
H3	-0.0603	0.37933	0.75
N1	-0.5	0	0.75
N2	-0.5	0.5	0.75
N3	0	0	0.75
N4	0	0.5	0.75
N5	-0.5	0.25	0.75
N6	-0.5	0.75	0.75
N7	0	0.75	0.75
N8	-0.25	0.5	0.75
N9	0.25	0	0.75
N10	0.25	0.5	0.75
N11	-0.25	0.75	0.75
N12	0.25	0.25	0.75
N13	0.25	0.75	0.75

Table A.8 Heptazine-based partially polymerised graphitic carbon nitride (A-A). Unit cell information: Space group: P1, Unit cell: hexagonal, $a = b = 13.9246 \text{ \AA}$, $c = 6.49 \text{ \AA}$, $\alpha = \beta = 90^\circ$ and $\gamma = 120^\circ$. For second layer: $z = 0.75$ and same x,y coordinates. (Figure 3.19)

Atom	x	y	z
N1	0	0	0.25
N2	0	0.5	0.25
N3	0.5	0	0.25
N4	0	0.16667	0.25
N5	0	0.66667	0.25
N6	0.5	0.16667	0.25
N7	0	0.33333	0.25
N8	0	0.83333	0.25
N9	0.5	0.83333	0.25
N10	0.16667	0	0.25
N11	0.16667	0.5	0.25
N12	0.66667	0	0.25
N13	0.16667	0.33333	0.25
N14	0.16667	0.83333	0.25
N15	0.66667	0.33333	0.25
N16	0.66667	0.83333	0.25
N17	0.33333	0	0.25
N18	0.83333	0	0.25
N19	0.83333	0.5	0.25
N20	0.16667	0.16667	0.25
N21	0.16667	0.66667	0.25
N22	0.66667	0.16667	0.25

N23	0.33333	0.83333	0.25
N24	0.83333	0.33333	0.25
N25	0.83333	0.83333	0.25
C1	0.1111	0.05555	0.25
C2	0.1111	0.55555	0.25
C3	0.6111	0.05555	0.25
C4	0.1111	0.2222	0.25
C5	0.1111	0.7222	0.25
C6	0.6111	0.2222	0.25
C7	0.1111	0.38889	0.25
C8	0.1111	0.88889	0.25
C9	0.6111	0.88889	0.25
C10	0.27777	0.88889	0.25
C11	0.77777	0.38889	0.25
C12	0.77777	0.88889	0.25
C13	0.44443	0.88889	0.25
C14	0.94443	0.38889	0.25
C15	0.94443	0.88889	0.25
C16	0.44443	0.05555	0.25
C17	0.94443	0.05555	0.25
C18	0.94443	0.55555	0.25
H1	0.62644	0.75287	0.25
H2	0.62644	0.37356	0.25
H3	0.24711	0.37356	0.25

Table A.9 Heptazine-based partially polymerised graphitic carbon nitride (A-B). Fractional coordinates of the shifted layer. For first layer see Table A.8. Unit cell information: Space group: P1, Unit cell: hexagonal, $a = b = 13.9246 \text{ \AA}$, $c = 6.49 \text{ \AA}$, $\alpha = \beta = 90^\circ$ and $\gamma = 120^\circ$. (Figure 3.19)

Atom	x	y	z
C1	0.6111	0.55555	0.75
C2	0.6111	1.05555	0.75
C3	1.1111	0.55555	0.75
C4	0.6111	0.7222	0.75
C5	0.6111	1.2222	0.75
C6	1.1111	0.7222	0.75
C7	0.6111	0.88889	0.75
C8	0.6111	1.38889	0.75
C9	1.1111	1.38889	0.75
C10	0.77777	1.38889	0.75
C11	1.27777	0.88889	0.75
C12	1.27777	1.38889	0.75
C13	0.94443	1.38889	0.75
C14	1.44443	0.88889	0.75
C15	1.44443	1.38889	0.75

C16	0.94443	0.55555	0.75
C17	1.44443	0.55555	0.75
C18	1.44443	1.05555	0.75
H1	1.12644	1.25287	0.75
H2	1.12644	0.87356	0.75
H3	0.74711	0.87356	0.75
N1	0.5	0.5	0.75
N2	0.5	1	0.75
N3	1	0.5	0.75
N4	0.5	0.66667	0.75
N5	0.5	1.16667	0.75
N6	1	0.66667	0.75
N7	0.5	0.83333	0.75
N8	0.5	1.33333	0.75
N9	1	1.33333	0.75
N10	0.66667	0.5	0.75
N11	0.66667	1	0.75
N12	1.16667	0.5	0.75
N13	0.66667	0.83333	0.75
N14	0.66667	1.33333	0.75
N15	1.16667	0.83333	0.75
N16	1.16667	1.33333	0.75
N17	0.83333	0.5	0.75
N18	1.33333	0.5	0.75
N19	1.33333	1	0.75
N20	0.66667	0.66667	0.75
N21	0.66667	1.16667	0.75
N22	1.16667	0.66667	0.75
N23	0.83333	1.33333	0.75
N24	1.33333	0.83333	0.75
N25	1.33333	1.33333	0.75

Table A.10 Melon with closer chains. Unit cell information: space group: P1, unit cell: orthorhombic, $a = 16.4 \text{ \AA}$, $b = 12.4 \text{ \AA}$, $c = 6.49 \text{ \AA}$, $\alpha = \beta = \gamma = 90^\circ$. For second layer, same coordinates x and y , but $z = 0.75$. (Figure 3.13)

Atom	x	y	z
C1	0.3448	0.472	0.25
C2	0.6552	0.528	0.25
C3	0.22159	0.798	0.25
C4	0.77841	0.202	0.25
C5	0.26945	0.63	0.25
C6	0.73055	0.37	0.25
C7	0.13605	0.648	0.25
C8	0.86395	0.352	0.25

C9	0.98716	0.683	0.25
C10	0.01284	0.317	0.25
C11	0.07292	0.82	0.25
C12	0.92708	0.18	0.25
C13	0.83442	0.028	0.25
C14	0.16558	0.972	0.25
C15	0.7112	0.702	0.25
C16	0.2888	0.298	0.25
C17	0.75906	0.87	0.25
C18	0.24094	0.13	0.25
C19	0.62567	0.852	0.25
C20	0.37433	0.148	0.25
C21	0.47801	0.817	0.25
C22	0.52199	0.183	0.25
C23	0.56253	0.68	0.25
C24	0.43747	0.32	0.25
H1	0.87494	0.8891	0.25
H2	0.12506	0.1109	0.25
H3	0.38533	0.6109	0.25
H4	0.61467	0.3891	0.25
H5	0.91649	0.5576	0.25
H6	0.08351	0.4424	0.25
H7	0.40734	0.9424	0.25
H8	0.59266	0.0576	0.25
H9	0.35826	0.8217	0.25
H10	0.64174	0.1783	0.25
H11	0.86741	0.6783	0.25
H12	0.13259	0.3217	0.25
N1	0.14216	0.762	0.25
N2	0.85784	0.238	0.25
N3	0.08819	0.935	0.25
N4	0.91181	0.065	0.25
N5	0.22668	0.904	0.25
N6	0.77332	0.096	0.25
N7	0.28269	0.733	0.25
N8	0.71731	0.267	0.25
N9	0.19817	0.588	0.25
N10	0.80183	0.412	0.25
N11	0.05765	0.608	0.25
N12	0.94235	0.392	0.25
N13	0.99734	0.788	0.25
N14	0.00266	0.212	0.25
N15	0.3336	0.568	0.25
N16	0.6664	0.432	0.25
N17	0.92097	0.638	0.25
N18	0.07903	0.362	0.25

N19	0.63178	0.738	0.25
N20	0.36822	0.262	0.25
N21	0.57781	0.565	0.25
N22	0.42219	0.435	0.25
N23	0.71629	0.596	0.25
N24	0.28371	0.404	0.25
N25	0.7723	0.767	0.25
N26	0.2277	0.233	0.25
N27	0.68778	0.912	0.25
N28	0.31222	0.088	0.25
N29	0.54726	0.892	0.25
N30	0.45274	0.108	0.25
N31	0.4882	0.712	0.25
N32	0.5118	0.288	0.25
N33	0.82321	0.932	0.25
N34	0.17679	0.068	0.25
N35	0.41182	0.862	0.25
N36	0.58818	0.138	0.25

Table A.11 Buckled modified Melon. Unit cell information: space group: P1, unit cell: orthorhombic, $a = 16.4 \text{ \AA}$, $b = 12.4 \text{ \AA}$, $c = 6.49 \text{ \AA}$, $\alpha = \beta = \gamma = 90^\circ$. For second layer, same coordinates x and y , but $z_{II} = z_I + 0.5$. (Figure 3.15)

Atom	x	y	z
C1	0.3448	0.472	0.2951
C2	0.6552	0.528	1.2042
C3	0.22159	0.798	0.3024
C4	0.77841	0.202	1.1979
C5	0.26945	0.63	0.3031
C6	0.73055	0.37	1.1968
C7	0.13605	0.648	0.2888
C8	0.86395	0.352	1.2112
C9	0.98716	0.683	1.2473
C10	0.01284	0.317	0.2527
C11	0.07292	0.82	0.2736
C12	0.92708	0.18	1.2276
C13	0.83442	0.028	1.2046
C14	0.16558	0.972	0.2954
C15	0.7112	0.702	1.1978
C16	0.2888	0.298	0.3022
C17	0.75906	0.87	1.1968
C18	0.24094	0.13	0.3032
C19	0.62567	0.852	1.2117
C20	0.37433	0.148	0.2883
C21	0.47801	0.817	0.252

C22	0.52199	0.183	1.248
C23	0.56253	0.68	1.227
C24	0.43747	0.32	0.2718
H1	0.87494	0.8891	1.2173
H2	0.12506	0.1109	0.2827
H3	0.38533	0.6109	0.2866
H4	0.61467	0.3891	1.2154
H5	0.91649	0.5576	1.2238
H6	0.08351	0.4424	0.2775
H7	0.40734	0.9424	0.2773
H8	0.59266	0.0576	1.2217
H9	0.35826	0.8217	0.2896
H10	0.64174	0.1783	1.2115
H11	0.86741	0.6783	1.2117
H12	0.13259	0.3217	0.2879
N1	0.14216	0.762	0.2906
N2	0.85784	0.238	1.2085
N3	0.08819	0.935	0.2772
N4	0.91181	0.065	1.224
N5	0.22668	0.904	0.3026
N6	0.77332	0.096	1.1972
N7	0.28269	0.733	0.3029
N8	0.71731	0.267	1.1971
N9	0.19817	0.588	0.3002
N10	0.80183	0.412	1.1998
N11	0.05765	0.608	0.2686
N12	0.94235	0.392	1.2301
N13	0.99734	0.788	1.2486
N14	0.00266	0.212	0.2514
N15	0.3336	0.568	0.2971
N16	0.6664	0.432	1.2035
N17	0.92097	0.638	1.2252
N18	0.07903	0.362	0.2748
N19	0.63178	0.738	1.2089
N20	0.36822	0.262	0.2911
N21	0.57781	0.565	1.2246
N22	0.42219	0.435	0.2754
N23	0.71629	0.596	1.1973
N24	0.28371	0.404	0.3027
N25	0.7723	0.767	1.197
N26	0.2277	0.233	0.303
N27	0.68778	0.912	1.2001
N28	0.31222	0.088	0.2999
N29	0.54726	0.892	1.2307
N30	0.45274	0.108	0.2693
N31	0.4882	0.712	1.2493

N32	0.5118	0.288	0.252
N33	0.82321	0.932	1.2026
N34	0.17679	0.068	0.2986
N35	0.41182	0.862	0.2754
N36	0.58818	0.138	1.2258

A.2.D(r) residual plots

For each neutron scattering model discussed in Chapter 3, the following figures illustrates the comparison between the observed pattern and the calculated one. The residual curve is also included.

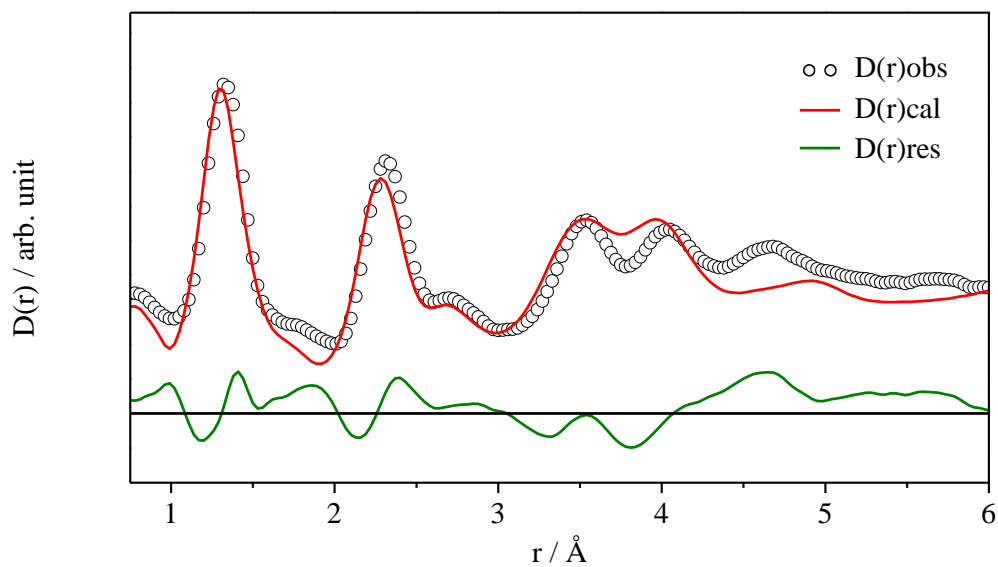
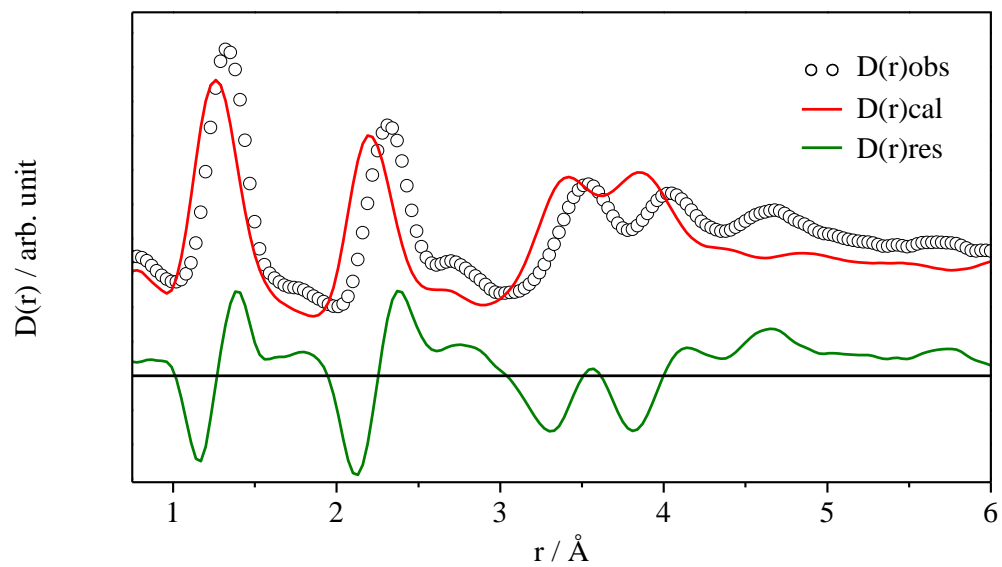
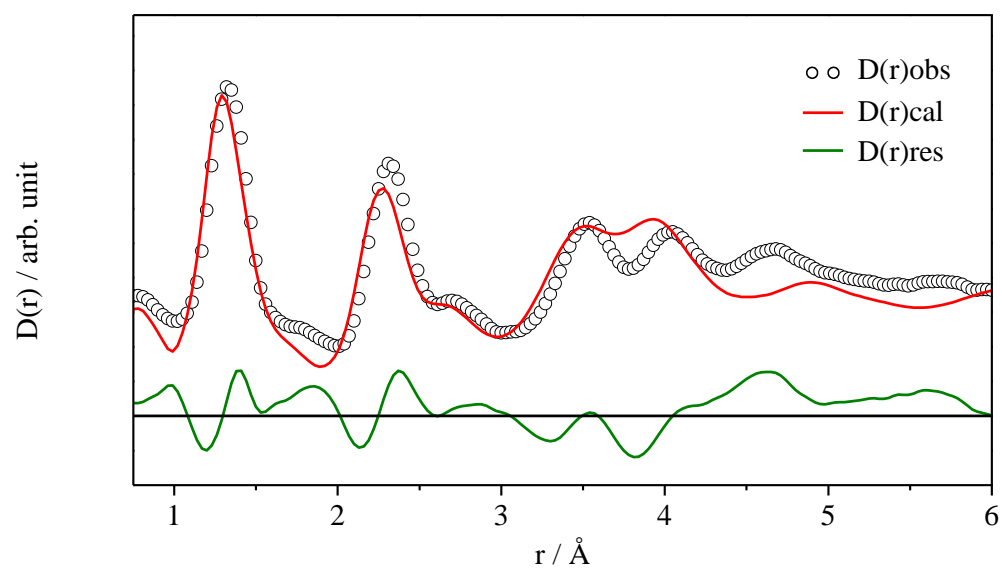


Figure A.1 D(r) plot of modified Melon.

**Figure A.2** $D(r)$ plot of Tyborski's Melon.**Figure A.3** $D(r)$ plot of Melon $\gamma = 88^\circ$.

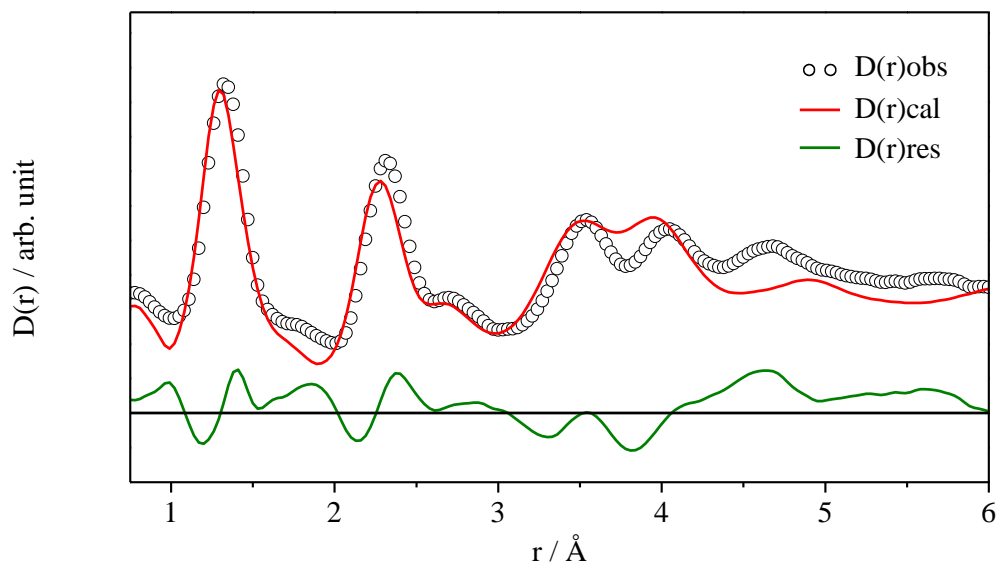


Figure A.4 $D(r)$ plot of Melon $\gamma = 89^\circ$.

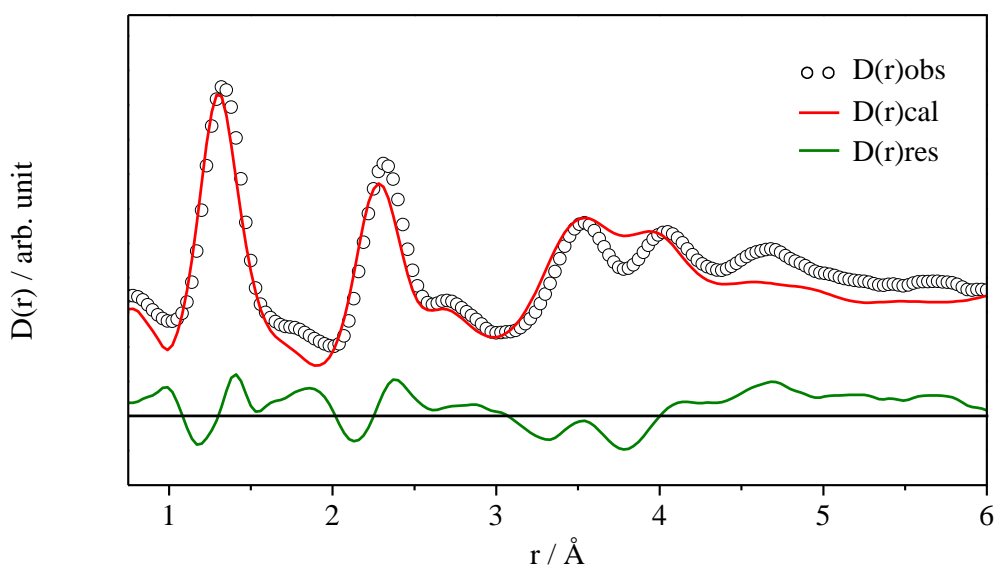


Figure A.5 $D(r)$ plot of Melon $\alpha = 98^\circ$.

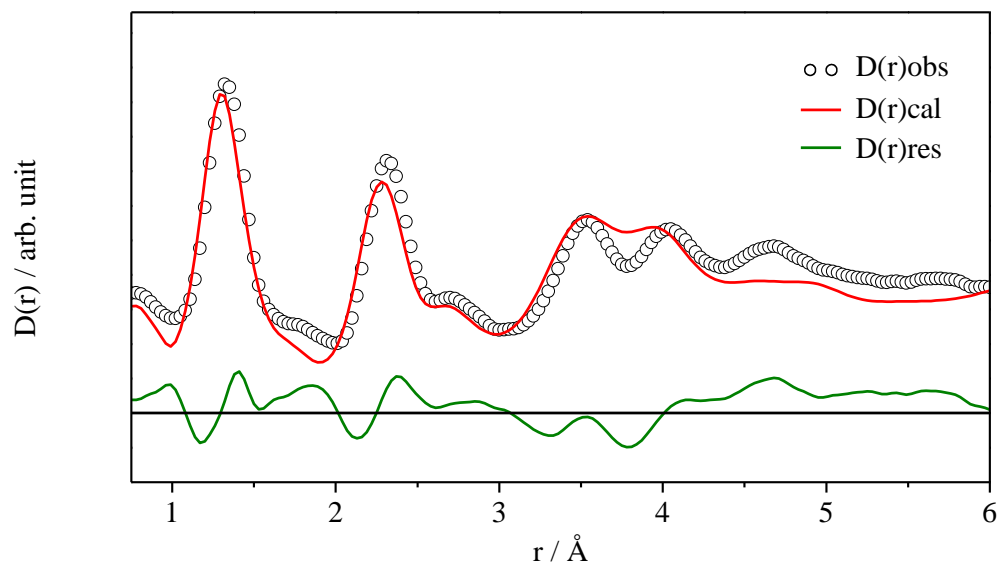


Figure A.6 $D(r)$ plot of Melon $\beta = 98^\circ$.

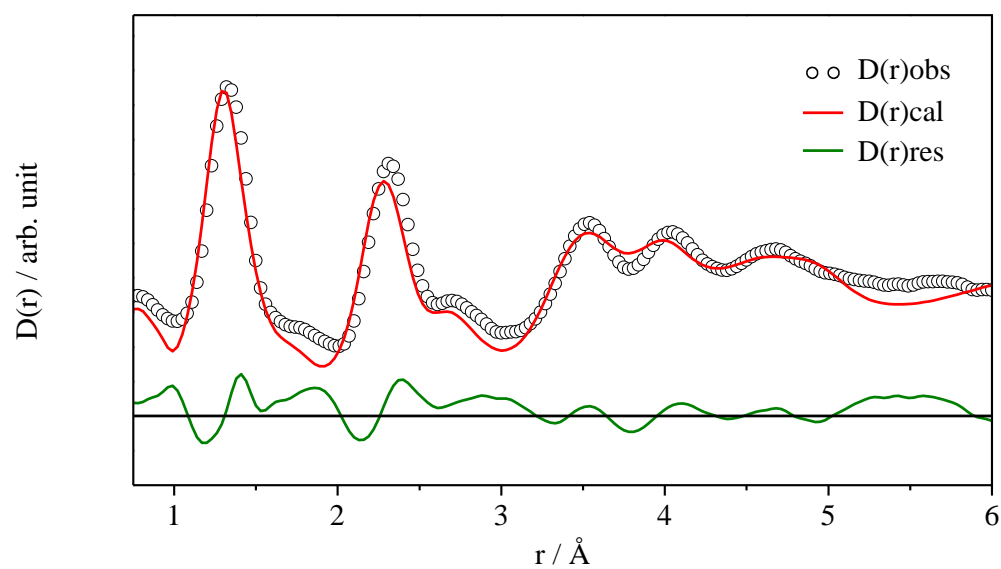


Figure A.7 $D(r)$ plot of Melon with shifted layers.

Bibliography

1. J. Verne, *The Mysterious Island*, Plain Label Books.
2. *International Energy Outlook: 2013*, U.S. Energy Information Administration, 2013.
3. N. S. Lewis and D. G. Nocera, *Proc. Natl. Acad. Sci. U. S. A.*, 2006, **103**, 15729-15735.
4. N. Z. Muradov and T. N. Veziroğlu, *Int. J. Hydrogen Energy*, 2008, **33**, 6804-6839.
5. *Renewable Energy Medium-Term Market Report: Executive Summary*, International Energy Agency, 2013.
6. *Renewable Energy Outlook*, International Energy Agency, 2012.
7. J. Andrews and B. Shabani, *Int. J. Hydrogen Energy*, 2012, **37**, 1184-1203.
8. HyWays, *The European Hydrogen Roadmap*, 2008.
9. K. Rajeshwar, R. McConnell, K. Harrison and S. Licht, in *Solar Hydrogen Generation*, eds. K. Rajeshwar, R. McConnell and S. Licht, Springer New York, 2008, pp. 1-18.
10. Z. Wang, R. R. Roberts, G. F. Naterer and K. S. Gabriel, *Int. J. Hydrogen Energy*, 2012, **37**, 16287-16301.
11. Y. Tachibana, L. Vayssieres and J. R. Durrant, *Nat. Photonics*, 2012, **6**, 511-518.
12. A. Fujishima and K. Honda, *Nature*, 1972, **238**, 37-38.
13. A. Kudo and Y. Miseki, *Chem. Soc. Rev.*, 2009, **38**, 253-278.
14. X. Chen, S. Shen, L. Guo and S. S. Mao, *Chem. Rev.*, 2010, **110**, 6503-6570.
15. K. Takanabe and K. Domen, *Green*, 2011, **1**, 313-322.
16. A. Kudo, *Pure Appl. Chem.*, 2007, **79**, 1917-1927.
17. A. R. West, *Basic Solid State Chemistry*, John Wiley & Sons, 1999.

18. B. G. Streetman and S. K. Banerjee, *Solid State Electronic Devices*, Prentice-Hall, 2006.
19. W. H. Strehlow and E. L. Cook, *J. Phys. Chem. Ref. Data*, 1973, **2**, 163-200.
20. K. Maeda, *J. Photochem. Photobiol., C*, 2011, **12**, 237-268.
21. D. R. Lide, ed., *CRC Handbook of Chemistry and Physics*, 71st edn., CRC Press, Boca Raton, 1990.
22. J. Yang, D. Wang, H. Han and C. Li, *Acc. Chem. Res.*, 2013, **46**, 1900-1909.
23. J. Lee and W. Choi, *J. Phys. Chem. B*, 2005, **109**, 7399-7406.
24. B. Ohtani, K. Iwai, S.-i. Nishimoto and S. Sato, *J. Phys. Chem. B*, 1997, **101**, 3349-3359.
25. X. Xu, G. Liu, C. Random and J. T. S. Irvine, *Int. J. Hydrogen Energy*, 2011, **36**, 13501-13507.
26. D. Hufschmidt, D. Bahnemann, J. J. Testa, C. A. Emilio and M. I. Litter, *J. Photochem. Photobiol., A*, 2002, **148**, 223-231.
27. L. Zhang, Y.-N. Liu, M. Zhou and J. Yan, *Appl. Surf. Sci.*, 2013, **282**, 531-537.
28. J. M. Thornton and D. Raftery, *ACS Appl. Mater. Interfaces*, 2012, **4**, 2426-2431.
29. B. Kraeutler and A. J. Bard, *J. Am. Chem. Soc.*, 1978, **100**, 4317-4318.
30. I. Tsuji, H. Kato and A. Kudo, *Angew. Chem., Int. Ed.*, 2005, **44**, 3565-3568.
31. R. Georgekutty, M. K. Seery and S. C. Pillai, *J. Phys. Chem. C*, 2008, **112**, 13563-13570.
32. G. L. Chiarello, E. Selli and L. Forni, *Appl. Catal., B*, 2008, **84**, 332-339.
33. T. Sreethawong, Y. Suzuki and S. Yoshikawa, *Int. J. Hydrogen Energy*, 2005, **30**, 1053-1062.
34. P. D. Tran, L. Xi, S. K. Batabyal, L. H. Wong, J. Barber and J. S. Chye Loo, *Phys. Chem. Chem. Phys.*, 2012, **14**, 11596-11599.
35. D. Duonghong, E. Borgarello and M. Graetzel, *J. Am. Chem. Soc.*, 1981, **103**, 4685-4690.
36. B. Ma, F. Wen, H. Jiang, J. Yang, P. Ying and C. Li, *Catal. Lett.*, 2010, **134**, 78-86.
37. E. Borgarello, J. Kiwi, E. Pelizzetti, M. Visca and M. Grätzel, *Nature*, 1981, **289**, 158-160.
38. K. Maeda, K. Teramura, D. Lu, T. Takata, N. Saito, Y. Inoue and K. Domen, *J. Phys. Chem. B*, 2006, **110**, 13753-13758.
39. K. Maeda, D. Lu, K. Teramura and K. Domen, *J. Mater. Chem.*, 2008, **18**, 3539-3542.

40. K. Maeda, K. Teramura, D. Lu, N. Saito, Y. Inoue and K. Domen, *Angew. Chem., Int. Ed.*, 2006, **45**, 7806-7809.
41. J. Jitputti, S. Pavasupree, Y. Suzuki and S. Yoshikawa, *J. Solid State Chem.*, 2007, **180**, 1743-1749.
42. G. Liu, C. Sun, H. G. Yang, S. C. Smith, L. Wang, G. Q. Lu and H.-M. Cheng, *Chem. Commun.*, 2010, **46**, 755-757.
43. A. Deshpande and N. M. Gupta, *Int. J. Hydrogen Energy*, 2010, **35**, 3287-3296.
44. E. Borgarello, J. Kiwi, M. Graetzel, E. Pelizzetti and M. Visca, *J. Am. Chem. Soc.*, 1982, **104**, 2996-3002.
45. M. Altomare, K. Lee, M. S. Killian, E. Selli and P. Schmuki, *Chem. – Eur. J.*, 2013, **19**, 5841-5844.
46. G. Liu, H. G. Yang, X. Wang, L. Cheng, J. Pan, G. Q. Lu and H.-M. Cheng, *J. Am. Chem. Soc.*, 2009, **131**, 12868-12869.
47. S. In, A. Orlov, R. Berg, F. García, S. Pedrosa-Jimenez, M. S. Tikhov, D. S. Wright and R. M. Lambert, *J. Am. Chem. Soc.*, 2007, **129**, 13790-13791.
48. G. Wu, T. Nishikawa, B. Ohtani and A. Chen, *Chem. Mater.*, 2007, **19**, 4530-4537.
49. K. Maeda and K. Domen, *J. Phys. Chem. C*, 2007, **111**, 7851-7861.
50. A. Kudo, *MRS Bulletin*, 2011, **36**, 32-38.
51. A. Patsoura, D. I. Kondarides and X. E. Verykios, *Catal. Today*, 2007, **124**, 94-102.
52. H. Yi, T. Peng, D. Ke, D. Ke, L. Zan and C. Yan, *Int. J. Hydrogen Energy*, 2008, **33**, 672-678.
53. T. Berger, A. Rodes and R. Gomez, *Phys. Chem. Chem. Phys.*, 2010, **12**, 10503-10511.
54. X. Wang, K. Maeda, A. Thomas, K. Takanabe, G. Xin, J. M. Carlsson, K. Domen and M. Antonietti, *Nat. Mater.*, 2009, **8**, 76-80.
55. D. S. Su, J. Zhang, B. Frank, A. Thomas, X. Wang, J. Paraknowitsch and R. Schlögl, *ChemSusChem*, 2010, **3**, 169-180.
56. Y. Wang, X. Wang and M. Antonietti, *Angew. Chem., Int. Ed.*, 2012, **51**, 68-89.
57. A. Thomas, A. Fischer, F. Goettmann, M. Antonietti, J.-O. Muller, R. Schlögl and J. M. Carlsson, *J. Mater. Chem.*, 2008, **18**, 4893-4908.
58. E. C. Franklin, *J. Am. Chem. Soc.*, 1922, **44**, 486-509.
59. L. E. Sansores and B. Molina, *Mod. Phys. Lett. B*, 1999, **13**, 193-201.
60. B. V. Lotsch, M. Döblinger, J. Sehnert, L. Seyfarth, J. Senker, O. Oeckler and W. Schnick, *Chem. – Eur. J.*, 2007, **13**, 4969-4980.

61. X. Wang, X. Chen, A. Thomas, X. Fu and M. Antonietti, *Advanced Materials*, 2009, **21**, 1609-1612.
62. Y. Gu, L. Chen, L. Shi, J. Ma, Z. Yang and Y. Qian, *Carbon*, 2003, **41**, 2674-2676.
63. Q. Guo, Y. Xie, X. Wang, S. Lv, T. Hou and X. Liu, *Chem. Phys. Lett.*, 2003, **380**, 84-87.
64. J. Liu, T. Zhang, Z. Wang, G. Dawson and W. Chen, *J. Mater. Chem.*, 2011, **21**, 14398-14401.
65. J. Liu, Y. Zhang, L. Lu, G. Wu and W. Chen, *Chem. Commun.*, 2012, **48**, 8826-8828.
66. Y. Zhang, J. Liu, G. Wu and W. Chen, *Nanoscale*, 2012, **4**, 5300-5303.
67. F. Dong, L. Wu, Y. Sun, M. Fu, Z. Wu and S. C. Lee, *J. Mater. Chem.*, 2011, **21**, 15171-15174.
68. K. Maeda, X. Wang, Y. Nishihara, D. Lu, M. Antonietti and K. Domen, *J. Phys. Chem. C*, 2009, **113**, 4940-4947.
69. B. Jürgens, E. Irran, J. Senker, P. Kroll, H. Müller and W. Schnick, *J. Am. Chem. Soc.*, 2003, **125**, 10288-10300.
70. M. Groenewolt and M. Antonietti, *Adv. Mater.*, 2005, **17**, 1789-1792.
71. Y. Cui, Z. Ding, P. Liu, M. Antonietti, X. Fu and X. Wang, *Phys. Chem. Chem. Phys.*, 2012, **14**, 1455-1462.
72. S. C. Yan, Z. S. Li and Z. G. Zou, *Langmuir*, 2009, **25**, 10397-10401.
73. X. Li, J. Zhang, L. Shen, Y. Ma, W. Lei, Q. Cui and G. Zou, *Appl. Phys. A*, 2009, **94**, 387-392.
74. J. Yu, S. Wang, B. Cheng, Z. Lin and F. Huang, *Catal. Sci. Technol.*, 2013, **3**, 1782-1789.
75. X.-H. Li, X. Wang and M. Antonietti, *Chem. Sci.*, 2012, **3**, 2170-2174.
76. J. Cao, Y. Zhao, H. Lin, B. Xu and S. Chen, *Mater. Res. Bull.*, 2013, **48**, 3873-3880.
77. Y.-S. Xu and W.-D. Zhang, *ChemCatChem*, 2013, **5**, 2343-2351.
78. Y. Di, X. Wang, A. Thomas and M. Antonietti, *ChemCatChem*, 2010, **2**, 834-838.
79. F. Yu, X. Xu, C. J. Baddeley, R. M. Bellabarba, P. Lignier, R. P. Tooze, F. Fina, J. S. T. Irvine and W. Zhou, *CrystEngComm*, 2014, **16**, 1714-1723.
80. Y. Zheng, J. Liu, J. Liang, M. Jaroniec and S. Z. Qiao, *Energy Environ. Sci.*, 2012, **5**, 6717-6731.
81. Y. Wang, Y. Di, M. Antonietti, H. Li, X. Chen and X. Wang, *Chem. Mater.*, 2010, **22**, 5119-5121.

82. G. Liu, P. Niu, C. Sun, S. C. Smith, Z. Chen, G. Q. Lu and H.-M. Cheng, *J. Am. Chem. Soc.*, 2010, **132**, 11642-11648.
83. J. Zhang, J. Sun, K. Maeda, K. Domen, P. Liu, M. Antonietti, X. Fu and X. Wang, *Energy Environ. Sci.*, 2011, **4**, 675-678.
84. J. Zhang, X. Chen, K. Takanahe, K. Maeda, K. Domen, J. D. Epping, X. Fu, M. Antonietti and X. Wang *Angew. Chem., Int. Ed.*, 2010, **49**, 441-444.
85. S. C. Yan, S. B. Lv, Z. S. Li and Z. G. Zou, *Dalton Trans.*, 2010, **39**, 1488-1491.
86. Q. Xiang, J. Yu and M. Jaroniec, *J. Phys. Chem. C*, 2011, **115**, 7355-7363.
87. X. Wang, K. Maeda, X. Chen, K. Takanahe, K. Domen, Y. Hou, X. Fu and M. Antonietti, *J. Am. Chem. Soc.*, 2009, **131**, 1680-1681.
88. J. Xu, L. Zhang, R. Shi and Y. Zhu, *J. Mater. Chem. A*, 2013, **1**, 14766-14772.
89. Y. Zhang, A. Thomas, M. Antonietti and X. Wang, *J. Am. Chem. Soc.*, 2008, **131**, 50-51.
90. B. V. Lotsch and W. Schnick, *Chem. Mater.*, 2006, **18**, 1891-1900.
91. F. Zhang, J. Chen, X. Zhang, W. Gao, R. Jin, N. Guan and Y. Li, *Langmuir*, 2004, **20**, 9329-9334.
92. Y. Mei, G. Sharma, Y. Lu, M. Ballauff, M. Drechsler, T. Irrgang and R. Kempe, *Langmuir*, 2005, **21**, 12229-12234.
93. B. D. Cullity, *Elements of X-Ray Diffraction*, Addison-Wesley Publishing Company, inc., 1956.
94. J. I. Langford and A. J. C. Wilson, *J. Appl. Crystallogr.*, 1978, **11**, 102-113.
95. U. Holzwarth and N. Gibson, *Nat. Nanotechnol.*, 2011, **6**, 534-534.
96. V. D. Mote, Y. Purushotham and B. N. Dole, *J. Theor. Appl. Phys.*, 2012, **6**, 1-8.
97. A. Khorsand Zak, W. H. Abd. Majid, M. E. Abrishami and R. Yousefi, *Solid State Sci.*, 2011, **13**, 251-256.
98. D. Keen, *J. Appl. Cryst.*, 2001, **34**, 172-177.
99. A. K. Soper, Science and T. F. Council, *GudrunN and GudrunX: Programs for Correcting Raw Neutron and X-ray Diffraction Data to Differential Scattering Cross Section*, Science & Technology Facilities Council, 2011.
100. L. Liang, R. Rinaldi and H. Schober, eds., *Neutron Applications in Earth, Energy and Environmental Sciences*, Springer, 2009.
101. D. T. Bowron, A. K. Soper, K. Jones, S. Ansell, S. Birch, J. Norris, L. Perrott, D. Riedel, N. J. Rhodes, S. R. Wakefield, A. Botti, M.-A. Ricci, F. Grazzi and M. Zoppi, *Rev. Sci. Instrum.*, 2010, **81**, -.

102. A. K. Soper, *Mol. Phys.*, 2009, **107**, 1667-1684.
103. C. L. Farrow, P. Juhas, J. W. Liu, D. Bryndin, E. S. Božin, J. Bloch, T. Proffen and S. J. L. Billinge, *J. Phys.: Condens. Matter*, 2007, **19**, 335219.
104. M. J. Duer, *Introduction to Solid-State NMR Spectroscopy*, Blackwell Publishing, 2004.
105. J. Keeler, *Understanding NMR Spectroscopy*, Wiley, 2010.
106. P. J. Hore, *Nuclear Magnetic Resonance*, Oxford University Press, 1915.
107. P. Atkins, T. Overton, J. Rourke, M. Weller and F. Armstrong, *Shriver & Atkins Inorganic Chemistry*, 4th edn., Oxford University Press, 2006.
108. David B. Williams and C. B. Carter, *Transmission Electron Microscopy A Textbook for Materials Science*, Springer, 2009.
109. S. C. Y. Tsen, P. A. Crozier and J. Liu, *Ultramicroscopy*, 2003, **98**, 63-72.
110. W. Zhou and Z. L. Wang, eds., *Scanning Microscopy for Nanotechnology*, Springer, 2006.
111. H.-L. Lee and N. T. Flynn, in *Handbook of Applied Solid State Spectroscopy*, ed. D. R. Vij, Springer, 2006.
112. L. Pauling and J. H. Sturdivant, *Proc. Natl. Acad. Sci. U. S. A.*, 1937, **23**, 615-620.
113. C. E. Redemann and H. J. Lucas, *J. Am. Chem. Soc.*, 1940, **62**, 842-846.
114. E. Kroke and M. Schwarz, *Coord. Chem. Rev.*, 2004, **248**, 493-532.
115. W. Schnick, *Angew. Chem., Int. Ed.*, 1993, **32**, 1580-1581.
116. D. M. Teter and R. J. Hemley, *Science*, 1996, **271**, 53-55.
117. S. Matsumoto, E. Q. Xie and F. Izumi, *Diamond Relat. Mater.*, 1999, **8**, 1175-1182.
118. I. Alves, G. Demazeau, B. Tanguy and F. Weill, *Solid State Commun.*, 1999, **109**, 697-701.
119. E. G. Gillan, *Chem. Mater.*, 2000, **12**, 3906-3912.
120. M. Kawaguchi and K. Nozaki, *Chem. Mater.*, 1995, **7**, 257-264.
121. B. V. Lotsch and W. Schnick, *Chem. Mater.*, 2005, **17**, 3976-3982.
122. M. Döblinger, B. V. Lotsch, J. Wack, J. Thun, J. Senker and W. Schnick, *Chem. Commun.*, 2009, 1541-1543.
123. T. Tyborski, C. Merschjann, S. Orthmann, F. Yang, M.-C. Lux-Steiner and T. Schedel-Niedrig, *J. Phys.: Condens. Matter*, 2013, **25**, 395402.
124. L. Costa and G. Camino, *J. Therm. Anal. Calorim.*, 1988, **34**, 423-429.
125. L. Ge, *Mater. Lett.*, 2011, **65**, 2652-2654.
126. B. V. Lotsch, PhD Thesis, Ludwig-Maximilian University of Munich, 2006.

127. Y. Iwano, T. Kittaka, H. Tabuchi, M. Soukawa, S. Kunitsugu, K. Takarabe and K. Itoh, *Jpn. J. Appl. Phys.*, 2008, **47**, 7842.
128. Y. Zhang, Q. Pan, G. Chai, M. Liang, G. Dong, Q. Zhang and J. Qiu, *Sci. Rep.*, 2013, **3**.
129. T. Tyborski, C. Merschjann, S. Orthmann, F. Yang, M.-C. Lux-Steiner and T. Schedel-Niedrig, *J. Phys.: Condens. Matter*, 2012, **24**, 162201.
130. M. J. Bojdys, J.-O. Müller, M. Antonietti and A. Thomas, *Chem. Eur. J.*, 2008, **14**, 8177-8182.
131. E. Kroke, M. Schwarz, E. Horath-Bordon, P. Kroll, B. Noll and A. D. Norman, *New J. Chem.*, 2002, **26**, 508-512.
132. J. K. Walters, R. J. Newport, W. S. Howells and G. Bushnell-Wye, *J. Phys.: Condens. Matter*, 1996, **8**, 4739.
133. A. K. Soper, *GudronN and GudronX*, 2012.
134. V. F. Sears, *Neutron News*, 1992, **3**, 26-37.
135. F. H. Allen, O. Kennard, D. G. Watson, L. Brammer, A. G. Orpen and R. Taylor, *J. Chem. Soc., Perkin Trans. 2*, 1987, S1-S19.
136. Z. Q. Tian, S. P. Jiang, Y. M. Liang and P. K. Shen, *J. Phys. Chem. B*, 2006, **110**, 5343-5350.
137. Y. Ikuma and H. Bessho, *Int. J. Hydrogen Energy*, 2007, **32**, 2689-2692.
138. R. Li, W. Chen, H. Kobayashi and C. Ma, *Green Chem.*, 2010, **12**, 212-215.
139. W. Hou and S. B. Cronin, *Adv. Funct. Mater.*, 2013, **23**, 1612-1619.
140. S. Linic, P. Christopher and D. B. Ingram, *Nat. Mater.*, 2011, **10**, 911-921.
141. M. A. Garcia, *J. Phys. D: Appl. Phys*, 2011, **44**, 283001.
142. S. Sarina, H.-Y. Zhu, Q. Xiao, E. Jaatinen, J. Jia, Y. Huang, Z. Zheng and H. Wu, *Angew. Chem., Int. Ed.*, 2014, doi: 10.1002/anie.201308145.
143. P. V. Kamat, *J. Phys. Chem. Lett.*, 2012, **3**, 663-672.
144. V. Iliev, D. Tomova, L. Bilyarska, A. Eliyas and L. Petrov, *Appl. Catal., B*, 2006, **63**, 266-271.
145. Q. Guo, Y. Xie, X. Wang, S. Zhang, T. Hou and S. Lv, *Chem. Commun.*, 2004, **0**, 26-27.
146. M. Kim, S. Hwang and J.-S. Yu, *J. Mater. Chem.*, 2007, **17**, 1656-1659.
147. J. T. Titantah and D. Lamoen, *Diamond Relat. Mater.*, 2007, **16**, 581-588.
148. A. P. Dementjev, A. de Graaf, M. C. M. van de Sanden, K. I. Maslakov, A. V. Naumkin and A. A. Serov, *Diamond Relat. Mater.*, 2000, **9**, 1904-1907.

149. B. Yue, Q. Li, H. Iwai, T. Kako and J. Ye, *Sci. Technol. Adv. Mater.*, 2011, **12**, 034401.
150. Z.-H. Sheng, L. Shao, J.-J. Chen, W.-J. Bao, F.-B. Wang and X.-H. Xia, *ACS Nano*, 2011, **5**, 4350-4358.
151. B. Yue, Y. Ma, H. Tao, L. Yu, G. Jian, X. Wang, X. Wang, Y. Lu and Z. Hu, *J. Mater. Chem.*, 2008, **18**, 1747-1750.
152. J. R. McBride, G. W. Graham, C. R. Peters and W. H. Weber, *J. Appl. Phys.*, 1991, **69**, 1596-1604.
153. Y. Mu, H. Liang, J. Hu, L. Jiang and L. Wan, *J. Phys. Chem. B*, 2005, **109**, 22212-22216.
154. B. V. Crist, *Handbooks of Monochromatic XPS Spectra*, XPS International, Inc., 1999.
155. A. S. Aricò, A. K. Shukla, H. Kim, S. Park, M. Min and V. Antonucci, *Appl. Surf. Sci.*, 2001, **172**, 33-40.
156. S. H. Yang, W. H. Shin, J. W. Lee, H. S. Kim, J. K. Kang and Y. K. Kim, *Appl. Phys. Lett.*, 2007, **90**, -.
157. A. Zamudio, A. L. Elías, J. A. Rodríguez-Manzo, F. López-Urías, G. Rodríguez-Gattorno, F. Lupo, M. Rühle, D. J. Smith, H. Terrones, D. Díaz and M. Terrones, *Small*, 2006, **2**, 346-350.
158. L. J. Durndell, C. M. A. Parlett, N. S. Hondow, K. Wilson and A. F. Lee, *Nanoscale*, 2013, **5**, 5412-5419.
159. A. F. Lee, K. Wilson, R. M. Lambert, C. P. Hubbard, R. G. Hurley, R. W. McCabe and H. S. Gandhi, *J. Catal.*, 1999, **184**, 491-498.
160. J. E. Drawdy, G. B. Hoflund, S. D. Gardner, E. Yngvadottir and D. R. Schryer, *Surf. Interface Anal.*, 1990, **16**, 369-374.
161. G. L. Bezemer, J. H. Bitter, H. P. C. E. Kuipers, H. Oosterbeek, J. E. Holewijn, X. Xu, F. Kapteijn, A. J. van Dillen and K. P. de Jong, *J. Am. Chem. Soc.*, 2006, **128**, 3956-3964.
162. K. Kinoshita, *J. Electrochem. Soc.*, 1990, **137**, 845-848.
163. O. M. Wilson, M. R. Knecht, J. C. Garcia-Martinez and R. M. Crooks, *J. Am. Chem. Soc.*, 2006, **128**, 4510-4511.
164. A.-X. Yin, X.-Q. Min, Y.-W. Zhang and C.-H. Yan, *J. Am. Chem. Soc.*, 2011, **133**, 3816-3819.

165. N. Markovic, H. Gasteiger and P. N. Ross, *J. Electrochem. Soc.*, 1997, **144**, 1591-1597.
166. Y. Li, G. Lu and S. Li, *Appl. Catal., A*, 2001, **214**, 179-185.
167. S. Horikoshi, N. Watanabe, M. Mukae, H. Hidaka and N. Serpone, *New J. Chem.*, 2001, **25**, 999-1005.
168. J. Wu and H. Yang, *Acc. Chem. Res.*, 2013, **46**, 1848-1857.
169. S. Rawalekar and T. Mokari, *Adv. Energy Mater.*, 2013, **3**, 12-27.
170. Q. Zhai, S. Xie, W. Fan, Q. Zhang, Y. Wang, W. Deng and Y. Wang, *Angew. Chem.*, 2013, **125**, 5888-5891.
171. X. Zhang, F. Han, B. Shi, S. Farsinezhad, G. P. Dechaine and K. Shankar, *Angew. Chem., Int. Ed.*, 2012, **51**, 12732-12735.
172. E. Kowalska, M. Janczarek, L. Rosa, S. Juodkazis and B. Ohtani, *Catal. Today*, 2014, **230**, 131-137.
173. D. Tsukamoto, A. Shiro, Y. Shiraishi, Y. Sugano, S. Ichikawa, S. Tanaka and T. Hirai, *ACS Catal.*, 2012, **2**, 599-603.
174. Y. Shiraishi, H. Sakamoto, Y. Sugano, S. Ichikawa and T. Hirai, *ACS Nano*, 2013, **7**, 9287-9297.
175. A. Gallo, M. Marelli, R. Psaro, V. Gombac, T. Montini, P. Fornasiero, R. Pievo and V. D. Santo, *Green Chem.*, 2012, **14**, 330-333.
176. R. T. Tung, *Appl. Phys. Rev.*, 2014, **1**, -.
177. D. E. Aspnes and A. Heller, *J. Phys. Chem.*, 1983, **87**, 4919-4929.
178. P. A. Cox, *The Electronic Structure and Chemistry of Solids*, Oxford Science Publications, 1987.
179. I. Pašti and S. Mentus, *Mater. Chem. Phys.*, 2009, **116**, 94-101.
180. J. Kugai, J. T. Miller, N. Guo and C. Song, *J. Catal.*, 2011, **277**, 46-53.
181. V. Y. Borovkov, D. R. Luebke, V. I. Kovalchuk and J. L. d'Itri, *J. Phys. Chem. B*, 2003, **107**, 5568-5574.
182. M. Ammam and E. B. Easton, *J. Power Sources*, 2013, **222**, 79-87.
183. D. Zhao, B. Yan and B.-Q. Xu, *Electrochem. Commun.*, 2008, **10**, 884-887.
184. F. Epron, F. Gauthard, C. Pinéda and J. Barbier, *J. Catal.*, 2001, **198**, 309-318.
185. Z. Xu, H. Zhang, S. Liu, B. Zhang, H. Zhong and D. S. Su, *Int. J. Hydrogen Energy*, 2012, **37**, 17978-17983.
186. N. Barrabés, J. Just, A. Dafinov, F. Medina, J. L. G. Fierro, J. E. Sueiras, P. Salagre and Y. Cesteros, *Appl. Catal., B*, 2006, **62**, 77-85.

187. Z. Jiang, J. Zhu, D. Liu, W. Wei, J. Xie and M. Chen, *CrystEngComm*, 2014, **16**, 2384-2394.
188. R. Mu, Q. Fu, H. Liu, D. Tan, R. Zhai and X. Bao, *Appl. Surf. Sci.*, 2009, **255**, 7296-7301.
189. S. K. Singh and Q. Xu, *Inorg. Chem.*, 2010, **49**, 6148-6152.
190. Z.-C. Wang, Z.-M. Ma and H.-L. Li, *Appl. Surf. Sci.*, 2008, **254**, 6521-6526.
191. R. Loukrakpam, J. Luo, T. He, Y. Chen, Z. Xu, P. N. Njoki, B. N. Wanjala, B. Fang, D. Mott, J. Yin, J. Klar, B. Powell and C.-J. Zhong, *J. Phys. Chem. C*, 2011, **115**, 1682-1694.
192. D. Wang, H. L. Xin, R. Hovden, H. Wang, Y. Yu, D. A. Muller, F. J. DiSalvo and H. D. Abruña, *Nat. Mater.*, 2013, **12**, 81-87.
193. J. R. C. Salgado, E. Antolini and E. R. Gonzalez, *J. Power Sources*, 2004, **138**, 56-60.
194. W. S. Epling, P. K. Cheekatamarla and A. M. Lane, *Chem. Eng. J.*, 2003, **93**, 61-68.
195. T. Komatsu and A. Tamura, *J. Catal.*, 2008, **258**, 306-314.
196. S. Zhou, B. Varughese, B. Eichhorn, G. Jackson and K. McIlwrath, *Angew. Chem., Int. Ed.*, 2005, **44**, 4539-4543.
197. M. Liu, Y. Lu and W. Chen, *Adv. Funct. Mater.*, 2013, **23**, 1289-1296.
198. Z. Peng and H. Yang, *Nano Today*, 2009, **4**, 143-164.
199. D. Alloyeau, C. Ricolleau, C. Mottet, T. Oikawa, C. Langlois, Y. Le Bouar, N. Braidy and A. Loiseau, *Nat. Mater.*, 2009, **8**, 940-946.
200. C. Wang, H. Daimon, T. Onodera, T. Koda and S. Sun, *Angew. Chem., Int. Ed.*, 2008, **47**, 3588-3591.